HotFire Final Design Report

The Design of a Hot Plume Test Facility

Simon Baar
Joris van den Berg
Dobbin Huang
Timo Keil
Mikael Kaandorp
Jongseok Lee
Felix Lindemann
Jim Rojer
Jan Rose

Delft University of Technology

TU Delft Delft University of Technology

Challenge the future

HotFire Final Design Report

The Design of a Hot Plume Test Facility

by

S. Baar	**4173686**	**J. Lee**	**4176901**
J. van den Berg	**4164636**	**F. Lindemann**	**4192850**
D. Huang	**4031083**	**J. Rojer**	**4080726**
T.H. Keil	**4155637**	**J.N. Rose**	**4152891**
M.L.A. Kaandorp	**4137795**		

as part of the

Design Synthesis Exercise
B.Sc. in Aerospace Engineering

at Delft University of Technology.

Tutors:	Dr. F.F.J. Schrijer,	Aerodynamics
	Dr. A.H. van Zuijlen,	Aerodynamics
Coaches:	Dr. D.I. Gransden,	Structural Integrity & Composites
	A. Chaves Jiménez,	Space Systems Engineering

A copy of this report is available on request.

TU Delft Delft University of Technology

Cover: Image ©ESA
Photo of an Ariane 5 launcher after lift-off.

PREFACE

The Design Synthesis Exercise (DSE) is an integral part of the curriculum of the Bachelor of Science at the Faculty of Aerospace Engineering, Delft University of Technology. It concludes the Bachelor program in an 11 week-long, full-time project, where a team of 8–10 students conducts a design exercise. Here, all knowledge acquired from prior courses as well as analytical skills and design experience gained over the course of three years come together.

The HotFire DSE project aims at designing a hot plume test facility able to investigate the base region of a launcher by means of a wind tunnel model. The challenge at hand is the miniaturization of a full-size rocket launcher to a model that fits within a wind tunnel. If successful, the HotFire test facility will help in gathering valuable scientific data to contribute to a better design of launch vehicles. Currently, their design is based on inaccurate predictions of the base pressure, the underestimation of which results in over-designed thrusters and decreased payload capabilities.

The purpose of this Final Technical Design Report is to present the final design of this HotFire test facility. It is the fourth and last in a series of reports delivered, which are depicted in Figure 1 in chronological order. It follows the Project Plan in which the project was defined and the group organization was presented; the Baseline Report, where a requirement analysis was performed, the impact of the product was assessed, an extensive literature study was performed, and risks were identified; and the Mid-Term Technical Design Report that selected the concept elaborated in this report.

Following this report a Final Review will be held, in which the final design is presented in detail and the justification behind the design choices is further explained. This presentation is the final technical milestone of the project. The symposium, which is organized afterwards to give every DSE group the chance to present their project publicly, will conclude this project.

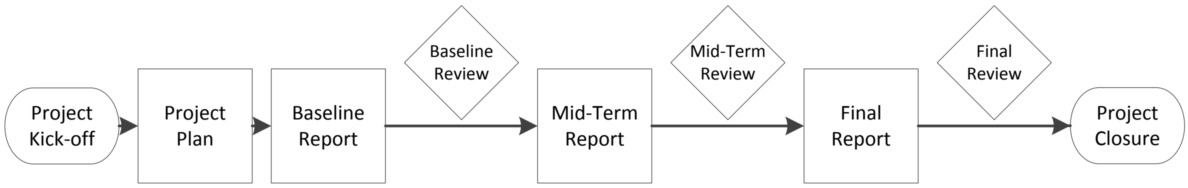

Figure 1: Timeline of DSE project deliverables and milestones

Readers interested in a concise overview of the design as a whole are referred to Chapter 3. For a detailed design description of each subsystem, the relevant chapters should be consulted. All technical drawings of these subsystems are presented in Appendix A. Those particularly interested in the operational considerations are kindly referred to Chapter 11. Persons worried about the safety of this miniature rocket engine can find information in the same chapter. Furthermore, for an outlook into the future of HotFire, the interested reader is directed to Chapter 12.

We would like to express our gratitude to our tutors, Dr. F.F.J. Schrijer and Dr. A.H. van Zuijlen, and coaches, Dr. D.I. Gransden and A. Chaves Jiménez, for their constant support and valuable feedback throughout the project. Furthermore, the group wants to thank Ir. B.T.C. Zandbergen for his input during the selection of the propellant and for sharing his experience in thermal rocket propulsion. Appreciations also go to Dr. A. Cervone for his interesting and helpful ideas regarding the feed system and to H. J. Siemer for his help regarding the safety of HotFire. Finally, credit goes to all other staff members at Delft University of Technology who contributed to this project in various ways.

Delft, June 30, 2014

SUMMARY

In this report the analysis and design of a hot plume test facility is presented, which is able to investigate the base region of a launcher by means of a wind tunnel model. There is a lack of knowledge about the aero- and thermodynamics in the base region of rockets; the base pressure and temperature cannot be predicted accurately. By creating a hot plume test facility with a plume similar to that of a real launcher, valuable scientific data can be obtained to better understand the flow in the base region. Previous experimental research used cold plumes to investigate the flow in the base region. It has been found that there is a large difference between using a hot and a cold plume: for a cold plume, the base pressure is underestimated and the fluctuating pressures do not match. Furthermore, the base heating cannot be simulated. Creating a hot plume test facility is much more challenging than a cold plume test facility due to the miniaturization of only the model, but also the combustion process. Until now, this challenge has been avoided by relying on cold plumes that simulate everything but the temperature effect.

In order to design the hot plume test facility, first the different subsystems and their interfaces are analyzed. A rendering of the entire HotFire system including the subsystems inside the wind tunnel is depicted in Figure 2. The subsystems, which are analyzed in this report, are the propellant, the feed system, the aerodynamic shape, the mount, the ignition system, the combustion chamber, the nozzle, and the instrumentation.

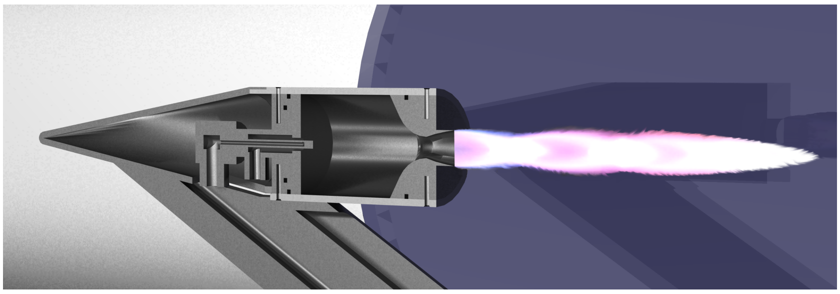

Figure 2: Artist impression of the complete HotFire system

For the propellant, a fuel and an oxidizer were selected based on their toxicity, commercial availability, and characteristic length (defines the required combustion chamber length). The performance of the propellant was judged by analyzing five similarity parameters using the HotFire Design Analysis Tool (HFDAT), namely the pressure ratio (I), the initial inclination angle (II), the momentum flux ratio (III), the mass flux ratio (IV), and the kinetic energy ratio (V) between plume and freestream. These parameters are used to assess the similarity of the hot plume to a real launcher and to the cold plume. Data for the combustion characteristics was created using the commercial software Rocket Propulsion Analysis (RPA). The best propellant option for the hot plume was found to be a combination of kerosene and gaseous oxygen. Compared to the Vulcain 2 engine, the hot plume meets similarity parameters I, II, III, IV, and V by 7%, 15%, 56%, 116%, and 12%, respectively. Analogously to the approach for the hot plume, different concepts for cold plumes were analyzed, which should be similar to the hot plume. The best option for the cold plume was helium. The cold plume compares to the launcher with deviations of 7%, 15%, 56%, 6%, and 157%, and thus performs better on mass flux ratio compared to the hot plume, but worse with respect to the kinetic energy ratio. Since both parameters depend on the temperature, and all other parameters are matched to a similar extend, HotFire allows for comparison of one parameter between hot and cold plume.

Safety considerations are crucial for the design of the feed system, as high pressures are needed for operation. The feed system is designed as a blow down system using commercially available pressurized tanks to ensure safe operation while storing a minimal amount of propellant. An oxygen tank is selected with a pressure of 200 bar and a volume of 20 L. The kerosene tank is pressurized by means of a nitrogen tank, which also has a pressure of 200 bar and a volume of 20 L. Commercially available feed lines were selected, which are able to withstand the pressure and deal with the reactive characteristics of the propellant. The tanks and the feed lines are connected via electronically operated valves to enable remote control. Relief valves were added to the system to avoid single points of failure. Optimal mixing and minimal complexity for the injector is obtained by using a combination of a coaxial and splash injector. In the end, the total pressure loss over the whole system was calculated to be 9.25 bar for the kerosene branch and 15.68 bar for the oxygen branch.

The aerodynamic shape of HotFire was designed to have the desired flow field around the model. Shock waves and their reflections from the wind tunnel walls were analyzed to prevent them from entering the base region by using analytical and CFD (ANSYS and NUMECA) calculations. The operational forces and start-up loads were analyzed as well; the drag was determined to be 250 N, the thrust was determined to be 325 N, and the start-up loads for x-, y- and z-direction were determined to be 391 N, 1002 N, and 1848 N, respectively. The model was designed to have a diameter of 50 mm with a nose cone length of 135 mm for optimal shock wave propagation and a body length of 105 mm to fit the internal components.

A sting mount is designed to hold the model in place and to accommodate the feed lines. Choosing a sting mount over a window mount decreases the blockage of the wind tunnel. The mount was analyzed for static, dynamic, and thermal loads. The static and dynamic analysis is done both analytically and using FEM software (ANSYS). Using a safety factor of 2, the mount was designed to sustain a maximum von Mises stress of ca. 440 MPa, which is below the specified 450 MPa for the chosen "Uddeholm Impax Supreme" steel with a yield stress of 900 MPa. The lowest eigenmodes were found to be ca. 40 Hz. The frequency caused by the base pressure pulsation frequency was calculated to be about 1200 Hz, but experimental research is needed to validate this and to determine other frequencies caused by the aerodynamic behavior and the engine. The maximum temperature of the mount was calculated to be 504 K.

The ignitor should ignite the kerosene-oxygen mixture, which has an oxidizer to fuel ratio of 1.2. Information about the flammability and autoignition of this mixture at 30 bar is not available, but it has been shown that it is possible to ignite the mixture using a ignitor with an energy of 151.6 J. Using a spark plug as ignitor type is considered the easiest option. It is recommended to test this possibility first by means of a static test.

The propellant is ignited inside the combustion chamber and expanded through the nozzle to create a plume with the desired conditions. The concept of a cylindrical chamber was selected as it provided the minimum cross-section area of all concepts. For the nozzle a bell shaped nozzle was selected since it is shorter and makes it easier to achieve the required lip angles of 7 degrees for the hot plume and 10 degrees for the cold plume. The area ratios for the hot and cold plume were determined to be 2.8 and 1.6, respectively. As the lip angle and the area ratio for hot and cold plume are different, an interchangeable nozzle is necessary, keeping the combustion chamber the same. The thickness of the combustion chamber was determined by structural and thermal analysis. The results of the analysis showed that steel with a thickness of 2.5 mm can be used for the combustion chamber. For the nozzle, graphite was selected due to high temperatures at the throat and uncertainty of the base heating for the divergent part of the nozzle. Lastly, a CFD-based estimation of the plume dimensions showed that the current design of the thrust chamber results in the required plume size.

In order to measure the phenomena in the base region of the model pressure sensors, temperature sensors, and Particle Image Velocimetry (PIV) have been identified as the required sensors types. Two pressure sensors of types "HI2200" and "Parker ASIC" will be placed at the base plate and inside the combustion chamber to measure the chamber pressure and unsteady pressures at the base region, respectively. A K-type thermocouple will be placed at the base plate to measure the base heating. Furthermore, a load cell will measure the mass flow of propellants by measuring the change in weight of the tanks over time, and a thermal camera will determine the chamber wall temperature for safety reasons. Lastly, PIV equipment will measure the velocity of the base region flow field, the actual scientific measurement.

In a later stage after the DSE of the HotFire system design, funds need to be obtained by submitting research proposals, a test series is needed to verify and validate the detailed design, and finally HotFire needs to be built. Therefore, joining methods will still need to be analyzed and further research in the subsystem design considerations needs to be conducted. The production and material costs are expected to be small compared to the development costs. Static tests are proposed to analyze the plume stability conditions and to analyze the combustion instabilities.

Summarizing, all the above subsystems compose a final product that will obtain additional knowledge about the aerodynamic properties of flow near the base region of rockets, ultimately leading to more efficient and sustainable launchers.

TABLE OF CONTENTS

LIST OF FIGURES

List of Tables

Nomenclature

Roman letters

$\dot{m}$	Mass flow rate	[kg/s]
$\dot{q}$	Heat flux	[W/m^2]
$\dot{r}$	Regression rate	[m/s]
V	Velocity	[m/s]
σ_{boltz}	Boltzman coefficient	[J/(s m^2 K^4)
A	Area	[m^2]
a	Speed of sound	[m/s]
AR	Nozzle exit to throat ratio	[-]
c	Damping coefficient	[(N s)/m]
$c^\star$	Characteristic velocity	[m/s]
C_d	Coefficient of discharge	[-]
C_i	Internal energy	[J]
c_p	Heat capacity at constant pressure	[J/kg K]
c_m	Specific heat	[J/kg K]
D	Larger diameter	[m]
d	(Smaller) diameter	[m]
E	Energy	[J]
e	Specific internal energy	[J/kg^1]
F	Force	[N]
f	Darcy-Weisbach friction factor	[-]
f	Frequency	[Hz]
F/O	Fuel to oxidizer ratio (volume)	[-]
f_n	Eigenfrequency	[Hz]
G	Shear modulus	[GPa]
G_0	Oxidizer mass velocity	[kg/(m^2 s)]
H	Enthalpy	[J/kg]
h	Convection coefficient	[W/(m^2 K)]
I	Area moment of inertia	[m^4]
K	Loss coefficient	[-]
k	Stiffness	[N/m]
L	Length	[m]
$L^\star$	Characteristic length of combustion chamber (liquid propellant engine)	[m]
M	Mach number	[-]
m	Mass	[kg]
N	Pressure ratio $\sqrt{\frac{p_j}{p_\infty}}$	[-]
Nu	Nusselt Number	[-]
O/F	Oxidizer to Fuel Ratio (mass)	[-]
P	Power	[J/s]
P	Pressure	[Pa]
Pr	Prandtl number	[-]
Q	Volumetric flow rate	[m^3/s]
q	Heat flow	[W]
R	Radius	[m]
R	Specific gas constant	[J/(kg K)]
r	Radius	[m]
R_{carbon}	Thermal resistivity of carbon deposit layer	[m^2 K/W]
R_u	Radius of curvature	[m]
Re	Reynolds number	[-]

S	Shear force	[N]
St	Strouhal number	[-]
T	Temperature	[K]
t	Time	[s]
V	Volume	[m^3]
v	Prandtl Meyer function	[deg]
Y	von Mises stress	[Pa]
y	Ratio of total to static pressure drop across the orifice	[-]
Greek letters		
α	Thermal expansion coefficient	[-]
β	Expression of the Mach number $\sqrt{M^2-1}$	[-]
β	Oblique shock wave angle	[rad]
Δ	Deflection	[m]
Δ	Differential	[-]
δ	Initial inclination angle	[deg]
ϵ	Emissivity coefficient	[-]
ϵ	Surface roughness	[m]
γ	Ratio of specific heats	[-]
κ	Thermal conductivity	[W/(m K)]
μ	Dynamic viscosity	[kg/(m s)]
ν	Prandtl-Meyer function	[rad]
Φ	Angle of twist	[rad]
Φ	Equivalence ratio	[-]
ϕ	Shock wave reflection angle	[deg]
ρ	Density	[kg/m^3]
σ	Stress	[Pa]
τ	Shear stress	[Pa]
Θ	Circumferential position along mount cross-section	[rad]
θ	Angle of inclined beam for mount	[deg]
θ	Cone angle	[deg]
θ	Feed line bend angle	[deg]
θ	Wedge/flow deflection angle	[rad]
θ_c	Real cone angle	[deg]
θ_N	Nozzle exit angle	[deg]
ς	molecular fraction	[-]
ζ	Damping ratio	[-]
Subscripts		
0	Total	
1	Upstream	
2	Downstream	
∞	Free stream or outside of model	
θ	Angular component	
avg	Average	
b	Burn	
c	Combustion chamber	
$circ$	Circumferential component	
d	Drag	
e	Exit	
i	Index	
inn	Inner	
j	Jet	
l	Longitudinal component	
m	Model	
n	Normal to the shock wave	
out	Outer	
p	Propellant	

pl	Plume
r	Radial component
T	Thrust
t	Throat
v	Vehicle
Acronyms	
AHP	Analytical Hierarchy Process
CFD	Computational Fluid Dynamics
DARE	Delft Aerospace Rocket Engineering
DSE	Design Synthesis Exercise
FEM	Finite Element Method
FESTIP	Future European Space Transportation Investigations Programme
HFDST	HotFire Design Space Tool
RPA	Rocket Propulsion Analysis
DNW	Duits-Nederlandse Windtunnels
ESA	European Space Agency
HFDAT	HotFire Design Analysis Tool
LFL	Lower flammability limit
OSW	Oblique Shock Wave
PIV	Particle Image Velocimetry
PME	Prandtl-Meyer Expansion
PME	Prandtl-Meyer Expansion
SRB	Solid Rocket Booster
UFL	Upper flammability limit

1
INTRODUCTION

The purpose of this report is to present a feasible preliminary design of the HotFire test facility. It contains a description of the system as a whole and on subsystem level, and it justifies the design decisions that have been made.

1.1. BACKGROUND AND PROBLEM IDENTIFICATION

Nowadays, a variety of different launchers exist, capable of lifting payloads into orbit around Earth. A selection of these can be seen in Figure 1.1. While all have different shapes and payload capabilities, they share one crucial "feature"—all are overdesigned.

During the first flights of the Space Shuttle, it was found that the pressure in the base region of the Solid Rocket Boosters (SRBs) had been underestimated. This resulted in 453.6 kg of additional payload that could be launched in later missions [1]. Although this equates to only 0.1% of the Space Shuttle mass in relative terms, the absolute number cannot be neglected in an industry that is willing to spend thousands of dollars for every saved kilogram.

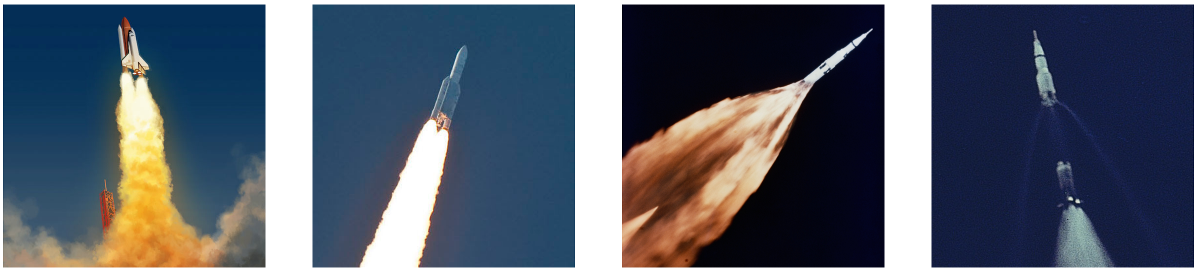

(a) Space Shuttle: RS-25 engine with SRBs, [2]

(b) Ariane 5: Vulcain 2 engine with SRBs, [3]

(c) Saturn V: F-1 engine as first stage, [4]

(d) Saturn V: Separation, J-2 engine as second stage, [5]

Figure 1.1: Plume of various launching rockets

But how could NASA, the institute employing arguably the best aerospace engineers worldwide, have misjudged this? The overdesign cannot be attributed to a mistake by the engineering team; in fact, it is a direct result of the lack of knowledge about the aero- and thermodynamics in the base region of rockets. The exact base pressure and temperature could not and still cannot be predicted accurately.

This has two effects on the launcher design: First of all, not knowing the exact thermal loads on the base plate requires larger design margins for the thermal protection of the base plate. And two: the underestimation of the base region pressure means that the drag is overestimated. Secondly, the design is thought to require more thrust. Both issues mean that launchers carry too much fuel and/or too little payload into orbit.

For the design of more efficient future launchers, it is therefore desired to gain better knowledge of this base region. As in-flight measurements are too expensive, wind tunnel tests must be performed to understand the base flow phenomena and to develop accurate and validated computational methods.

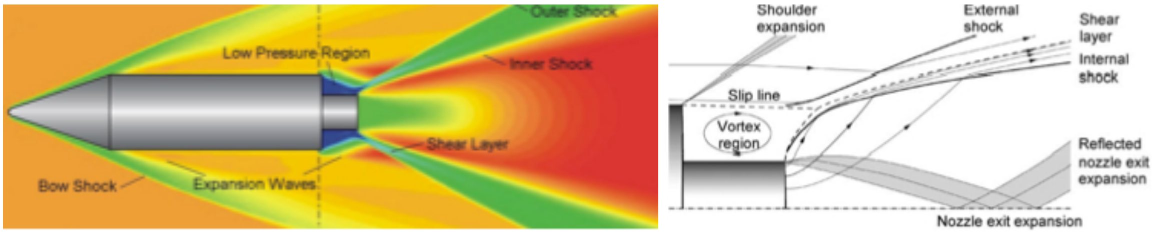

(a) Mach number contours around launcher body, [6, p.41]

(b) Sketch of the flow field in the base region, [6, p.30]

Figure 1.2: Description of the problem and sketch of the base region

Only the global picture of what happens in the base region is well understood. Figure 1.2a illustrates the flow field around a launcher. The low pressure in the vortex/dead air region seen in Figure 1.2b is a result of the interaction of the exhaust plume with the exterior flow. This area, dominated by a highly unsteady flow field, induces pressure and heat loads and causes the entrainment of the hot exhaust gases, resulting in significant base heating. Up until now, non-experimental methods have not succeeded in accurately predicting this heating or the underlying flow patterns. Therefore, various attempts (e.g. [7], [8], [1], [9], [10], [11], [12]) have been made to obtain better data from wind tunnel tests, using rocket models exhausting cold gas.

Half a century of tests, from early attempts in the 1960s [8] to the most recent experiments performed in 2013 [7], has shown that cold exhaust plumes fail to provide sufficiently accurate and detailed information about pressure loads. However, these tests did yield very useful information about the causes for the failures. Parameters were found that need to be reproduced for the simulation of rocket exhaust plumes in ground tests. It was shown that in order to recreate the flow patterns associated with an exhaust plume, the significant ones of those so-called “similarity parameters” are the initial inclination angle of the plume and the pressure, momentum flux, mass flux, and kinetic energy ratios of plume to freestream. For a more detailed discussion of the similarity parameters and their use in the design of the HotFire test set-up, the reader is kindly referred to Section 4.4.

Achieving all those similarity parameters with a cold plume proved very difficult. Beyond the obvious lack of capability of reproducing temperature effects, cold plumes also do not reach the required mass and momentum flux ratios or pressure ratio [7]. Despite this, up until now cold plumes remain the only option to perform experiments on the flow field around the base region of a rocket. The reason for this are the technical difficulties associated with miniaturizing a rocket engine. DSE Group 14 has been working on exactly this for the past eleven weeks in spring 2014: the development of a model rocket engine that is small and safe enough to be operated inside a wind tunnel. With this model, hopefully knowledge of base flow physics will be gained that can be used to improve future generations of launchers.

1.2. DEFINITION OF HOTFIRE

From the problem identification in the previous section, the need was derived that

> *”for the optimal design of future launchers, knowledge about the actual heat and pressure loads in the base region in presence of a hot exhaust plume is needed.”*

“HotFire” strives to close this gap of knowledge. As discussed, there has not been much progress in building a fully functional rocket engine small enough to be operated inside a supersonic wind tunnel, mainly due to the challenges associated with miniaturization.

Therefore, the mission statement is that

> *”the hot plume test facility “HotFire” will investigate the interaction of the hot exhaust plume with the external flow in the base region of a launcher model.”*

This rocket model will be used by research staff in the TST-27 supersonic wind tunnel at the aerodynamics laboratory at Delft University of Technology. To give a clear impression of what the HotFire test set-up is and is not going to be, an “IS–IS-NOT” comparison is outlined in Table 1.1.

Table 1.1: Overview of what HotFire is and what it is not

IS	–	IS NOT
a plume generator installation in the TST-27	–	meant for different wind tunnels
a model of a rocket motor	–	a model of a whole launcher
a measurement set-up	–	meant for flight
able to predict experimental conditions	–	a detailed flow prediction tool
meant for fundamental scientific research	–	meant for rocket engine design/testing

1.3. IMPACT ASSESSMENT OF HOTFIRE

An impact assessment is performed to investigate the commercial attractiveness of the project and to judge its environmental impact. This is separated into a market analysis and strategy for sustainability.

1.3.1. MARKET ANALYSIS

A market analysis has the purpose to identify the attractiveness of the product for the market. This is done by

- identifying the customers and their needs,
- identifying the strategies and the impact of the product, and
- identifying market share, competition, opportunities, and threats.

IDENTIFYING THE CUSTOMERS AND THEIR NEEDS

There are multiple companies and institutes working on the development of new launchers. A current problem in designing these launchers is that the base flow of the rocket is still very hard to predict, which leads to overdesigned launchers.

DSE Group 14 is working on a solution for this problem, by designing a hot plume test facility that will simulate the base region inside the wind tunnel. The knowledge gained by the test facility can be of interest for several parties. These parties will be identified as the potential customers for HotFire. Delft University of Technology has taken the initiative to start this project. Furthermore, the knowledge that will be gained by the product may be of interest to other parties active in the aerospace industry, such as NLR, DLR, ESA, NASA, or SpaceX.

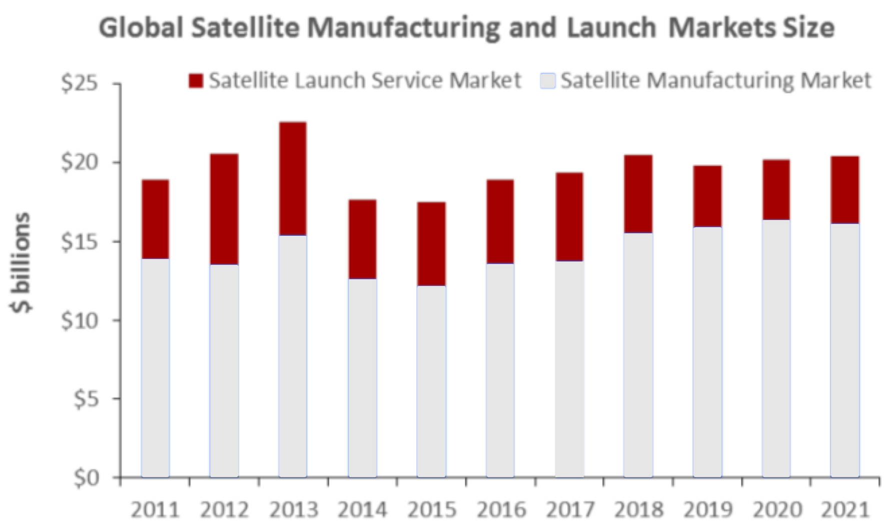

Figure 1.3: Expected global satellite manufacturing and launch market size, [13]

Figure 1.3 shows an estimation of the satellite and launcher market size for the near future. For launchers, it is predicted to be 4 billion Dollar per year. According to [13], the global satellite and launch market appear to face a period of stagnation, given the cyclical nature of the market. Radical changes are needed according to [13] to attract new costumers and stimulate further growth of the space sector.

IDENTIFYING THE STRATEGIES AND THE IMPACT OF THE PRODUCT

Delft University of Technology aims to gain knowledge on the base region to improve launcher design and thereby reduce the cost of launching satellites/humans into space. The reduced cost can increase the potential of the market. Therefore, the impact of the product is expected to be significant and could possibly bring about the radical changes needed to stimulate the space sector.

Strategies that are incorporated are to develop a cheap product that can be released in a relatively short time. Since HotFire will be integrated into the existing TST-27 wind tunnel, it is expected to be of low cost. The use of an existing wind tunnel also reduces the development time significantly.

IDENTIFYING MARKET SHARE, COMPETITION, OPPORTUNITIES, AND THREATS

Since there is no product able to investigate the base region properly yet, releasing a test set-up on the market that is able to do this will immediately lead to a potential of a large market share. It is known that other companies and institutions are currently researching this topic, too, meaning that they are classified as competitors.

For the success of the product, it is essential to stay ahead of the competition. An opportunity to do so is by releasing the product before the competitors, at a lower price. In case the competitors release their product earlier, an opportunity is to release a more cost-effective product to be more competitive. Another option would be to invest more time and resources to arrive at a better-performing product.

The fact that theory on the base region is a relatively unknown area means that designing a test set-up measuring this region contains a certain risk: It is hard to predict whether the final model actually represents the desired conditions.

1.3.2. CONSIDERATIONS ON SUSTAINABILITY

A successful development of the hot plume test facility should provide a path towards more sustainable launchers. Since launchers are overdesigned, a better sustainability can be achieved by improving their design.

However, there is another consideration besides the beneficial influence on future development that must be addressed when considering sustainability. HotFire as a product has an environmental impact during the three phases production, operation, and disposal are considered.

There is no need to produce more than one operational model (in addition to possible prototypes and/or mock-ups). Therefore, the sustainability factors in production, namely materials, manufacturing techniques, and transportation, do not apply here to a significant extent. Also, the end-of-life disposal of the model does not need significant investigation regarding sustainability; it will most likely be stored in a shelf at the university.

The biggest consideration is the negative impact of the product during operations. The use of toxic seeding particles for flow visualization such as PIV measurements as well as the polluting character of the propellant pose potential risks. The need for numerous runs for prototype testing and verification purposes means that a significant amount of propellant will be exhausted before the actual scientific mission of the product begins. It is therefore desirable to limit the amount of tests to the minimum and perform verification by analysis wherever this is considered accurate enough.

To conclude, HotFire is intended for use in scientific research and will thus only have a marginal negative impact. Overall, it is clear that the relatively short run time, small scale and the future scientific value gained from developing and using the product outweigh the immediate negative impact of HotFire.

2
Concept Selection

The chapter aims to introduce the previous work of the DSE group and therefore contains a brief summary of the Mid-Term Report (MTR). For that, the functions of the system HotFire are presented in the form of a Functional Flow Diagram (FFD, see Figure 2.1a) and Functional Breakdown Structure (FBS, see Figures 2.1b and 2.1c) to offer a clear overview of what the system is supposed to perform during operation.

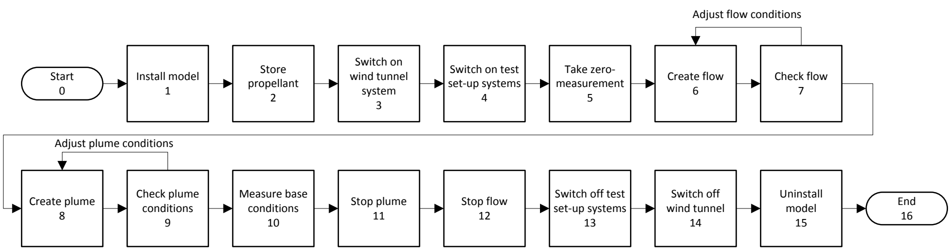

(a) Functional Flow Diagram

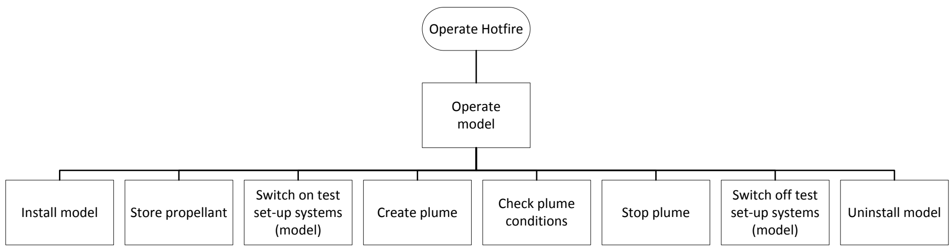

(b) Functional Breakdown Structure, part 1

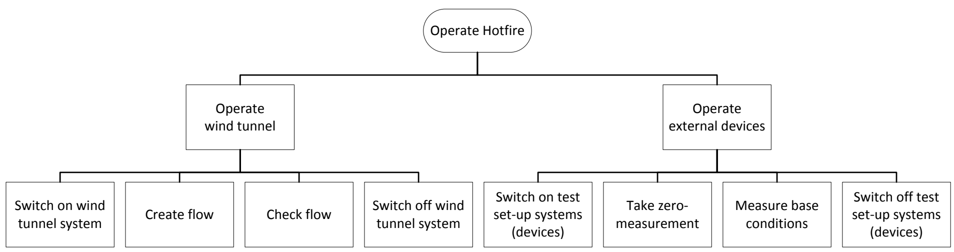

(c) Functional Breakdown Structure, part 2

Figure 2.1: Functional analysis of the HotFire product

Having identified all the functions, the HotFire requirements and their revision since the MTR are presented. Furthermore, the results of the concept trade-off and the conceptual design of the HotFire are briefly discussed.

2.1. REQUIREMENTS ON HOTFIRE

Table 2.1 shows the top-level requirements on the HotFire product. It also gives the scheme of identifiers used in the report.

Table 2.1: Top-level requirements

Identifier	Top-level requirement
HF-TEC-HPL-##	The HotFire system shall be able to generate a hot plume.
HF-TEC-CPL-##	The HotFire system shall be able to generate a cold plume.
HF-TEC-SIM-##	The HotFire system shall simulate the base region of a launcher.
HF-TEC-PRE-##	The HotFire system shall predict the experimental conditions during testing.
HF-TEC-MEA-##	The HotFire system shall allow for measurements to be conducted.
HF-CON-WTO-##	The HotFire system shall enable wind tunnel operations.
HF-CON-COS-##	The HotFire system shall be affordable (low-cost) for the customer.
HF-CON-SAF-##	The HotFire system shall be safe.
HF-CON-SUS-##	The HotFire system shall have low environmental impact.
HF-CON-SUR-##	The HotFire system shall survive the mission.
HF-CON-DEV-##	The HotFire system shall be developed within the time-frame of the DSE.

In Table 2.2, the list of requirements for “Perform mission technically” is presented, whereas the list of requirements for “Perform mission within constraints” can be found in Table 2.3. The rationale for the requirements can be deduced from the Mid-Term Report. However, a few noticeable changes were made since then:

Firstly, “to generate a hot plume” and “to generate a cold plume” were decoupled from “simulate the base region of a launcher” and added as top-level requirements `HF-TEC-HPL` and `HF-TEC-CPL`. This was done since the comparison in similarity parameters between the hot and the cold plume experiments has been identified as important. Additionally, the detailed regulatory safety requirements `HF-CON-SAF-02` to `HF-CON-SAF-06` are discarded and emphasis is put on the advice of the AeroLab technical staff. Assuming that Delft University of Technology complies with all the existing laws and safety regulations of the Dutch government, it is deemed sufficient to comply only with regulations of Delft University of Technology.

Table 2.2: Requirements for “Perform mission technically”

Identifier	Requirement
HF-TEC-HPL-01	The hot plume shall be similar to the plume of a launcher.
HF-TEC-CPL-01	The cold plume shall be similar to the hot plume.
HF-TEC-SIM-01	~~The hot plume shall be similar to the plume of a launcher.~~
HF-TEC-SIM-02	~~The cold plume shall be similar to the hot plume.~~
HF-TEC-SIM-03	The external flow entering the base region shall be steady.
HF-TEC-SIM-04	Shock waves shall not reflect from the wind tunnel wall into the model base region.
HF-TEC-SIM-05	Shock waves created by the mount shall not enter the model base region.
HF-TEC-PRE-01	The thermal loads during the experiment shall be predicted and analyzed.
HF-TEC-PRE-02	The stresses and strains during the experiment shall be predicted and analyzed.
HF-TEC-PRE-03	The velocity field during the experiment shall be predicted and analyzed.
HF-TEC-MEA-01	The plume diameter shall be at least 2 cm.
HF-TEC-MEA-02	The system shall allow for a constant visual access to the base region.
HF-TEC-MEA-03	~~The system shall allow for load measurements.~~
HF-TEC-MEA-04	The system shall allow for non-visual temperature measurements.
HF-TEC-MEA-05	The system shall allow for non-visual pressure measurements.
HF-TEC-MEA-06	The system shall operate for at least 5 s.
HF-TEC-MEA-07	The system shall allow for measurements of plume conditions.
HF-TEC-MEA-08	The plume conditions shall not vary by more than 1% over time.

Table 2.3: Requirements for "Perform mission within constraints"

Identifier	Requirement
HF-CON-WTO-01	The wind tunnel blockage shall not exceed 5%.
HF-CON-COS-01	The material costs shall not exceed 10,000 €.
HF-CON-COS-02	The tests shall be executed in the TST-27 wind tunnel of Delft University of Technology.
HF-CON-COS-03	The costs of additional modifications to the wind tunnel shall be low.
HF-CON-COS-04	The overall integrity of the wind tunnel shall not be compromised by modifications.
HF-CON-SAF-01	The system shall comply with regulations set forth by Delft University of Technology.
HF-CON-SAF-02	~~The system shall comply with laws regarding safety of workers during operation.~~
HF-CON-SAF-03	~~The system shall comply with laws regarding storage of explosive materials.~~
HF-CON-SAF-04	~~The system shall comply with laws regarding disposal of materials and fuels.~~
HF-CON-SAF-05	~~The system shall comply with laws regarding use of hazardous materials.~~
HF-CON-SAF-06	~~The system shall comply with laws regarding use of fuels.~~
HF-CON-SAF-07	The system shall not damage itself/infrastructure during storage.
HF-CON-SAF-08	The system shall provide instructions on how to avoid operational risks.
HF-CON-SAF-09	The system shall provide instructions on how to mitigate operational risks.
HF-CON-SUS-01	The amount of exhaust gases classified as harmful to the environment shall be low.
HF-CON-SUS-02	The system shall allow for the use of different propellants.
HF-CON-SUS-03	The system shall provide instructions on how to properly dispose of the system.
HF-CON-SUR-01	The temperature of the wind tunnel walls shall not exceed 400 K anywhere.
HF-CON-SUR-02	During operations, the model shall not fail statically due to loads.
HF-CON-SUR-03	During operations, the model shall not fail dynamically due to vibrations.
HF-CON-SUR-04	During operations, the model shall not fail due to temperature.
HF-CON-SUR-05	The model shall not fail during wind tunnel starting due to shock loads.
HF-CON-SUR-06	The model shall not fail during wind tunnel starting due to flutter.
HF-CON-DEV-01	The preliminary design of the system shall be done after a project duration of 11 weeks.

2.2. CONCEPT TRADE-OFF

The Analytical Hierarchy Process (AHP) trade-off method [14] was used to judge the applicability of solid, hybrid, and liquid engine concepts for the HotFire test facility. In the trade-off process, the weights shown in Table 2.4 were assigned to the main criteria. The outcome of the trade-off was clear: the liquid engine concept reached a score of 48.8% and won—compared to 27.1% for the hybrid and 24.1% for the solid engine concept. By judging the inconsistency provided by the AHP algorithm, the outcome is deemed insensitive to judgement errors: due to the large difference in score between the liquid rocket engine and the other two concepts, misjudging safety and performance still yields liquid as winner by 12% over hybrid.

Table 2.4: Weights for the main trade-off criteria

Criterion	Cost	Similarity	Performance	Operations	Safety	Complexity	Producibility	Sustainability	Experience
Weight	3.6%	20.1%	20.1%	4.9%	29.5%	8.7%	2.0%	2.2%	8.9%

2.3. SELECTED CONCEPT

Having selected the liquid engine concept from the trade-off, the conceptual design of the HotFire was further elaborated to derive its subsystems and the overall layout. All the subsystems of HotFire have been derived from their main functions. They can be seen in Table 2.5.

The feed system includes the propellant tanks, lines, flow regulator, valves, and injector. The overall layout of the HotFire conceptual design is shown in Figure 2.2.

The further development of the HotFire conceptual design will be the main focus of the coming chapter in this report.

Table 2.5: Derivation of the subsystems from the main functions of HotFire

ID	Main function	Corresponding subsystem
1	Install model	Mount
2	Store propellant	Feed system
3	Switch on wind tunnel system	Wind tunnel
4	Switch on test set up systems	Feed system
5	Take zero measurement	Instrumentation
6	Create flow	Wind tunnel, Aerodynamic shape
7	Check flow	Instrumentation
8	Create plume	Ignition, Combustion chamber, Nozzle, Temperature control
9	Check plume conditions	Instrumentation
10	Measure base conditions	Instrumentation
11	Stop plume	Feed system
12	Stop flow	Wind tunnel
13	Switch off set up systems	Instrumentation
14	Switch off wind tunnel system	Wind tunnel
15	Uninstall model	Mount

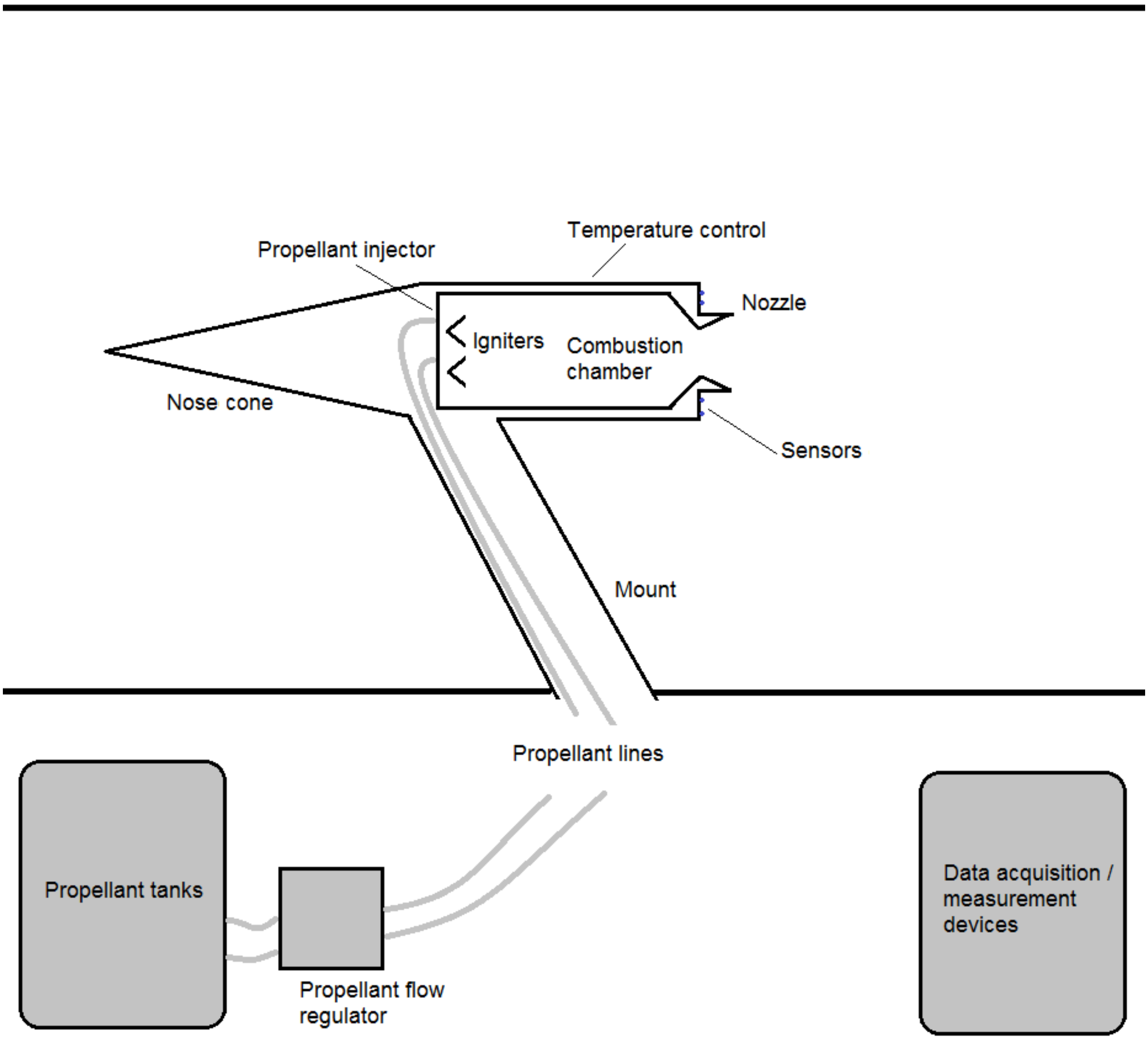

Figure 2.2: Concept layout drawing

3

Design Overview

Before presenting the design of all subsystems of HotFire in the subsequent chapters in more detail, an overview is given here to inform the reader about the outcome of the design process.

3.1. Design Description

This section will shows the total of the subsystems which were designed for the HotFire test set-up. Figure 3.1 shows a render indicating the overall locations of several subsystems. Subsystems indicated in the picture are the nose cone, the injector, the nozzle, the mount, and the combustion chamber. Subsystems which were designed but are not present in this figure are the instrumentation, ignitor and feed system.

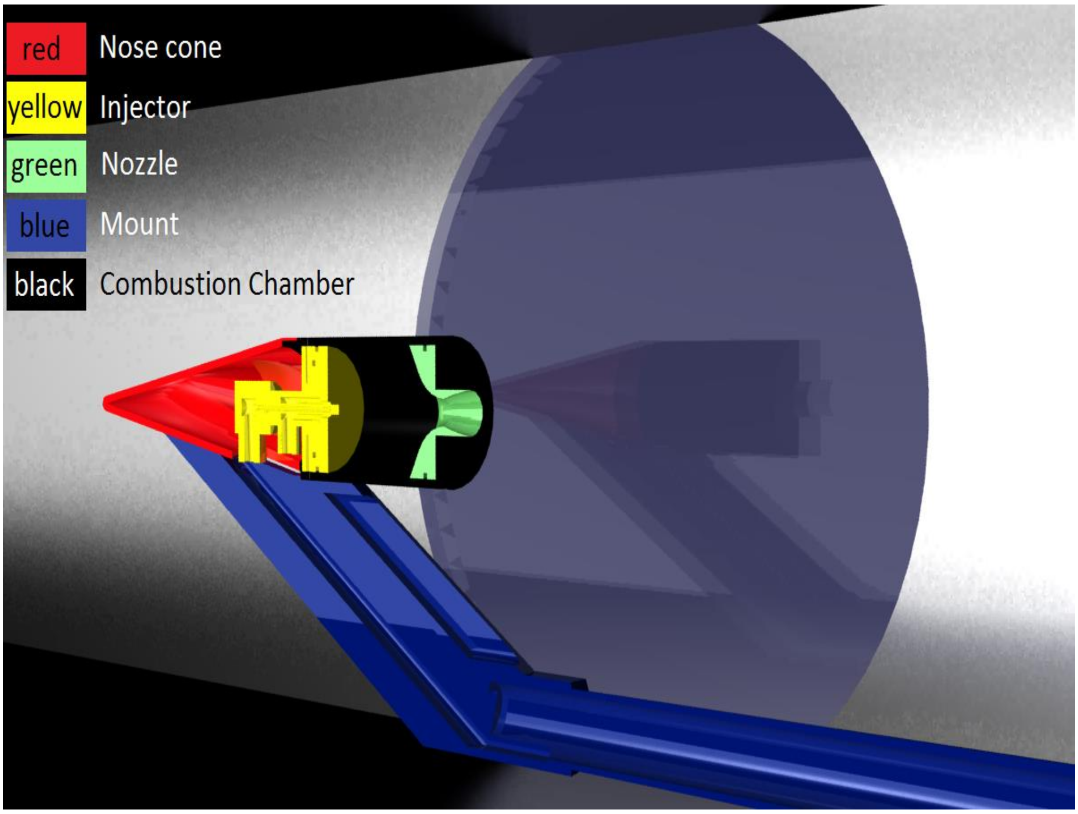

Figure 3.1: Render of the final design of HotFire. All parts are differentiated by color

A technical drawing with the general dimensions of the model is shown in Figure 3.2. The total length of the model is about 240 mm, with a radius of 50 mm.

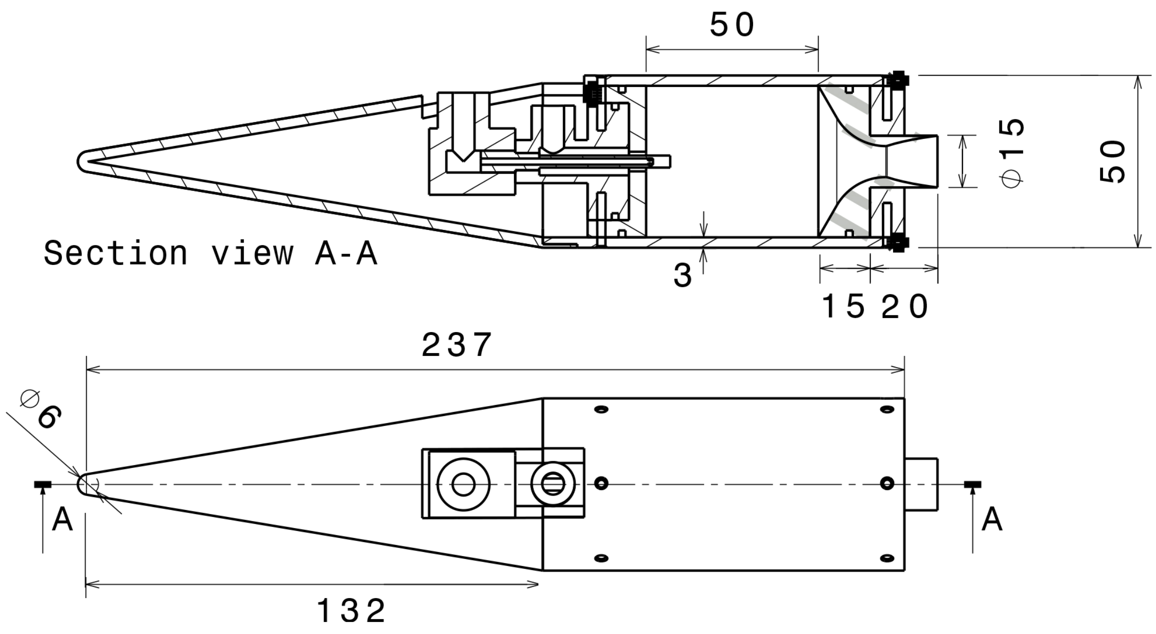

Figure 3.2: Characteristic dimensions of the HotFire combustion chamber, nozzle, and nose cone

3.1.1. INJECTOR

The injector will make sure that the propellants, consisting of oxygen as oxidizer and kerosene as fuel, will be injected in the combustion chamber at the right conditions. This will be done by a combination of a splash-plate and coaxial injector. The exact dimensions of the injector design can be seen in Figure 5.2. The injector consists of three parts: the injector casing, an oxidizer injector, and a fuel injector. The fuel injector is placed inside the oxidizer injector, which is then connected to the injector casing. The methods which were used for the design are presented in Section 5.3.1.

3.1.2. NOSE CONE

The nose cone will make sure that the flow around the model has the desired properties, without shock waves reflected by by the wind tunnel walls entering the base region. The design methods used to design the nose cone are presented in Chapter 6. Overall dimensions of the nose cone are 50 mm for the diameter and 132 mm for the length, as shown in Figure 3.2. To reduce flow separation resulting from perturbations of the model the nose cone has been given a radius of 6 mm. The nose cone is attached to the combustion chamber and can be installed our separately from the mount.

3.1.3. COMBUSTION CHAMBER

The combustion chamber will make sure to encase the whole combustion process. Propellants are injected, mixed, and then ignited in the combustion chamber, after which they are led to the nozzle in the aft part of the combustion chamber. The combustion chamber should allow for fixing of these parts, and should withstand high pressures and temperatures caused by the combustion process. These are a total pressure of 30 bar and total temperature of 1700 K. A wall thickness of 3 mm withstands the pressure loads under elevated temperatures. Dimensions of the combustion chamber are presented in Figure 3.2 as well; the methods used for the design are presented in Chapter 9.

3.1.4. NOZZLE

In the end of the combustion chamber a convergent-divergent nozzle is fixed, which need to make sure that the propellants expand to required exit conditions. The exit diameter needs to be 1.5 cm in order to create a plume large enough to perform measurements. Two different nozzles were designed; one for the cold plume and one for the hot plume. The expansion ratio for the hot plume is 2.77, for the cold plume the expansion ratio is 1.56. The nozzle part is also detachable from from the combustion chamber and is made out of graphite to withstand elevated temperatures in the throat. The design methods of the nozzle are presented in Chapter 9.

3.1.5. MOUNT

The mount is the connecting element between the model and the wind tunnel. It should keep the model in its place and could be joined by bolting, welding our gluing. Furthermore it needs to provide space for the propellant lines, space for the electrical wiring, and space for instrumentation. Sensors measuring the base temperature and pressure will be placed in the mount and not in the base plate, since there is not enough space here and the temperatures will be high in this region. General dimensions of the mount are presented in Figure 3.3. The structural and aerodynamics design methods of the mount are presented in Chapter 7.

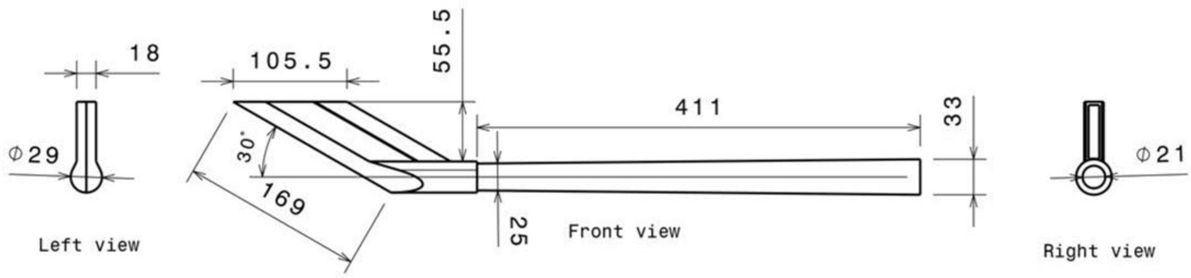

Figure 3.3: Overview of mount dimensions of HotFire

3.1.6. FEED SYSTEM

The feed system was determined to be of the blow-down type, using pre-pressurized propellants. Because kerosene is not compressible, it has to be pressurized by an external pressurant. The choice fell on nitrogen. Safety was incorporated into the design according to the philosophy of not allowing any single points of failure, resulting in the addition of dual control valves and relief valves. The system can be controlled and shut down remotely in case of failure and will also turn to a safe state in case of power failure. Estimations of the pressure loss over the entire feed system were made, resulting in 9.25 bars and 15.68 bars for fuel and oxidizer branches, respectively. These estimates will have to be validated using tests in order to determine the exact setting of the pressure regulator connected to the storage tanks. The storage tanks are pressurized at 200 bars. With a volume of 20 L, this allows for a run time well exceeding the required 5 s. The design methods of the feed system can be found in Chapter 5.

3.1.7. IGNITOR AND INSTRUMENTATION

The remaining subsystems which were analyzed but for which no drawings are made are the ignitor and the instrumentation.

For the ignitor type, several options are available. A spark plug is proposed for the ignition tests which should analyze whether this type of ignitor is powerful enough to ignite the kerosene/oxygen mixture. The ignitor analysis is presented in Chapter 8. Instrumentation will consist of visual and non-visual equipment. For visual equipment a PIV system is proposed, which will be capable of measuring the flow field in the base region. Non visual sensors will consist of pressure sensors and thermocouples to measure the temperature. The analysis and selection of the instrumentation is presented in Chapter 10. Suggested sensor locations are indicated in Figure 3.4.

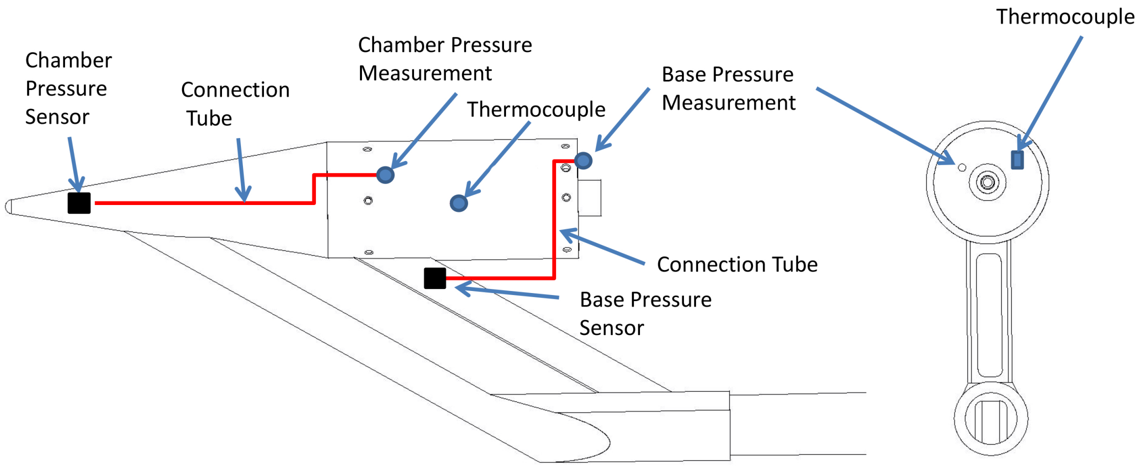

Figure 3.4: An initial consideration of the sensor locations.

3.2. REQUIREMENT COMPLIANCE

Now the separate subsystems are designed and combined to form the HotFire system, the system has to be validated to check whether it fulfills the previously determined requirements. This is presented in the following Compliance Matrices with tick marks for the level of compliance to each requirement. The comments column states in which section the requirement is discussed.

Table 3.1: Compliance to top-level requirements

ID	Associated top-level requirement	Compliance		
		Full	Partial	None
HF-TEC-HPL-##	The HotFire system shall be able to generate a hot plume.	✓		
HF-TEC-CPL-##	The HotFire system shall be able to generate a cold plume.	✓		
HF-TEC-SIM-##	The HotFire system shall simulate the base region of a launcher.	✓		
HF-TEC-MEA-##	The HotFire system shall allow for measurements to be conducted.		✓	
HF-CON-WTO-##	The HotFire system shall enable wind tunnel operations.	✓		
HF-CON-COS-##	The HotFire system shall be affordable (low-cost) for the customer.	✓		
HF-CON-SAF-##	The HotFire system shall be safe.	✓		
HF-CON-SUS-##	The HotFire system shall have low environmental impact.		✓	
HF-CON-SUR-##	The HotFire system shall survive the mission.		✓	
HF-CON-DEV-##	The HotFire system shall be developed within the time-frame of the DSE.	✓		

Table 3.2: Compliance to requirements for “Perform mission technically”

ID	Requirement	V&V method	Compliance	Comments
HF-TEC-HPL-01	The hot plume shall be similar to the plume of a launcher.	Analysis	✓	Propellant
HF-TEC-CPL-01	The cold plume shall be similar to the hot plume.	Analysis	X	Propellant
HF-TEC-SIM-01	The external flow entering the base region shall be steady.	Simulation	✓	Aerodynamic Shape
HF-TEC-SIM-02	Shock waves from the wind tunnel wall shall not enter the base region of the model.	Analysis	✓	Aerodynamic Shape

— Continued on next page —

Table3.2 – continued from previous page

ID	Requirement	V&V method	Compliance	Comments
HF-TEC-SIM-03	Shock waves created by the model shall not enter the base region of the model.	Analysis	✓	Aerodynamic Shape
HF-TEC-MEA-01	The plume diameter shall be at least 2 cm.	Analysis	✓	Combustion Chamber
HF-TEC-MEA-02	The system shall allow for a constant visual access to the base region.	Test	✓	Mount
HF-TEC-MEA-04	The system shall allow for non-visual temperature measurements.	Review of Design	✓	Instrumentation
HF-TEC-MEA-05	The system shall allow for non-visual pressure measurements.	Review of Design	✓	Instrumentation
HF-TEC-MEA-06	The system shall operate for at least 5 s.	Analysis	✓	Combustion, Feed system
HF-TEC-MEA-07	The system shall allow for measurements of plume conditions.	Demonstration	X	Instrumentation
HF-TEC-MEA-08	The plume conditions shall not vary by more than 1% over time.	Analysis / Test	X	Feed system, Future development

Table 3.3: Compliance to requirements for "Perform mission within constraints"

ID	Requirement	V&V method	Compliance	Comments
HF-CON-WTO-01	The wind tunnel blockage shall not exceed 5%.	Reviwe of Design	✓	Mount, Aerodynamic Shape, Combustion Chamber
HF-CON-COS-01	The material costs shall not exceed €10,000.	Reviwe of Design	✓	Design Overview
HF-CON-COS-02	The tests shall be executed in the TST-27 wind tunnel of Delft University of Technology.	Review of the Design	✓	Concept Selection
HF-CON-COS-03	The costs of additional modifications to the wind tunnel shall be low.	Review of Design	✓	Integration
HF-CON-COS-04	The overall integrity of the wind tunnel shall not be compromised by modifications.	Review of Design	✓	Integration
HF-CON-SAF-01	The system shall comply with regulations set forth by Delft University of Technology.	Review of Design	✓	Propellant
HF-CON-SAF-07	The system shall not damage itself/infrastructure during storage.	Review of Design	✓	Feed System, Operations
HF-CON-SAF-08	The system shall provide instructions on how to avoid operational risks.	Review of Design	✓	Operations

— Continued on next page —

Table3.3 – continued from previous page

ID	Requirement	V&V method	Compliance	Comments
HF-CON-SAF-09	The system shall provide instructions on how to mitigate operational risks.	Review of Design	✓	Operations
HF-CON-SUS-01	The amount of exhaust gases classified as harmful to the environment shall be low.	Analysis	✓	Feed System, Propellant
HF-CON-SUS-02	The system shall allow for the use of different propellants.	Analysis	X	Feed Syste, Propellant
HF-CON-SUS-03	The system shall provide instructions on how to properly dispose of the system.	review of Design	✓	Operations
HF-CON-SUR-01	The temperature of the wind tunnel walls shall not exceed 400 K anywhere.	Test / Analysis	✓	Mount
HF-CON-SUR-02	During operations, the model shall not fail statically due to loads.	Analysis	✓	Mount, Combustion Chamber
HF-CON-SUR-03	During operations, the model shall not fail dynamically due to vibrations.	Analysis	X	Mount
HF-CON-SUR-04	During operations, the model shall not fail due to temperature.	Analysis	✓	Combustion Chamber, Mount
HF-CON-SUR-05	The model shall not fail during wind tunnel starting due to shock loads.	Analysis	✓	Mount
HF-CON-SUR-06	The model shall not fail during wind tunnel starting due to flutter.	Test	X	Mount
HF-CON-DEV-01	The preliminary design of the system shall be done after a project duration of 11 weeks.	Review of Design	✓	

3.3. BUDGET MANAGEMENT AND LIMITATIONS

The HotFire project has to be realized under certain constraints. One of these constraints is the limited amount of resources that are allocated to the project. For this project, two different resource budgets can be identified. These are the cost budget, which is a monetary value that the combined cost of the HotFire should not exceed and the space budget, which limits the size of the wind tunnel model. These budgets can be derived from the below listed top-level requirements.

HF-TEC-SIM-02 Shock waves from the wind tunnel wall shall not enter the base region of the model.

HF-CON-WTO-01 The wind tunnel blockage shall not exceed 5%.

HF-CON-COS-01 The material cost shall not exceed €10,000.

HF-CON-COS-02 The tests shall be executed in the TST-27 wind tunnel of Delft University of Technology.

3.3.1. COST BUDGET

For the cost budget analysis, the HotFire system can be divided up in to four parts, which are the rocket model, mount, propellant feed system and instrumentation. The rocket model can be manufactured entirely out of steel S355, which is selected as material in Section 9.6 and costs €97 for a solid rod of 60 mm diameter and 1 m length.

Table 3.4: Cost estimation for the main components of the HotFire system

Part	Cost	Detailed budget
Rocket Model	€367	See Table 9.3
Mount	€720	See Section 7.6
Feed System	€3401	See Table 5.5
Instrumentation	€1770	See Table 10.1
Total	€6258	N/A

All the required parts for the rocket model can be produced out of the 1 m long rod. The exception is the nozzle insert, which has to be created from graphite, considering the thermal loads. This material costs €270 for a rod of 54 mm diameter and 1.25 m length. Adding up the material cost of these 2 rods results in a rocket model cost of €367. For the mount, a steel alloy called Uddeholm Impax Supreme was selected in Section 7.5, on the recommendation of the wind tunnel technician. The price of this is estimated to be €720. The cost of the propellant feed system can be broken down to the cost of the individual components that are expected to be needed to create the propellant feed system. This cost break down has been performed in Section 5.7.3, which resulted in a total cost of €3401. The total instrumentation cost as described in Section 10.4 adds up to €1770. The cost of the PIV system and the seeding particles are excluded from the budget estimation, since these are already available at the Delft University of Technology. The costs of the main parts with the total cost is summarized in Table 3.4. Note that the cost budget only takes the production cost into consideration. It does not include development cost and operational cost due to uncertainties that cannot be predicted during the time of the DSE.

The estimated total cost of €4840 for the HotFire system does not even reach half of available budget of €10,000. Note that the estimated cost of €4840 in Table 3.4 does not include the ignition system. However, the typical spark plug costs less than €100 [15].

3.3.2. SPACE BUDGET

The space budgeting is done to check the volume and length margins of any subsystems that could cause discrepancies within the wind tunnel test section. During the detailed design only three requirements were deemed relevant to include in the space budgetting: Blockage, shock wave interaction with the exhaust plume and the combustion chamber volume. The wind tunnel test cross-section is 270 by 270 mm.

Blockage

The first priority of the space budgeting in the test section is the blockage requirement: `HF-CON-WTO-01` "The wind tunnel blockage shall not exceed 5%". A too high blockage could prevent the wind tunnel from starting, preventing experimental testing. The total blockage was determined from the mount and model geometries and turned out be 3623 mm^2, which satisfies the 5% blockage criteria (3645 mm^2). The assigned space budgets of 40% for the mount and 60% for the model are met with a few percent deviation.

Shock Wave Interaction with Base Region

The second space margin priority is the base region-shock wave interaction. The nose cone shape of the model influences the shock wave angle induced by it in a supersonic freestream flow. A wider cone angle causes the shock wave to move upstream, potentially interacting with the base region. An interaction is undesirable, since it affects the base and plume conditions. For $M_{\text{inf}} = 2$ which is a design parameter, the distance between shock wave and base of the model is ≈ 3 times the model diameter, hence no interference would occur. The shock wave interaction analysis of the model is explained in detail in Chapter 6. This resulted in a total length of 24 cm for the model from which 13.5 cm is the nose cone.

3.4. INTERFACE DEFINITION

The interface between the subsystems during the design processes has been identified and presented in the form of a N^2 chart in Figure 3.5. The subsystems are placed diagonally whereas inputs and outputs of the blocks are placed on the horizontal and vertical cells respectively. The greatest challenge in the integration is to make all subsystems fit in the tight space in the model. The fuel lines for example have to fit through the mount and should be able to make the turn in nose cone to reach the injector inlet. The exact assembly can be found in the technical drawings in Appendix A.

Wind Tunnel	Safety regulations						Size requirement	Size requirement, free stream conditions	Free stream conditions	Freestream static temperature	Connection/ dimensions and size requirement	Placement of sensors
Safety measures	Propellant	Propellant properties	Propellant properties	Propellant properties	Propellant properties/ required mixing	Minimum ignition energy	Propellant and combustion properties		Combustion properties	Combustion propeties		
	Tank specifications	Propellant tanks		Pressure drop over time / pressure limit								
	Line specifications	Pressure limit of lines, connection/ dimensions	Propellant lines	Pressure drop	Connection/ dimensions						Dimensions of lines	
	Regulator specifications		Valve closing / pressure limit	Pressure regulator / electrical valves	Regulated pressure	Sending ignition signal						Sending start signal
	Injector specifications		Connection/ dimensions	Pressure limit	Propellant injector	Pressure / mass flow	Pressure / mass flow					
	Maximum energy available				Pressure / mass flow	Ignition system					Dimensions ignition lines	
	Combustion chamber specifications					Igniter location	Combustion chamber	Connection/ dimensions	Connection/ dimensions / pressure of chamber	Heat transfer/ Material selection	Connection/ dimensions	
Wind tunnel setting						Igniter location	Blockage and length requirement	Aerodynamic shape		Heat transfer/ Material selection	Connection/ dimensions	Shape and surface available
							Connection/ dimensions		Nozzle	Heat transfer/ Material selection		Plume size
Heat transfer							Heat transfer/ Material selection	Heat transfer/ Material selection	Heat transfer/ Material selection	Passive temperature control	Heat transfer/ Material selection	
Mount size needed			Internal mount space			Internal mount space		Connection/ dimensions		Heat transfer/ Material selection	Mount	Internal mount space
Access needed (optical and physical)				Data current state state				Placement of sensors			Data lines	Instrumentations

Figure 3.5: N^2 chart showing all system interfaces of HotFire

4
Propellant Selection

As was discussed in Section 1.1, there have been attempts to simulate launcher plumes using cold gas. According to [8], this "has the primary advantage of relative simplicity in set-up and operation. Cold gases are particularly appealing when the simulation of jet temperature is considered of little importance." Up to this point, the temperature effects have been neglected in the scientific community. HotFire therefore aims at creating a hot exhaust plume that can be studied. From this follows the need for propellants and a combustion process.

In this chapter, the selection of the propellants is discussed. Since the customer requires the set-up to also produce a cold plume for reference conditions (top-level requirement `HF-TEC-CPL`), the selection of this is addressed, too. First, the requirements on this subsystem and the integration within HotFire are mentioned. Then, the concepts under consideration are introduced and analyzed, to finally arrive at one combination of fuel and oxidizer as well as a cold gas.

4.1. Requirements on the Propellant

The subset of the HotFire requirements applicable to the selection of the propellant is given here:

`HF-TEC-HPL-01` The hot plume shall be similar to the plume of the launcher.

`HF-TEC-CPL-01` The cold plume shall be similar to the hot plume.

`HF-TEC-MEA-08` The plume conditions shall not vary by more than 1% over time.

`HF-CON-SAF-01` The system shall comply with regulations set forth by Delft University of Technology.

`HF-CON-SAF-07` The system shall not damage itself/infrastructure during storage.

`HF-CON-SUS-01` The amount of exhaust gases classified as harmful to the environment shall be low.

The first two technical requirements (`HF-TEC-HPL-01` and `HF-TEC-CPL-01`) are critical for the success of the product. To recreate a launcher using a hot plume that is also similar to a cold plume for reference purposes is the scientific objective of HotFire. This has a direct effect on the approach of selecting the propellant: first, a set of combinations of similar hot and cold plumes was found, and those were compared to a launcher to pick the best of them.

The third technical requirement (`HF-TEC-MEA-08`) cannot be designed for. It is included here because a sensitivity study is conducted to show that the effect of varying combustion chamber properties over time have a low impact on the similarity parameters.

Finally, the remaining requirements affect the propellant selection by excluding certain propellants from the list of concepts for safety (`HF-CON-SAF-01` and `HF-CON-SAF-02`) or sustainability (`HF-CON-SUS-01`) reasons.

4.2. INTEGRATION WITHIN HOTFIRE

The choice of propellant has strong implications for various other subsystems of HotFire. Not only is the type of fuel and oxidizer an input for the design of most of these subsystems, the exact combustion and nozzle exit conditions required for plume similarity are driving factors as well.

Furthermore, the use of a hot plume and a cold plume almost inevitably leads to an interchangeable nozzle design, because the nozzle exit angle required for flow similarity—as shown later in this chapter—must be different for different exhaust media [8, 9].

4.3. PROPELLANT CONCEPTS

Before presenting the analysis method employed in the propellant selection process, the concepts under consideration need to be discussed. This will be done separately for the hot plume by investigating different oxidizer-fuel combinations and for the cold plume by addressing pure gases and gas mixtures.

4.3.1. PROPELLANT COMBINATIONS FOR THE HOT PLUME

As summarized in Chapter 2, the decision was made to use a liquid engine as means of creating a hot plume for the HotFire system. There is a large variety of liquid and gaseous propellants that can be combusted together. To focus the research, typical rocket propellants were investigated. The ones under consideration are presented in Table 4.1 along some of their properties.

Because the HotFire model needs to be optimized for diameter and length (for shock wave propagation reasons, explained in Chapter 6), the volume of the combustion chamber is limited. The driving selection factor to judge if a propellant concept is feasible is its characteristic length, or

$$L^\star = \frac{V_c}{A_t}. \tag{4.1}$$

It relates the combustion chamber volume V_c with the nozzle throat area A_t and thus gives an indication about the combustion chamber geometry required for combusting the propellant and accelerating the mixture to sonic speed.

For a given propellant density ρ and mass flow $\dot{m}$, the characteristic length can also be interpreted as a measure of the average time of the particles in the combustion chamber—otherwise know as the chamber residence time of the reacting propellants [16]. As the available volume in the HotFire model is limited and the nozzle throat cross-sectional area A_t can only be lowered to a certain minimum, this measure can be used to identify propellants who require a longer time and hence distance to react.

Table 4.1: Investigated propellant combinations for the hot plume, [17, 18]

Oxidizer	Fuel	$L^\star_{\text{min}}$	$L^\star_{\text{max}}$	Toxicity
Gaseous oxygen	Hydrocarbon fuels	1.25 m	2.50 m	None
Gaseous oxygen	Gaseous hydrogen	0.55 m	0.70 m	None
Gaseous oxygen	Kerosene	1.02 m	1.25 m	None
Liquid oxygen	Liquid hydrogen	0.76 m	1.02 m	None
Liquid oxygen	Gaseous hydrogen	0.56 m	0.71 m	None
Liquid oxygen	Ethyl alcohol	2.50 m	3.00 m	None
Liquid oxygen	Ammonia	0.76 m	1.02 m	High
Nitrogen tetroxide	Hydrazine	0.60 m	0.89 m	High
Hydrogen peroxide	Rocket Propellant (RP-1)	1.52 m	1.78 m	High
Nitric acid	Unsymmetrical Dimethylhydrazine	1.50 m	2.50 m	High
Nitric acid	Hydrocarbon fuels	2.00 m	3.00 m	High
Nitric acid	Unsymmetrical Dimethylhydrazine	1.50 m	2.00 m	High
Liquid fluorine	Hydrazine	0.61 m	0.71 m	High
Liquid fluorine	Gaseous hydrogen	0.56 m	0.66 m	High
Liquid fluorine	Liquid hydrogen	0.64 m	0.76 m	High

As can be seen in Table 4.1, the values for $L^\star$ for some concepts vary by ranges of up to 1.25 m. This uncertainty stems from the fact that the characteristic length cannot be found analytically and is instead obtained experimentally. To ensure proper functionality of HotFire, the upper end of the range is used for all calculations. While this is a conservative estimate, it ensures maximum probability of desired combustion conditions.

The toxicity of a certain oxidizer-fuel combination is another key criterion in deciding which concept will be implemented in HotFire. It was assessed based on [17, 18]. Toxic fuels need special operational and safety consideration, which may affect the cost and/or violate regulations/laws.

4.3.2. COLD GAS MIXTURES FOR THE COLD PLUME

According to [8], there exist several cold gases and cold gas mixtures that should be considered for use as exhaust medium. They are listed in Table 4.2 together with their gas properties (specific heat ratio γ and gas constant R) as these cannot be altered like e.g. pressure. Also, a comment on the use of those gases is given.

Table 4.2: Investigated cold gases/gas mixtures for the cold plume, properties at T = 288 K [8]

Gas/Mixture	γ [-]	R [J/(kg K)]	Comment
0.78 N_2 + 0.21 O_2 + 0.01 Ar (Air)	1.40	287	Easily available, cheap
1.00 He (pure Helium)	1.67	2077	Easily available, prior experience
1.00 H_2 (pure Hydrogen)	1.41	4132	Potentially dangerous
1.00 CO_2 (pure Carbon Dioxide)	1.29	188	Potentially harmful, cheap
0.46 H_2 + 0.54 CO_2	1.40	2012	Potentially dangerous, complicated

4.4. ANALYSIS METHOD

The combustion chamber and resulting nozzle exit conditions of the hot plume concepts was created using the commercial software Rocket Propulsion Analysis (RPA). The concepts were analyzed using the HotFire Design Analysis Tool (HFDAT), a derivative of the HotFire Design Space Tool (HFDST) that had been developed in the previous project phase. Its purpose is to compute the flow similarity parameters for the concepts and compare them to the parameters calculated for a launcher. The deviation in similarity is then used to select a propellant combination.

The tools function independent of plume type; hot and cold plumes work equally well. This is exploited for comparing hot and cold plumes to one another and finding the best combination.

4.4.1. CALCULATION OF FLOW SIMILARITY PARAMETERS

The parameters that were found to be of interest in simulating an exhaust plume in a wind tunnel are

I the ratio of jet to freestream static pressures (henceforth “pressure ratio”),

II the initial inclination angle of the jet (henceforth “initial inclination angle”),

III the ratio of jet to freestream momentum flow/flux (henceforth “momentum flux ratio”),

IV the ratio of jet to freestream mass flow or flux (henceforth “mass flux ratio”), and

V the ratio of jet to freestream kinetic energy per unit mass (henceforth “kinetic energy ratio”).

Of the parameters in this list, the pressure ratio and initial inclination angle are the most important that should be matched; momentum and mass flux ratios are also important, while matching the kinetic energy ratio is slightly less relevant. This ranking in importance, also given in Table 4.3, was determined from various wind tunnel experiments carried out across the different literature presented in this section.

The main source for the mathematical relations describing these parameters is [8, p.32]. Unless stated otherwise, this is the reference for all equations. Most of the found literature also referred back to this article, and [19] derived the similarity parameters from a different starting point as well.

I – PRESSURE RATIO

Matching the ratio of jet (j) to freestream (∞) static pressures of a launcher and the model is a simple and straightforward, yet powerful approach in replicating the flow in the base region. The relation is given by

$$\left(\frac{P_j}{P_\infty}\right)_m = \left(\frac{P_j}{P_\infty}\right)_v, \tag{4.2}$$

where the subscript m stands for the wind tunnel model and v for the launcher vehicle. The importance of this similarity parameter in simulating hot plumes in on-ground tests is stressed in [20, p.6] and [21, p.3] (in addition to [8], saying that the ratio has the greatest effect on performance characteristics). Its influence is predominantly seen in size and shape of the plume. Additionally, the pressure ratio appears in three other similarity parameters (explicitly in momentum and mass flux ratio, implicitly in initial inclination angle).

II – INITIAL INCLINATION ANGLE

In addition to being the parameter that is claimed to be the most important in [8, p.13], the initial inclination angle is also used in [9, p.3] and further [20, p.5]. This parameter affects the conditions in the immediate vicinity of the base due to the fact that it governs the initial plume boundary.

Figure 4.1 shows an illustration of the base region and the relevant angles and parameters. The angle δ that the plume boundary has initially is called the initial inclination angle. While there exists the simplified equation

$$\left(\frac{(P_2-P_\infty)}{(P_j-P_2)}\cdot\frac{\left(P\gamma M^2/\sqrt{M^2-1}\right)_j}{\left(P\gamma M^2/\sqrt{M^2-1}\right)_\infty}\right)_m = \left(\frac{(P_2-P_\infty)}{(P_j-P_2)}\cdot\frac{\left(P\gamma M^2/\sqrt{M^2-1}\right)_j}{\left(P\gamma M^2/\sqrt{M^2-1}\right)_\infty}\right)_v \tag{4.3}$$

that was derived by [8], it only applies to small angles and assumes the nozzle exit angle θ_N to be zero. Both assumptions are violated with current launchers and the wind tunnel model, and therefore a numerical approximation of the initial inclination angle δ is used in this report

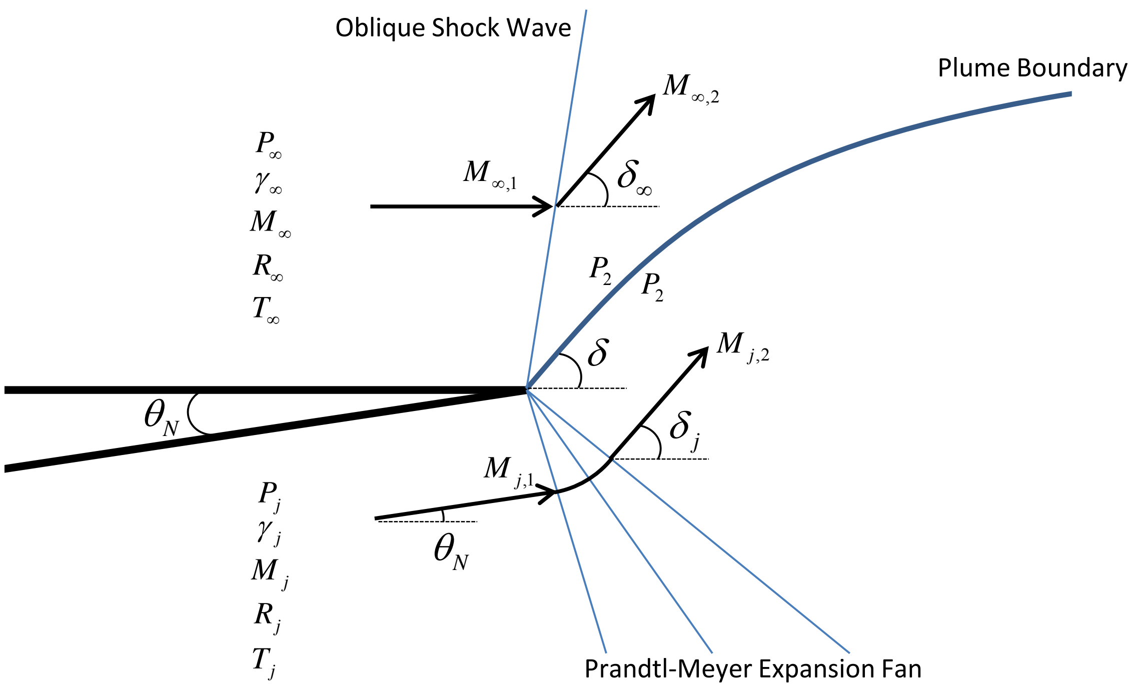

Figure 4.1: Sketch of the nozzle exit and initial plume boundary

It is known that the pressure P_2 is equal on both sides of the plume boundary. For the oblique shock wave (OSW), this pressure is found by using the initial inclination angle δ_∞ as the deflection angle of the incoming freestream flow in the M-β-θ relation

$$\tan(\delta_\infty) = 2\cot(\beta)\frac{M_{\infty,1}^2\sin^2(\beta)-1}{M_{\infty,1}^2\left(\gamma_\infty+\cos(2\beta)\right)+2}. \tag{4.4}$$

After solving this equation implicitly for the shock wave angle β—for this, a self-written MATLAB function `MachTheta2Beta.m` was used, which is based on [22]—, the static pressure behind the OSW is obtained via

$$\frac{P_2}{P_\infty} = 1+\frac{2\gamma_\infty}{\gamma_\infty+1}\left(M_\infty^2\sin^2\beta-1\right). \tag{4.5}$$

The resulting pressure ratio can be plotted for different values of $\delta = \delta_\infty$, as was done for the curve "Oblique Shock Wave" in Figure 4.2.

To obtain the pressure on the inner side of the plume boundary (represented by the curve "Prandtl-Meyer Expansion" in Figure 4.2), the Prandtl-Meyer expansion (PME) fan is considered. The direction of the jet after passing through the PME fan is $\delta_j = \theta_N + \Delta\nu$, where $\Delta\nu = \nu(M_{j,2}) - \nu(M_{j,1})$ is the PME turn angle [23]. Therefore, by trying for different δ_j values and using

$$\nu\left(M_{j,2}\right) = \left(\delta_j-\theta_N\right)+\nu\left(M_{j,1}\right), \tag{4.6}$$

the Mach number $M_{j,2}$ after the PME fan can be found. For that purpose, one of MATLAB's built-in functions, `flowprandtlmeyer.m`, is used, which is able to invert the Prandtl-Meyer function

$$\nu(M) = \sqrt{\frac{\gamma+1}{\gamma-1}}\cdot\arctan\sqrt{\frac{\gamma-1}{\gamma+1}\left(M^2-1\right)}-\arctan\sqrt{M^2-1} \tag{4.7}$$

to find M for a given γ and ν.

Because a PME is isentropic, the stagnation pressure P_0 and γ_j remain constant. Thus, the stagnation pressure in the exit is used to find the static pressure after the PME fan (P_2) by using the isentropic relation [23]

$$\frac{P_2}{P_j} = \left(\frac{1+\frac{\gamma_j-1}{2}M_{j,1}^2}{1+\frac{\gamma_j-1}{2}M_{j,2}^2}\right)^{\dfrac{\gamma_j}{\gamma_j-1}}. \tag{4.8}$$

Since P_j and P_∞ are known, $\frac{P_2}{P_\infty}$ can be plotted for different $\delta = \delta_j$, analogously to the OSW pressure. This can also be seen in Figure 4.2. The intersection is found using recursive bisection to speed up the program.

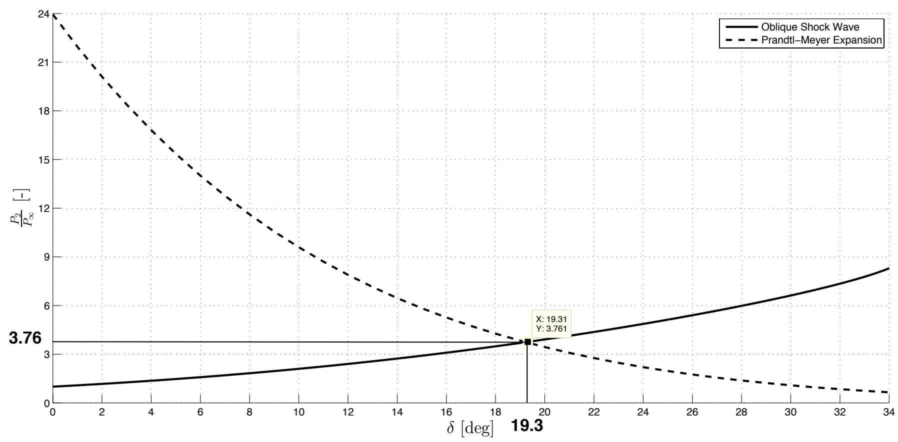

Figure 4.2: Method of intersecting pressure curves for finding the initial inclination angle, in this case for the Vulcain 2 launcher (design point <40,2,4>)

The graph in Figure 4.2 shows the result of the approximation of the initial inclination angle δ of Vulcain 2 for the chosen design point. The same analysis can be carried out for the wind tunnel model. The resulting similarity condition is thus formulated as

$$\delta_m = \delta_v. \tag{4.9}$$

III – MOMENTUM FLUX RATIO

Using the ideal gas law $P = \rho RT$ and the definition of the Mach number $\mathrm{V} = M\sqrt{\gamma RT}$, the general definition of momentum flux $\rho \mathrm{V}^2$ can be transformed to

$$\left(\frac{\left(P\gamma M^2\right)_j}{\left(P\gamma M^2\right)_\infty}\right)_m = \left(\frac{\left(P\gamma M^2\right)_j}{\left(P\gamma M^2\right)_\infty}\right)_v. \tag{4.10}$$

This equation relates the momentum flux of the jet to that of the freestream, for both wind tunnel model and launcher vehicle. Alongside mass flux, this parameter is essential to represent downstream jet conditions (according to [8]). It also affects the plume trajectory. This similarity parameter is found in [9, p.3]. Its importance is mentioned in [21, p.3] and [7, p.2].

IV – MASS FLUX RATIO

By relating the mass flux of the jet to that of the freestream, the downstream jet conditions can be simulated (as stated previously, see [8, p.32] and [21, p.3]). Starting with the general expression of mass flux ratio

$$\frac{\left(\rho \mathrm{V}\right)_j}{\left(\rho \mathrm{V}\right)_\infty}, \tag{4.11}$$

squaring the expression and applying again the ideal gas law and Mach number relation, the following equation for the mass flux ratio is derived:

$$\left(\frac{\left(\frac{P^2\gamma M^2}{RT}\right)_j}{\left(\frac{P^2\gamma M^2}{RT}\right)_\infty}\right)_m = \left(\frac{\left(\frac{P^2\gamma M^2}{RT}\right)_j}{\left(\frac{P^2\gamma M^2}{RT}\right)_\infty}\right)_v \tag{4.12}$$

V – KINETIC ENERGY RATIO

The final parameter that one should attempt to keep similar is the ratio of kinetic energy per unit mass. This is defined as V^2, and—using $\mathrm{V} = M\sqrt{\gamma RT}$ as was done for the other parameters—can be expressed as

$$\left(\frac{\left(\gamma M^2 RT\right)_j}{\left(\gamma M^2 RT\right)_\infty}\right)_m = \left(\frac{\left(\gamma M^2 RT\right)_j}{\left(\gamma M^2 RT\right)_\infty}\right)_v. \tag{4.13}$$

A source for the importance of this parameter can be found in [9, p.3]. The kinetic energy ratio governs the plume entrainment and mixing. It can be noted that this parameter is independent of pressure ratio.

4.4.2. SELECTION ALGORITHM IN HFDAT

In the Mid-Term Report, the selection of the design point <40,2,4> was discussed. Using the HFDST, an ideal model exit pressure of $P_j \approx 2.34$ bar had been identified, which was obtained by matching all similarity parameters to 100%. However, in the Mid-Term Report it was discussed in length that relaxation of some similarity parameters is required to obtain a feasible design. As a consequence, combinations of hot and cold plumes are analyzed by varying over the following parameters:

- Different combustion chamber temperatures T_c; a temperature of more than 2500 K was deemed very difficult or impossible for the model to sustain, and therefore this maximum was defined. This resulted in different O/F ratios of the propellant combinations.

- Combustion chamber pressures P_c, with the range 10–30 bar; again, a preliminary investigation estimated pressures of above 30 bar to be too high for the combustion chamber to handle.
- Exit pressures P_j, with the range 2.20–2.40 bar; because the pressure ratio is seen as the most important similarity parameter, the exit pressure is kept close to the ideal while still allowing for the positive relaxation effect of a lower exit pressure.

The nozzle exit angle θ_N (see Figure 4.2) was selected as the maximum angle that is allowed for the method of intersecting pressures. For a given Mach number (and hence turn angle $\Delta\nu$), a too high θ_N results in a δ_j that exceeds the maximum deflection angle of the external flow, leading to a detached shock wave. As this is an undesired effect, the nozzle exit angle is restricted.

To evaluate the hot plume – cold plume combinations, the method of Weighted Least Absolute Deviations (WLAD) was used to find the overall best match in similarity. The relative weights assigned to deviations in each similarity parameter are given in Table 4.3.

Table 4.3: Relative importance of plume similarity parameters

	Parameter	Weight
I	Pressure Ratio	27%
II	Initial Inclination Angle	27%
III	Momentum Flux Ratio	18%
IV	Mass Flux Ratio	18%
V	Kinetic Energy Ratio	10%

4.4.3. CALCULATION OF EXIT PARAMETERS USING RPA

The RPA tool is capable of analyzing the combustion processes of various propellant mixtures, combustion chamber conditions (e.g. chamber pressure and temperature), and thermodynamics of the chamber and the nozzle. Detailed lists of its main features can be found in [24].

The output of RPA was directly used as input data for the HFDAT analysis of similarity parameters. As stated earlier, the O/F ratio, combustion chamber pressure P_c, and exit pressure P_j were varied. To speed up the process, a command line script was used to extract data from RPA and loop over combinations of inputs.

4.5. RESULTS

The results of the analysis described previously are presented for hot and cold plume separately. Also, a concept elimination based on toxicity and safety considerations is performed. The results in this section will arrive at one hot plume and one cold plume and present their similarity to one another and to a launcher.

4.5.1. ELIMINATION OF PROPELLANT OPTIONS BASED ON SAFETY AND TOXICITY

Generally, it was found that hydrogen is undesirable for use with HotFire. The regulations of Delft University of Technology require high safety measures to comply with safety and also law [25]. This has effects on both the hot and cold plume concepts, as elaborated below. Furthermore, the approach was taken that any chemical/gas that is easily available is selected over one that is expensive, but slightly better performing. This was done to ensure the feasibility of HotFire and to limit costs (given the limited budget).

Finally, potentially harmful or dangerous substances are excluded. The safety of HotFire is important for the success of the product, to attract other wind tunnel facilities, and to prevent additional costs due to damaging of facilities.

HOT PLUME

The propellant options to be studied further have been selected based on their characteristic length, toxicity, and commercial availability. They can be found in Table 4.1.

To improve the operations of HotFire the propellant should be non-toxic. HotFire will be operated in the TST-27 wind tunnel, which is a blow-down wind tunnel. By selecting a non-toxic propellant combination the environmental impact can be limited. Furthermore, the propellant combinations should also be easily available. The propellant will be used in very small quantities and should not need additional certification.

First, all toxic propellant combinations were eliminated. This left six possible combinations. The options of ethyl alcohol with liquid oxygen was eliminated because of the large value of $L^{\star}$. Then, all options involving hydrogen were eliminated because of the additional safety considerations related to using hydrogen. Fuels based on hydrocarbons were eliminated due too their long characteristic length as well.

This leaves one propellant option, namely kerosene with gaseous oxygen. Both fuel and oxidizer are commercially available, non-toxic, and have a characteristic length of maximum 1.25 m. This choice will be elaborated further in Section 4.5.2, when different oxidizer-fuel (O/F) combinations are investigated.

COLD PLUME

From the five concepts listed in Table 4.2, the pure hydrogen concept is eliminated due to safety considerations. While pure carbon dioxide has a favorable value of $\gamma = 1.29$, its low gas constant $R = 188$ J/(kg K) is a major drawback and therefore is eliminated, too. Combining it with hydrogen for a two-component mixture gives a better R value, but must also be dropped because of hydrogen being potentially dangerous.

The remaining two concepts are conventional air and pure helium, both easily available and either cheap (air) or have been used before (helium).

4.5.2. ELIMINATION OF PROPELLANT OPTIONS BASED ON FLOW SIMILARITY PARAMETERS

Above, the range of propellant combinations was narrowed down to one hot plume concept (kerosene as fuel and gaseous oxygen as oxidizer) and two cold plume concepts (air and helium). To continue the selection more criteria needed to be taken into account, namely the flow similarity parameters discussed previously.

The approach was to find a subset—a number of hot plume – cold plume combinations of different exit pressure ratios, that match each other well in similarity—from the full set of all possible combinations. This subset was then judged against launcher plumes to make the final selection. The analysis method was described in Section 4.4.

COMPARISON OF HOT AND COLD PLUMES

Table 4.4 shows the “winners” of the comparison run with HFDAT. The last columns present the similarity parameters computed for the plume, with roman number identifiers as used throughout this section.

With the given weights, it was found that—irrespective of the exit pressure—the parameters not influenced by RT show deviations of less than 3%, while the mass flux (more than 50%) and kinetic energy (more than 120%) have large deviations. The exact values are presented in Table 4.5.

Table 4.4: Pairs of most similar hot (H) and cold (C) plumes for different exit pressures

	P_j [bar]	Propellant	P_c [bar]	T_c [K]	I [-]	II [deg]	III [-]	IV [-]	V [-]
H	2.20	O/F=1.2	26	1705	8.6	22.9	10.1	6.9	14.8
C	2.15	Helium	18	280	8.4	22.8	10.1	15.3	6.7
H	2.25	O/F=1.2	28	1706	8.8	22.7	10.6	7.4	15.1
C	2.25	Helium	19	280	8.8	23.0	10.6	16.9	6.7
H	2.30	O/F=1.2	30	1706	9.0	22.7	11.1	8.0	15.4
C	2.30	Helium	20	280	9.0	22.7	11.1	18.2	6.7
H	2.35	O/F=1.2	30	1706	9.2	22.9	11.2	8.2	15.3
C	2.35	Helium	20	280	9.2	22.8	11.1	18.6	6.7
H	2.40	O/F=1.2	29	1706	9.4	22.7	11.1	8.3	15.0
C	2.40	Helium	20	280	9.4	22.9	11.2	18.9	6.6

These large differences are attributed to the effect of temperature. For this reason, the cold plumes using regular air do not appear in the set of winning combinations: The large R_j value of 2077 for Helium allows for some compensation of the low T_j of the cold plume; air does not show this effect. However, the temperature difference in one order of magnitude (slightly more than 1000 K for hot, 120 K for cold, thus a factor of ca. 10) cannot be alleviated by a gas constant that is merely 4 times higher than that of the hot plume.

A quick investigation indicated that mass flux and kinetic energy ratio can be matched reasonably well by adjusting the relative weight—but at the cost of the deviations in other similarity parameters being orders of magnitude higher.

Table 4.5: Deviations in similarity parameters of winning hot and cold plume pairs to one another

Combination	ΔI [%]	ΔII [%]	ΔIII [%]	ΔIV [%]	ΔV [%]
Hot (P_j = 2.20 bar) vs Cold (P_j = 2.15 bar)	2.3	0.4	0.3	54.9	123.1
Hot (P_j = 2.25 bar) vs Cold (P_j = 2.25 bar)	0.0	1.3	0.1	56.0	126.9
Hot (P_j = 2.30 bar) vs Cold (P_j = 2.30 bar)	0.0	0.2	0.0	56.3	129.0
Hot (P_j = 2.35 bar) vs Cold (P_j = 2.35 bar)	0.0	0.2	0.5	55.8	129.0
Hot (P_j = 2.40 bar) vs Cold (P_j = 2.40 bar)	0.0	1.0	0.6	56.2	125.8

COMPARISON OF MODEL PLUMES TO LAUNCHER

As seen in the results above, for every hot plume there exists a suitable cold plume (in this case helium). This is in-line with requirement `HF-TEC-CPL-01`. To find which combination, characterized by the exit pressure, is the best, the similarity of the hot plume (and for reference purpose the cold plume) to a launcher plume is considered (relevant for requirement `HF-TEC-HPL-01`).

An investigation has been conducted to determine the relevant launcher plume conditions to allow for comparison between hot and launcher plume. Although there exists data, presented in Table 4.6, for four rocket engines, it was shown in the Mid-Term Report that only the J-2 and Vulcain 2 motors can be simulated reasonably well. Because the Vulcain 2 is a more modern engine, it was selected as the reference launcher. It should be noted, though, that the two launchers are very similar.

Table 4.6: Nozzle exit parameters for plumes of various launchers, [26–29]

Engine	P_j [Pa]	γ_j [-]	M_j [-]	R_j [J/(kg K)]	T_j [K]	Fuel type
Rocketdyne F-1	38,815	1.24	3.76	358	1225	LOX/RP-1
Rocketdyne J-2	14,267	1.24	4.28	640	1019	LOX/LH_2
Space Shuttle SRB	332,397	1.22	2.85	299	1732	NH_4ClO_4/Al
Vulcain 2	15,190	1.20	4.50	537	1156	LOX/LH_2

In Table 4.7, the result of this comparison can be viewed. It can be observed that for higher exit pressures, the pressure ratio is met better. Also, hot plumes cannot resemble the mass flux ratio as well, while cold plumes fail in representing the kinetic energy ratio. Of the combinations presented, the hot and cold plume pair with P_j = 2.30 bar resembles the initial inclination angle second best, and relatively scores best in mass flux and kinetic energy ratio. Because their similarity between one another is deemed best as well, the decision was made to select this concept for HotFire. This row is also highlighted.

4.6. DESIGN OUTCOME

In the previous sections, the analysis and results for the propellant selection for HotFire were discussed. Table 4.8 shows the outcome of this selection process and also compares the plumes to the Vulcain 2 launcher. Afterwards, a short sensitivity study is presented, and recommendations are given.

The analysis of the concepts yielded a hot plume consisting of gaseous oxygen as oxidizer and kerosene as fuel, at an O/F-ratio of 1.2, combusting at a pressure of 30 bar and a temperature of 1706 K. The cold plume uses pure helium, at a total pressure of 20 bar and 280 K temperature in the settling chamber.

Table 4.7: Deviations in similarity parameters of hot and cold plume pairs to the Vulcain 2 engine of the Ariane 5 launcher (the chosen concept is highlighted)

Combination	ΔI [%]	ΔII [%]	ΔIII [%]	ΔIV [%]	ΔV [%]
Hot (P_j = 2.20 bar) vs Launcher (Vulcain 2)	11.5	16.0	70.3	149.1	16.4
Cold (P_j = 2.15 bar) vs Launcher (Vulcain 2)	14.1	15.7	70.8	12.4	159.6
Hot (P_j = 2.25 bar) vs Launcher (Vulcain 2)	9.0	15.1	62.4	131.3	14.1
Cold (P_j = 2.25 bar) vs Launcher (Vulcain 2)	9.0	16.3	62.2	1.7	158.9
Hot (P_j = 2.30 bar) vs Launcher (Vulcain 2)	6.6	15.4	55.5	115.6	12.1
Cold (P_j = 2.30 bar) vs Launcher (Vulcain 2)	6.6	15.2	55.5	5.8	156.7
Hot (P_j = 2.35 bar) vs Launcher (Vulcain 2)	4.4	15.8	53.7	109.2	12.9
Cold (P_j = 2.35 bar) vs Launcher (Vulcain 2)	4.4	15.7	54.5	7.6	158.3
Hot (P_j = 2.40 bar) vs Launcher (Vulcain 2)	2.2	15.2	54.5	107.1	15.1
Cold (P_j = 2.40 bar) vs Launcher (Vulcain 2)	2.2	16.1	53.5	9.3	159.9

Table 4.8: Properties of the hot (H), cold (C), and Ariane 5 launcher (L) plumes

	P_c [bar]	T_c [K]	P_j [bar]	γ_j [-]	M_j [-]	R_j [J/(kg K)]	T_j [K]	θ_N [deg]	AR [-]
H	30	1706	2.30	1.23	2.37	503	1111	7	2.77
C	20	280	2.30	1.67	2.03	2077	118	10	1.56
L	116	3340	0.15	1.20	4.50	537	1156	10	58.20

4.6.1. SENSITIVITY OF FLOW SIMILARITY

The design needs to be judged on its sensitivity to variations in conditions, namely a changing area ratio AR due to thermal expansion of the nozzle during operation as well as a mismatch in combustion chamber pressure P_c. The affected plume properties are displayed in Table 4.9.

Table 4.9: Variation of plume parameters for the sensitivity study of the plume. Affected values are typeset in bold face.

	P_c [bar]	T_c [K]	P_j [bar]	γ_j [-]	M_j [-]	R_j [J/(kg K)]	T_j [K]	θ_N [deg]	AR [-]
H_0	30	1706	2.30	1.23	2.37	503	1111	7	2.77
AR	30	1706	**2.17**	1.23	**2.40**	503	**1104**	7	**2.79**
P_c	**28**	**1705**	**2.05**	1.23	2.37	503	**1102**	7	2.77

The resulting deviations in similarity compared to the Vulcain 2 are given in Table 4.10. As can be seen, the case of a changing area ratio causes variations of no more than 20% at most compared to the baseline (H). The P_c-case is more critical, and therefore meeting the design pressure is highly advised.

Table 4.10: Deviations in similarity parameters of winning hot and cold plume pairs to the Vulcain 2 engine of the Ariane 5 launcher

	ΔI [%]	ΔII [%]	ΔIII [%]	ΔIV [%]	ΔV [%]
H_0	6.64	15.40	55.45	115.59	12.09
AR	12.88	13.88	60.34	134.06	9.83
P_c	19.65	12.55	73.76	168.33	12.52

4.6.2. RECOMMENDATIONS REGARDING THE PROPELLANT

From the similarity analysis it became apparent that higher combustion chamber pressures P_c and temperatures T_c results in better similarity, because the values come closer in magnitude to those of a real rocket.

Additionally, it is suggested to do further research into the characteristic length $L^\star$ of gaseous hydrocarbons, such as butane. They are expected to be lower than the liquid fuels investigated, even though the data from [17] contradicts this. That may be, on the other hand, because "hydrocarbons" is a too general term.

5

FEED SYSTEM

One of the most critical subsystems within HotFire is the feed system. Its function is to supply the propellants to the combustion chamber at the desired conditions. This chapter deals with the design of the feed system and its various components by starting with a general design and the integration within HotFire. Subsequently, the various components of the feed system are analyzed in terms of their flow performance, and the chapter concludes with a cost overview and recommended actions or changes for the current design.

The feed system interacts with the other subsystems of HotFire only in terms of a small number of variables. Driving inputs for the feed system design are the mass flow rate and pressure in the combustion chamber, as well as the type of propellants used; the only output that is of interest to other subsystems is the feed line size, which will determine the geometry of mount and model. This size is determined in cooperation with the mount and model subsystem design team, meaning that constraints put forth by the mount and model might limit the maximum size of the feed system.

5.1. REQUIREMENTS ON THE FEED SYSTEM

The feed system design has to take the following requirements into account:

`HF-TEC-CPL-01` The cold plume shall be similar to the hot plume.

`HF-TEC-MEA-06` The system shall operate for at least 5 s.

`HF-TEC-MEA-08` The plume conditions shall not vary by more than 1% over time.

`HF-CON-COS-01` The material costs shall not exceed €10,000.

`HF-CON-SAF-01` The system shall comply with regulations set forth by Delft University of Technology.

`HF-CON-SAF-07` The system shall not damage itself/infrastructure during storage.

Most of these requirements apply to several subsystems. For the feed system, `HF-TEC-MEA-06` directly dictates the minimum amount of fuel and oxidizer that the feed system needs to deliver per test. Additionally, `TEC-MEA-08` also dictates that this supply of fuel and oxidizer should be constant. The total costs of the feed system are estimated in Section 5.7.3 in order for the HotFire system to meet `HF-CON-COS-01`. For the remaining safety requirements (`HF-CON-SAF-01` and `HF-CON-SAF-07`), the wind tunnel technical supervisors of the AeroLab were consulted. The following advice influenced the design philosophy significantly:

- The entire set-up should be remote controlled.
- There shall be no single points of failure.
- The amount of stored propellants should be as small as possible.
- In case of power failure, the system should turn to a safe state.
- A safety factor of 2 should be implemented for all loads.

Finally, `HF-TEC-CPL-01` dictates that the feed system should allow for creation of a similar plume with cold gas.

Besides the requirements on the HotFire system as a whole, some additional requirements on the feed system can be derived from its interaction with other subsystems. From Section 4.6, it is known that the propellants that will be used are oxygen as oxidizer and kerosene as fuel. This selection will be the defining factor for many aspects of the feed system. An example would be the feed lines, where only components that are rated for the use with oxygen or kerosene (for the respective branches of the feed system) will be considered. For the cold plume, the working gas will be helium (see Section 4.6). This influences the design of the cold plume feed system as explained in Section 5.5.

5.2. CONCEPT SELECTION

Two main concepts are conceivable for the feed system: a turbopump-driven one, and a simpler blow-down system. Given the short run time of HotFire and the complexity and high cost of a turbopump-driven system, the decision was made to use a blow-down propellant feed system. In the particular case of HotFire, the oxidizer is stored in a pressurized reservoir and directly fed into the combustion chamber. The fuel - being incompressible - has to be pressurized by a separate pressurant.

A blow-down feed system consists of relatively few components, namely an **injector**, **feed lines**, a **kerosene tank** for the fuel, an **oxidizer tank** containing gaseous oxygen, a **fuel pressurant tank** used to force the kerosene into the combustion chamber, and finally a number of **valves** and **pressure regulators**.

5.3. COMPONENT DESIGN AND SELECTION

All components of the feed system have to be either self-designed or selected from commercially available products. This section presents this process for the components of the HotFire feed system as outlined in Section 5.2.

5.3.1. INJECTOR DESIGN

One of the most important parts of a rocket engine is the injector. Its design influences the quality and steadiness of the mixing of the propellants, which determines the overall stability and performance of the engine.

INJECTOR CONCEPTS

[30] and [16] describe various types of injectors. In principle, any of them could be used in HotFire. However, a number of limitations apply given the small size of the model. Complexity should also be kept to a minimum, while the concept has to be as safe as possible.

A **showerhead injector** works by injecting oxidizer and fuel in separate streams. No direct contact of oxidizer and fuel occurs. This increases the mixing time, meaning that the propellants will not mix properly within the combustion chamber. Therefore, a showerhead injector is discarded from the list of possible injector types.

In **impingement injectors**, the propellant streams meet in one point, ensuring proper mixing. This type of injector is discarded based on a lack of available space. The combined velocity vector of the propellant streams should be directed in the direction of the nozzle. Given the different injection velocities of fuel and oxidizer, this can only be achieved by directing two streams of one propellant at a single stream of the other propellant. This means that at least one of the feed lines has to be split up. Connecting three feed lines to the injector is considered not feasible due to the small space available in the model.

The **coaxial injector** is a type of injector where one stream is flowing inside another stream. Mixing is achieved by the development of a mixing layer between the two streams. A **ring slot injector** is very similar to this concept, with the only difference being the injection of multiple streams rather than just one. Given the lack of available space and the high complexity of a ring slot injector, it is also removed from the list of possible injectors for the HotFire test facility.

In a **splash plate injector**, oxidizer and fuel streams are directed against a plate. Mixing occurs due to the splashing when hitting this plate.

Finally, oxidizer and fuel can be mixed before injection. This can be done inside a premixing chamber or in the feed lines. For safety reasons, this **premix injector** is discarded. Premixing a gaseous oxidizer with a liquid fuel can also cause issues with maintaining a constant oxidizer-fuel ratio.

PRELIMINARY INJECTOR DESIGN

Two injector concepts remain, namely a splash plate and the coaxial injector. These two concepts are combined in HotFire by closing the end of the inner tube of a coaxial injector and drilling holes in the side walls. The propellant flow in the inner tube splashes against the end cap and sprays out through the holes in the side walls, thereby mixing with the propellant flow in the outer tube. This combination of concepts has the advantage of ensuring proper mixing of the propellants without being very complex or spacious.

Figure 5.1 shows the overall dimensions of the preliminary design of this injector. Its separation into three components, as well as more detailed dimensions, are indicated in Figure 5.2. The casing limits the cross-sectional area of the oxidizer flow. It can be easily exchanged if validation testing shows that the injector area does not create the required combustion chamber conditions. It was decided that the inner tube should contain the fuel. This is due to the fact that the fuel injection velocity is much smaller than the oxidizer injection velocity, thereby reducing the velocity component perpendicular to the desired flow direction towards the nozzle. Three holes of one millimeter diameter are present close to the end cap.

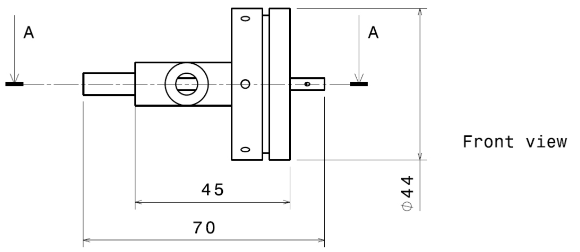

Figure 5.1: Technical drawing of the preliminary injector design

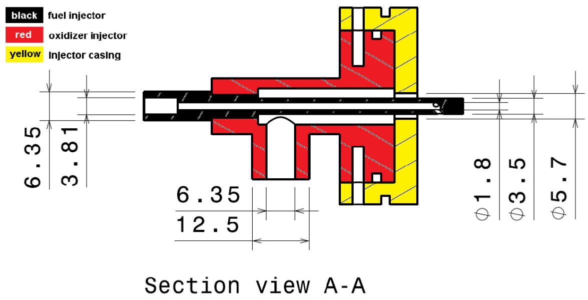

Figure 5.2: Technical drawing along section A–A from Figure 5.1

The oxidizer is fed into the injector from the side. The connection piece has dimensions according to the oxidizer feed line properties, see Table 5.1. Using a corner of 90 degrees, the oxidizer is guided into the outer tube. At the end of this tube, the cross-sectional area of the flow is further reduced by the injector casing. For the fuel connector piece, the same dimensions as for the fuel lines are used (see Table 5.1). After this connection the cross-sectional area of the fuel flow is decreased in a number of steps to the final value of the combination of three 1 mm-diameter holes.

5.3.2. FEED LINE SELECTION

The operation of the part of the feed system containing oxygen will have to be investigated very thoroughly, and the feed lines themselves are selected based on whether they are rated for oxygen flow [31]. For the fuel, nylon lines are selected because of their flexibility, strength and resistance to hydrocarbons [32]. Both lines are taken with a burst pressure of at least twice the expected operation pressure. The expected length of both lines is indicated in Figure 5.5 (feed system schematic) and based on the line length through the mount and space around the wind tunnel. These lengths are just preliminary estimates and can easily be modified. Since the lines travel through the mount, they have to make a tight turn when coupled to the injector, see Section 5.3.1. The minimum bend radius for the lines is 2.5 cm, which is sufficiently small to fit within the nose cone. Finally, the inner and outer diameters of the feed lines had to be selected. For the inner diameter, the driving factor was the resulting pressure loss in the feed system (see Section 5.4.3); the outer diameter was limited by the available space in the mount as specified in Section 7.6.

In addition to that, feed lines were selected for the generation of a cold plume. Here, another limiting factor was the issue of choking of the feed lines due to the absence of a combustion process. This is discussed in detail in Section 5.5.2.

Table 5.1 presents the final choice of feed lines for both hot and cold plume generators of the HotFire test facility.

Table 5.1: Feed line specifications

	Type	P_{burst} [bar]	D_{inside} [mm]	$D_{outside}$ [mm]
Oxygen [31]	SunFlex 744-04	1240	6.35	12.50
Kerosene [32]	Parker NBR-4-050	170	3.81	6.35
Helium [32]	Parker NNR-8-075	150	8.89	12.70

5.3.3. KEROSENE TANK DESIGN

Since kerosene is incompressible, another gas or liquid has to be used to drive out the kerosene from a container to the injector. This section presents a conceptual design for this set-up. To drive out the kerosene, nitrogen is selected because of its inert properties and the fact that it is easily available and used for other purposes in the wind tunnel laboratory as well. The kerosene tank (as shown in Figure 5.5) is a very simple structure that could be made out of a tube and two end-caps to which the fittings and hoses can be attached. The same method is applied to the PIV particle tank currently in use at the TST-27 wind tunnel (Figure 5.3). The kerosene tank is different insofar as a physical barrier is needed between the pressurant and the kerosene to prevent the pressurant from flowing into the combustion chamber. This can be achieved by installing a flexible fuel bladder containing the kerosene inside the pressure tank.

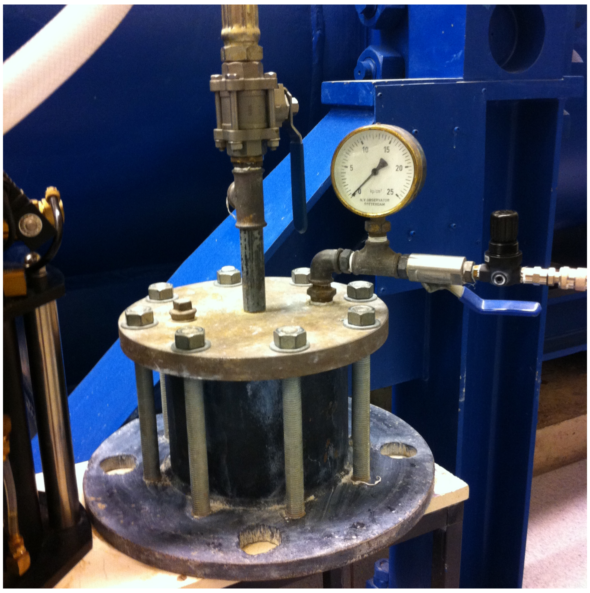

Figure 5.3: Tank in use at the TST-27 to feed the PIV particles into the free stream flow of the wind tunnel

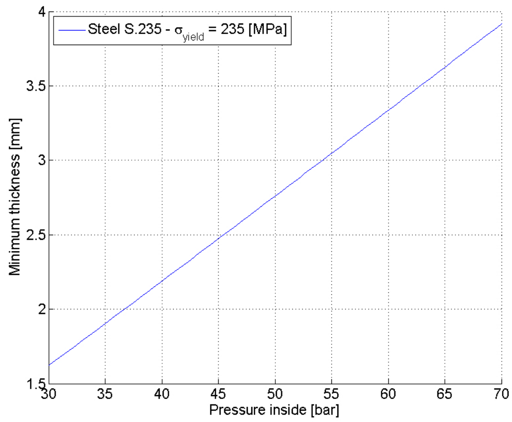

Figure 5.4: Required cylindrical wall-thickness of the kerosene tank walls (Safety factor of 2 is applied)

The volume of the tank around the (completely filled) bladder should be kept as small as possible in order to keep the expansion of nitrogen upon opening of the nitrogen control valve small. Given the kerosene mass flow of 0.0627 kg/s (see Table 5.3), equaling 0.0765 L/s at a density of 820 kg/m^3, a 2 L fuel bladder is selected to allow for a theoretical run-time of approximately 26 s. Some margin is required to ensure that any kerosene flow that occurs before the injection does not reduce the actual run-time. In addition to that, no fuel bladders with an even lower volume could be found. A small volume is desirable to limit the amount of combustibles present in the wind tunnel building (see Section 5.6). The total volume of the kerosene tank has to be slightly larger to allow for some play between the wall and the bladder and is set to 2.5 L. To determine the required wall thickness, the same closed pressure vessel relation can be used as in Section 9.8. For convenient handling, a base diameter of 15 cm and a height of 14 cm is taken. For simplicity, the same steel as the model is used to analyze the required dimensions. Figure 5.4 shows the required wall thickness of the cylindrical tube. With a safety factor of 2 applied, a wall thickness of 3.75 mm allows for a inside pressure of 67 bar given the outside pressure is 1 bar. This is clearly above the pressures encountered during operation.

Both the tube and the end-caps for the tank are available commercially. They can be ordered at the shops listed in [33] and [34].

5.3.4. OXYGEN AND FUEL PRESSURANT TANK SELECTION

The tanks containing the pressurized gases took place amongst commercially available ones due to safety reasons and ready availability. The standard pressure of non-cryogenic oxygen is 200 bar [35]. A 20 L tank is selected to limit the amount of potentially dangerous gases in the wind tunnel building (Section 5.6). According to the feed system analysis tool (see Section 5.7.2), this would allow for approximately 45 s of test time before the pressure in the tank drops below the pressure required to create a mass flow from the tank to the combustion chamber.

While the oxygen is stored in a pressurized tank and directly fed into the combustion chamber, the kerosene is pressurized by an external gas bottle containing a pressurant. Nitrogen was chosen because of its availability, low price and the fact that it does not support combustion. In addition to that, it is already in use at the aerodynamics laboratory. As for the oxygen tank, a 20 L / 200 bar gas bottle is selected.

5.3.5. VALVE SELECTION

For the valves, no special considerations except for a sufficiently high pressure rating were needed. Two types of valves will be used in the feed system: control valves and relief valves.

The purpose of the control valves is twofold. First of all, they can be used to adjust the mass flow rate of fuel and oxidizer during operation in order to for example throttle the engine. This functionality will most likely not be used in the HotFire test facility. However, the exact, invariable setting needed to achieve the desired combustion chamber conditions will have to be determined experimentally. In addition to that, the control valves are used during operation in order to start and stop the fuel and oxidizer flows. This is achieved using remote control. Therefore, electrically operated valves are needed. The selected valves are of the type ”PARKER 2-Way Solenoid Valve 0-3000psi” [36].

The incorporation of relief valves, as well as the number and placement of both control and relief valves, is mainly driven by safety factors. For the discussion of this aspect, the reader is kindly referred to Section 5.6. ”Parker RH4A-Series Adjustable Relief Valves” [37] are used.

5.3.6. PRESSURE REGULATOR SELECTION

The pressure in the reservoir will not only be higher than the pressure at which the propellants should be injected, but will also vary over time due to emptying of the tank (see Sections 5.4.5 and 5.4.6). Therefore, a pressure regulator is needed. This pressure regulator will ensure a constant pressure in the feed lines.

The pressure setting of the regulator will depend on the total pressure loss in the components of the feed system before the pressure regulator. The exact value of the pressure loss has to be determined experimentally by measuring the achieved combustion chamber conditions and adjusting the pressure regulator until the desired conditions are reached.

A pressure regulator has been selected that is rated for input and output pressures as determined using the feed system analysis tool (Section 5.7.2), namely the ”Parker HPR800 High Pressure Regulator” [38].

5.4. COMPONENT ANALYSIS

The core of the feed system is the driving force behind the propellant flow. In the case of the simple blowdown system adopted for HotFire, this force stems from pressurized reservoir tanks. The pressure in these tanks has to always be large enough to supply the required propellant mass flow to the combustion chamber. This means that the reservoir pressure has to be larger than the sum of combustion chamber pressure and all pressure losses for the entire duration of the test. Therefore, the components of the feed system as mentioned in Section 5.2 have to be analyzed in terms of their pressure losses. In addition to that, the reservoir tanks will also experience significant temperature changes. For a discussion of this effect, see Sections 5.4.5 and 5.4.6.

5.4.1. FLOW PROPERTY DETERMINATION

Before analyzing the individual components, some general equations need to be derived to determine the flow properties for a given cross section. The properties of interest are the density, average flow velocity and

Reynolds number. In addition to that, some elaboration on the relative magnitudes of static and dynamic pressure can provide insight into the origins of pressure losses.

Because the feed system is not insulated with respect to the ambient temperature, heat exchange is expected to take place between the flow in the feed system and the ambient air. Since no cryogenic propellants are used, this results in the assumption that the propellant flow is isothermal, meaning that it does not change temperature to any (significant) extent throughout the feed system. The only exception to this are the pressurant tanks, which will experience a significant pressure and temperature change (see Section 5.4.5)

Finally, the dynamic viscosity μ and the specific gas constant R of the flow are also assumed to be constant throughout the feed system.

INCOMPRESSIBLE FLUIDS

For incompressible fluids (i.e. liquids), determining density and average flow velocity is rather straightforward. The density is constant throughout the entire feed system and equal to the density of the propellant at ambient pressure. Therefore, the average flow velocity across the cross-section of the pipe can be determined directly according to

$$\mathrm{V}_{avg} = \frac{\dot{m}}{\rho A} \tag{5.1}$$

where A is the cross-sectional area of the flow through the component under consideration. The mass flow rate $\dot{m}$ is constant throughout the entire feed system.

Dynamic pressure is given by $P_{dynamic} = \frac{1}{2}\rho \mathrm{V}_{avg}^2$. In order to reach significant pressure losses, the dynamic pressure has to be of the same order of magnitude as the static pressure. In order to reach such a high dynamic pressure, kerosene would need to be flowing at a velocity of approximately 85 [ms^{-1}] (using a pressure of 30 bars and a density of 820 kg/m3). This value is far higher than what can be expected in most parts of the feed system according to Equation (5.1) (with the exception of the injector, see Section 5.4.2). Therefore, the dynamic pressure will be much smaller than the static pressure throughout most of the kerosene-filled part of the feed system. By itself, this is not an interesting fact; however, in the discussion of the individual components, pressure losses will be shown to be proportional to the dynamic pressure of the flow. Since the dynamic pressure is only a fraction of the total pressure, the pressure losses in many components will be very small.

COMPRESSIBLE FLUIDS

For gases, the situation is more complicated. Unlike for liquids, compressibility has to be taken into account. This can be achieved beginning from the energy equation: $\frac{P}{\rho} + e + \frac{\mathrm{V}^2}{2} = \text{const}$, which can be rewritten to yield $\frac{\gamma}{\gamma-1}\frac{P_0}{\rho_0} = \frac{\gamma}{\gamma-1}\frac{P}{\rho} + \frac{\mathrm{V}^2}{2}$. Using the isentropic flow relations as well as the definition of mass flow rate as stated in Equation (5.1), this can be rearranged to arrive at an expression for the density ρ as a function of known properties only:

$$\frac{\gamma}{\gamma-1}\frac{P_0}{\rho_0^{\gamma}}\rho^{\gamma+1} - \frac{\gamma}{\gamma-1}\frac{P_0}{\rho_0}\rho^2 + \frac{1}{2}\frac{\dot{m}}{A}^2 = 0. \tag{5.2}$$

Unfortunately, no closed-form solution was found for this equation; therefore, it has been solved for every point of interest using MATLAB's symbolic math functionality. While this is an acceptable solution if only values at a few points are considered, calculating the density changes in a flow with a continuously varying cross-sectional area could become quite time-consuming.

A parameter used in Equation (5.2) is the total density ρ_0. This value is obtained using the equation of state $\rho_0 = \frac{P_0}{RT_0}$, where P_0 is the total pressure in the part of the feed system under consideration (that is, the sum of the combustion chamber pressure and all pressure losses in components of the feed system between the combustion chamber and the component being analyzed). The total temperature T_0 is the temperature of the gas in the storage tank due to the assumption of isothermal flow.

Once the local density of the flow is known, its velocity can be determined from the definition of mass flow rate (Equation (5.1)).

5.4.2. INJECTOR ANALYSIS

The injector analysis is split up into two parts. While the kerosene injector is designed based on incompressible flow theory, the oxygen injector has to be treated differently to include compressibility effects.

KEROSENE INJECTOR

As presented in Figure 5.1 and Figure 5.2, the kerosene flows from the fuel line to the injector tube and then through the injector holes into the combustion chamber. Along this path, different pressure losses occur. These losses can be separated into losses due to the sudden change in cross-sectional area at the beginning of the injector tube and losses over the holes.

The total pressure loss for a sudden contraction is given by

$$\Delta P = K\frac{1}{2}\rho \mathrm{V}_{avg}^2 \tag{5.3}$$

where K is the loss coefficient and V_{avg} is the flow velocity after the contraction. This parameter is dependent on the geometry of the contraction according to

$$K = 0.42\left(1-\frac{d^2}{D^2}\right) \tag{5.4}$$

(see [39, p.373])where d and D are the diameters of the smaller and larger pipe, respectively.

For the flow through an orifice into a large reservoir (in this case the combustion chamber), [40, pp.6-21–6-22] gives the relation

$$\Delta P = \frac{1}{2\rho}\left(\frac{\dot{m}}{A_{\text{orifice}}}\right)^2\left[\frac{1}{{C_d}^2}\left(1-\frac{A_{\text{orifice}}}{A}\right)^2\right]. \tag{5.5}$$

In this case, the mass flow $\dot{m}$ has to be divided over the three orifices employed in the current design.

For Reynolds numbers larger than 20 000, the coefficient of discharge C_d in this relation is approximately equal to 0.62 [40]. Determining the flow properties (see Section 5.4.1) showed that the Reynolds number did indeed exceed this value for the current design.

Adding the pressure losses as calculated by Equation (5.3) and Equation (5.5) yields the total pressure loss over the kerosene injector. Unlike for bends in feed lines (Section 5.4.3) and valves (Section 5.4.7), the resulting value will not be negligible compared to the loss in the feed lines. Even though K is much smaller than the parameter $f\frac{L}{D}$ for a typical feed line (see Equation (5.6)), the dynamic pressure will be much higher due to the smaller cross-sectional area. Therefore, the pressure loss over the injector will be one of the most significant pressure losses in the feed system.

OXYGEN INJECTOR

Determining the pressure loss for the gas injector is more complex due to the fact that the theory presented for the kerosene injector is valid for incompressible flow only. There exists an analytical solution for total pressure loss over a sudden expansion according to [41]. However, corners and sudden contractions remain subject to empirical relations and were not investigated in detail due to time constraints.

The flow velocities in the oxygen injector are expected to be around 120 m/s according to the analysis described in Section 5.4.1. This translates into a Mach number of around 0.4. In this regime, compressibility effects begin to influence the pressure losses. However, the Mach number is not very far outside of the incompressible regime of 0.3 and lower. Therefore, the pressure loss is still analyzed using incompressible theory to yield at least an indication of the resulting values. It is strongly recommended to carry out a more thorough analysis of the flow behavior through the oxygen injector.

5.4.3. FEED LINE ANALYSIS

Two different parts of the feed lines have to be distinguished in order to determine the total pressure loss: straight sections, and sections that contain a bend. In both cases, the basic theory is the pressure loss as given by the Darcy-Weisbach equation (see [41, p.228])

$$\Delta P = f \frac{L}{D} \frac{1}{2} \rho V_{avg}^2 \tag{5.6}$$

where f is the Darcy-Weisbach friction factor, L and D refer to the feed line length and diameter, respectively, ρ specifies the propellant density and V_{avg}^2, finally, is the average flow velocity in the feed lines.

For losses around a bend, this equation has to be modified to include the loss coefficient K as follows:

$$\Delta P = \left(f \frac{L}{D} + K \right) \frac{1}{2} \rho V_{avg}^2 \tag{5.7}$$

In this case, the length is given from geometrical considerations to be $L = \pi R \theta / 180$, where R and θ are the bend radius and angle, respectively. The losses can be evaluated by using the mass flows from Tables 5.3 and 5.4 and the cross-sectional area of the feed lines.

The loss coefficient is assumed to be $K = 1.0$ to take the worst case scenario into account ([39, p.371]). In bends, the loss coefficient K outweighs $f \frac{L}{D}$ (values found for this parameter during the design process were on the order of 0.2 to 0.3). However, in a typical section of pipe, $f \frac{L}{D}$ is at least an order of magnitude larger. Therefore, the overall pressure loss due to the presence of bends is small compared to the pressure loss due to the rest of the feed lines. This means that the exact value of the loss coefficient K is insignificant.

Finally, the Darcy-Weisbach friction factor f results from an iterative solution of the Colebrook-White equation (see [41, p.239])

$$\frac{1}{\sqrt{f}} = -2 log_{10} \left(\frac{\epsilon}{3.7D} + \frac{2.51}{Re\sqrt{f}} \right) \tag{5.8}$$

where ϵ is the surface roughness of the pipe. The Reynolds number is given by $Re = \frac{\rho V_{avg} D}{\mu}$, with μ being the dynamic viscosity of the flow. It is important to note that this equation is only valid for Reynolds numbers larger than 4000.

Together, these equations allow for an estimation of the pressure loss that will occur over the feed lines, both for compressible and incompressible flow. One very important note is that the pressure loss is roughly proportional to D^5. Therefore, the feed line pressure loss is extremely sensitive to changes in diameter. This has to be taken into account when iterating during the design process: reducing the feed line diameter by a very small amount will have drastic effects on the rest of the feed system.

5.4.4. KEROSENE TANK ANALYSIS

In terms of pressure losses, the kerosene tank and any other components placed afterwards in the fuel feed system (see Section 5.7.1) are assumed to not have any influence. The flow velocity of the nitrogen into the tank is very small. This is caused by the fact that the volume flow rate of kerosene out of the tank and nitrogen into the tank should be the same. Assuming the same cross-sectional area for the pipes, the flow velocity of kerosene and nitrogen are the same. Therefore, the kinetic energy of the pressurant (having a small density because nitrogen is a gas, and having a small velocity because the driving factor is the flow velocity of the kerosene) is very small. Finally, this means that the pressure losses - which are proportional to the kinetic energy of the fluid - are also negligible in the parts of the feed system filled with nitrogen, which are all parts between kerosene tank and reservoir.

5.4.5. OXYGEN TANK ANALYSIS

The pressure in the reservoir tanks varies over time due to the emptying of the storage tanks. Assuming the worst-case scenario of isentropic flow, the pressure in the tank can be calculated as

$$P(t) = \left(\frac{\rho(t)}{\rho_0} \right)^{\gamma} P_0 \tag{5.9}$$

where rho_0 and P_0 are the density and pressure at the beginning of the test, respectively. The density is given by $\rho = m/V$.

The cause of the pressure drop is different for oxygen and nitrogen tanks. For the oxygen tank, the pressure changes due to a change in contained mass. This means that $\Delta m = -\dot{m}t$ assuming a constant mass flow. Therefore,

$$P_{\text{oxygen}}(t) = \left(\frac{\rho(t)}{\rho_0}\right)^{\gamma} P_0 = \left(\frac{m_0 - \dot{m}t}{m_0}\right)^{\gamma} P_0 = \left(1 - \dot{m}t\frac{RT_0}{P_0 V_0}\right)^{\gamma} P_0 \tag{5.10}$$

meaning a pressure drop of

$$\Delta P_{\text{oxygen}}(t) = \left[\left(1 - \dot{m}t\frac{RT_0}{P_0 V_0}\right)^{\gamma} - 1\right] P_0. \tag{5.11}$$

During the emptying of the tank, the temperature drops according to the isentropic flow equations. This drop is given by

$$T = T_0 \frac{P}{P_0}^{\frac{\gamma-1}{\gamma}} \tag{5.12}$$

5.4.6. NITROGEN TANK ANALYSIS

In the fuel-supplying part of the system, the situation is slightly different from the pressure drop analysis in Section 5.4.5 because the kerosene is pressurized by an additional gas tank containing nitrogen. This means that the pressure varies not due to a decrease in mass at a constant volume but rather due to an increase in volume at constant mass.

A relation for the pressure drop can be derived from the volume change, starting with $\Delta V_p = -\Delta V_f$, where subscripts p and f refer to the pressurant (nitrogen) and fuel (kerosene), respectively.

From this, the equation for the pressure in the tank (Equation (5.9)) can be rewritten to yield

$$P_{\text{nitrogen}}(t) = \left(\frac{V_0}{V_0 + \frac{\dot{m}t}{\rho_f}}\right)^{\gamma} P_0 \tag{5.13}$$

resulting in a pressure drop given by

$$\Delta P_{\text{nitrogen}}(t) = \left[\left(\frac{V_0}{V_0 + \frac{\dot{m}t}{\rho_f}}\right)^{\gamma} - 1\right] P_0. \tag{5.14}$$

The analysis of the temperature tank in the nitrogen tank is identical to the one presented in Section 5.4.5 (Equation (5.12)).

5.4.7. VALVE ANALYSIS

In terms of pressure loss, valves are very simple to analyze. Assuming that their cross-sectional area is the same as that of the feed lines, they will be opened fully during operation (disregarding minor adjustments to regulate the mass flow). In this case, the loss coefficient K is equal to 0.17 for a gate valve (see [40, p.469]). The pressure loss is then given by

$$\Delta P = K\frac{1}{2}\rho \mathrm{V}_{avg}^2. \tag{5.15}$$

As argued in the discussion of the pressure loss for bends in the feed lines (see Section 5.4.3), the resulting value of ΔP will most likely be negligible compared to the loss along the feed lines themselves.

5.4.8. PRESSURE REGULATOR ANALYSIS

It is assumed that any total pressure losses between pressure regulator and storage tank can be disregarded. This is a reasonable assumption because a pressure regulator is used to specify an output pressure, with the difference between reservoir and output pressures being far larger than any conceivable pressure losses.

5.5. COLD PLUME GENERATION

As outlined in Section 5.1, the HotFire test facility - and therefore also the feed system - has to be able to create a cold exhaust plume for reference purposes. On first glance, creating a cold plume seems to be easier than creating a hot plume. However, in reality a number of difficulties are encountered. They arise from the attempt to incorporate a cold plume generator into a system designed to generate a hot plume. In order to solve those difficulties, several components of the feed system will have to be changed significantly.

5.5.1. STORAGE TANK MODIFICATIONS

The most obvious change is the connection of a different storage tank containing helium (see Section 4.5). This tank has to be sufficiently large to provide the required, large mass flow of 0.2153 kg/s (see Table 9.2). Preliminary estimates based on the oxygen tank used for the hot plume (see Table 5.4) indicate a tank of 200 L at a pressure of 200 bar. The larger volume compared to the oxygen tank is required to adjust for the higher mass flow rate. However, this value needs to be analyzed properly.

5.5.2. MODIFICATIONS TO INJECTOR AND FEED LINES

Less directly visible, yet even more crucial, is the fact that the feed line diameter needs to be increased. For the cold plume, no heat is added in the combustion chamber. Combined with the increased cross-sectional area of the throat of the nozzle (see Section 9.5), this means that the critical conditions would be reached somewhere in the feed system rather than in the throat. Therefore, the cross-sectional area of every part of the feed system must be made larger than that of the throat. This also includes a redesign of the injector in order to prevent choking of the mass flow at that location.

For the feed lines, a preliminary analysis has been carried out to find the required diameters to prevent choking of the mass flows. Given the throat cross-sectional area of the nozzle of 1.1327 cm^2 (see Section 9.5), and using the maximum width available in the mount of 1.3 cm (see Section 7.6), it becomes clear that one feed line will not be able to provide the required cross-sectional area. The inside diameter would have to be larger than $\sqrt{\frac{4}{\pi}1.1327}$ or 1.2 cm, meaning a maximum wall thickness of 0.5 mm. For a flexible, commercially available line, this value is not feasible.

Therefore, splitting up the helium flow into two feed lines is suggested. The resulting inside diameter is 0.8492 cm. A feed line was found providing a sufficiently large inside diameter without violating the available width of the hole in the mount. The line under consideration - NNR-8-075 - (see [32]) has an inside diameter of 0.889 cm and an outside diameter of 1.27 cm while being rated to 37.9 bar.

In this case, the available length of the hole in the mount would have to increase from 2.2 cm to 2.6 cm (see Section 7.6) to encase two of the selected feed lines. Similarly, the inside diameter of the sting has to increase from 2.1 cm to 2.6 cm as well (see Section 7.6). These changes should - according to consultation with the mount design team - not cause structural or other difficulties. Due to time constraints, the required modifications and calculations have not taken place and therefore fall under the category of recommendations for completing the design.

5.6. SAFETY CONSIDERATIONS

The safety of the feed system is critical for the acceptance of ”HotFire” as a test set-up in the TST-27 wind tunnel. Therefore, the individual components and their placement are determined carefully according to the design philosophy outlined in Section 5.1.

5.6.1. COMPONENT CONSIDERATIONS

This philosophy directly determines some properties of the feed system components.

TANKS

The oxygen, nitrogen and kerosene tank need to be as small as possible to limit the amount of combustible mixtures in the wind tunnel area. This limits the possible damage resulting from a detonation of the entire contents of the propellant tanks in case of a complete system failure. The tanks themselves are acquired commercially and therefore assumed to be save.

FEED LINES

The tanks are connected to the combustion chamber by flexible feed lines. While there are no special safety concerns associated with pipes filled with kerosene, high-speed oxygen flow is inherently dangerous. Pure oxygen is highly reactive, potentially causing degradation of the feed line material. Spontaneous combustion of the feed line is another issue, especially at elevated pressures; in this case, pipes made of, for example, steel can act as fuel that will burn in an atmosphere of pure oxygen.

The safety risk of bursting feed lines or connections cannot be mitigated directly. Instead, it is limited by keeping the amount of propellants in the storage tanks as small as possible and by including control valves in the feed lines that can stop the fuel and oxidizer flows in case of failure.

CONTROL VALVES

All control valves - both in the oxygen and in the kerosene branch - are electronically operated to allow for remote control. In case of power failure, they will automatically close due to being spring-loaded, stopping fuel and oxidizer flows.

PRESSURE REGULATORS

Ideally, the pressure regulators should be directly connected to the pressurant tanks. This limits the part of the feed system operating under high pressures, causing a need for additional safety precautions and components capable of carrying very high pressures.

RELIEF VALVES

Directly connected to the pressure regulators are relief valves, meant to relief any overpressure that could result from a possible failure of the pressure regulator. Such a failure could be dangerous because only the part of the feed system before the pressure regulators is designed for the full pressure of the pressurant tanks. The components afterwards would most likely not be able to withstand this load case, resulting in a catastrophic failure.

5.6.2. COMPONENT PLACEMENT

In addition to the considerations regarding the individual components, their relative placement will strongly influence the safety of the system. The most important aspect in this case is to avoid any single points of failure.

OXYGEN BRANCH

In the oxygen branch, there are two possible components that could fail: the pressure regulator and the control valve.

The most critical case would be a failure of the pressure regulator, pressurizing the entire feed system at the storage pressure of 200 bars rather than the intended combustion chamber pressure of 30 bar (with the addition of some losses).

To mitigate this failure, a relief valve is added after the pressure regulator that will depressurize the system by venting into the outside room. Since this is not free of safety issues in case of oxygen, the control valves with which the flow can be stopped are located between the tank and the pressure regulator. Therefore, if failure of the pressure regulator and subsequent venting of the oxygen occurs, the flow can be stopped remotely or even automatically (provided an appropriate feedback system is installed). This ensures that in case of failure of the pressure regulator, only a limited amount of oxygen is vented via the relief valves.

In normal operation, the control valve is meant to start and stop the oxygen flow. It is duplicated to mitigate a single point of failure of this action as well.

KEROSENE BRANCH

The kerosene branch is slightly more complex since a kerosene tank is part of the system.

To prevent undesired kerosene flow caused by the low ambient pressure in the wind tunnel before the engine start-up, the start/stop control valve is placed between the injector and the kerosene tank. As for the oxygen branch, this valve is duplicated for safety reasons.

The pressure regulator is placed directly after the nitrogen tank such that the pressure in the feed lines is kept below the tank pressure of 200 bar. This pressure regulator is also followed by a relief valve, as in the case of the oxygen branch.

An additional control valve is added before the regulator to stop the flow, should the pressure valve fail. This valve is not duplicated because it is not a single point of failure: in case this valve fails, the flow in the kerosene branch can still be stopped by the (dual) control valves following the kerosene tank. Venting of the entire content of the nitrogen tank will only occur if both the pressure regulator and the control valve fail, and will still not result in a safety risk because nitrogen is not an inherently dangerous gas.

5.7. DESIGN OUTCOME

The following section intends to present the reader with a concise overview of the result of the design process for the feed system. It contains a schematic drawing of the entire preliminary design including relevant properties of the components, the resulting pressure losses, and an estimation of the costs of all elements. In addition to that, the compliance with the requirements stated in Section 5.1 is investigated. For a summary of remaining issues, please refer to Section 5.8.

5.7.1. FEED SYSTEM SCHEMATIC

The layout of the feed system is kept simple to increase the reliability of the system as a whole. It contains the elements in the order specified in Section 5.6. Pressure gauges are attached to the combustion chamber and kerosene tank. Their purpose is to enable fine-tuning of the system using static tests and to possibly incorporate a feedback loop that automatically controls the pressure regulators and control valves. This automatic control system could be used both to keep the combustion chamber properties constant and to provide automatic shutdown functionality in case of a failure. In reality, the system will also contain fill, drain and vent valves, and so on. However, these are not part of the basic functionality of the feed system (while of course still being essential) and have therefore been skipped in the simple overview presented in Figure 5.5.

The feed system schematic also contains the relevant properties of the various elements of the feed system. An exception has been made for the injector, the dimensions of which could not be included due to size constraints. For a technical drawing of this component, please refer to Section 5.3.1.

5.7.2. FEED SYSTEM DESIGN TOOL RESULTS

In the analysis of the individual components of the feed system (Section 5.4), equations for pressure losses and pressure drops have been stated. These are required because the total pressure in the reservoir tanks has to be large enough to supply the necessary propellant flow to the combustion chamber.

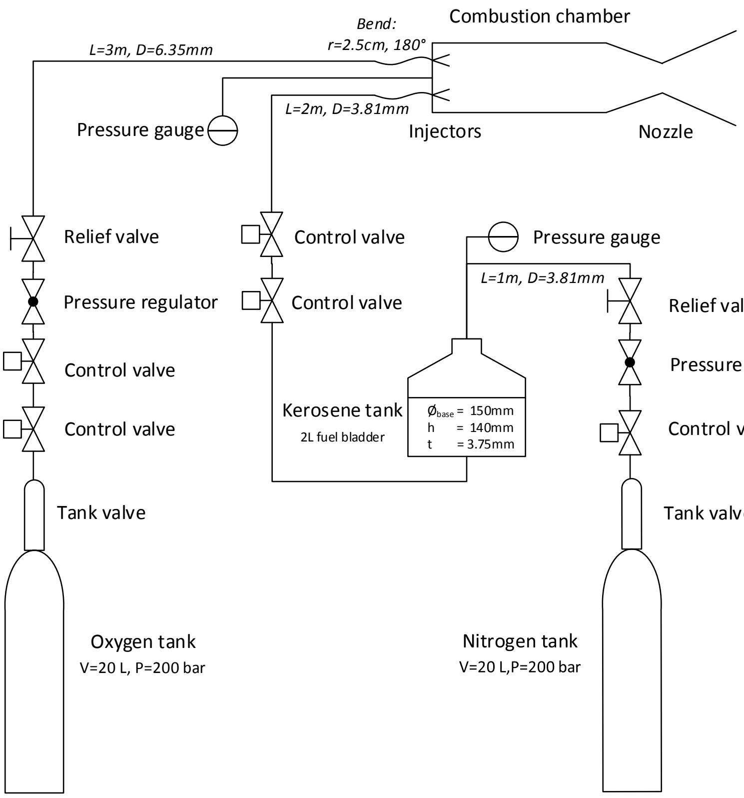

Figure 5.5: Schematic overview of the feed system

A tool has been written to accomplish the task of determining all pressure losses, as well as supplying other parameters of interest such as the pressure drop in the oxygen and nitrogen tanks during operation. The use of this tool consists of a single step only: in the main file, the input parameters such as fuel and oxidizer properties have to be specified; following this, the components of the feed system have to be added in the order in which they are used using the provided functions to for example add a bend to a feed line. Running the tool will then produce the pressure losses and changes in tank pressure and temperature. Because this procedure is perceived to be a straightforward and because no iterations take place within the program (the program simply sums the pressure losses created by the different components), block diagrams of the user interaction and the program structure would not contain any useful information and are omitted.

The results obtained with this software tool are summarized in Tables 5.3 and 5.4. Table 5.2 lists the parameters that were used in addition to the ones presented in Section 5.7.1. For screenshots of the exact program output, please see Figure B.1.

Table 5.2: Input parameter used for feed system pressure loss calculations

Parameter	Value	Unit	Obtained from
Combustion chamber pressure	30e5	[Pa]	Section 4.6
Mass flow rate of fuel and oxidizer combined	0.138	[kg/s]	Table 9.2
Oxidizer/fuel ratio	1.2	[-]	Table 4.4
Kerosene density	820	[kg/m^3]	[42]
Kerosene dynamic viscosity	1.3e-3	[Pa s]	[43]
Oxygen dynamic viscosity	20.4e-6	[Pa s]	[44]
Total temperature of propellants	293	[K]	room temperature
Surface roughness of feed lines	0.0015e-3	[m]	[39, p.357]

Clearly, the predictions made regarding the relative magnitude of pressure losses (the pressure loss due to bends and valves should be much smaller than the pressure loss due to feed lines and injector, see Section 5.4) have been verified. The pressure loss over the oxygen injector is only an indication of the exact value, based on incompressible theory (see Section 5.4.2).

Table 5.3: Fuel system design results

Injector pressure loss (sudden contraction)	1.21 bar
Injector pressure loss (orifices)	5.37 bar
Injector pressure loss (total)	6.58 bar
Pressure loss over the bend	0.28 bar
Pressure loss over the first 2m of feed line	2.33 bar
Pressure loss over the first control valve	0.03 bar
Pressure loss over the second control valve	0.03 bar
Total pressure loss over the feed system	9.25 bar
Initial nitrogen tank pressure	200 bar
Final nitrogen tank pressure	189.76 bar
Initial nitrogen tank temperature	293 K
Final nitrogen tank temperature	288.63 K
Kerosene mass flow rate	0.0627 kg/s

Table 5.4: Oxidizer system design results

Pressure loss over the injector (assumption)	(11.4 bar)
Pressure loss over the bend	0.62 bar
Pressure loss over the 3m of feed line	3.58 bar
Pressure loss over the relief valve	0.08 bar
Total pressure loss over the feed system	15.68 bar
Initial oxygen tank pressure	200 bar
Final oxygen tank pressure	161.08 bar
Initial oxygen tank temperature	293 K
Final oxygen tank temperature	275.42 K
Oxygen mass flow rate	0.0753 kg/s

The mass flow rates of kerosene and oxygen have been calculated using the overall mass flow and oxidizer fuel ratio according to $\dot{m}_{\text{fuel}} = \frac{1}{1+O/F}\dot{m}_{\text{fuel+oxidizer}}$ and $\dot{m}_{\text{oxidizer}} = \frac{O/F}{1+O/F}\dot{m}_{\text{fuel+oxidizer}}$ where O/F is the oxidizer to fuel ratio. These results are almost identical to the ones shown in Table 9.2; any differences are probably due to rounding of the oxidizer-fuel ratio.

Finally, the nitrogen and oxygen tank pressures and temperatures are stated for reference purposes. They show that the selected fuel, oxidizer and pressurant tanks (Sections 5.3.3 and 5.3.4) have sufficient capacity to ensure operation over a duration of far more than the required run-time of 5s (see Section 5.1).

5.7.3. COST

In order to meet the budget specified by requirement HF-CON-WOS-01, the costs of the total feed system are estimated. The price for each component is taken from various (online) stores and serves as an indication. Compatibility between hoses, valves etc. is not taken into account; this remains to be done when developing the system in more detail. Although larger hoses might be required for the helium feeding, the hoses will be roughly of the same price as the fuel hoses. Table 5.5 shows the estimated prices of all the components mentioned in Section 5.2, as well as estimations for some additional components such as manometers, couplings, clamps, and so on. With a total of €3,401.10, the feed system takes up a large amount of the budget. The main reason is that all components are of industrial-heavy duty quality and thus of the highest possible reliability.

Table 5.5: Cost estimation of feed system components

Component	Name/type used for cost determination	#	Unit price [€]	Total price [€]	Source
Fittings	Various	25	14.71	367.65	[45]
Electronic valves	PARKER 2-Way Solenoid Valve 0-3000psi	5	99.26	496.30	[36]
Relief valves	Parker RH4A-Series Adjustable Relief Valve	2	132.35	264.71	[37]
Pressure regulator	Parker HPR800 High Pressure Regulator	2	439.71	879.41	[38]
Oxygen line	Parker 7293-0750, per 100ft (similar to actual feed line)	0.1	774.26	77.43	[31]
Fuel line	Parker NBR-4-050, per 250ft	0.1	280.88	28.09	[46]
Cold plume line	Same as fuel line (similar to actual cold plume line)	0.1	280.88	28.09	
Injector	Approximation; two injectors (for hot and cold plumes)	2	100.00	200.00	
Nitrogen tank	20L, 200bar	1	196.60	196.60	[47]
Oxygen tank	20L, 200bar	1	250.00	250.00	[48]
Kerosene tank - 1	Hollow tube, D=20 cm, t=3.25 mm	1	60.00	60.00	[33]
Kerosene tank - 2	Plate for end-caps, t=3 mm	1	70.00	70.00	[34]
Kerosene tank - 3	Bolts, sealings, etc. (estimate)	1	50.00	50.00	
Bladder	3L fuel bladder (for indication; actually 2L)	1	66.18	66.18	[49]
Manometer	WIKA 7656072 Analogue Gauge 100bar	2	83,32	166.63	[50]
Additional	Couplings, clamps etc. (estimate)	1	200.00	200.00	
			Total:	**€ 3,401.10**	

5.7.4. MEETING OF REQUIREMENTS

A number of requirements were put forth for the feed system part of the HotFire test facility (see Section 5.1). As argued above, the requirement that the system shall operate for at least 5 s (`HF-TEC-MEA-06`) is clearly met by the feed system.

While the material cost of the feed system is relatively high (see Section 5.7.3), it does not exceed its budget (see Section 3.3). This fulfills the requirement that the material costs shall not exceed €10,000 (according to `HF-CON-COS-01`).

Regarding the cold plume generation capabilities, the feed system currently does not fulfill the requirement of creating a cold plume that is similar to the hot plume (`HF-TEC-CPL-01`). However, several suggestions are made to include this possibility without major changes to the HotFire test facility. For a more detailed discussion, please see Section 5.5.

In terms of plume stability, it was stated that the plume conditions shall not vary by more than 1% over time (`HF-TEC-MEA-08`). The adherence to this requirement is difficult to determine theoretically. As explained in Section 5.8, extensive testing including measurement of mass flow rates and combustion chamber pressure will be required to fine-tune the setting of control valves and pressure regulators and to ensure plume stability. In addition to that, the detailed design of the injector also influence the combustion chamber and will be a delicate task.

The remaining two requirements (`HF-CON-SAF-01` and `HF-CON-SAF-07`) concern the safety of the feed system during both operation and storage. As explained in Section 5.1, these two requirements translate into design philosophies that are meant to ensure the safety of the system. These design philosophies have been followed throughout the design of the HotFire feed system, meaning that both safety requirements are met.

5.8. RECOMMENDATIONS

In the discussion of the feed system, a number of recommendations was discovered. To facilitate the further design of the feed system, these recommendations are summarized below.

CONVERGENCE OF PRESSURE AND MASS FLOW RATE

An uncertainty that could not be resolved was whether the pressure and mass flow rate in the combustion chamber will actually attain the desired values. This is due to the fact that pressure and mass flow are interdependent, with various combinations yielding theoretically feasible solutions to the equations specifying pressure loss over components or dependency of mass flow on pressure differences. While the overall mass flow is controlled due to choking of the nozzle, there might still be variations in the individual mass flows of fuel and oxidizer. Any such variations will severely affect the combustion process, possibly also (e.g. via a change in total temperature) altering the overall mass flow through the choked nozzle. In order to control this, it might be advisable to control the mass flow in the feed system by choking the flow (for gases) or employing a cavitating Venturi tube (for liquids). However, the exact effect of such devices and their placement should be investigated in more detail, for example by performing a test of the entire feed system.

PRESSURE REGULATOR AND CONTROL VALVE SETTING

Connected to this issue is the fact that the pressure losses determined for the individual components are usually worst-cases values and at any rate have to be validated. Therefore, the pressure and mass flow rate in the combustion chamber should be measured during testing, and the pressure regulators and control valves should be adjusted such as to achieve the desired conditions (see Sections 5.3.5 and 5.3.6).

SAFETY ASPECTS

As stated in Section 5.6, pure oxygen flow can be highly dangerous. This has to be investigated very thoroughly, and the safety of the oxygen-containing part of the feed system has to be validated using outdoor tests at a safe distance from the HotFire test setup. In addition to that, the fire hazard due to venting pure oxygen into the wind tunnel room has to be investigated.

DESIGN TOOL / ANALYSIS METHOD IMPROVEMENTS - APPLICABILITY TO (IN)COMPRESSIBLE FLUIDS

While the analysis method is using well-established equations to determine pressure losses, some improvements can still be made. The majority of the code is applicable for both compressible and incompressible fluids. However, at the point of writing of this report, the analysis of the injector is only valid for incompressible (i.e. liquid) propellants (see Section 5.4.2). Depending on whether oxidizer and fuel change (e.g. to test a methane-based engine), this has to be updated.

DESIGN TOOL / ANALYSIS METHOD IMPROVEMENTS - TOTAL DENSITY

At the moment, the total density of the oxidizer after the pressure regulator has been determined by manual iterations. The current value is only valid for the current set-up of the feed system, yielding the current pressure losses. If the pressure losses change, so will the total density; this has to be included in the tool in form of an automatic iteration procedure.

DESIGN TOOL / ANALYSIS METHOD IMPROVEMENTS - LOCAL DENSITY

In terms of density, another improvement could be made regarding the determination of the density and flow velocity for a given cross-sectional area. At the moment, using MATLAB's symbolic math capabilities does not cause any issues with computation time. However, if these parameters need to be determined for a large number of points, problems might occur. In this case, it should be tried to optimize the existing function to find the density by specifying known (e.g. incompressible) cases or using an iterative solution procedure.

COMPATIBILITY

On a more practical note, the compatibility between the different components that were selected for the feed system has to be investigated.

DESIGN FOR COLD PLUME

Most of the design of the cold plume generator (see Section 5.5) is based on assumptions and preliminary estimates only. Therefore, a very important recommendation is to properly design the part of the feed system responsible for creating a cold plume. This involves analyzing the required storage capacities of the helium tank and adapting the entire design (including mount and model) to provide sufficient space for the feed lines, as well as designing an injector that is compatible with the forward pressure bulkhead of the combustion chamber.

TEMPERATURE EFFECTS

Finally, to improve the accuracy of the tool even more, the isothermal assumption made in Section 5.4.1 should be removed if possible.

ELECTRONIC CONTROL SYSTEM

Instead of a human controlling the system from the control room, an electronic system could be designed to automatically shut down the flow in case of failure. Additionally, instead of manually adjusting the pressure regulator valves, electronically regulated valves could be used. Of course, these are more expensive, but they would enable adjustment of the pressure regulators during operation. Feedback from the combustion chamber pressure gauge to the pressure regulator is then required.

PROPELLANT COMBINATIONS

It may be advisable to investigate the use of other fuels and oxidizers than the ones currently being used. No major redesign of the feed system is required; however, the pressure losses in the system have to be re-evaluated by static tests and the settings of control valves and pressure regulators have to be adjusted accordingly. In case of a gaseous rather than liquid fuel being used, the fuel branch of the system will have to be changed into a duplicate of the oxidizer branch of the current design. The only component that could require major changes it the injector, as its design is directly driven by the exact types of propellants used.

6

Aerodynamic Shape

The aerodynamic shape of the HotFire test set-up should make sure that the resulting flow around the model has the desired properties. The flow should be similar to that experienced in real launchers, shock waves caused by the model should not negatively affect the performance of the test set-up, and instability of the flow should be limited. For the aerodynamic design the shape of the nose cone, of the body, and of the mount are analyzed and presented in this chapter.

6.1. Requirements on the Aerodynamic Shape

Before designing the aerodynamic shape of the model, the requirements which apply for the design are analyzed:

`HF-TEC-HPL-01` The hot plume shall be similar to the plume of a launcher.

`HF-TEC-SIM-03` The external flow entering the base region shall be steady.

`HF-TEC-SIM-04` Shock waves shall not reflect from the wind tunnel wall into the model base region.

`HF-TEC-SIM-05` Shock waves created by the model shall not enter the base region of the model.

`HF-CON-WTO-01` The wind tunnel blockage shall not exceed 5%.

Most importantly the aerodynamic shape should create the shock waves such that they do not interfere with the base region. Furthermore the flow in the base region should be steady to allow for proper measurements. The last requirement is about the wind tunnel blockage; it should be attempted that the blockage area of the model does not exceed 40% of the total blockage as presented in Section 3.3.

6.2. Integration within HotFire

The aerodynamic shape is closely related to the design of the combustion chamber and the mount.

The nose cone size is influenced by the diameter of the combustion chamber, as presented in Chapter 9. At the same time the nose cone shape affects the combustion chamber sizing: the nose cone shape influences the distance between the base plate and the reflected shock wave which should be as large as possible to avoid shock wave interactions with the base region. This means that during the design of the aerodynamic shape iterations will be made together with the design of the combustion chamber.

Aerodynamic shape design is also related to the design of the mount, whose structural design is presented in Chapter 7. The aerodynamic shape analysis of the mount is included in this chapter to get an indication of the drag it causes and about the shock waves it is creates.

6.3. ANALYSIS

For the aerodynamic analysis analytical and CFD calculations are done. The CFD calculations will mainly be done to validate the analytical calculations. It is easier to use analytical calculations for designing the HotFire since the computational time for the MATLAB tool will be much lower and the script can quickly be iterated to optimize the design.

6.3.1. ANALYTICAL METHOD

SHOCK WAVE PROPAGATION

In order to calculate the shock wave propagation around the model an aerodynamic tool was created. The shock wave created by the model creates a reflected shock wave when interacting with the wind tunnel walls. This reflected shock wave should not interact with the base region since this would affect the flow here. The aerodynamic tool is able to give an indication of how much space there is between the model and this reflected shock wave.

Inputs and Outputs
In order to run the aerodynamic tool, a definition of all the dimensions is required. For the nose cone, the length and width are defined. For the body the length is defined, as well as the width at the base of the model. The different dimensions are shown in Figure 6.1a.

The output of the program is visualized in a figure, where the outline of the model is plotted, as well as the shock wave caused by the nose cone, the reflection of this shock wave from the wind tunnel wall and the expansion wave caused by the nose cone of the model. An example is shown in Figure 6.1b.

The distance between the reflected shock wave and the base of the rocket on the axis of symmetry of the model was defined to be minimal three to four times the diameter of the model. This comes from requirements `HF-TEC-SIM-04` and `HF-TEC-SIM-05`, saying that shock waves should not enter the base region. In order to visualize this, a line after the base region of the rocket is plotted with a length of four times the diameter. It can be seen in Figure 6.1b as the horizontal blue line behind the model.

The flow properties in different areas around the model are calculated. The different areas and dimensions are defined as shown in Figure 6.1a. The flow properties in area 1 are equal to the free stream properties. An oblique shock wave at an incidence angle of β changes the properties, resulting in Area 2. In Area 2 the flow is parallel to the nose cone angle θ. The flow near the model is turned out of itself by the expansion fan at the end of the nose cone. This is Area 3 in the tool. In Area 4 the flow properties change again when passing the reflecting shock wave, which has an reflection angle ϕ.

The tool was implemented in an iteration program which is able to calculate the optimum nose cone angle. This optimal nose cone angle gives the maximum amount of space between the reflected shock wave and the model base. A smaller nose cone angle would make the oblique shock wave angle smaller as well, which would result in the reflected shock wave being further downstream. Making the nose cone too small however, would lead in a long nose cone as well, resulting in less space between the base of the model and the reflected shock wave. A higher nose cone angle would result in a higher oblique shock wave angle. This means that the reflected shock wave starts more upstream, leaving less space between the base of the model and the reflected shock wave.

Theory
This paragraph will shortly discuss the theory which is used in order to create the aerodynamic tool. First the standard equations that are used to calculate the properties across an oblique shock wave will be stated. All equations were obtained from [23]. The normal component of the flow relative to the shock wave is calculated with

$$M_{n,1} = M_1 \sin(\beta). \tag{6.1}$$

Having the normal component of the flow before the shock, it is possible to calculate the properties after the shock. The relation between the flow properties before and after the shock are given with Equations (6.2) to (6.5).

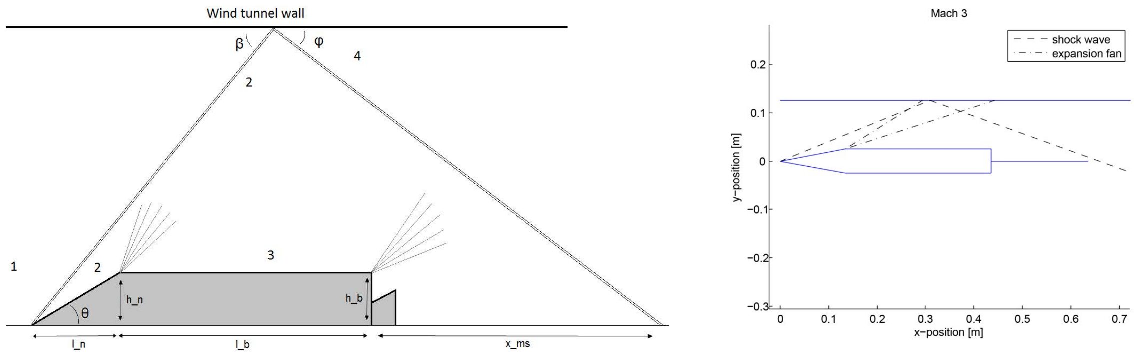

(a) Defined areas and dimensions

(b) Example of the program output

Figure 6.1: Input overview and example output of the aerodynamics tool

$$M_{n,2}^2 = \frac{1 + [(\gamma - 1)/2] M_{n,1}^2}{\gamma M_{n,1}^2 - (\gamma - 1)/2} \tag{6.2}$$

$$\frac{\rho_2}{\rho_1} = \frac{(\gamma + 1) M_{n,1}^2}{2 + (\gamma - 1) M_{n,1}^2} \tag{6.3}$$

$$\frac{P_2}{P_1} = 1 + \frac{2\gamma}{\gamma + 1}(M_{n,1}^2 - 1) \tag{6.4}$$

$$\frac{T_2}{T_1} = \frac{P_2 \rho_2}{P_1 \rho_1} \tag{6.5}$$

$$\tag{6.6}$$

Having the normal component of the flow after the shock, the downstream Mach number is obtained by using Equation (6.7).

$$M_2 = \frac{M_{n,2}}{\sin(\beta - \theta)} \tag{6.7}$$

The relation between the Mach number, shock wave angle and deflection angle is given by Equation (6.8). A MATLAB function (`theta_beta_mach_relation.m`) was implemented in the tool which was able to obtain the shock wave angle or Mach number for a certain deflection angle [51] using this relation.

$$\tan\theta = 2\cot\beta \frac{M_1^2 \sin^2\beta - 1}{M_1^2(\gamma + \cos 2\beta) + 2} \tag{6.8}$$

Since the model will have a three-dimensional shape, the shock waves near the model will behave differently than when considering a two dimensional shape. A cone experiences a three-dimensional relieving effect with respect to a wedge when looking at the strength of the resulting shock wave. In order to estimate how the shock wave over a cone behaves, the Taylor-Maccoll analysis was used. A given shock wave will be assumed, after which the cone that supports this shock wave is calculated [23]. The analysis consists of the following steps:

- An initial shock angle θ_s is estimated for a certain M_∞. Using the oblique shock relations, the velocity and flow deflection downstream of the shock are determined.
- The flow velocity is divided into a radial and normal component, denoted by V_r and V_θ respectively.
- The Taylor-Maccoll equation, which is shown in Equation (6.9), is solved for V_r at incremental steps of $\Delta\theta$ using a numerical solution technique.
- At each $\Delta\theta$ the value of V_θ is calculated. When V_θ is zero (the normal velocity condition near a surface), this means this certain value of θ represents the cone angle θ_c which supports the shock angle which was estimated in step one.
- The goal is to match the θ_c and the real cone angle. In order to do this, the whole process is iterated until θ_c and the real cone angle match.

The Taylor-Maccoll differential equations used for the process are shown in Equations (6.9) and (6.10) [52]. The script which was used to solve the Taylor-Maccoll equations uses the Runge-Kutta method to perform the integration.

$$\frac{\gamma-1}{2}\left[1-V_r^2-\left(\frac{\mathrm{d}V_r}{\mathrm{d}\theta}\right)^2\right]\left[2V_r+\cot\theta\frac{\mathrm{d}V_r}{\mathrm{d}\theta}+\frac{\mathrm{d}^2V_r}{\mathrm{d}\theta^2}\right]-\frac{\mathrm{d}V_r}{\mathrm{d}\theta}\left[V_r\frac{\mathrm{d}V_r}{\mathrm{d}\theta}+\frac{\mathrm{d}V_r}{\mathrm{d}\theta}\frac{\mathrm{d}^2V_r}{\mathrm{d}\theta^2}\right]=0 \tag{6.9}$$

$$V_\theta=\frac{\mathrm{d}V_r}{\mathrm{d}\theta} \tag{6.10}$$

To calculate the flow across the expansion fans, the Prandtl-Meyer function in Equation (6.11) is used. This equation relates the Mach number before and after the shock to the turn angle as shown in Equation (6.12) [23]. The Prandtl-Meyer function is already available in MATLAB's own aerospace toolbox as the function `flowprandtlmeyer.m`. Since the flow in the expansion wave is isentropic, the isentropic relations can be used to calculate the properties after the expansion fan.

$$\nu(M)=\sqrt{\frac{\gamma+1}{\gamma-1}}\cdot\tan^{-1}\sqrt{\frac{\gamma-1}{\gamma+1}(M^2-1)}-\tan^{-1}\sqrt{M^2-1} \tag{6.11}$$

$$\theta=\nu(M_2)-\nu(M_1) \tag{6.12}$$

Limitations

The tool which was created was intended to give a rough indication of whether the shock waves created by the different concepts interact with the plume. The tool is not capable of predicting aerodynamic behavior like the interactions between the shock waves and expansion fans. The expansion fan caused by the transition from nose cone to body will likely have an influence on both the shock wave caused by the nose cone and the reflected shock wave, which is not taken into account by the tool. The expansion fan results in the shock wave angle and the reflected shock wave angle to be smaller by making the flow more horizontal. This results in the reflected shock wave to impinge on the plume at a larger distance from the model.

The tool also does not take into account the boundary layers which will be present around the model and wind tunnel walls during experiment. This will mean the shock wave will reflect at a shorter distance from the model. These aerodynamic interactions which are not taken into account limit the tool in the sense that it will not predict the shock wave behavior with a large accuracy.

While designing a conservative distance of three times the diameter of the model is taken as a minimum for the distance between the base plate and the reflected shock wave. Further CFD analysis should be used to aid the design and to validate the results from the analytical calculations.

The results which were obtained for the Taylor-Maccoll function and the M-β-θ relation were verified using the graphs in [23, pp.618,835]. For both functions the values were the same. During verification, the Taylor-Maccoll function showed errors for small nose cone angles at low Mach numbers; for these conditions the program does not converge. This means that when running the tool at Mach 2 the nose cone angle θ should not be too small (below 5-6 degrees).

START-UP LOADS

The model will experience the highest loads during the start-up of the wind tunnel. During the start-up a normal shock wave travels across the wind tunnel, resulting in high pressure differences and thus high forces. The pressure difference across a normal shock wave at $M_\infty = 1.3$ was calculated, and this was multiplied by the projected area to get the force. This projected area differs for the x-, y-, and z-direction.

The wind tunnel technicians were also consulted to see what is usually done for the start up forces. Usually a pressure of 1 bar is taken in account acting on the model to calculate the start-up loads [53].

OPERATIONAL LOADS

Forces during the operation acting on the model consist of drag and thrust, for which the calculation method will be presented in the following paragraphs.

Drag on the Model

The drag on the model was calculated by evaluating the pressure around the model, and taking the axial component of the pressure acting on the surface of the model. The pressures were obtained using the same script which calculated the shock wave interactions around the model which was shown in Section 6.3.1. This script uses the Taylor-Maccoll equations to calculate the aerodynamic properties around a three-dimensional cone.

Since one of the reasons this model will be built is to measure the base pressure, it was not possible to calculate the pressure behind the model. This means that the calculated drag will be a conservative estimate since the axial component of the pressure acting forwards will be neglected.

Drag on the Mount

The drag caused by the mount was evaluated in a similar way as that of the model. The only difference is that the mount was approximated by a wedge instead of a cone, which made it possible to use the two-dimensional M-θ-β relation instead of the Taylor-Maccoll function. The pressure acting on the front of the mount was obtained by using the oblique shock wave relations, and the pressure behind the mount was calculated by using the Prandtl-Meyer relation for flow across an expansion fan.

The axial components of the pressure were multiplied by the cross sectional area they acted on to evaluate the drag. The aerodynamic shape design of the mount is closely related to the design of the mount in Chapter 7, where most of the dimensions of the mount are set. These dimensions mainly come from structural requirements and requirements with respect to internal space to allow for propellant lines.

Thrust

Calculating the thrust from the model is quite straightforward; data from Chapter 9 can be used to evaluate Equation (6.13) [54].

$$F_T = \dot{m}V_e + (p_e - p_\infty)A_e \tag{6.13}$$

6.3.2. CFD SET-UP

The analytical method of determining the shock angles and the shock reflection including the use of three dimensional relief effects produced results. In order to check if those results are correct and in order to validate the tool itself, a computational fluid dynamics (CFD) program was used. The program itself is called FLUENT and is a CFD solver within the ANSYS workbench. Figure 6.2a shows the general shape that is put into the program. The HotFire body was modelled inside the TST-27 wind tunnel, which has a total distance of 0.27m from top to bottom. This shape is afterwards meshed with overall 109000 nodes and 54000 elements. A mesh refinement is done along four main lines. Along those lines shock waves are expected and a refinement will lead to a better convergence. The mesh is shown in Figure 6.2b.

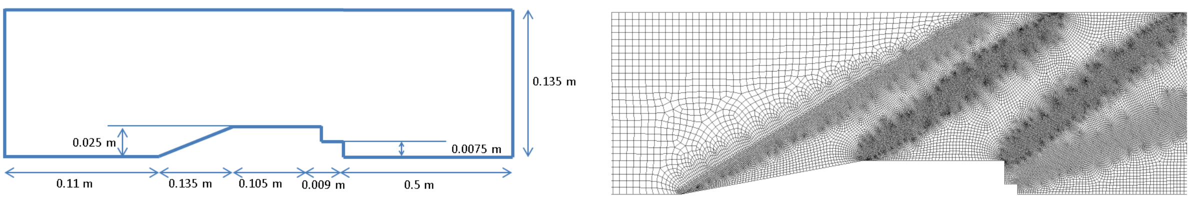

(a) Main dimensions used for the CFD model

(b) Mesh used for the CFD model

Figure 6.2: Geometric shape and resulting mesh for CFD (ANSYS) simulation

For the top boundary a wall boundary is enforced, for the inlet and outlet a pressure-far-field boundary is used and for the axis a symmetric boundary is put. This axis symmetry enables the calculation of three dimensional relief effects by the nose cone. The nozzle and the plume itself are modeled in a later stage, therefore, the whole model including the nozzle part are defined as interior. Now that the program has been set-up and the boundary conditions are defined, the problem can be solved using FLUENT. The solver setting used and the results are shown in Section 6.4.2.

6.4. RESULTS

6.4.1. ANALYTICAL RESULTS

MODEL SHAPE AND FLOW INTERACTION

The analytical results from the aerodynamic tool are presented in Figure 6.3. The results show the oblique shock wave and the reflected shock wave, along with the expansion fan caused by the directional change from the nose cone to the body, at a Mach number of 2. According to the calculations there is 3.06 times the model diameter left between the base of the model and the reflected shock wave. This would mean there is no interference from the reflected shock wave on the flow around the base region. Further CFD analysis is needed to validate this result.

The nose cone shape was determined by iterating the shock wave propagation tool by varying the nose cone length and selecting the nose cone size at which the distance from the base plate to the reflected shock wave was maximum. Making the nose cone angle θ (Figure 6.1a) small, results in the reflected shock wave moving downstream, but increases the nose cone length. Making the nose cone angle too large gives a small nose cone but moves the reflected shock wave upstream. The model diameter was iterated to 50 mm to have enough space for the combustion chamber and other components inside the model. This resulted in a nose cone length of 135 mm for the maximum distance between the base plate and reflected shock wave.

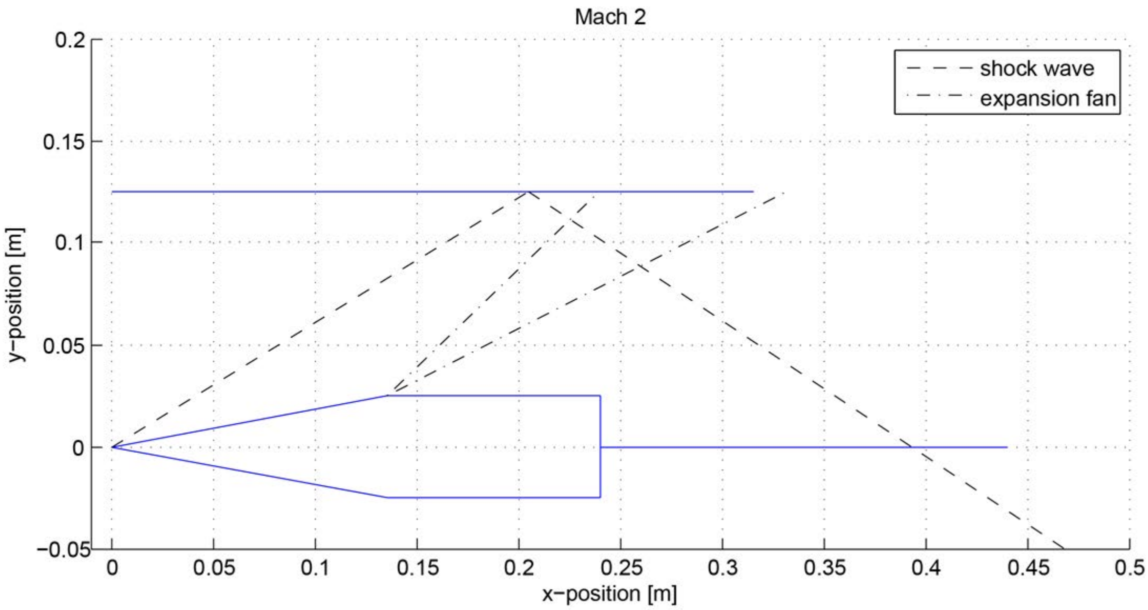

Figure 6.3: Shock wave propagation (Analytical results)

A table with the flow properties around the model, in the regions as defined in Figure 6.1a, is presented in Table 6.1.

Table 6.1: Flow field parameters around HotFire model

Region	M [-]	P [Pa]	T [K]	V [m s^{-1}]
1	2.00	$5.11{\cdot}10^4$	155	499
2	1.82	$6.73{\cdot}10^4$	168	473
3	2.20	$3.71{\cdot}10^4$	142	525
4	1.45	$1.14{\cdot}10^5$	197	408

MOUNT SHAPE

The mount shape is mainly defined by the structural loads as analyzed in Chapter 7. Making the front of the mount more sharp results in an oblique shock wave with a lower deflection angle β. This will lower the

Mach number reduction across the shock, which means the static pressure acting on the front of the mount is less than for a shock wave with a high deflection angle β. This means a reduction in drag. The width of the inclined beam was designed to be 18 mm, where the minimum width is constrained by the size of the fuel lines. The length of the sharp frontal section of the mount was designed to have a length of 30 mm to reduce the drag. These dimensions combined give a deflection angle θ for the mount of 16.7 deg.

START-UP LOADS

The resulting start-up forces calculated by using a normal shockwave at $M_\infty = 1.3$, and the start-up forces recommended by the wind tunnel technician are presented in Table 6.2. As can be seen the calculated start up forces are higher than the forces which were recommended by the wind tunnel technician. For the structural analysis of the mount, which is presented in Chapter 7, the forces will be used which were calculated from the pressure drop across a normal shock in order to create a conservative design.

Table 6.2: Wind tunnel start-up loads

	F_x [N]	F_y [N]	F_z [N]
Δp at M= 1.3	391	1002	1848
WT technician recommended	336	863	1591

The results from the wind tunnel start-up load calculations are comparable when looking at experiments which were done in the past. A ramjet projectile with a diameter of 52 mm and a nominal length of 344 mm experienced 2100 N of start up loads in a high speed wind tunnel [55].

OPERATIONAL LOADS

The drag forces calculated by the MATLAB scripts which were explained in Section 6.3.1 are presented in Table 6.3.

Table 6.3: Operational loads

	F_D [N]
Mount	118
Model	132
Total	250

The thrust was calculated to be 325 N, using Equation (6.13). The values used are $\dot{m} = 0.1337$ kg s^{-1}, an exit velocity for vacuum of $V_e = 2194$ m s^{-1}, $p_e = 2.3$ bar, $p_\infty = 0.5$ bar, and $A_e = 1.77 \cdot 10^{-4}$ m^2. Having thrust means that it will relieve some of the force caused by the drag on the mount. The operational forces will be used for the structural design of the mount, which is presented in Chapter 7.

6.4.2. CFD RESULTS

2D CFD ANALYSIS

In order for FLUENT to generate results, different settings have to be specified for the solver. For the visualization of the shock waves, the energy equation was included in the inviscid modeling of the problem. The pressure-far-field boundary condition was set to a Mach number of two and a total pressure of two bar. Residuals of 0.01 are defined for all parameters and an implicit second order upwind method has been used for solving the problem. The result in terms of Mach number are shown in Figure 6.4.

It is clearly visible that the initial shock wave as well as the expansion fan due to the angle change from the nose cone to the combustion chamber are modelled. The initial Mach number of 2 decreases to a Mach number of and increases again after the expansion fan as expected. The lowest Mach number is reached in the base plate region, where the flow has almost zero velocity. The highest velocity of $Mach = 3$is reached in the base plate expansion. The interaction zone between the reflected shock wave and the symmetry line is at about 17 cm from the base plate.

Figure 6.4: Results of the CFD (ANSYS) analysis for $M = 2$ and $P = 0.2$ bar

3D CFD RESULTS

A sequence of cross sectional views of the flow at different locations perpendicular to the model is shown in Figure 6.5. The results can be used to see how much influence the designed mount has on the flow around the model.

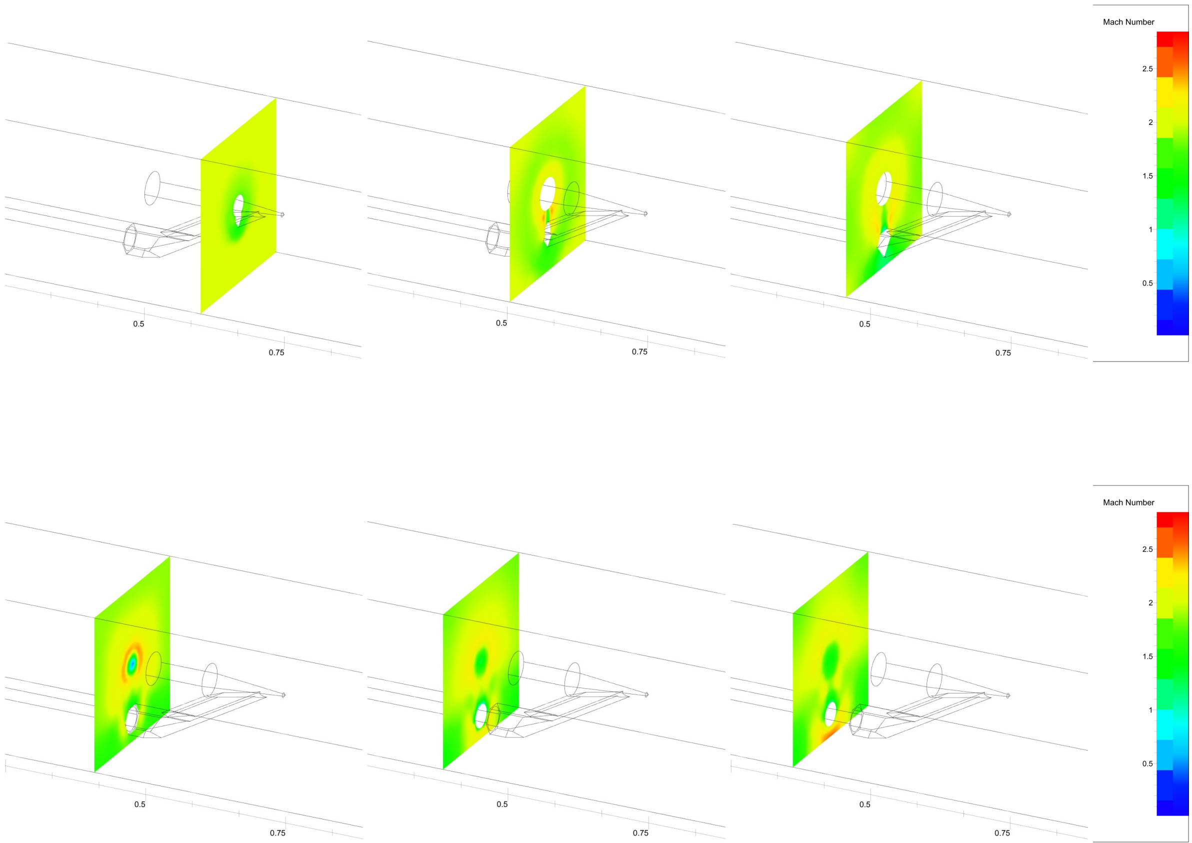

Figure 6.5: Flow Mach number across several cross-sections

From the figures it can be concluded that the mount will not influence the flow on the top half of the model significantly. As can be seen in Sections 6.4.2 and 6.4.2 the mount causes disturbances which influence the lower half. This can be seen by looking at Sections 6.4.2 and 6.4.2, where the flow after the model is not symmetrical when looking at the top and lower half. The mount should not influence the flow in the top half significantly as can be seen in Sections 6.4.2 and 6.4.2 when looking at the flow after the model.

6.4.3. COMPARISON ANALYTICAL AND CFD RESULTS

The comparison between the CFD results from FLUENT and the analytical solution is shown in Figure 6.6. In this figure the analytical solution has been put over the solution from FLUENT, to facilitate the comparison. Furthermore the color scheme has been edited to make the shock waves more visible. Due to this adaptation of the color scheme, Mach numbers which exceed the defined range are shown in the same color.

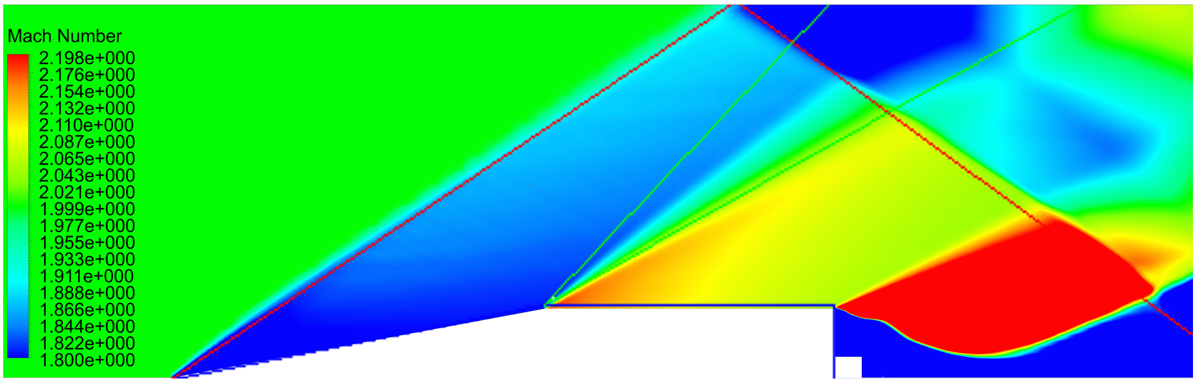

Figure 6.6: Comparison between analytical and CFD (ANSYS) solution of the shock wave interaction for $M = 2$ and $P = 0.2$ bar

When comparing the analytical solution to the numerical solution by FLUENT, has the same angle and propagation for both cases. However, the expansion fan at the transition zone between nose and body tube is modeled less accurate by the analytical solution. This is mainly due to the fact that two dimensional equation were used for the calculation of the expansion fan. The shock wave reflection of the initial shock wave is similarly modeled in both cases. It can generally be concluded that the analytical tool, used for the design of the model is correct and more conservative than the CFD results. The design of the model is therefore conservative and no interactions of the plume and the reflected shock waves are expected between the base region and three times the base diameter. It should be noted that there is no boundary layer present in both the CFD calculations and the analytical calculations.

6.5. DESIGN

In order to show the design of the aerodynamic shape first a overview with the general dimensions is presented, after which the budget and requirements of the design will be discussed.

6.5.1. OVERVIEW

An indication of the aerodynamic shape is shown in Figure 6.7. Figure 6.7a presents the general dimensions of the model, and how the model is aerodynamically connected to the mount. Figure 6.7b presents the aerodynamic shape of the mount. It shows the cross section of the aerodynamic shape, the general dimensions of the mount and what the shape of the mount looks like.
In order to meet requirement `HF-TEC-HPL-01` which states that the flow near the base region should be similar to the flow in real launchers, a strip of zig-zag tape will be placed on the model. This is a kind of tape that makes flow turbulent when passing it. The tape will be placed on the model, somewhere after the nose cone, in order to make the flow entering the base region turbulent.

The nose cone of the model is designed to have a radius. This radius is first of all necessary for manufacturing. Secondly it is not possible to analyze an infinitesimally sharp nose cone in CFD. Finally a round nose cone is beneficial for the aerodynamic behavior; a sharp nose cone will cause flow separation when the model is subjected to small deflections. Making the nose round will avoid this.

6.5.2. BUDGETS

The blockage budget of the aerodynamic shape can be calculated by analyzing the cross-sectional area as $\pi\left(\frac{50\text{ mm}}{2}\right)^2 = 1963\text{ mm}^2$. With a total blockage of 3645 mm^2 this means that the model takes up 53.9% of the

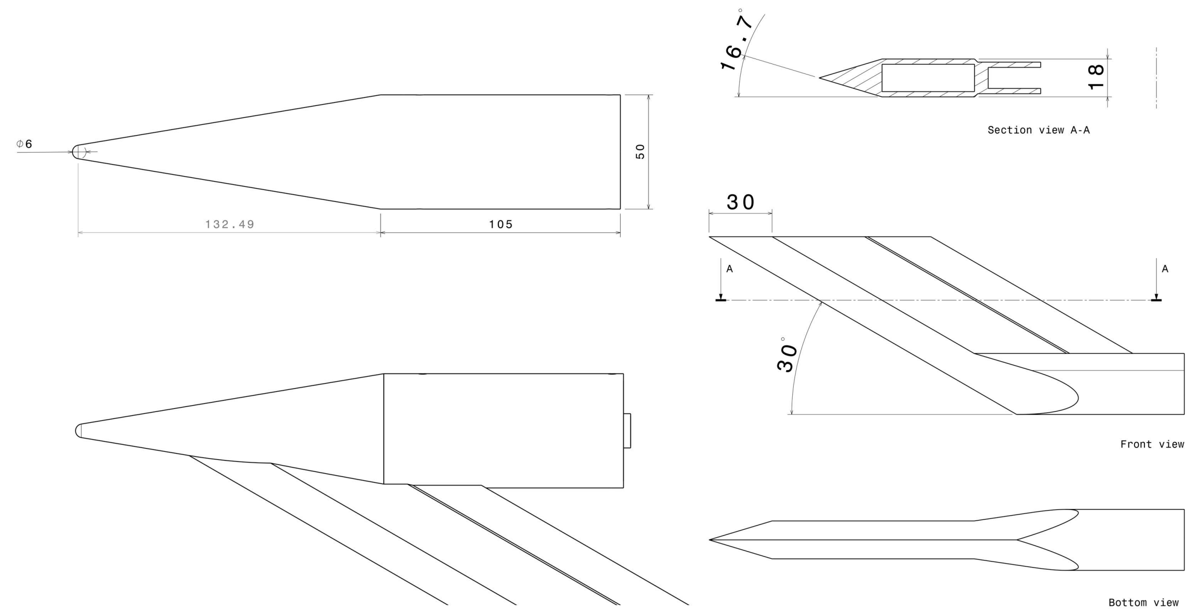

(a) Design of the model shape

(b) Design of the mount shape

Figure 6.7: Aerodynamic design of the model and mount

blockage budget.

6.5.3. DISCUSSION

Requirements `HF-TEC-SIM-04`, `HF-TEC-SIM-05`, and `HF-CON-WTO-01` are met when looking at the design. Shock waves do not enter the base region according to the analytical analysis and calculations done using CFD. The wind tunnel blockage of 53.9% is sufficient when combining it with the blockage of the mount, which is 45.5%. It is not known yet whether the external flow entering the base region is steady. This should be analyzed in the future, or experimentally tested. This means requirement `HF-CON-WTO-01` is not met.

6.6. RECOMMENDATIONS

A 3D analysis was done to see the aerodynamic behaviour around the model and the mount. So far this analysis indicated that the mount which was designed does not cause any problems with respect to the flow around the base plate. It is recommended to look more into the aerodynamic interactions between the mount and model to see whether this is really true.

The aerodynamic analysis was performed on a model with a sharp nose. The nose should have a radius to decrease flow separation caused by disturbances of the model and for manufacturing. It is recommended to investigate how much the flow differs for a sharp nose and a nose with a small radius.

7
MOUNT

The mount is the connecting element between the model and the wind tunnel, which makes it essential to perform a proper analysis on this subsystem. It needs to be strong enough to sustain all loads acting on the model, both start-up loads, drag during operation, and thrust. Furthermore, the eigenfrequency of the mount-model system should be high in flutter. Therefore, it also needs to be stiff.

In this chapter, the requirements on and the integration of the mount are discussed first to know what needs to be considered in the design. Then, a structural and vibrational analysis is performed on the chosen concept—the sting mount. The results of both simplified models (via MATLAB) and finite element models (via ANSYS) are presented to arrive at a design.

7.1. REQUIREMENTS ON THE MOUNT

Before starting the design of the mount, it is necessary to know what requirements the mount should fulfill. The following requirements were identified as important for the design of the mount:

`HF-TEC-MEA-02` The system shall allow for a constant visual access to the base region.

`HF-CON-WTO-01` The wind tunnel blockage shall not exceed 5%.

`HF-CON-COS-01` The material costs shall not exceed €10,000.

`HF-CON-COS-03` The costs of additional modifications to the wind tunnel shall be low

`HF-CON-SAF-01` The system shall comply with regulations set forth by Delft University of Technology.

`HF-CON-SUR-02` During operations, the model shall not fail statically due to loads.

`HF-CON-SUR-03` During operations, the model shall not fail dynamically due to vibrations.

`HF-CON-SUR-04` During operations, the model shall not fail due to temperature.

`HF-CON-SUR-05` The model shall not fail during wind tunnel starting due to shock loads.

`HF-CON-SUR-06` The model shall not fail during wind tunnel starting due to flutter.

Since the goal of this experiment is to measure the behavior in the base region of the model, it is essential that the mount does not obstruct visual access to the base region (`HF-TEC-MEA-02`). This means that the mount should be designed to be out of the line of sight between the base region and the windows from which the measurements are taken.

There is only limited space in the wind tunnel due to the blockage requirement `HF-CON-WTO-01`. This limits the size of the mount, while it should still be strong enough to carry all the loads, and still large enough to provide enough space to lead the fuel lines to the model. In Section 3.3 it was specified that the design should aim at a mount with a maximum cross-sectional area of 40% of the total blockage.

In order to keep the costs of the mount below the amount specified in Section 3.3, it is important to look at the materials from which the mount will be constructed (`HF-CON-COS-01`). Additionally, the mount should keep the wind tunnel modification costs low as well (`HF-CON-COS-03`).

In order to comply with the regulations as set forth by Delft University of Technology (`HF-CON-SAF-01`), the mount will be designed with a safety factor of 2 on every load carrying part of the design. This results in a design yield stress of $\sigma_y/2$.

The other requirements define the structural loadings that the mount should be able to survive, both static and dynamic ones. Therefore a static and vibrational analysis are conducted, but also a thermal analysis is needed to investigate if the heating of the mount due to the plume compromises its strength.

7.2. INTEGRATION WITHIN HOTFIRE

All loads acting on the model are introduced in the mount and then led to the wind tunnel support. These loads can consist of wind tunnel start-up loads and thrust/drag during operations, as described in Chapter 6. The loads should not cause excessive deformation of the mount, as this would influence the overall performance of the system. Therefore, a structural analysis is needed to see how the mount reacts to possible loads.

Besides being a structural element supporting the model, the mount will also be used to transport fuel and oxidizer to the model. The propellant lines of the feed system, which are described in Chapter 5, are led through the mount to the model. The mount will keep the propellant lines in place, and will serve as an aerodynamic fairing around it. Because of size constraints, the available cross-sectional area for feed lines is limited. The mount will further accommodate electrical wiring and measurement devices (see Chapter 10).

7.3. CONCEPTS AND MOUNT PROPERTIES

7.3.1. CONCEPTS

Chapter 2 identified two concepts for mounting the model. The first one is the sting mount shown in Figure 7.1a. In this concept the model is attached to a horizontal "sting", which extends downstream and is attached aft of the test section in a carriage. In the case of a window mount (Figure 7.1b) the model is attached to a mount that extends perpendicular to the model through a window in the test section.

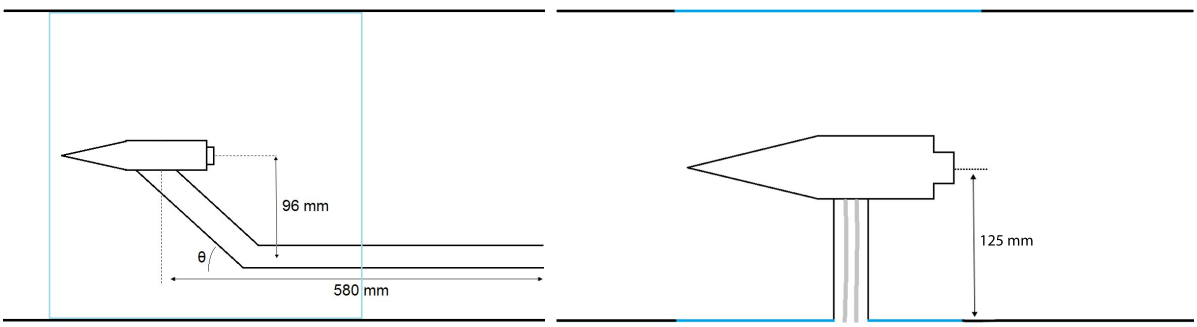

(a) Sting mount concept (side view)

(b) Window mount concept (top view)

Figure 7.1: Mount concepts

While the window mount is easy to design structurally, it has two negative side effects. First, the mount extends through a window, which means that it obstructs measurement techniques like Schlieren visualization through this window. Secondly, the window mount introduces more blockage than the sting mount since the projected area of this type of mount will be larger for a given fuel line diameter.

Because of these downsides of the window mount, it was decided to design a sting mount. If the sting mount would prove to be unfeasible structurally, or if the length of fuel lines in a sting mount would be too long, the window mount concept could be selected.

7.3.2. MOUNT SHAPE

In order to start with the design, preliminary calculations were done to estimate the angle of the inclined beam θ as shown in Figure 7.1a. For the total blockage, the frontal projected area is used to get a conservative design. For the design of the mount, the local cross sectional blockage is used to optimize the mount design and make the design safer. This local cross-sectional area is minimized by decreasing θ. The angle, however, should not be too small either, since this means that the incline beam will need to be longer wider in order to fit the fuel lines (the effective cross-sectional area reduces). For the design, 30 degrees have been chosen since this reduces the local cross sectional area as much as possible and still keeps a feasible mount length.

Technical drawings of the wind tunnel were used to obtain the lengths of the horizontal beam and incline beam of the mount. The mount was designed to have the base plate of the model in the center of the window. The horizontal beam is given a length of 460 mm, and the horizontal length of the incline beam is designed to have a length of 120 mm. The distance between the center line of the mount and model is 96 mm.

It was decided to give the horizontal beam of the mount a tapered shape. The reason for this comes mainly from the blockage requirement. When looking at the cross sectional area of the model and mount combined, the largest cross sectional area will be located near the base plate of the model. In order to minimize the blockage here the cross sectional area of the beam was made as small as possible to reduce the percentage of blockage. The internal moment in the mount increases when moving downstream. For this reason the outside diameter needs to be bigger near the root of the mount compared with the mount located near the model.

In order to facilitate instrumentation, space was allocated in the inclined beam of the mount. Due to space and temperature near the base plate of the model, it was not possible to put pressure sensors next to the base plate. For this reason it was decided to put the sensors in the mount (trailing edge of the structure), and to connect these sensors by means of tubing to the flow at the base plate. The sizing of the space allocated for instrumentation is shown in Figure 7.2.

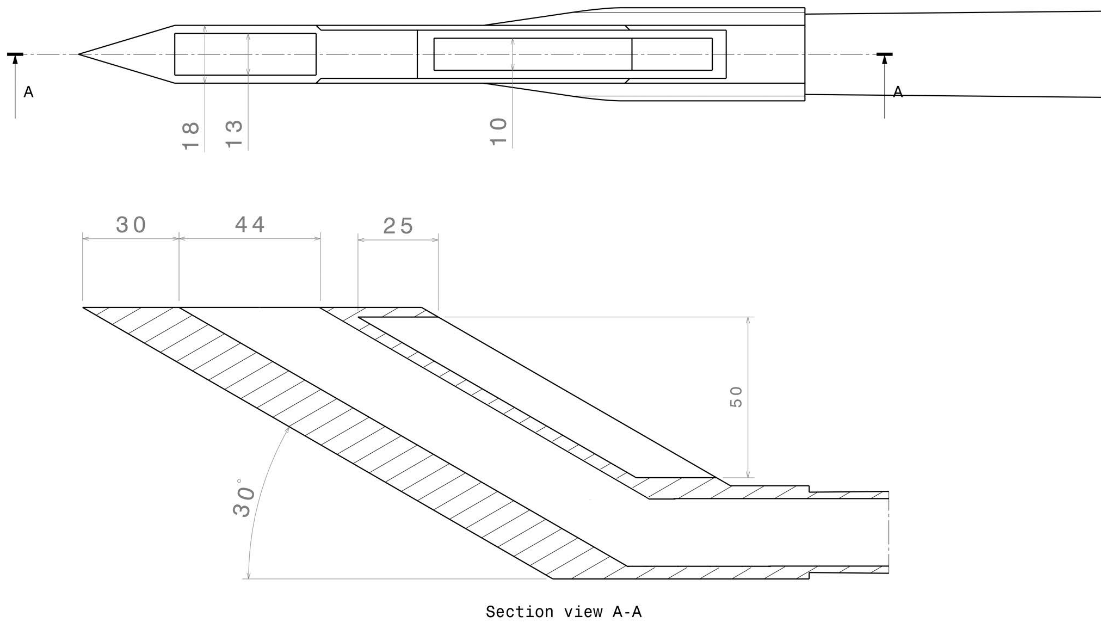

Figure 7.2: Dimensions of inclined beam design

With all aspects listed above, a preliminary shape for the inclined part of the mount was made. Internal space for fuel lines and instrumentation, aerodynamics, and minimizing the blockage resulted in the design as presented in Figure 7.2 for the inclined beam. If, from analysis, it turns out that this beam will fail, the design is revised. The horizontal beam is designed as a tapered cylindrical beam. The exact tapering will be determined by analysis.

7.3.3. MATERIAL SELECTION

A preliminary analysis of the mount showed that in order to design a mount for the relatively high start-up loads and the high safety factor of 2, it would be necessary to select a strong material. Steels have a high range of yield strengths and stiffnesses resulting from different alloy combinations and heat treatments.

It was decided to use a steel called “Uddeholm Impax Supreme”, which was recommended by the wind tunnel technician. This steel has been used before for wind tunnel models, and does not become too brittle at low temperatures [56]. Uddeholm Impax Supreme is a pre-hardened Cr-Ni-Mo-alloyed mould steel. Its properties are presented in Table 7.1. Values are obtained from [57, 58], where further information and machining recommendations can be found as well.

Table 7.1: Material properties of Uddeholm Impax Supreme steel

Property	Value
Density [kg/m^3]	7800
Modulus of elasticity [GPa]	205
Shear modulus of elasticity [GPa]	80
Ultimate tensile strength [MPa]	1020
Tensile yield strength [MPa]	900
Compressive yield strength [MPa]	850

The mount is designed to have a safety factor of 2. Since the tensile yield stress is 900 MPa, this means the equivalent von Mises stress in the mount should not exceed 450 MPa.

7.4. ANALYSIS OF THE MOUNT

In order to see whether the mount fails at the determined in Chapter 6, a structural analysis will be performed. This will be done for both the static and the dynamic (vibrational) case. Furthermore, a thermal analysis was performed, the outcome of which is presented in Section 7.5. The analysis method for this is not presented here, but is derived from Chapter 9.

7.4.1. FORCES AND EXCITATIONS ACTING ON THE MODEL

The forces acting on the mount are calculated in Chapter 6. They consist of forces acting on the model and on the mount, and the resulting forces are presented in Tables 7.2 and 7.3. When comparing the two tables, it can be seen that it is sufficient to design the mount for the start-up forces only. Forces due to small angles of attack as a result of disturbances in the flow are neglected.

Table 7.2: Resulting forces acting on the mount during start-up

$F_{x,\text{start-up}}$	$F_{y,\text{start-up}}$	$F_{z,\text{start-up}}$
391 N	1002 N	1848 N

Table 7.3: Resulting forces acting on the mount during operations

$F_{x,\text{drag}}$	$F_{x,\text{thrust}}$
250 N	325 N

It should also be ensured that the eigenfrequency of the system is not triggered by the vibrations that excite the system. This would lead to resonance, and subsequently failure of the structure. Three possible sources of unsteadiness are identified, namely the base region, the combustion chamber/engine, and wind tunnel upstream flow. The latter one, however, is neglected because the TST-27 has a background turbulence of only 1% (assessed with Hot-Wire Anemometry, [59]).

For the first source, the fluctuation of base pressure is considered. The frequency of the base pressure pulsation f_b can be calculated using

$$f = \frac{St\,\mathrm{V}}{L}. \tag{7.1}$$

A Strouhal number of 0.15 is used for the base region flow [60]. In the reference, it is derived from the actual base pressure pulsation frequency of Ariane V by solving Equation (7.1) for St with the base region dimensions and flow velocity.

In the case of the wind tunnel model, the base plate radius is used as reference length, resulting in $L = 2.5$ cm. The flow velocity V is estimated from Figure 7.3, showing the results from a CFD simulation of the base region velocity flow field with ANSYS and PIV measurements of a cold plume.

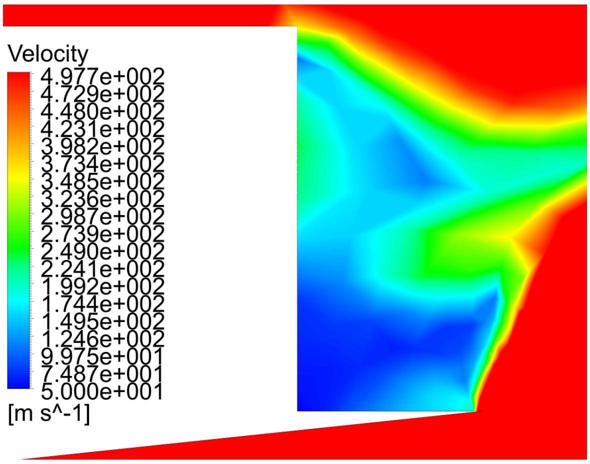

(a) Results of an ANSYS Fluent CFD simulation on the HotFire model, using $P_j = 2.3$ bar, $\gamma = 1.4$, $M_j = 2.37$

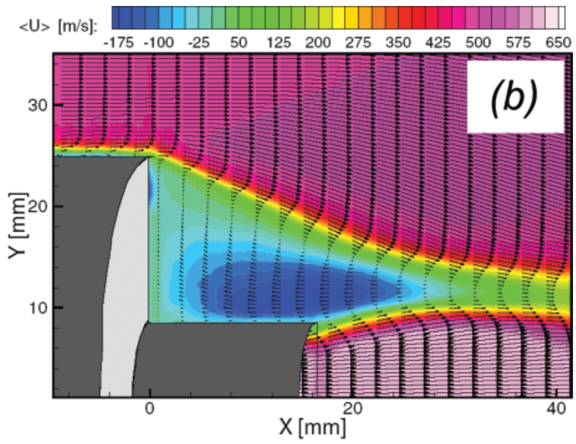

(b) Results of a PIV measurement on the FESTIP model, using a cold plume [61, p.471]

Figure 7.3: Base region velocity flow field in presence of a plume

Even though the numbers are unreliable predictions of the actual velocities (the purpose of HotFire is to investigate this exactly), they give a good estimation of what velocities are to be expected. For Equation (7.1), the velocity was chosen to be V = 200 m/s. This results in a base pressure pulsation frequency $f_b = 1200$ Hz.

Another source of excitation is the vibration due to the combustion process in the engine: combustion instability could induce periodic forces on the model. This is not possible to predict, however, and should be verified experimentally.

7.4.2. ANALYTICAL METHOD

An analytical analysis on the structure of the mount was performed to compare the calculations to the output of the FEM analysis. This is needed to verify the results from ANSYS, to ensure that the inputs and boundaries have been defined properly. Also, the analytical model in MATLAB was used for designing the mount as it provides a faster tool than ANSYS—provided the outcome of both is similar.

DISCRETIZATION

The mount was discretized as two cantilever beams. Figure 7.4a presents how the lengths of the two beams are defined. The first beam is inclined and runs from the the model to the connection with the second beam, where it is assumed to be clamped. This horizontal beam then runs to the wind tunnel support, where it is also clamped.

The cross-sectional shapes and the local coordinate systems that were used for the calculations of e.g. the area moments of inertia are presented in Figure 7.4b. For the horizontal beam, Beam 2, the same axis system as for the global system can be used. For the inclined beam, Beam 1, a local coordinate system is set up for the cross-section, defined as $x'y'z'$.

STATIC STRUCTURAL ANALYSIS

For the static structural analysis of the stresses in the mount, only the horizontal beam was considered. The reason behind this is that failure is not expected in the thick and short inclined beam as the moment arm of the forces is highest at greater distances away from the model along the sting. The combined loading will thus be highest close to the wind tunnel support.

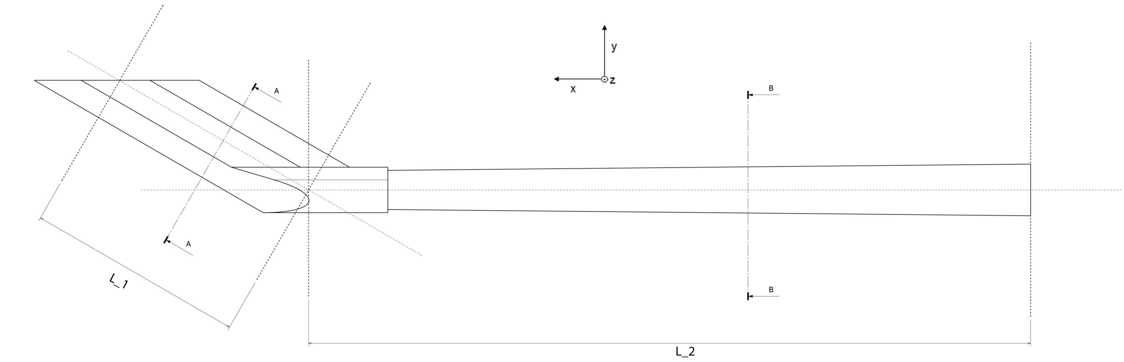

(a) Lengths as defined in discretizing the mount

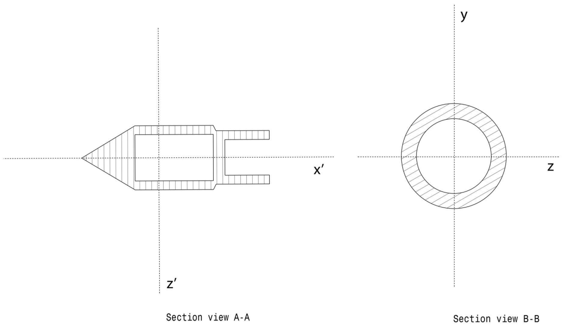

(b) Section views A–A and B–B with local axis system

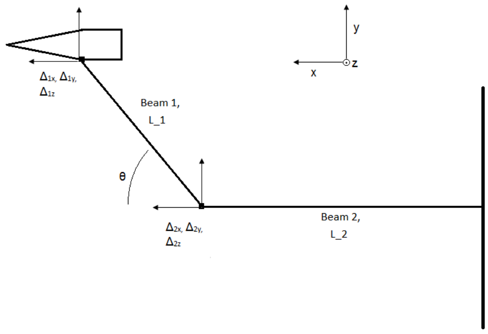

(c) Discretized mount with coordinate systems and deflections

Figure 7.4: Vibrational discretization of the mount

For computing the stresses, the von Mises yield criterion was considered. Therefor, the normal and shear stresses are computed and then combined.

The sting is slightly tapered to not exceed the blockage around the model but still have sufficient strength at the root. The effect of this is neglected as the taper angle is small.

Normal Stress

The normal stress in the beam consists of a direct normal stress (from internal normal forces) and bending normal stress (from internal bending moment).

The direct normal stress is given by $\sigma_{\text{direct}} = F/A$ for a force F acting on a cross-sectional area A. The bending normal stress σ_{bending} for a cross-section under the two internal bending moments

$$M_y(x) = -F_z(L_1 \cos\theta + x) \tag{7.2}$$

$$M_z(x) = F_x L_1 \sin\theta + F_y(L_1 \cos\theta + x) \tag{7.3}$$

as a function of x along the beam is found to be

$$\sigma_{\text{bending}} = \frac{M_y z}{I_y y} + \frac{M_z y}{I_z z}. \tag{7.4}$$

Shear Stress

Like with the normal stress, there are two types of shear stresses: the transverse shear stress caused by internal shear forces, and the torsional shear stress caused by internal torques. For the circular sting, they are defined in circumferential direction, with $\tau > 0$ according to the right hand rule (around the outward x-axis).

For the latter one, a straightforward relation exists. The torque around the x-axis is given by $T_x = -F_z L_1 \sin\theta$ (negative to comply with sign convention). This causes the shear stress

$$\tau_{\text{torsion}} = \frac{T_x r}{I_y z}. \tag{7.5}$$

For the transverse shear, no analytical relation exists for a thick-walled cylinder—this is restricted to fully circular or thin-walled cross-sections only, and the sting has a thickness-to-diameter ratio of only ≈ 1/6. There is, however, an equation relating the maximum shear stress to the average shear stress $\tau_{\text{avg}} = S/A$ under a shear force S [62]:

$$\tau_{\text{max}} = \tau_{\text{avg}} \frac{4(R_o^2 + R_o R_i + R_i^2)}{3(R_o^2 + R_i^2)} \tag{7.6}$$

The minimum shear stress (equal to zero) is located on the line of action of the shear force acting on the cross section. The maximum shear stress found from Equation (7.6) is located furthest away from the line of action, on the neutral line corresponding to bending due to the shear force. The stresses along the circumference as a function—in polar coordinates—of Θ were found by interpolating with a quadratic relation, which becomes

$$\tau(\Theta) = \tau_{\text{max}}(1 - \cos^2\Theta) \tag{7.7}$$

Equation (7.6) only gives the maximum shear stress at location Θ, which is expected to appear at the outer radius R_o. As a conservative estimate, this is accepted and the shear stress is assumed to be the same for every radius.

von Mises Stress

Using the von Mises yield criterion

$$Y_{\text{vM}} = \sqrt{\frac{1}{2}\left((\sigma_x - \sigma_y)^2 + (\sigma_y - \sigma_z)^2 + (\sigma_z - \sigma_x)^2\right) + 3\left(\tau_{xy}^2 + \tau_{yz}^2 + \tau_{xz}^2\right)} \tag{7.8}$$

for the normal stresses $\sigma_x = \sigma_{\text{bending}} + \sigma_{\text{direct}}$ and $\sigma_y = \sigma_z = 0$ and the shear stresses $\tau_{xy} = \tau_{\text{transverse}} + \tau_{\text{torsion}}$ and $\tau_{xz} = \tau_{yz} = 0$, the stresses are computed and can be compared to the design yield stress of the material.

VIBRATIONAL ANALYSIS

In order to perform the vibrational analysis, the stiffnesses of the mount need to be calculated. First the deflections from a certain force need to be determined. In order to do this, the mount was discretized into two separate beams as explained earlier. Castiligiano's second theorem

$$\Delta = \frac{\partial C_i}{\partial P} \tag{7.9}$$

was used to calculate the deflections. The deflection of a structure Δ in the direction of load P is given by the partial derivative of the internal energy C_i with respect to that applied load [63].

The internal energy can be evaluated once all internal forces and moments are known. However, for the standard case of a point load applied at the tip of a cantilevered beam, the internal energy is given by

$$C_i = \frac{F^2 L}{2EA} \tag{7.10}$$

for a beam in tension/compression. The internal energy due to a shear force is calculated using

$$C_i = \frac{S^2 L^3}{6EI}. \tag{7.11}$$

Evaluating Equation (7.9) using Equations (7.10) and (7.11) gives the following expressions for the deflections of the horizontal beam:

$$\Delta_{x,2} = \frac{F_x L_2}{EA_2} \qquad \Delta_{y,2} = \frac{F_y L_2^3}{3EI_{zz,2}} \qquad \Delta_{z,2} = \frac{F_z L_2^3}{3EI_{yy,2}} \tag{7.12}$$

The slope ϕ at the end of the horizontal beam is determined by: [64]

$$\phi_y = \frac{F_y L_2^2}{2EI_{zz,2}} \qquad \phi_z = \frac{F_z L_2^2}{2EI_{yy,2}} \tag{7.13}$$

This slope of the horizontal beam will induce the following deflections at the tip of the inclined beam:

$$\Delta_{x,1,\phi} = L_1(\cos\theta - \cos(\theta - \phi_y)) \tag{7.14}$$
$$\Delta_{y,1,\phi} = L_1(\sin(\theta + \phi_y) - \sin\theta) \tag{7.15}$$
$$\Delta_{z,1,\phi} = L_1 \cos\theta \sin\phi_z \tag{7.16}$$
$$\tag{7.17}$$

Evaluating Castigliano's second theorem for the inclined beam, adding the deflections caused by the slope of the horizontal beam and adding the deflections of the horizontal beam caused by the loads, gives the following deflections for the inclined beam:

$$\Delta_{x,1} = \frac{\left(F_x \sin\theta + F_y \cos\theta\right) L_1^3}{3EI_{zz,1}} \sin\theta - \frac{\left(F_y \sin\theta - F_x \cos\theta\right) L_1}{EA_1} \cos\theta + \Delta_{x,2} + \Delta_{x,1,\phi} \tag{7.18}$$
$$\Delta_{y,1} = \frac{\left(F_x \sin\theta + F_y \cos\theta\right) L_1^3}{3EI_{zz,1}} \cos\theta + \frac{\left(F_y \sin\theta - F_x \cos\theta\right) L_1}{EA_1} \sin\theta + \Delta_{y,2} + \Delta_{y,1,\phi} \tag{7.19}$$
$$\Delta_{z,1} = \frac{F_z L_1^3}{3EI_{yy,1}} + \Delta_{z,2} + \Delta_{z,1,\phi} \tag{7.20}$$

In addition to these deflections, the rotation of the sting caused by the torque due to the side force F_z is analyzed as well. The long length of this beam could induce deflections of the model if the torsional stiffness is not high enough to "counter" the torque T_x computed earlier. The angle of twist caused by torsion on a beam is

$$\Phi(x) = \frac{T_x(L_2 - x)}{GI_{yz}} \qquad L_1 \cos\theta \leq x \leq L_1 \cos\theta + L_2 \tag{7.21}$$

The sine of the angle of twist Φ is multiplied by $L_1 \sin\theta$ to obtain the Δ_z caused by the torsion. This is then added to $\Delta_{z,1}$.

From the total deflections and the applied forces, the stiffness is determined via $F = \Delta \cdot k$. The stiffness is obtained for the y-direction and z-direction. For calculating the stiffness in y-direction the influence of F_x is neglected, which is justified when evaluating Equation (7.19) for $\theta = 30°$. This is used to decouple the movement in y-direction from that in x-direction.

The effective mass of the spring mass system is needed for the analysis: not only the model acts as a mass on the system, the spring (in this case the mount) has a mass as well. The effective mass of the mount is found as a fraction of the actual mass (0.2235 m, [65]), and by including the mass of the model, the following is found:

$$m_{\text{eff}} = 0.2235 m_{\text{mount}} + m_{\text{model}} \tag{7.22}$$

Using MATLAB, a state-space representation can be created to further analyze the vibrational response of the system further [66]. Using the state-space representation, it can be studied how a system reacts to a certain input. This is done for the vibrations in y-direction and z-direction; the first two eigenmodes (so the lowest frequencies) of the system are expected to be in these directions. First, the equations of motion are set up. As an example, this is done for the y-direction:

$$m\ddot{\Delta}_y = -(\Delta_y k_{eq} + \dot{\Delta}_y c) + F_y \tag{7.23}$$

The damping coefficient is obtained by evaluating equation Equation (7.24), where ζ is assumed to be 0.07 [67].

$$c = \zeta 2\sqrt{mk} \tag{7.24}$$

In order to write the equations of motion in state-space form, they are rewritten using $\Delta_y = x_1$, $\Delta_z = x_2$, $\dot{\Delta}_y = x_3$, and $\dot{\Delta}_z = x_4$. This gives $\dot{x}_1 = x_3$ and $\dot{x}_2 = x_4$ as auxiliary equations. The state-space system is then given by Equations (7.25) and (7.26). In these equations, $\bar{u}$ denotes the input of the system—in this case F_y and F_z—, and $\bar{y}$ denotes the output of the system. In this case, both the positions and the velocities are given as outputs for this particular **C**-matrix. The state space systems allows simulating the vibrational system with arbitrary input forces.

$$\underbrace{\dot{\begin{pmatrix} x_1 \\ x_2 \\ x_3 \\ x_4 \end{pmatrix}}}_{\dot{\bar{x}}} = \underbrace{\begin{bmatrix} 0 & 0 & 1 & 0 \\ 0 & 0 & 0 & 1 \\ -\frac{k_y}{m} & 0 & -\frac{c_y}{m} & 0 \\ 0 & -\frac{k_z}{m} & 0 & -\frac{c_z}{m} \end{bmatrix}}_{\mathbf{A}} \underbrace{\begin{pmatrix} x_1 \\ x_2 \\ x_3 \\ x_4 \end{pmatrix}}_{\bar{x}} + \underbrace{\begin{bmatrix} 0 & 0 \\ 0 & 0 \\ \frac{1}{m} & 0 \\ 0 & \frac{1}{m} \end{bmatrix}}_{\mathbf{B}} \underbrace{\begin{bmatrix} F_y \\ F_z \end{bmatrix}}_{u} \tag{7.25}$$

$$\underbrace{\begin{pmatrix} \Delta_y \\ \Delta_z \\ \dot{\Delta}_y \\ \dot{\Delta}_z \end{pmatrix}}_{\bar{y}} = \underbrace{\begin{bmatrix} 1 & 0 & 0 & 0 \\ 0 & 1 & 0 & 0 \\ 0 & 0 & 1 & 0 \\ 0 & 0 & 0 & 1 \end{bmatrix}}_{\mathbf{C}} \underbrace{\begin{pmatrix} x_1 \\ x_2 \\ x_3 \\ x_4 \end{pmatrix}}_{\bar{x}} + \underbrace{\begin{bmatrix} 0 & 0 \\ 0 & 0 \\ 0 & 0 \\ 0 & 0 \end{bmatrix}}_{\mathbf{D}} \underbrace{\begin{bmatrix} F_y \\ F_z \end{bmatrix}}_{\bar{u}} \tag{7.26}$$

MATLAB is able to calculate the eigenfrequencies of the state space system by using the function `damp`. It can be easily verified: by using the equivalent stiffness k_{eq} and the effective mass of the model-mount-system m_{eff}, it is possible to determine the eigenfrequency using

$$f_n = \sqrt{\frac{k_{eq}}{m_{\text{eff}}}}. \tag{7.27}$$

THERMAL ANALYSIS

Figure 7.5 shows that the rear of the mount is the closest to the center of the plume. Therefore, it will experience most heating. A preliminary analysis was done on the heating of the mount, assuming that all heat transfer between the plume and the mount is caused by radiation, no energy is absorbed by the surrounding flow and that the plume is a black body with an emissivity coefficient of 1.

These are conservative assumptions since the plume will have an emissivity coefficient below 1 and the surrounding flow will absorb energy. There will be no conduction between the plume and the mount since the flows are moving. In reality, there will be convection cooling of the mount, which is neglected in this calculation to get a first conservative estimation on the temperature.

Furthermore, it is assumed that all conduction energy flow is in radial direction so that an infinite plate finite difference model can be used (similar to the finite difference method in Section 9.7.7). This is also a conservative assumption since in reality, there will be conduction in other directions through the material towards regions that receive less radiation energy flux.

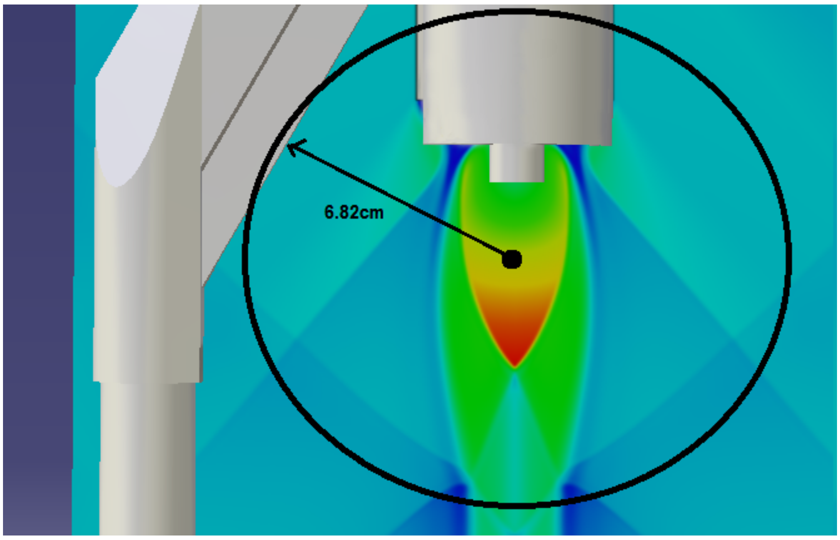

Figure 7.5: Overview of the part of the mount receiving most thermal radiation

7.4.3. FEM ANALYSIS

Doing a FEM analysis is more detailed than the analytical solution for several reasons: the structural shape can be imported from the CAD drawing made in CATIA, meaning that the beam does not have to be discretized and no information is lost in the analysis. Furthermore, the FEM analysis is able to calculate stress concentrations. Finally, the ANSYS accounts for the effect of deflections of the mount.

STATIC STRUCTURAL ANALYSIS

For the static structural analysis, the static structural workbench in ANSYS is used. In order to get the geometry, first the CAD drawing of the mount is created using CATIA. This file is exported as an `IGS` file, which can be imported in ANSYS. The material properties are defined in the engineering data. The mechanical workbench in ANSYS is then started. The mesh is created by ANSYS, after which the fixed support and the applied forces are defined. After this it is possible to calculate the results: plots of, for example, the stresses, strains, and deformations of the model can be created.

VIBRATIONAL ANALYSIS

The method used for the vibrational analysis is not much different from that of the static structural analysis. The modal workbench is used instead of the static structural workbench. Again the materials are defined, the geometry is imported, the mesh is created, and the fixed support is defined. A point mass is added on top of the mount to simulate the mass of the model. The modal analysis finds the eigenmodes of the system and shows how the model deforms for these modes.

7.5. RESULTS

7.5.1. STATIC STRUCTURAL ANALYSIS

This subsection presents the comparison between the analytical results and the results calculated by ANSYS. This was done to verify whether the results in ANSYS were calculated correctly with the proper input.

ANALYTICAL STRESS RESULTS

The mount is designed to have a maximum von Mises stress of 450 MPa, since this is the yield strength of the material divided by the safety factor. The horizontal beam of the mount is tapered, and therefore an analysis of the stresses is done for both the root and the end of the beam. The internal moment will be the highest at the root of the beam, which means that the required thickness will be higher here.

The internal diameter of the horizontal beam is fixed at 21 mm, to have enough space for the propellant lines, as specified in Chapter 5. This means that only the outside diameter of the beam is varied, until the minimum outside diameter is obtained at which the beam will withstand the specified loads with a safety factor of 2.

For the root of the mount, the minimum outside diameter was determined to be 33 mm, which means that the beam has a wall thickness of 6 mm at this location. The von Mises stress across the cross sectional area is presented in Figure 7.6a.

For the end of the horizontal beam, which is at a distance of 460 mm from the root of the mount, the minimum diameter of the beam was determined to be 25 mm. The von Mises stress across the cross sectional area is presented in Figure 7.6b.

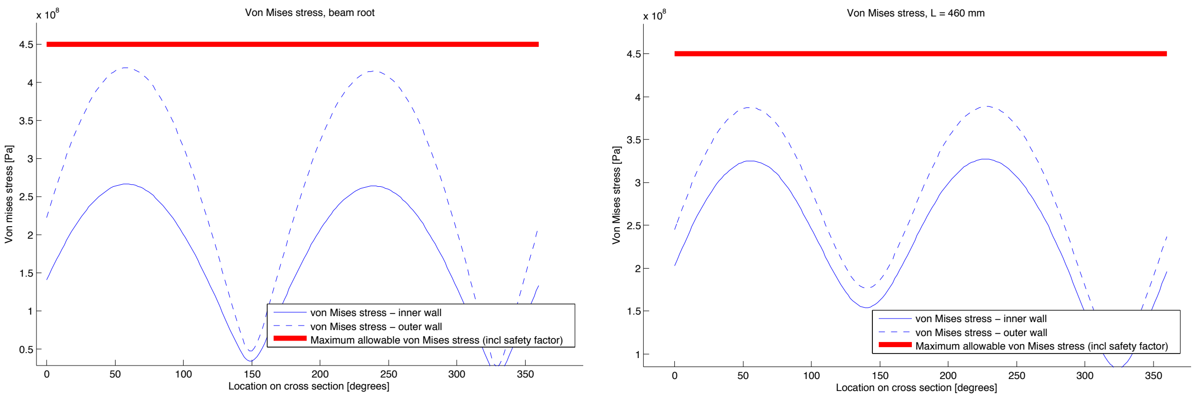

(a) von Mises stress at the root of the mount

(b) von Mises stress at the tip of the horizontal beam of the mount

Figure 7.6: von Mises stress due to start-up loads as calculated analytically (plotted with MATLAB)

FEM STRESS RESULTS

The amount of von Mises stress as a result of the start up loads as calculated by ANSYS is presented in Figure 7.7a. As expected the maximum amount of stress is present in the horizontal beam. Since the beam is tapered, the maximum amount of stress is similar over the length of the horizontal beam.

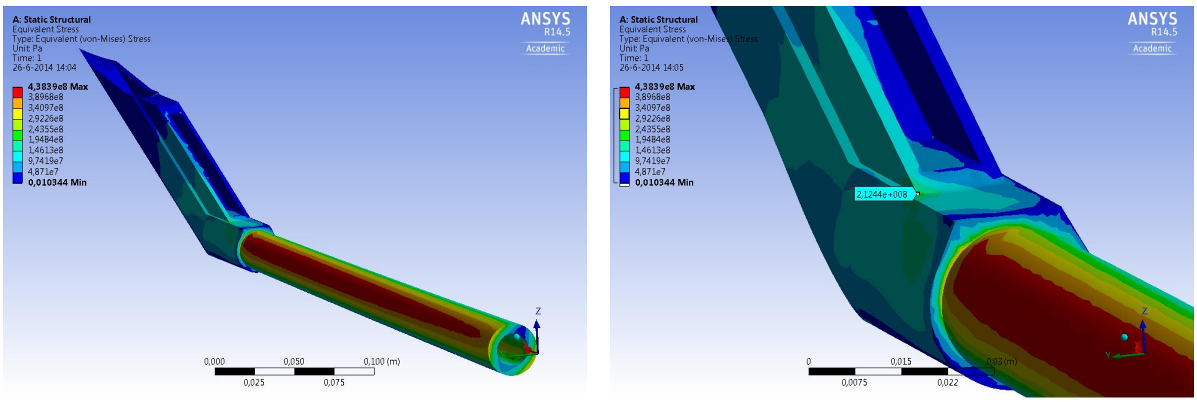

(a) Distribution of von Mises stress along mount

(b) Stress concentration close-up

Figure 7.7: von Mises stress due to the start-up loads as calculated with FEM (ANSYS)

Some stress concentrations are present in the inclined part of the beam. A close-up is shown in Figure 7.7b. The maximum von Mises stress is approximately 212 MPa at the kink of the beam. This stress concentration should not cause any problems when both parts of the mount are constructed from the Uddeholm Impax Supreme steel with a tensile yield strength of 900 MPa, giving an allowable maximum stress of 450 MPa.

COMPARISON ANALYTICAL AND FEM STRESS RESULTS

The results from the stress tool in MATLAB were compared to the calculations in ANSYS using a mount with a straight, round, horizontal beam. In theory the tool can also verify the results for a tapered beam in ANSYS. In this case it is expected there is more discrepancy however caused by the changing cross sectional area.

A comparison between the results from MATLAB and ANSYS is presented in Figure 7.8. As can be seen the results match closely. The maximum stress in the outer wall according to MATLAB is 248 MPa. Compared to the result from ANSYS of 234 MPa this gives a discrepancy of 5.7%.

The locations of the maximum stresses match as well. For the result from ANSYS the maximum stress lies at approximately 60 deg. The maximum stress from the calculations in MATLAB is located at 56 deg.

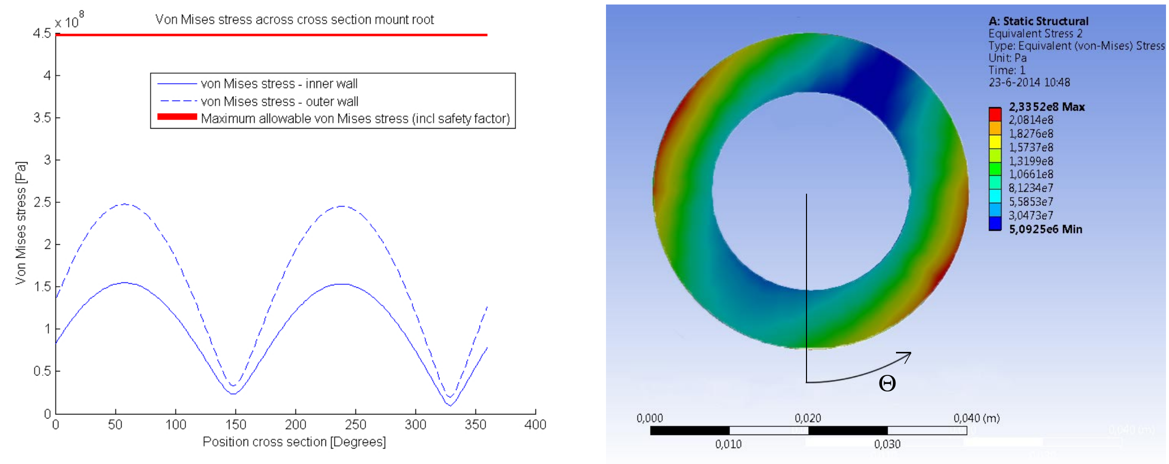

(a) MATLAB von Mises stress calculation

(b) ANSYS von Mises stress calculation

Figure 7.8: Comparison between von Mises stress as calculated analytically and with FEM (ANSYS)

7.5.2. Vibrational Analysis

Analytical Vibrational Results

The calculated stiffnesses and the effective masses are presented in Table 7.4. The beam mass was calculated to be 1.64 kg using ANSYS. The mass of the model was estimated to be 1.00 kg using CATIA. The eigenfrequencies of the model and mount system are presented in Table 7.4 as well.

Table 7.4: Values used for the analytical vibrational analysis, and the resulting computed eigenfrequencies

$k_{y,tot}$ [N/m]	$k_{z,tot}$ [N/m]	c_y [Ns/m]	c_z [Ns/m]	m_{model} [kg]	m_{eff} [kg]	$f_{n,y}$ [Hz]	$f_{n,z}$ [Hz]
$1.12 \cdot 10^5$	$1.03 \cdot 10^5$	39.17	37.56	1.00	1.37	45.6	43.7

A power spectral density plot is presented in Figure 7.9a. As can be seen the highest peak corresponds to the lowest eigenfrequency, $f_{n,z}$. It will therefore absorb more energy, which poses a larger risk with respect to resonance, resulting in possible failure. Both frequencies are quite similar; no excitations should be present with frequencies of around 40 Hz according to this analysis. Figure 7.9b presents the response of the system due to start up loads for the z-direction. The start-up loads are an input for the state-space system: the loads created by the shock wave are modeled to act for 0.2 s, starting from t=0.1 s (compare Figure 7.9b. As can be seen the vibrations die out quite quickly due to the damping of the system.

FEM Vibrational Results

The first 10 modes were calculated using the ANSYS modal analysis. The results are presented in Table 7.5.

Table 7.5: Eigenmodes of the system as calculated by FEM (ANSYS)

Mode	1	2	3	4	5	6	7	8	9	10
f [Hz]	41.0	41.5	306.7	317.6	675.3	899.3	1077.2	1702.2	1725.5	2313.5

Eigenmodes 1 and 2 correspond to the vibrations in z- and y-direction, respectively. The deformations are shown in Figures 7.10a and 7.10b. Note that this is only a modal analysis and not the response to a certain force; this means that the magnitude of the deformations in the figures does not correspond to a physical deformation from a certain force.

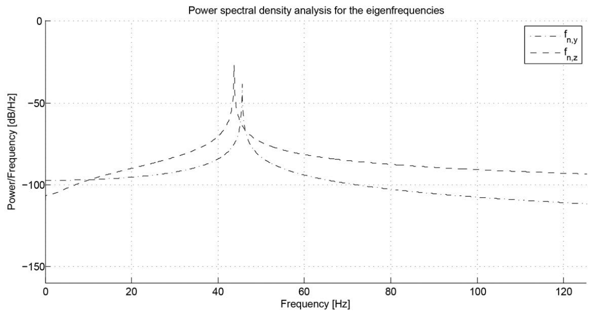

(a) Power spectral density plot of the analytical eigenfrequencies

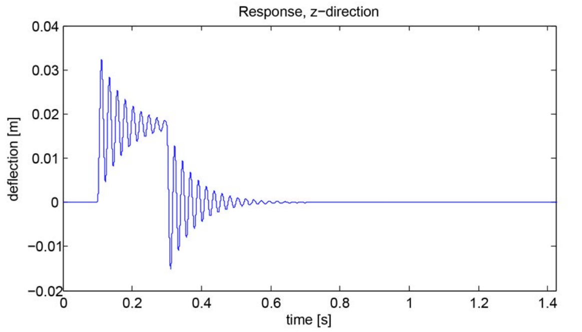

(b) Response of the system due to start-up loads of 0.2 s, z-direction

Figure 7.9: Analytical calculations for the vibrational analysis (plotted with MATLAB)

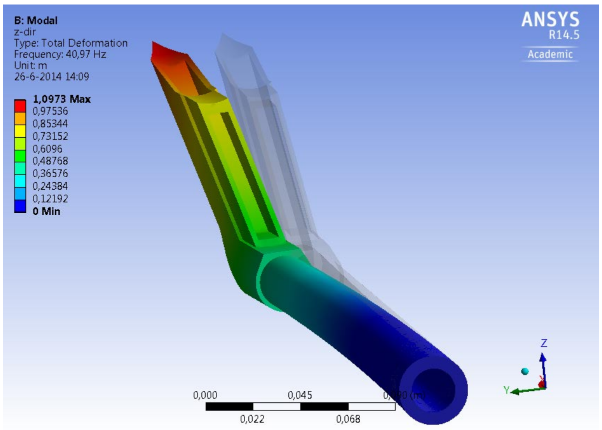

(a) Eigenmode 1, deformation in z-direction

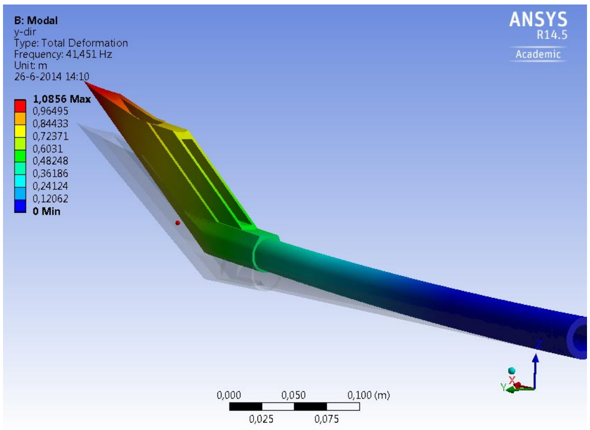

(b) Eigenmode 2, deformation in y-direction

Figure 7.10: Eigenmodes obtained via FEM (ANSYS)

COMPARISON ANALYTICAL AND FEM VIBRATIONAL RESULTS

Before the eigenfrequencies from the analytical calculations are compared with the results from ANSYS, the calculated deflections will be compared to the deflections in ANSYS for verification. The results are presented in Table 7.6. The deflection in ANSYS was taken at the neutral point of the cross-section.

Table 7.6: Difference in deflections for analytical and FEM (ANSYS) calculations

	Analytical	ANSYS	Discrepancy
Δ_x [mm]	1.6	2.2	27.2%
Δ_y [mm]	8.9	9.6	7.2%
Δ_z [mm]	17.5	18.7	6.4%

As can be seen, only the deflection in x-direction has a relatively large discrepancy. This deflection will not be used to evaluate $f_{n,y}$ and $f_{n,z}$, however, since the deflections in these directions were assumed as decoupled from the x-direction. The deflections used for the eigenfrequencies, Δ_y and Δ_z match closely with a maximum discrepancy of 7.2%.

The comparison between the analytical and FEM vibrational results is presented in Table 7.7. As can be seen there is a good match between the analytical results and the results from ANSYS. This means that the results from ANSYS can be trusted, and that this model can be used to analyze the eigenmodes of the system.

As a comparison, the deflections as calculated by ANSYS were used instead of the analytical deflections to calculate the eigenfrequencies. This gives results as presented in Table 7.8.

Table 7.7: Difference in eigenfrequencies for analytical and FEM (ANSYS) calculations

	Analytical	ANSYS	Discrepancy
f_y [Hz]	45.6	41.5	9.0%
f_z [Hz]	43.7	41.0	6.2%

Table 7.8: Difference in eigenfrequencies, analytical calculations with deflections from FEM (ANSYS)

	Analytical	ANSYS	Discrepancy
f_y [Hz]	44.0	41.5	5.7%
f_z [Hz]	42.3	41.0	3.1%

As can be seen, the discrepancies decrease when using the deflections as calculated by ANSYS. This means that the analytical calculations for the deflections induce some error when calculating the eigenfrequencies. The excitation caused by the base pressure pulsation frequency was determined to be 1200 Hz. Looking at the results from the ANSYS this could cause problems. It cannot be said with certainty whether the base pressure pulsation frequency will cause resonance in the model, so this should be analyzed by using an experimental set-up.

7.5.3. THERMAL ANALYSIS

According to the simulation, the maximum temperature of the mount for a plume temperature of 1700 K is 504 K. At 504 K, the yield stress of steel is almost unaffected [68]. The total temperature was assumed for the plume temperature. It is unknown how hot the plume will get due to the mixing with the surrounding flow and possible afterburning. To investigate the plume temperature it is recommended to do a CFD simulation or testing.

On a side note: It can be expected that the walls of the wind tunnel will stay well below the 400 K as required by `HF-CON-SUR-01`: The walls are farther away from the sting, have relatively more convection and conduction cooling capacities, and, above all, the estimation using radiation is already conservative.

7.6. DESIGN OUTCOME

7.6.1. PRESENTATION OF DESIGN

In order to get an impression of the overall design of the mount, Figure 7.11 presents a CAD drawing with the main dimensions of the mount.

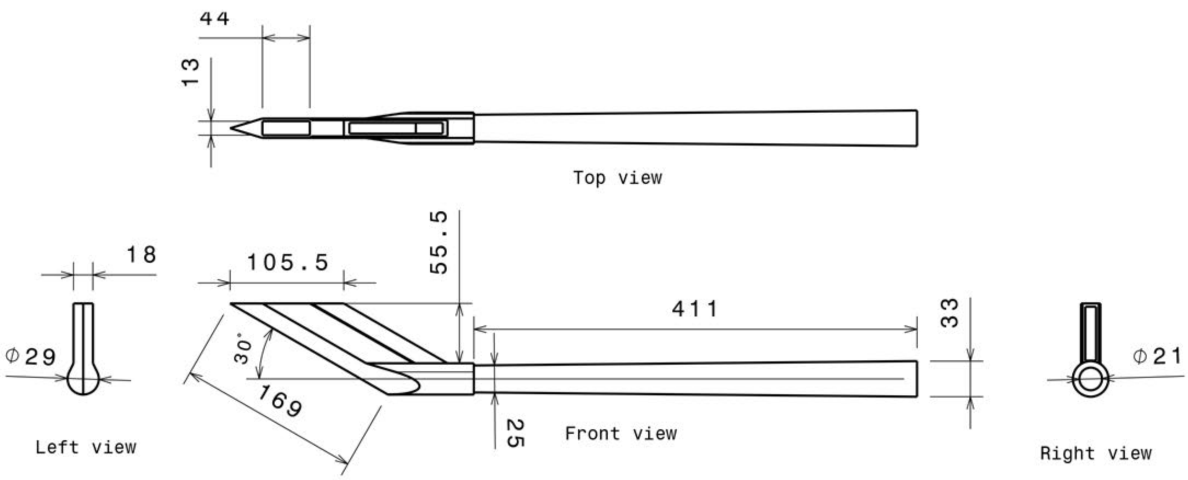

Figure 7.11: Overall dimensions of the designed mount

The fuel lines that run through the mount will enter the model through the nose cone and reach the injector. This was done in order to make the model length smaller and thus to increase the distance from the model to the reflected shock wave, as explained in Chapter 6. The joining methods that can be used to connect the mount to the combustion chamber and nose cone are explained in Chapter 12.

The two parts of the mount, the horizontal beam and the inclined beam, are designed such that they can be manufactured separately. Both parts could be machined from two solid blocks of steel to increase the structural integrity. The horizontal beam can be inserted in the incline beam. They can be joined in several ways. The two beams could be welded together, or both beams can be threaded and then screwed together.

A render with a close up of the front of the mount is presented in Figure 7.12a. As can be seen, the corners are filleted from the part that connects the horizontal beam to the beam under 30 deg. A view of the mount from the back is presented in Figure 7.12b. The slot where the instrumentation can be seen in this figure.

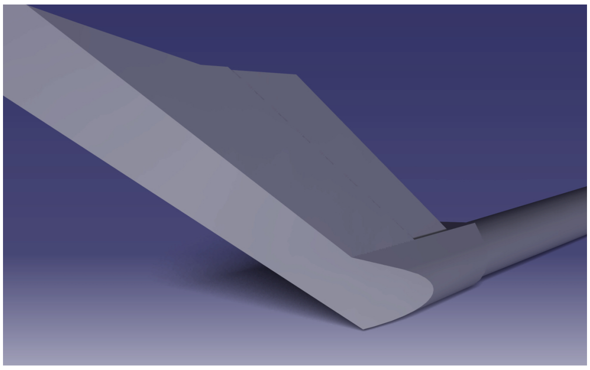

(a) Render of the mount, seen from the front

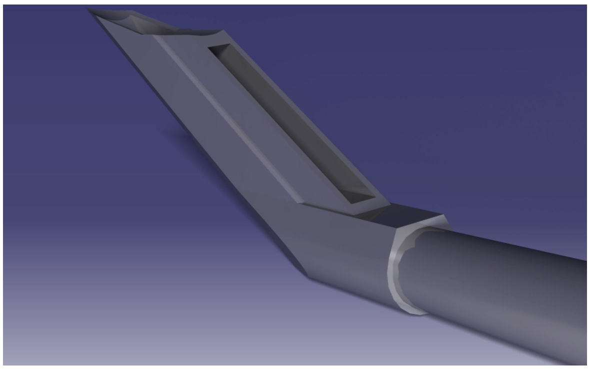

(b) Render of the mount, seen from the back

Figure 7.12: Mount renders created by CATIA

7.6.2. BUDGET MANAGEMENT

In Section 3.3, the assigned budget for the mount was given as 40% of cross-sectional area for blockage and 2000 € for cost.

The blockage budget can easily be verified by using the drawing in Figure 7.11. The total blockage caused by the mount is approximately

$$55.5\text{ mm} \cdot 18\text{ mm} + \pi\left(\frac{29\text{ mm}}{2}\right)^2 = 1660\text{ mm}^2, \tag{7.28}$$

which are the projected areas of the inclined beam and the horizontal beam, respectively. With a total blockage of 3645 mm^2 this means that the mount takes up 45.5% of the blockage budget, which is slightly over the assigned budget. During iterations between the mount design and aerodynamic shape design it was made sure to keep the total blockage below 100%.

For the cost budgets, a conservative cost estimation is made by using [69], which states that the most expensive steel produced by Uddeholms AB is 600 kronor, or about 80 euros per kg. Making a square bar around both the horizontal beam of the mount and the inclined beam of the mount gives a volume of about 0.0011 m^3, which gives a weight of about 9 kg for a density of 7800 kg/m^3. This gives a maximum price of 720 euros.

7.6.3. DISCUSSION

By making the mount a sting mount, requirement `HF-TEC-MEA-02` has been met, since this allows for constant visual access to the base region. The design of the mount was done in close collaboration with the design of the model in order to meet requirement `HF-CON-WTO-01`. The blockage of the subsystems combined meets the requirement since they take up 99.4% of the available blockage area. The estimation of the costs regarding the mount is conservative, but is achievable with respect to requirement `HF-CON-COS-01`. No severe modifications of the wind tunnel are necessary for this design of the mount, which means it complies with requirement `HF-CON-COS-03`. By complying to the regulations set forth by Delft University of Technology of using the safety factor of 2 on all load-carrying parts, the design fulfill requirement `HF-CON-SAF-01`. For the requirements regarding the survival of the test set-up, the sub-requirements on the static loads, the temperatures, and shock loads are met. For vibrations and flutter, more research is needed to conclude whether the mount fulfills these requirements.

7.7. RECOMMENDATIONS

In order to increase the quality of the structural analysis of the mount, several recommendations can be made.

If analytical calculations are made in the future for the deflections of the beam, it is recommended to find a more precise way of doing so. The predicted deflections of the beam are lower than indicated in ANSYS. First of all, the discretization of the beams is inaccurate. The beam has a complex shape which will always induce error when discretizing it. It can be said that the inclined beam of the mount is already too complex for the discretization used in the analytical calculations. Secondly, the beam theory which is used should be more precise than what was used in this analytical analysis. Dividing the mount into two separate beams for analysis induces errors due to the fact that the mount is one beam in reality, with continuous curvature.

The propellant lines for the cold plume have a possibility of being larger than the propellant lines for the hot plume, for which the dimensions of this mount were designed. Increasing the cross-sectional area could cause a problem for the blockage. It is therefore recommended—once the right propellant lines have been selected in order supply the cold plume—to see whether the current mount is still large enough or if a redesign will need to be made. The length of the inclined beam could be decreased in order to reduce the blockage. This has the downside that the model will be closer to sting of the mount. This could increase heating of the sting in case of a hot plume, and an increase in interference between the mount and model.

The complete structure should still be analyzed for flutter. Deflections of the mount will induce aerodynamic forces. There is a possibility that these forces cause a potentially destructive vibration of the structure.

Further research is needed in vibrational excitations for which the frequency could be near the eigenfrequencies of the system. Like flutter, these excitations can possibly be destructive. Possible sources of vibrations are the aerodynamic behavior around the model and the combustion process in the engine. Testing these excitations in an experimental test set-up is recommended.

8
IGNITOR

In this chapter the requirements for the ignitor are analyzed, followed by the selection and positioning of this subsystem. An analysis about the ignition is of crucial importance, as ignition has to be ensured for a working HotFire system. Previously, the propellant analysis resulted in a liquid engine using kerosene and oxygen at an O/F ratio of 1.2. For this combination, the corresponding values of chamber pressure and temperature were specified. From this, an ignitor can be designed. Initially, a flammability analysis is performed to proof that the chosen engine with an O/F ratio of 1.2 lies within the flammability limits and is therefore ignitable and combustible. Secondly, an analysis about the autoignition temperature is done, in order to determine the temperature at which the gas mixture ignites. Afterwards, the energy needed to raise the temperature of a droplet to this autoignition temperature is calculated and detailed technical requirements for the ignitor are formulated. From these requirements an ignitor is chosen and positioned within the model.

8.1. REQUIREMENTS ON THE IGNITOR

The ignitor design has to comply with the following requirement:

`HF-TEC-HPL` The HotFire system shall be able to generate a hot plume.

This requirement is one of the top level requirements and needs to be fulfilled by the ignition system. Form it follows that the ignitor should be able to ignite the propellant mixture.

8.2. ANALYSIS

In this section the analysis of the ignition system is presented. It starts with a definition of flammability and flammability limits. These limits define whether a mixture is flammable and whether ignition and combustion is possible. Afterwards, an analysis on the autoignition temperature is performed. This defines the minimum temperature, to which a droplet of the mixture has to be heated, to ignite without any further energy input (on its own). As discussed in the following, a specific temperature could not be identified. However, [70] conducted an experiment on ignition delays, using Jet-A and air, which are comparable to kerosene and oxygen for the HotFire. The experiment was conducted for different pressures, mixture ratios and temperatures. From this experiment it is assumed that, in order for a mixture to have a certain ignition delay at a certain pressure and O/F-ratio, the temperature of this specific experiment can be used as an indication for the autoignition temperature. Therefore, the temperature at which a certain delay is measured is assumed to be the autoignition temperature. This assumption is conservative, as the experiment has shown that for this temperature at this pressure the mixture auto-ignited, and this is not the ignition method of HotFire.

8.2.1. FLAMMABILITY ANALYSIS

As the engine trade-off has shown, the liquid engine is the best option in order to realize a hot plume test within all the requirements. Different fuel and oxidizer combinations were analyzed, resulting in a kerosene -

oxygen liquid rocket engine with an O/F ratio of 1.2. This ratio is rather low compared to launchers operating with the same oxidizer - fuel combination, where typical ratios range between 2.3 and 2.7. The flammability of a substance is generally defined by two specific numbers, namely the lower flammability limit (LFL) and the upper flammability limit (UFL). Both terms are experimentally determined and are dependent on pressure, temperature, oxidizer fuel ratio, and the oxidizer fuel combination. Generally it can be said that when the flammability of a mixture lies between the upper and lower limit, ignition is possible [71]. Furthermore, it indicates that the flame propagation ensures further combustion. A collection of different flammability limits for different fuels and oxidizer are presented in [71], including values for a kerosene - air mixture. The numbers for these limits are shown in Table 8.1, where the value is given as a percentage of the oxidizer volume, so a F/O volume ratio.

Table 8.1: Different flammability limits for kerosene - air and kerosene - oxygen [71]

Oxidizer Fuel Combination	Lower flammability limit (LFL)	Upper flammability limit (UFL)
Kerosene - Air (sea level pressure)	0.6%	5%
Kerosene - Air (pressure increase)	$LFL < 0.6\%$	$UFL > 5\%$
Kerosene - Oxygen (at increased pressure)	$LFL < 0.6\%$	$UFL > 5\%$

For this reason the fuel has to have $0.6-5$ percent of the oxidizer volume, in order to lie within the flammability region. In [72] it is shown that the flammability region of an hydrocarbon air mixture widens when increasing the pressure. As the flammability limits in [71] are determined for sea level pressure conditions, it can be said that the flammability region in the combustion chamber environment will be larger than the one stated in [71]. The design of the engine uses oxygen as an oxidizer, which is more efficient compared to air because oxygen provides more oxidizer when considering the same volume. [71] is stating that changing the oxidizer from air to oxygen will therefore widen the flammability region, by increasing the UFL while keeping the LFL constant. This results in flammability limits for kerosene and oxygen as presented in the last row of Table 8.1.

In order to check whether the chosen combustion chamber properties lie within the flammability limits, and is therefore ignitable, a preliminary calculation was performed with an O/F mass ratio of 1.2 and a chamber pressure of 30 bar. As the flammability limit is defined in a volumetric F/O ratio, a conversion using the density is done. The different inputs and the outputs for start-up and for the running engine are shown in Table 8.2. Afterwards, the same calculation is performed for an engine, namely the F-1 engine. The Vulcain 2 is not used for comparison since it combusts liquid oxygen and liquid hydrogen. The results are again shown in Table 8.2. The density of the oxidizer is calculated using the equation of state $P = \rho RT$ for oxygen.

Table 8.2: Main calculations done on flammability limits

Parameter	HotFire	F-1
Oxidizer	Oxygen	Oxygen
Fuel	Kerosene	RP-1
O/F Mass Ratio	1.20	2.30
Pressure Start-Up $[bar]$	30.00	61.00
Pressure Running Engine $[bar]$	30.00	61.00
Temperature Start-Up $[K]$	288.00	288.00
Temperature Running Engine $[K]$	1700.00	3300.00
Density Oxidizer Start-Up $[kg/m^3]$	40.06	81.46
Density Oxidizer Running Engine $[kg/m^3]$	6.79	7.11
Density Fuel $[kg/m^3]$	820	820
Start-Up F/O Volume Ratio	4.04	4.28
Running Engine F/O Volume Ratio	0.68	0.37

In order to visualize the different values for start-up and running engine, Figure 8.1 has been created to show the relation between volumetric fuel to oxidizer ratios, temperature and pressure. For the same O/F mass ratio different F/O volume ratios result, as the density changes with pressure and temperature according to

$P = \rho RT$. The respective LFL and UFL of kerosene with air are indicated as a black dotted line for the UFL and as a red dotted line for the LFL. As shown in the graph for room temperature (288 K) and a pressure of 30 bar, the flammability of the kerosene-oxygen mixture lies within the flammability region, same for the operating condition of 30 bar and a temperature of 1700 K.

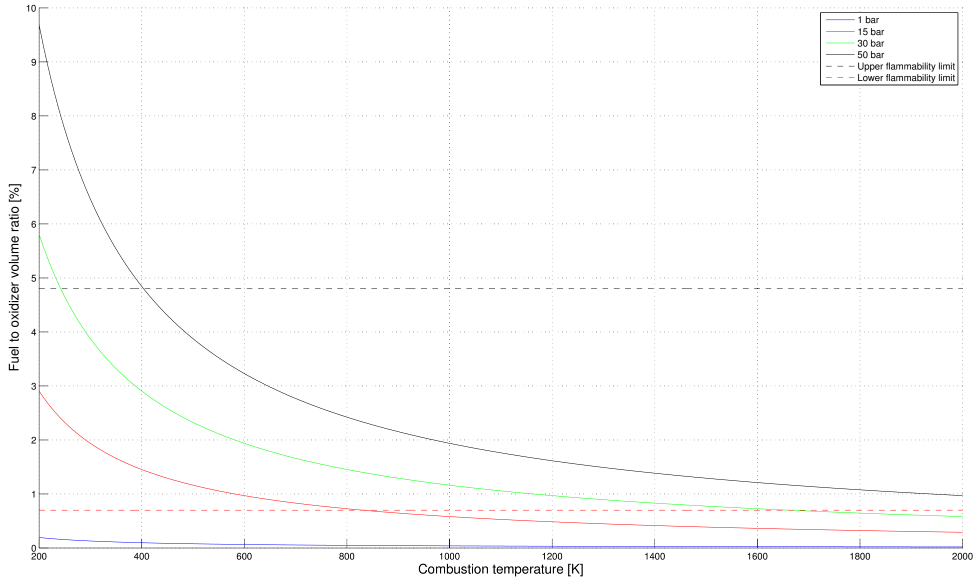

Figure 8.1: Flammability of kerosene - oxygen for different temperatures and pressures compared to the flammability limits of kerosene and air

This proves, that a mixture of 1.2 in mass O/F ratio is indeed applicable for the purpose of the HotFire.

8.2.2. Autoignition and Ignition Delay

The general purpose of an igniter is to provide enough energy to a part of the mixture to start ignition. A minimum ignition energy is required to ignite a kerosene-oxygen mixture, which generally depends on the autoignition temperature of the oxidizer fuel combination. The autoignition temperature is defined as the temperature where the mixture ignites spontaneously. The rule of thumb presented in [16] is $T_{\text{ignitor flame}} > T_{\text{autoignition}}$.

where $T_{\text{ignitor flame}}$ is the temperature of the igniter and $T_{\text{autoignition}}$ is the autoignition temperature of the mixture. The autoignition temperature of a oxidizer fuel mixture, which is determined experimentally, is found to be dependent on pressure, temperature, and oxidizer fuel ratio. Unfortunately, a literature study on the autoignition temperature of kerosene-oxygen at a pressure of 30 bar and room temperature showed that specific numbers for the autoignition temperature are not available.

Further literature study on the topic resulted in data about the ignition delay time of kerosene and air at different temperatures and pressures. Therefore, it is assumed that when there are experiments specifying the ignition delay of a certain gas mixture, the respective temperatures of the gas in those experiments is sufficiently high to ignite the gas mixture [73]. The values for ignition delay are generally received by performing a shock tube test.

The shock tube experiment is commonly used to simulate actual explosions or to investigate flow properties of gases and combustion reactions including ignition delays [75]. As shown in Figure 8.2a, a shock tube consist of two regions, a high pressure and a low pressure region, which are separated by a diaphragm. The gas in the pressure region is called driver gas, whereas the low pressure region is called driven gas. This driven gas is the gas the experiment is performed on, i.e. some combustible oxidizer fuel mixture. In the end of the low pressure region measurement equipment is positioned. This equipment can include pressure and temperature sensors, as well as optical analysis systems. During the operation of the shock tube, the pressure in the high pressure region is increased to a predefined value. At this predefined pressure, the pressure differential across the diaphragm is causing it to burst (in some cases a mechanical device is inducing an additional

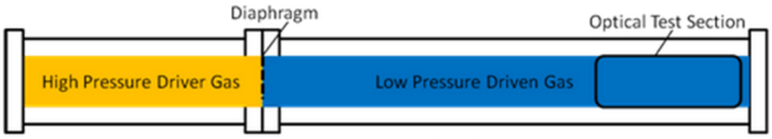

(a) Initial set-up of the Shock tube experiment.

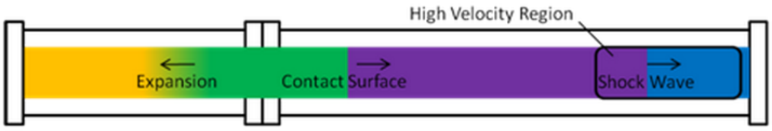

(b) Shock tube shortly after the burst of the diaphragm.

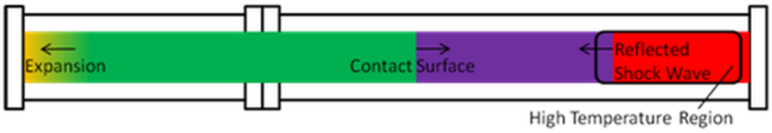

(c) Shock tube after the shock wave reflection.

Figure 8.2: Shock tube test set-up [74]

force onto the diaphragm), so that the high pressure gas is expanding into the low pressure region. During this expansion, an incidence shock wave forms, which is accelerating, compressing, and heating the test gas mixture, see Figure 8.2b. This shock wave reaches the end of the tube and is reflected, leaving the test gas in a constant pressure and temperature at zero velocity, as shown in Figure 8.2c. During this time, different measurements can be performed on the gas mixture.

In [70] the results of such a shock tube experiment using Jet-A / air mixtures as driven gas are presented for different pressures and temperatures. Using a laser Schlieren system, infrared absorption, and ultraviolet emission diagnostics, different emission from combustion products as OH^* and $-CH_3$ are measured, indicating the point of combustion. By the time the shock wave passed a specific region is known as well as the emission, an ignition delay time can be defined for a specific pressure and temperature. Different tests have been performed, using fuel-air equivalence ratios Φ of 0.5, 1.0, and 2.0. These ratios are representing a lean, stoichiometric and rich mixture, respectively. Φ can be calculated using

$$\Phi = \frac{\frac{m_{fuel}}{m_{ox}}}{\left(\frac{m_{fuel}}{m_{ox}}\right)_{st}} \tag{8.1}$$

which results in an equivalence ratio of 3 for the HotFire kerosene-oxygen engine option at a mass oxidizer fuel ratio of 1.2 and a stoichiometric mass mixture ratio of 3.7. The stoichiometric mass mixture ratio is iteratively determined from RPA, by checking which O/F results in the highest combustion chamber temperature.

The results [70] for the three different equivalence ratios 0.5, 1.0, and 2.0 at a pressure of 10 bar are shown in Figure 8.3. It can clearly be seen from this graph that for a higher equivalence ratio the temperature needed to get the same ignition delay is decreasing. Therefore, for an equivalence ratio of 3, as for HotFire, it is assumed that the temperature will be lower than for the equivalence ratio of 2.0, but to be on the safe side, the same curve is assumed as a reference value.

As the pressure in the HotFire engine is higher than the one measured of the experiment performed by [70], the behavior of the ignition time with respect to pressure is analyzed, and can be seen in Figure 8.4. It can be seen that with an increase in chamber pressure, the temperature needed to achieve the same ignition delay decreases. From this relation it can be concluded that for a pressure of 30 bar as for the HotFire engine, the temperature will further decrease. Again, the value for a pressure of 20 atm and an equivalence ratio of $\Phi = 2.0$ will be used as a reference.

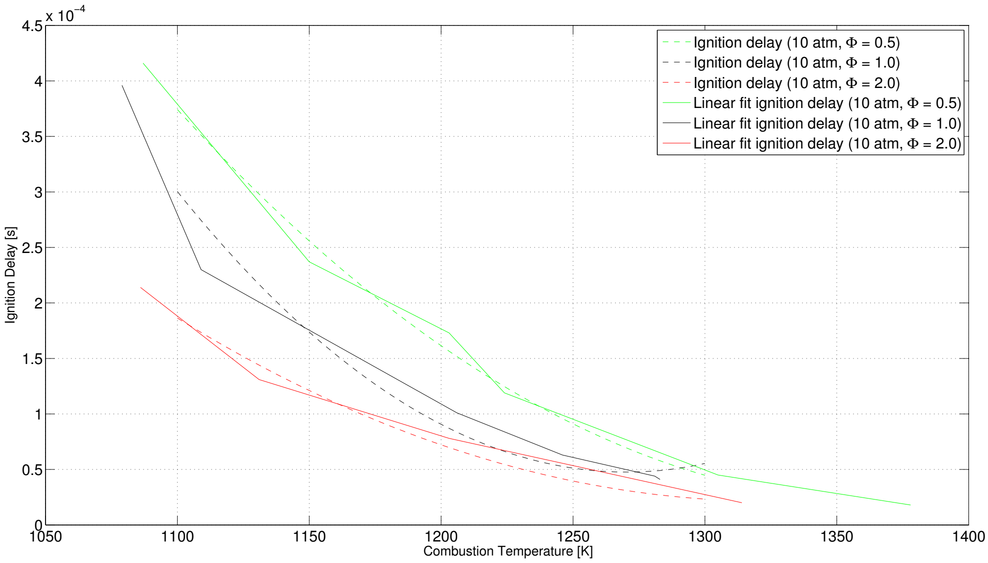

Figure 8.3: Change in ignition delay with a change in equivalence ratio at a pressure of 10 atm

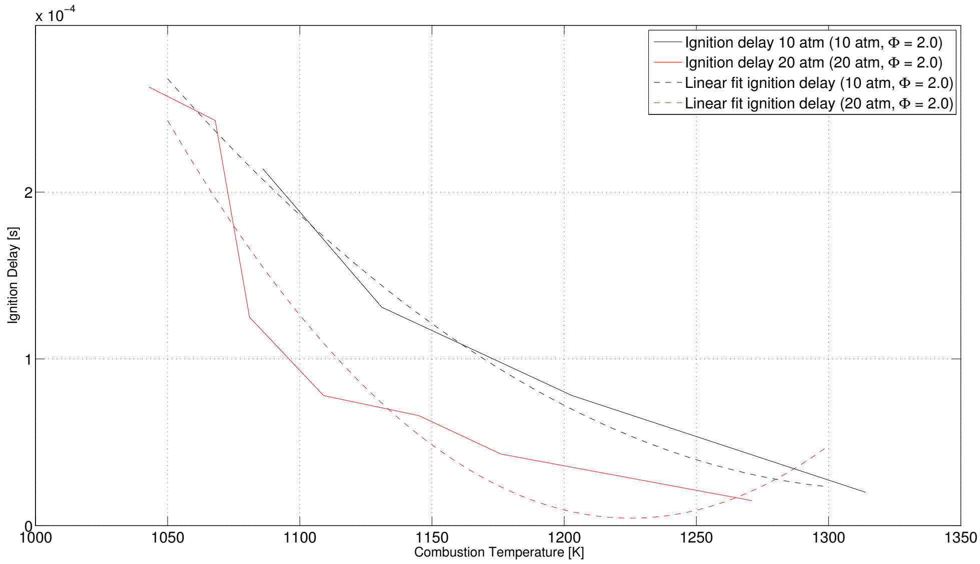

Figure 8.4: Change in ignition delay with a change in pressure at a constant equivalence ratio of $\Phi = 2.0$

HotFire is working with a kerosene-oxygen gas mixture, whereas the test data involved Jet-A fuel and air. Jet-A fuel is in fact a type of kerosene, therefore the fuel is comparable. The second largest volumetric part of air is oxygen with ($20\%_{vol}$ [76]). Therefore one can assume that highly compressed air has the same amount (by mass) of oxygen as pure oxygen. As a pressure increase in Figure 8.4 led into an decrease in temperature for the same ignition delay, the same can be assumed for changing the oxidizer from air to oxygen. The final graph showing the relation of oxidizer fuel ratio with temperature and pressure with respect to the LFL and UFL is shown in Figure 8.5. Additionally, the ignition delay curve for 10 atm and 20 atm pressure at an equivalence ratio of $\Phi = 2.0$ are included to indicate the autoignition temperatures. Therefore, a gas mixture of kerosene and oxygen has to be heated above 1200 K to ignite.

8.2.3. IGNITOR ENERGY

The energy that is needed to be delivered by the ignitor is a function of the specific heat capacity of oxidizer and fuel, the autoignition temperature, the mass flow, and the time the ignitor is delivering energy. This

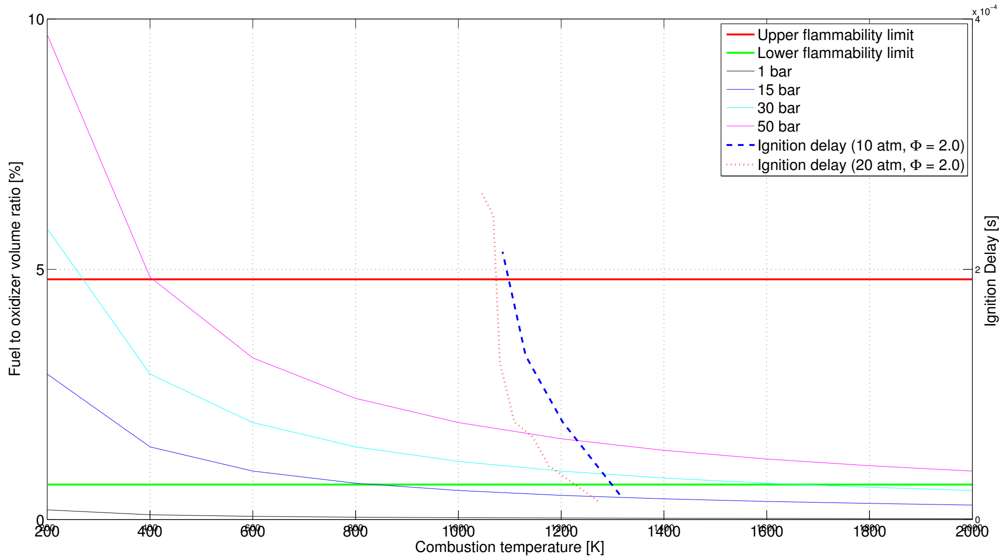

Figure 8.5: Flammability diagram including the autoignition limits estimated from the ignition delay experiment [70]

general equation is shown in Equation (8.2).

$$E = t\dot{m}c_p\Delta T \tag{8.2}$$

As discussed previously, the autoignition temperature is equal to $T_{\text{auto}} = 1200$ K and the mass flow is equal to $\dot{m} = 0.137$ kg/s. Furthermore, the mass oxidizer fuel ratio is equal to 1.2, resulting in a mass flow of the oxidizer of $\dot{m}_{\text{ox}} = 0.075$ kg/s and a mass flow of the fuel of $\dot{m}_{\text{fuel}} = 0.063$ kg/s. Generally it can be said that the ignitor needs to ignite only a fraction of the mass flow in order to start combustion in the whole chamber, where the fraction can be determined by the size of the sphere of influence for the respective igniter type. A spark plug, for example, has a small sphere of influence compared to an explosive igniter. As an initial approximation, the affected cross-sectional area of the ignitor is assumed to be a circle of diameter $d = 1.0$ mm, which can be also seen as the diameter of a droplet inside the chamber. From this approximation and assuming that the chamber has a diameter of 44 mm the area ratio between chamber area and affected area of the sphere is 1/1936. This ratio is multiplied with the oxidizer and fuel mass flow to achieve the mass flow through the 1.0 mm sphere, equal to $\dot{m}_{\text{ox}} = 3.88 \cdot 10^{-5}$ kg/s and $\dot{m}_f = 3.23 \cdot 10^{-5}$ kg/s. Using Equation (8.2) for these values of mass flow, a temperature change of $\Delta T = 912$ K, a $c_{p_{ox}} = 0.918$ kJ/(kg K), a $c_{p_f} = 2.01$ kJ/(kg K) and a time $t = 1$ s results in the energy values summarized in Table 8.3.

Table 8.3: Energy needed to ignite a kerosene - oxygen mixture at $\dot{m} = 1.26 \cdot 10^{-4}$ kg/s for one second

	Energy in [J]
Oxidizer	32.5
Fuel	59.3
Overall	91.8

The overall energy needed to be added to a circular area of d = 1mm is 91.77 J. A similar number is also mentioned in [16], where the minimum ignition energy needed to ignite kerosene with oxygen is said to be around 100 J for a mixture temperature between 35 and 40$^\circ C$. As the initial temperature for the calculations shown above is assumed to be 288 K, a higher value for the above shown calculation was expected.

In order to design an ignitor which is able to fulfil the main requirement of igniting the oxidizer fuel mixture, different sub-requirements are specified in this subsection. These sub-requirements follow from the general flammability analysis performed before, especially from the ignition temperature analysis in Section 8.2.2 and the considerations about the igniter energy in Section 8.2.3. Table 8.4 shows the resulting ignitor criteria.

As discussed in the previous subsection, the minimum energy required to ignite the system is $E = 151$ J. Furthermore, the ignitor shall be able to ignite the system a single time. Multiple ignitions are not needed

Table 8.4: Main sub-requirements for the ignitor

Requirement	Value	unit
Ignition Energy	151	J
Number of Ignitions	1	-
Duration of Ignition	max. 1	s
Size	Shall fit into the model	-

for this test, therefore it is disregarded again for the trade-off later on. The duration of the ignition shall be maximum 5 seconds. This requirement is determined from the fact that during this ignition time, fuel and oxidizer are fed into the chamber without generating a plume. This waste of propellants should be limited. The size of the igniter is the last important requirement, as the ignitor shall fit into the model. Now that all these requirements are determined, a proper ignitor system can be chosen. This is done in the following subsection, the igniter trade-off.

8.3. IGNITER SELECTION

There are different igniter which are commonly used in rocket engines [16][77] , namely: pyrotechnic ignitor, hypergolic ignitor, catalytic ignitor, spark plug, torch ignitor, and resistive heating ignitor.

Pyrotechnic ignitors produce the flame by burning a pyrotechnic mixture, similar fireworks. The burn time can range from a few milliseconds for explosive pyrotechnic igniter to a few seconds [77], but a reignition is not possible. In many cases they are placed inside the chamber trough the nozzle and get propelled out again when combustion has started. For small engines, the size of such a pyrotechnic ignitor is not a problem, whereas for big engines pyrotechnic igniter are getting impractical. One example for such an igniter type is an electrically triggered squid.

Hypergolic ignitors are characterized as a separate rocket motor, using separate ignitor feed lines [16]. This ignitor can be another liquid engine igniting the actual big engine. Another form of hypergolic ignitor is to inject another substance which forms a self igniting mixture with oxidizer or fuel in order to start the engine.

Catalytic ignitors are working on the catalytic reaction principle, where oxidizer or fuel is heated by a catalytic reaction. The time that is needed by such a reaction is rather long, compared to for example pyrotechnic ignition [16].

Spark plug ignition is considered one of the easiest way to ignite a liquid engine, as many liquid engines require little ignition energy. This is mainly also the drawback of a spark plug, as the energy that can be delivered is very limited. A typical spark plug, presented in [16], is considered to provide 5 watts of power per plug.

A torch ignitor is considered to be a small liquid engine ignited by a spark plug, much like a Bunsen-Brenner or a camping grill. This kind of ignitor includes again separate igniter feed lines or the storage of the igniter fuel and oxidizer inside the ignitor itself.

Resistive heating is based on the physical theory of electrically heating an elements, which has a low resistance. There are different materials applicable for this kind of ignitor, for example Nickel-Chrome wires, which are used to ignite amateur liquid rocket engines [78].

In order to find the best option, all the different requirements have to be fulfilled. In order to check, whether a certain system is able to fulfill a requirement a trade-off table is generated, which is shown in Table 8.5. This table is not judging the different igniter on how good they are fulfilling the requirement, but whether they are able to fulfil them.

A green box indicates when it is possible to meet the respective requirement and a red box indicates when it is impossible to meet the respective requirement. As the ignition system is generally determined by a test series [73] [79] a yellow box is included which indicates, when a test need to performed to determine whether a specific requirement can be met. The trade-off will than result in a set of possible igniter which are afterwards discussed in their performance and applicability. From this trade-off it can be concluded, that the spark

Table 8.5: Ignitor trade-off matrix – The green fields indicate that the ignitor type is able to meet the requirement, the red field indicates the opposite. A yellow box indicates, when the information has to be determined by testing. Note: A system including feed lines for the ignitor is considered unfeasable

	Ignition Energy	Ignition duration	Size
Pyrotechnic Ignitor	yellow	green	green
Hypergolic Ignitor	yellow	green	red
Catalytic Ignitor	yellow	red	yellow
Spark Plug	yellow	green	green
Torch Ignitor	yellow	green	red
Resistive Heating Ignitor	yellow	green	green

plug, the resistive heating igniter and the pyrotechnic igniter are possible design options for the igniter of the HotFire. The different igniter options have to be tested in order to find the igniter which is most suitable for the HotFire. A spark plug is considered the easiest option, as a lot of information about different spark plugs, manuals etc. are available. Therefore it is proposed to test the possibility of igniting the HotFire with a spark plug first.

8.4. IGNITOR POSITIONING

The positioning of a ignitor is generally independent on the type of ignitor, as an ignitor should always be positioned in the region where an ignition is most likely to be successful. In this region the mixture of oxidizer and fuel should be ignitable, furthermore, the ignitor should be position at a location where direct oxidizer flow is encountered. As discussed previously, the injection system used for the HotFire is a coaxial pintle injector. The ignitor should therefore be positioned at one of the impingement points of the inner fuel flow with the outer oxidizer flows as shown in Figure 8.6. The direct position inside the whole combustion chamber can just be estimated, as an exact position has to be determined by a test [73].

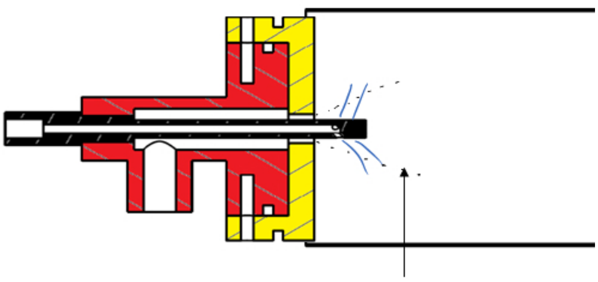

Figure 8.6: The blue lines are indicating the oxidizer flow and the red lines are indicating the fuel flow

8.5. RECOMMENDATIONS

The igniter is an important part of the rocket motor and is generally a significant source of errors. As described in the previous sections of the ignitor, information about the flammability and autoignition of a oxygen - kerosene rocket motor at 30 bar combustion chamber pressure and an $O/F = 1.2$ is not available. However, it has been shown that the mixture is ignitable with an energy of 91.8 J. This number and the general ignition behavior have to be verified in an igniter test series. In such a test series, the model is mounted to a test rig and an ignition sequence is performed. The burn time of such an igniter test can be shorter than the actual test, in order to safe oxidizer and fuel. This increases the number of tests that can be performed until a powerful enough ignitor is found. In order to facilitate the handling of Hotfire, the spark plug is proposed for the first ignition tests. The design of the whole system includes the necessary structure to test a spark plug as an igniter.

9

Combustion Chamber and Nozzle

To create the plume the propellant needs to be combusted and expanded to the required exit conditions. Therefore, a combustion chamber and a convergent-divergent nozzle are needed. This chapter will discuss concepts for these subsystems and analyze the concepts to obtain the most suitable design. Combustion chamber and nozzle are treated together since they require a similar methodology for analysis.

9.1. Concepts

The combustion chamber allows for the reaction of the propellants under the desired conditions. It is also exposed to stresses and heating by the gas mixture. For these reasons the shape of the combustion chamber is typically cylindrical, spherical and pear shaped [17], see Figure 9.1a. These shapes will be analyzed on their performance.

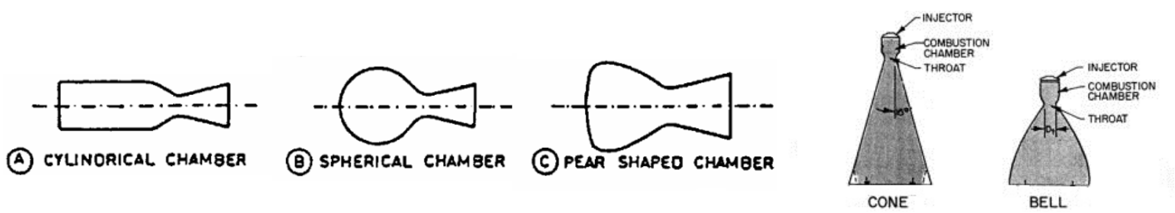

(a) Typically used combustion chamber shapes

(b) Shape of conical and bell shaped nozzle

Figure 9.1: Typical geometric shapes of combustion chamber and nozzle [17]

The function of the nozzle is to expand the flow to the desired exit conditions. It has a convergent and divergent part which can have different shapes and geometry. There are two widely used concepts, namely the conical nozzle and the bell shaped nozzle [17] [30], see Figure 9.1b. These two concepts will be analyzed for compliance with the requirements.

The nozzle must also be able to create a cold plume. This will not be possible with the same fixed area ratio nozzle. Therefore, the concepts of either an interchangeable nozzle or two separate models will be analyzed.

9.2. Requirements on Combustion Chamber and Nozzle

The design of combustion chamber and nozzle are influenced by multiple requirements for the HotFire system. The associated requirements are listed below.

`HF-TEC-CPL-01` The cold plume shall be similar to the hot plume.
The nozzle must allow to expand the flow such that similar plumes are created by the model.

`HF-TEC-SIM-04` Shock waves shall not reflect from the wind tunnel wall into the model base region.
The length and diameter of the combustion chamber should be set such that the reflected shock is outside of the region of interest.

`HF-TEC-MEA-01` The plume diameter shall be at least 2 cm.
The plume size gives a certain mass flow which the combustion chamber and nozzle should be able to produce.

`HF-CON-WTO-01` The wind tunnel blockage shall not exceed 5%.
The combustion chamber takes a large portion of the frontal projected area, which should not exceed its assigned budget of 60% of the total budget. Refer to Section 3.3.

`HF-CON-COS-01` The material costs shall not exceed 10,000 €.
The cost of the materials for the combustion chamber and nozzle should not exceed their assigned budgets. Refer to Section 3.3.

`HF-CON-SUR-02` During operations, the model shall not fail statically due to loads.
During operation the combustion chamber and nozzle experience pressure loads due to combustion.

`HF-CON-SUR-04` During operations, the model shall not fail due to temperature.
Due to heating the materials mechanical properties are lowered.

`HF-TEC-MEA-06` The system shall operate under constant conditions for at least 5 s.
The test time determines the temperature build up of the material.

`HF-TEC-MEA-08` The plume conditions shall not vary by more than 1% over time.
Over the test time, the material heats up and expands, which influences the area ratio. This should be limited such that the plume conditions do not vary more than 1%.

The following analysis will be done to guarantee that all requirements are met. For each analysis the relevant requirements are indicated.

Analysis of Geometry `HF-TEC-SIM-04`, `HF-TEC-MEA-01`, `HF-CON-WTO-01`

Analysis of Nozzle Geometry `HF-TEC-CPL-01`, `HF-TEC-MEA-01`

Analysis of Materials `HF-CON-COS-01`, `HF-CON-SUR-04`, `HF-TEC-MEA-06`

Thermal Analysis `HF-CON-SUR-04`, `HF-TEC-MEA-06`, `HF-TEC-MEA-08`

Structural Analysis `HF-CON-SUR-02`, `HF-TEC-MEA-06`

9.3. ANALYSIS OF CHAMBER GEOMETRY

First the inner geometry of the combustion chamber must be determined to enable a starting point for the thermal and structural analysis. The inner geometry of the combustion chamber is determined together with the mass flow.

The volume of the combustion chamber can be determined by the mass flow. This follows from the fact that a certain volume will give a certain residence time for a mass flow. It is found that for small deviations in pressure, O/F ratio, and mixing characteristics a characteristic length $L^\star$, can be defined, see Equation (9.1) [17]. The characteristic length $L^\star$ is given by dividing the volume V by the throat area A_t, which is a function of the mass flow.

$$L^\star = \frac{V}{A_t} \tag{9.1}$$

An exit diameter d_e=1.5 cm is used to create a plume diameter of 2 cm, which is explained in Section 9.4. The range of the characteristic length for kerosene with oxygen is 1 m to 1.25 m [17]. To make a feasible design and to stay conservative, the upper number of this range is taken for further calculations. The area ratio which is needed for the similarity is 2.77 (see Chapter 4), which results in a desired volume of $7.975 \cdot 10^{-5}$ m^3.

For the spherical combustion chamber concept, the radius can be calculated with the formula for volume of a sphere, see Equation (9.2).

$$V_{\text{sphere}} = 4/3 \cdot \pi \cdot r^3 \tag{9.2}$$

This gives an inner radius r_c=2.7 cm for the spherical combustion chamber, meaning that if the spherical combustion chamber would have an infinitely thin wall thickness it would already occupy 60% of the blockage requirement and thus, would definitely not be able to meet the requirement.

The pear shaped combustion chamber is optimized for thrust performance. In comparison with the cylindrical combustion chamber it needs more cross sectional area for the same volume. Preliminary research showed that the blockage and length is critical for the location of the reflected shock wave. Therefore in further analysis only the cylindrical combustion chamber concept will be considered.

The location where the reflected shock wave hits the plume depends on the geometry of the model. Hence, a smaller diameter for an optimized nose cone will allow the angle of the shock to become more shallow, which leads to the reflected shock wave hitting the plume further back. On the other hand a smaller diameter will also cause the length of the combustion chamber to increase, making the impact of the shock closer to the base region.

Since the volume is known, it is possible to iterate over the geometry, finding the dimensions that give the largest distance from the base plate and the reflected shock wave hitting the center-line. A tool was developed in previous stages of the design to determine the location of the reflected shock wave, see Chapter 6. The tool allows to calculate the optimum nose cone shape for a given chamber geometry. It was found that an outer diameter of 5 cm was optimal, still allowing for the feed lines bend radius, see Chapter 5.

From preliminary analysis with the analytical model (see Section 9.7.6) it was found that a wall thickness 2.5 mm for the combustion chamber will satisfy the requirements conservatively, see Section 9.10. An inner diameter of 4.5 cm will be used for the further analysis and design of the combustion chamber. This gives a length of 5.01 cm for the cylindrical combustion chamber.

9.4. ANALYSIS OF NOZZLE GEOMETRY

A prediction on the size of the plume has been performed to determine the exit diameter of the nozzle. Having the exit diameter and other features such as expansion ratio and diameter of the combustion chamber, the nozzle geometry can be determined. In the Mid-term the conical and bell shaped nozzle have been identified as the feasible design options for the nozzle. These two nozzle concepts can be compared based on the their length and ability to achieve the lip angle for both the hot and the cold plumes.

9.4.1. PLUME SIZE

The plume size of the HotFire has to be larger than $d = 2$ cm in diameter. This minimum diameter is enforced by requirement `HF-TEC-MEA-01`. Generally analytical estimations or calculations for the plume size in terms of diameter are not available. The reason for this is mainly that there is no proper definition of where a plume begins or ends and furthermore a simple calculation of the plume diameter is impossible.

Generally it can be said that the plume diameter is directly related to the exit nozzle diameter. As the area ratio is set, a certain throat diameter can be calculated when assuming an exit diameter. The area that can be recorder by the PIV cameras is $4x4$ cm^2 big. Within this area the plume has to reach a diameter of $d = 2$ cm. In order to get an initial estimation for the nozzle exit diameter, it is assumed that the plume shall reach a diameter of $d = 2$ cm at the horizontal center of the $4x4$ cm^2 frame covered by the camera. In Chapter 4 the initial inclination angle was calculated to be $\delta = 23$ deg. Assuming this angle and the positioning of the camera so that Figure 9.2a is produced as the recorded image a nozzle diameter of around 1.5 cm can be calculated using trigonometric relations.

In order to verify whether the plume size with a nozzle exit diameter of 1.5 cm meets the requirement, a CFD analysis in FLUENT is performed. The input dimensions for this analysis are shown in Figure 9.2b. The

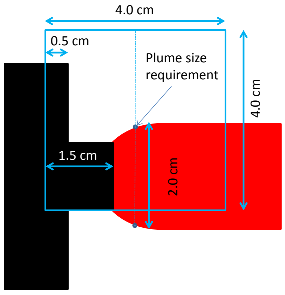

(a) Position of the model w.r.t. the recorded PIV camera image

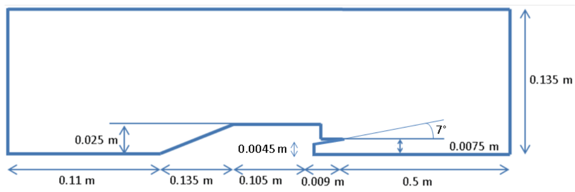

(b) Dimensions used for the simulation

Figure 9.2: Schematics for plume size

nozzle has been simplified to a conical nozzle. As the lip angle and all the exit conditions are kept the same, this assumption will not change the solution. Using axisymmetry to enable three dimensional relief effects and using a pressure source at the throat location to generate the plume inside the pressure field of the wind tunnel, the solutions are generated. The resulting Mach number and density field are shown in Figure 9.3a and Figure 9.3b. Those two plots are chosen, because they are showing the interactions between free stream and plume best.

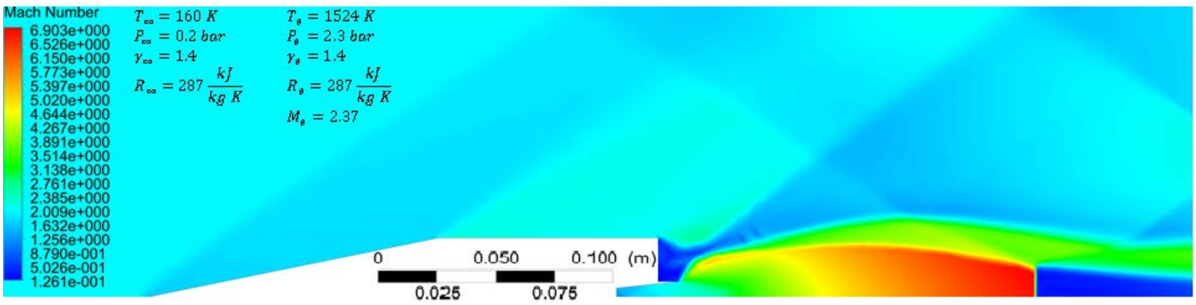

(a) Solution for the Mach number field

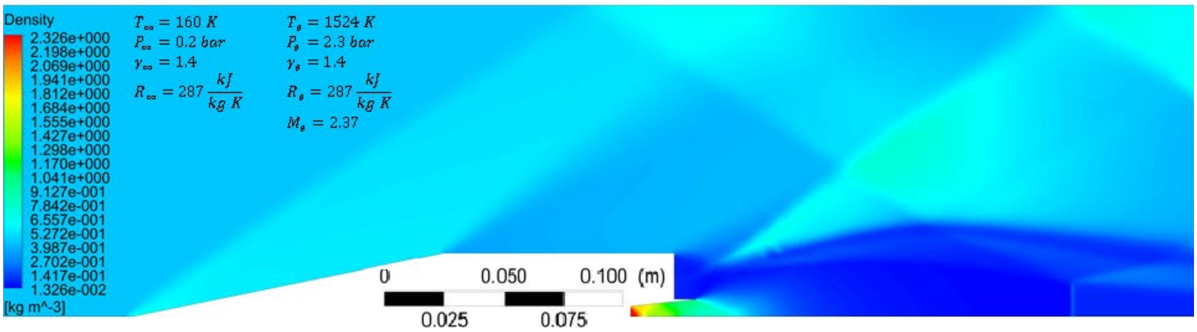

(b) Solution for the density field

Figure 9.3: Flow field for model with plume in wind tunnel as computed with CFD (ANSYS)

The respective input boundary conditions for the simulations are depicted in Figure 9.3a and Figure 9.3. From both plots a plume diameter can be read of using the scale in the figures. For the Mach number field Figure 9.3a, the plume diameter is at the previously specified location is d = 2.875 cm and the maximum diameter is d = 6.75 cm and for the density field Figure 9.3b, the plume diameter is maximum d = 7.45 cm and no plume diameter at the specified location can be determined as no clear boundary between free stream and plume is visible. The value from the Mach number field clearly fulfills the plume size requirement of d = 2 cm.

9.4.2. METHODOLOGY FOR NOZZLE DESIGN

Having determined the required exit diameter of the nozzle, the methodology for defining the geometry of both the conical and bell shaped nozzle can be presented.

CONICAL NOZZLE

According to [17], the typical angles for the convergent section of the nozzle are 30 to 45 degrees. However, [80] has shown that an angle of 60 degrees can also used. Therefore, the nozzle was designed with the convergent angle of 60 degrees, as this results in a shorter nozzle.

The typical angles for the divergent part of the nozzle are 12 to 18 degrees. [17] However, to match the lip angle for the similarity parameters (see Chapter 4), a nozzle with 7 degrees divergence angle has been designed.

[17] states that the radius of curvature R_u for the throat section typical ranges from $0.5R_t$ to $1.5R_t$. This is illustrated in Figure 9.4. Note that R_t is the radius of the throat. To have the shortest length of the throat, the radius of the curvature of $0.5R_t$ has been chosen.

Using these geometric parameters, the length of the conical nozzle for the hot plume has been estimated to be 0.0395 m. The hot plume nozzle was analyzed since it will be longer than the cold plume due to its larger area ratio.

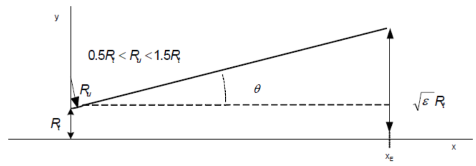

Figure 9.4: Divergent region of the conical nozzle, [17]

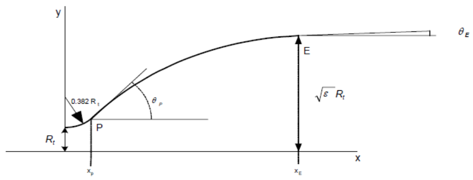

Figure 9.5: Divergent region of the bell shaped nozzle, [17]

BELL SHAPED NOZZLE

The bell shaped nozzle with 60 degrees of convergence angle has been designed. The values $1.5R_t$ and $0.382R_t$ have been chosen for the radius of curvature R_u of the throat for the convergent and divergent part respectively. These values are conventionally used for bell shaped nozzle [81]. Furthermore, initial divergence angles of 45 to 60 degrees are typically used [17]. The divergence angle of 45 degrees was found to result in the shortest length of divergence region. For the lip angle, 7 degrees for the similarity parameters has been taken.

To ensure a smooth transition from throat to divergent section of the nozzle, an intersection point p between the end of the throat section and the beginning of the divergent section is determined using Equation (9.3) and Equation (9.4) [17].

$$x_p = 0.382R_t \sin(\theta_p) \tag{9.3}$$

$$y_p = 1.382R_t - 0.382R_t \cos(\theta_p) \tag{9.4}$$

The shape of the divergent region can be approximated by a parabola $x = ay^2 + by + c$ that passes through the point E and point P in Figure 9.5 (ε is used for the expansion ratio). The coefficients of the parabola can be determined using the point p, exit radius R_E, initial angle of divergence θ_p and the lip angle θ_E (see Equations (9.5) to (9.7)).

$$a = \frac{\tan(\frac{\pi}{2} - \theta_E) - \tan(\frac{\pi}{2} - \theta_p)}{2(y_E - y_p)} \tag{9.5}$$

$$b = \tan(\frac{\pi}{2} - \theta_p) - 2\frac{\tan(\frac{\pi}{2} - \theta_E) - tan(\frac{\pi}{2} - \theta_p)}{2(y_E - y_p)} \tag{9.6}$$

$$c = x_p - ay_p^2 - by_p \tag{9.7}$$

Using above analysis, the length of the bell shape nozzle is estimated to be 22.9 mm.

9.4.3. COLD PLUME CONCEPTS

Different nozzles are required for the hot and cold plume because of the different area ratios and the lip angles. In the Mid-term, an interchangeable nozzle with the same combustion chamber as the hot plume and two completely separate models for the hot and the cold plume were proposed as possible concepts. An interchangeable nozzle has been selected as the most suitable concept due to the lower cost because only one combustion chamber needs to be manufactured for both the hot and the cold plume. Table 9.1 shows the geometric parameters of the hot and cold plume nozzle. The nose cone will be detachable which will allow interchanging the nozzle from the front. This also allows the use of different materials for the nozzle and combustion chamber. The same methodology as the hot plume model has been used to design the cold plume nozzle.

9.5. RESULTS GEOMETRY AND MASS FLOW

To conclude, a cylindrical combustion chamber is selected. It requires the smallest cross-sectional area per given volume. A interchangeable bell shaped nozzle is selected. It has the shortest length and it is able to achieve the desired lip angles. The final dimensions are presented in Table 9.1.

A bell shaped nozzle is selected for both the hot and the cold plume. The bell shaped nozzle will result in a shorter length an has the ability to meet the lip angle.

Table 9.1: Key geometrical parameters of combustion chamber and nozzle

	Hot plume dimensions	Cold plume dimensions
Chamber length [mm]	50.1	50.1
Chamber diameter [mm]	45	45
Half convergence angle [deg]	60	60
Length of convergent part [mm]	10.4	9.5
Length of divergent part [mm]	8.9	3.6
Length of throat part [mm]	3.6	4.8
Throat diameter [mm]	9.0	6.0
Radius of curvature of throat [mm]	4.5	3.0
Plume exit diameter [mm]	15	15
Initial divergence angle [deg]	45	45
Lip angle [deg]	7.0	10

The exit nozzle geometry in Table 9.1 along with the exit conditions shown in Table 4.8 allow for analytically determining the mass flow by using continuity ($\dot{m} = \rho A \mathrm{V}$ = constant) and assuming the exhaust mixture to be an ideal gas so $\rho = \frac{P_e}{R_e T_e}$. The ideal gas assumption is not trusted for the hot plume because of the large kerosene concentration. While being true for helium, the large hydrocarbons of kerosene do not support the assumptions of small molecules and elastic collision required for an ideal gas. This method is thus merely used as a verification for the mass flow determined via RPA (see Figure B.2). A comparison is shown in Table 9.2.

RPA specifies the mass flux at the nozzle exit (see Figure B.2). Since the exit diameter is known, the mass flow can be found to be 0.1375 kg/s. With the determined O/F ratio of 1.2, the individual mass flows of kerosene and oxygen can also be determined and are shown in Table 9.2.

9.6. ANALYSIS OF MATERIALS

For the material selection a set of typically used materials is shown in the Table 9.3. Analysis from Section 9.7.6 revealed that the temperatures will not exceed 1200 K for chamber and nozzle. Therefore, the typically used materials for temperatures under 1200 K, namely aluminium, steel and titanium [17] were identified as material options. Additionally, graphite was identified as possible nozzle materials as it is characterized by a low

Table 9.2: HotFire mass flow specification with $O/F = 1.2$ and $D_e = 1.5$ cm

Solution	Plume	Propellant	Mass Flux	Mass flow
Analytical	Cold	Helium	1218.77	0.2154
	Hot	Oxygen	441.07	0.0779
		Kerosene	367.55	0.0649
		Total	808.7	0.1429
RPA	Cold	Helium	-	-
	Hot	Oxygen	424.74	0.0751
		Kerosene	353.95	0.0625
		Total	777.52	0.1375

thermal expansion factor when compared to metals.

To guarantee that the combustion chamber meets the structural requirements, the change in the yield stress of the material over the increase in temperature had to be found. After a literature study, data for specific alloys/versions for each type of material were found. The properties of these materials are presented in Table 9.3. In the further analysis only these materials will be considered.

It can be seen from the properties of the materials in Table 9.3 that Aluminum can only be used at low temperatures up to 573K, but is able to maintain a high yield stress. Aluminum is relatively simple to manufacture making it the favorable material for low temperature applications. Steel and titanium can both be used for higher temperature application. However, steel loses at lot of yield strength at higher temperatures compared to titanium but is cheaper. Generally, thermal properties of steel and titanium are very comparable. Conductivity for both is relatively low and the product of specific heat and density is almost the same, leading to similar heat sink capacity for a given volume. Due to its low cost, steel is the favorable material for applications where it experiences low stress at elevated temperatures. Titanium is the better option at high stresses at elevated temperatures. Graphite is outstanding when it comes to the maximum temperature and the thermal expansion coefficient. However, graphite has lower mechanical properties. For applications where the applied loads are low and the temperature resistance and thermal expansion are critical, graphite is a suitable option.

Table 9.3: Nozzle and combustion chamber materials

Property	Aluminium AL-MS89 [82]	Steel S355 [68]	Titanium-Ti-SF61 [82]	Medium grained graphite [83]
Yield strength at T_{room} [MPa]	385	360	1050	14
Yield strength at T_{max} [MPa]	240	60	195	14
Max operational temperature [K]	573	1000	1000	2500
Shear modulus G [GPa]	27	79	41	4
Young's modulus E [GPa]	90	170	120	12.5
Melting temperature [K]	900	1800	2000	3700
Density ρ [kg/m^3]	2920	7850	4560	1800
Specific heat c_m [J/(kg K)]	910	450	540	710
Conductivity κ [W/(m K)]	150	16	8	120
Thermal Expansion coefficient α [m/(m K)]	19	14	8.6	2.6
Cost for a bar [Euros]	40 € $d = 60$ mm $L = 1$ m	97 € $d = 60$ mm $L = 1$ m	3350 € $d = 60$ mm $L = 1$ m	270 € $d = 54$ mm $L = 1.25$ m

9.7. THERMAL ANALYSIS

A thermal analysis was conducted in order to analyze the thermal loads on the combustion chamber and nozzle induced by the high temperature environment inside the thrust chamber. A set of self written tools was developed to estimate the temperature over time. This section will explain the principles behind the models.

9.7.1. GENERAL ASSUMPTIONS

For the thermal analysis, the following overall assumptions were made.

1. Steady state combustion is assumed. This assumption enables the use of combustion gas properties at steady state. The assumption is valid because in order to maintain the constant plume condition for 5 seconds, a steady combustion for 5 seconds of burn time must be achieved.
2. The time for the transient phase of the combustion is assumed to be less than 1 second. Therefore, the temperature computations were based on a 6 seconds steady state combustion (1 seconds of transient combustion and 5 seconds of steady state combustion). The computation based on this assumption results in conservative results, since the transient phase of the combustion would typically be less than 1 second as it can be seen for typical thrust curves or pressure curves of the liquid rocket engine. [17]
3. Instability of the combustion is neglected. The instability of the combustion is characterized by the fluctuations of combustion chamber pressure [30]. In order to check the validity of the assumption, a sensitivity study is performed on the most critical combustion chamber parameter, namely pressure.

9.7.2. TYPES OF HEAT TRANSFER

In the combustion chamber and nozzle convection is the most dominant form of heat transfer [17] [30] [84]. Radiation can be up to 25% of the total heat transfer, when the solid rocket motors are considered which have solid particles in the hot gas flow. Conduction takes place in the combustion chamber walls where the energy is distributed over the geometry.

9.7.3. CONVECTION

Convection is energy transfer between a solid surface and a moving gas or liquid. There are two forms of convection namely forced and natural. Forced convection occurs when the flow of the gas or liquid is introduced by external means whilst in natural convection the motion is introduced by temperature differences and gravitational forces. HotFire experiences forced convection. The convection energy flux is proportional to the temperature difference between gas and wall (see Equation (9.8)).

$$q_{\text{convection}} = h \cdot (T_2 - T_1) \tag{9.8}$$

The h is the convection coefficient. Its value cannot be calculated exactly. Therefore, multiple semi empirical relations are compared to determine the convection coefficient. For the convection coefficient from the combustion gases to the chamber wall and nozzle, three methods were compared, namely the Bartz, Cinjariv and Cornelisee. The convection coefficient according to Bartz [81] can be calculated using Equation (9.9).

$$h_{Bartz} = \frac{0.026}{D_t^{0.2}} \left(\frac{\mu^{0.2} c_p}{Pr^{0.6}} \right)_{\text{total}} \left(\frac{(P_c)_{total}}{c^\star} \right)^{0.8} \left(\frac{D_t}{R_u} \right)^{0.1} \left(\frac{A_t}{A_{\text{local}}} \right)^{0.9} \cdot \sigma \tag{9.9}$$

In Equation (9.9), D_t is the throat diameter, μ_{total} is the dynamic viscosity under total conditions, $c_{p_{\text{total}}}$ specific heat at constant pressure under total conditions (obtained from RPA), Pr_{total} is the Prandtl number under total conditions, $(P_c)_{\text{total}}$ is the total combustion pressure, $c^\star$ is the characteristic velocity, $R_{\text{curvature}}$ is the radius of nozzle curvature, A_t is the throat area, A_{local} is the local cross sectional area and σ is the boundary layer correction factor which can be calculated using Equation (9.13). For μ, Pr and R_u estimation formulas exist, which are given in Equations (9.10) to (9.12) [81].

$$\mu = 1.3634 \cdot 10^{-12} m_{\text{molecular}}^{0.5} T_{\text{gas}}^{0.6} \tag{9.10}$$

In Equation (9.10) $m_{\text{molecular}}$ is the molecular mass of the gas mixture which is obtained using RPA (see Figure B.2). The Prandtl number is given by

$$Pr = \frac{4\gamma}{9\gamma - 5} \tag{9.11}$$

while the radius of curvature is given by

$$R_u = (1.5 r_t + 0.382 r_t)/2 \tag{9.12}$$

where r_t is the radius of the throat. The correction factor for the boundary layer σ is shown in Equation (9.13) where M is the local Mach number.

$$\sigma = \left(\frac{1}{2}\frac{T_{\text{innerwall}}}{T_{\text{gas}}}\left(1 + \frac{\gamma - 1}{2}M^2\right) + \frac{1}{2}\right)^{-0.68}\left(1 + \frac{\gamma - 1}{2}M^2\right)^{-0.12} \tag{9.13}$$

The coefficient according to Cinjarev [84] can be calculated using Equation (9.14).

$$h_{\text{Cinjarev}} = 0.01975 \frac{\kappa_{\text{gas}}(\dot{m}c_p)^{0.82}}{D_{\text{local}}}\left(\frac{T_{\text{gas}}}{T_{\text{innerwall}}}\right)^{0.35} \tag{9.14}$$

Here, $kappa_{\text{gas}}$ is the conductivity coefficient of the gas mixture and D_{local} is the local diameter of the cross section. The conductivity coefficient was computed using RPA (see Figure B.2).

Cornelisse provides two equations, one for calculating the convection coefficient in the combustion chamber, Equation (9.15), and one at the nozzle throat, Equation (9.16) [17].

$$h_{\text{Cornelisse,chamber}} = 0.023 P_c^{0.8}\left(\frac{\mathrm{V}_c}{RT_{\text{gas}}}\right)^{0.8}\frac{1}{D_c^{0.2}}\frac{k_{\text{gas}}Pr^{0.33}}{\mu^{0.8}}\left(\frac{T_{\text{gas}}}{\frac{T_{\text{gas}}+T_{\text{innerwall}}}{2}}\right)^{0.68} \tag{9.15}$$

Here V_c is the velocity of the combustion chamber gases. The V_c was obtained using the principle of conservation of mass flow ($\dot{m}$=$\rho V_c A_c$) and assuming a constant gas velocity inside the combustion chamber. The area of the combustion chamber A_c is computed knowing the diameter of the combustion chamber and the gas density ρ was computed using the ideal gas law.

$$Sh_{\text{Cornelisse,throat}} = 0.0315 \dot{m}^{0.8}\mu^{0.2}c_p Pr^{-2/3} D_t^{-1.8}\left(\frac{T_{\text{gas}}}{\frac{T_{\text{gas}}+T_{\text{innerwall}}}{2}}\right)^{0.68} \tag{9.16}$$

Bartz and Cinjarev provide a method to calculate the convection coefficient throughout the entire geometry of the combustion chamber and throat whereas Cornelisse only gives a method for calculating the convection coefficient at the chamber wall and at the throat. The three methods were compared at the three locations namely the chamber wall, throat and the exit. The results are shown in Figure 9.6. At the chamber wall the three methods provide similar convection coefficients; at the throat the Bartz method starts to deviate from the other two methods, and at the exit Bartz is significantly higher than Cinjarevs method. These results confirm the conclusions of the [84], where it was also found that through the nozzle geometry Bartz method was deviating from Cinjarevs method and overestimating the heat flux.

The Bartz method is used in further analysis to compute h_{in}, since it is the most conservative.

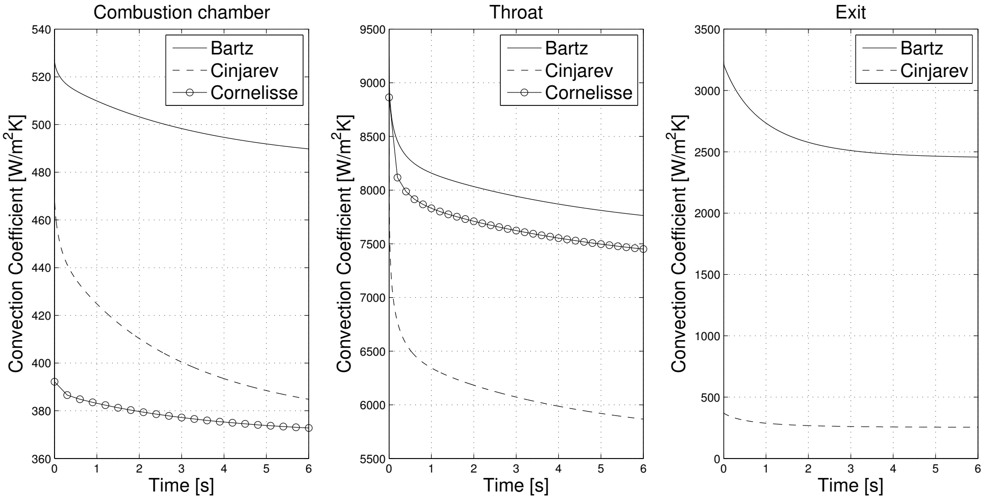

Figure 9.6: Comparison of convection coefficients calculated using different semi-empirical methods

The propellants used are kerosene with gaseous oxygen. It is known that during the combustion of this fuel a carbon deposit layer is builing up which has a thermal resistivity R_{carbon}. Information on the magnitude of this layer over the geometry of the combustion chamber and nozzle is available in [81]. The convection coefficient needs to be corrected for this layer, this can be done by Equation (9.17). [81]

$$h_{new} = \frac{1}{\frac{1}{h_{old}} + R_{\text{carbon}}} \tag{9.17}$$

For the convection coefficient from the thrust chamber wall to the surrounding wind tunnel flow, the convection coefficient h_{out} can be calculated using the concept of Nusselt number Nu as shown in the Equation (9.18). According to [17], it is the ratio of heat transferred by convection compared to that which would be transferred by conduction alone.

$$h_{\text{out}} = \frac{Nu\,\kappa_{\text{gas}}}{L_{\text{c}}} \tag{9.18}$$

To compute the Nusselt number, a semi-empirical relation was used which is shown in Equation (9.19). Equation (9.19) assumes the heat transfer over a flat plate. Using the Nusselt number for a flat plate despite the thrust chamber being cylinder is a conservative measure as the flat plate yields a higher Nusselt number.

$$Nu = 0.037 \cdot Re^{0.8} Pr^{1/3} \tag{9.19}$$

Here Re is the Reynolds number of the free stream flow, which can be calculated by Equation (9.20). The Prandtl number Pr of the free stream can be calculated with Equation (9.21).

$$Re = \frac{\rho_\infty \cdot L_{\text{c}} \cdot \text{V}_\infty}{\mu_\infty} \tag{9.20}$$

Here ρ_∞ is the density of the free stream flow, L_{c} is the length of the model, V_∞ is the velocity of the free stream flow and μ_∞ is the dynamic viscosity of the free stream.

$$Pr_\infty = \frac{c_{p_\infty} \cdot \mu_\infty}{\kappa_\infty} \tag{9.21}$$

In Equation (9.21) κ_∞ is the thermal conductivity of the free stream.

9.7.4. RADIATION

The other important form of heat transfer from the combustion gasses to the chamber wall and nozzle is radiation. Radiation energy flux is dependent on the temperature of the emitting body and on the coefficient of emissivity according to Equation (9.22).

$$\dot{q}_{\text{radiation}} = \sigma_{\text{Boltz}} \epsilon T^4 \tag{9.22}$$

In this equation σ_{Boltz} is the Boltzmann coefficient ($5.67 \cdot 10^{-8}$) and ϵ is the coefficient of emissivity.

The coefficient of emissivity is dependent on many factors such as material and surface roughness. To obtain this coefficient for the hot combustion mixture often advanced models are used, but these can only achieve a certain amount of accuracy. On the other hand, the Shack method (see Equation (9.23) and Equation (9.24) [84]) offers a simple semi empirical relation to estimate the radiation assuming that all radiation is emitted by carbon-dioxide and water molecules, which has been found to provide a good first order approximation [84].

$$\dot{q}_{\text{radiation}_{\text{CO}_2}} = 4(\varsigma_{\text{CO}_2} P_c r_c)^{0.3} \left(\frac{T_{\text{gas}}}{100}\right)^{3.5} \tag{9.23}$$

$$\dot{q}_{\text{radiation}_{\text{H}_2\text{O}}} = 5.74(\varsigma_{\text{H}_2\text{O}} P_c r_c)^{0.3} \left(\frac{T_{\text{gas}}}{100}\right)^{3.5} \tag{9.24}$$

In these equation ς_{CO_2} and $\varsigma_{\text{H}_2\text{O}}$ are the molecular fraction of the carbon-dioxide and water in the combustion gas mixture. The values were obtained from RPA (see Figure B.2). Note that in Equations (9.23) and (9.24), the unit of pressure is in bar.

By painting both chamber and nozzle black, an emissivity coefficient of 0.9 [17] can be achieve. This will result in maximum radiation cooling. Thus, the emissivity coefficient of 0.9 is used for modeling the radiation cooling of the outer surface.

9.7.5. CONDUCTION

Within the chamber wall and nozzle material, conduction occurs which distributes the energy. The conduction energy flux is dependent on the thermal conductivity of the material κ_{material}, the temperature difference T_2-T_1 and the distance over which it has the energy has traveled Δx according to Equation (9.25).

$$q_{\text{conduction}} = \kappa_{\text{material}} \frac{T_2 - T_1}{\Delta x} \tag{9.25}$$

9.7.6. ANALYTICAL SOLUTION (HEATSINK)

According to [30] the non-cooled walls of the thrust chamber act as a heat sink, absorbing the heat from the hot gases. Equation (9.26) shows the changes in the temperature of the chamber wall due to absorption of heat from the hot gases, which is visualized in Figure 9.7.

$$\dot{q}_{conv,in} + \dot{q}_{rad,in} - \dot{q}_{conv,out} - \dot{q}_{rad,out} = m c_m \frac{dT}{dt} \tag{9.26}$$

The difference between the heat flux in (convection in $\dot{q}_{conv,in}$ and radiation in $\dot{q}_{rad,in}$) and out (convection out $\dot{q}_{conv,out}$ and radiation out $\dot{q}_{rad,out}$) of the thrust chamber wall results in a temperature change over time for the thrust chamber wall. This rate of change in temperature also depends on the properties such as the mass m and the specific heat c_m of the material for the thrust chamber wall.

Assuming a uniform temperature throughout the wall (infinite conduction), a differential equation shown in Equation (9.26) can be solved to roughly estimate the temperature of the wall as a function of time. The

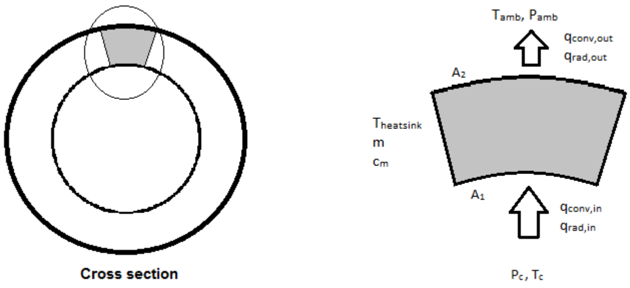

Figure 9.7: Overview of energy fluxes through the cross-section

heat flux into the chamber wall by convection was the only mode of heat transfer in deriving Equation (9.27) [17]. In other words, the Equation (9.26) is solved for chamber wall temperature T to obtain Equation (9.27) without $\dot{q}_{rad,in}$, $\dot{q}_{conv,out}$ and $\dot{q}_{rad,out}$.

$$T(t) = (T(0) - T_c(t))e^{-\frac{h_{in}A_1}{mc_m}t} + T_c(t) \tag{9.27}$$

In Equation (9.27), the $T(0)$ refers to initial temperature of the chamber wall whereas T_c is the flame temperature or combustion chamber temperature [17]. Lastly, A_1 is the surface area of the chamber wall that receives the heat flux. Refer to Figure 9.7 for clarity.

When incorporating all the modes of heat transfer and solving Equation (9.26) for thrust chamber wall temperature, an iterative scheme (see Equation (9.28)) was derived. Note that $\dot{q}$ is heat flux whereas q is the heat transferred. The surface areas A_1 and A_2 are indicated in Figure 9.7.

$$T^{i+1} = T^i + \frac{(q_{conv,in}A_1 + q_{rad,in}A_1 - q_{conv,out}A_2 - q_{rad,out}A_2)dt}{c_m m} \tag{9.28}$$

This simple heat sink model fails to estimate the temperature distribution over the thickness of the wall. As the rise in temperature of the inner wall would be higher than that of the outer wall, the temperature distribution over the thickness must be computed. However, the analytical solution or a simple heat sink model can be used as an first estimate and in the verification process of the numerical solution.

9.7.7. NUMERICAL SOLUTION

The followings assumptions have been made for the numerical model.

1. Constant conductivity of the thrust chamber wall material over the temperature is assumed. From [85], the conductivity of the commonly used steel (e.g S355) ranges from approximately 14 to 60 $Wm^{-1}K^{-1}$ at room temperature. For metals conductivity typically increases with temperature. The lower the value of conductivity, the higher temperature the inner wall experiences. Therefore, the lowest value at room temperature for conductivity will be assumed. To conclude, the assumption will produce results that are conservative.

2. The specific heat at room temperature has been used for computation. For X5CRNI18-10 steel, the variation of c_m was observed to be approximately 14% [85]. A sensitivity study in Section 9.7.9 shows that the temperature is insensitive to c_m (variations within 1%). Thus, the assumption can be deemed reasonable. For the results of the sensitivity, see Section 9.7.9.

3. Heat sink over an element (mesh) is assumed. Upon appropriate refinement of the mesh, the discrepancies due to this assumption is expected to become negligible.

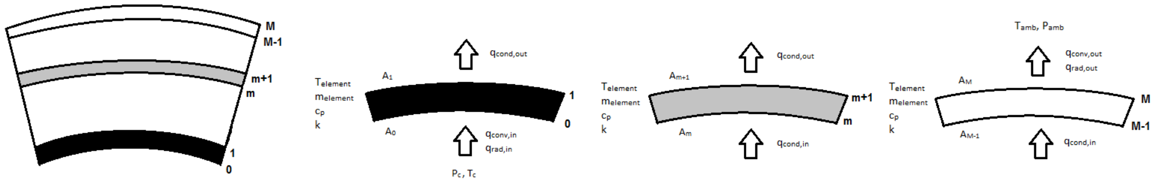

Figure 9.8: Overview of energy fluxes through the thickness of the cross-section

MODELING BY FINITE DIFFERENCE

The nature of the problem is the transient conduction heat equation (Equation (9.29)) between the thrust chamber walls with the boundary conditions of heat flux by convection and radiation, this is visualized in Figure 9.8. Note that the radius r equals $\sqrt{x^2+z^2}$ as the analysis of the finite difference will be restricted to one dimension.

$$mc_m \frac{\partial T(r,t)}{\partial t} = \kappa \frac{\partial^2 T(r,t)}{\partial r^2} \tag{9.29}$$

At the boundaries of the thrust chamber wall, the change in temperature is governed by the heat flux due to the convection and the radiation. At the initial boundary (r=0), the increase in temperature is governed by the convection and radiation from the heat source or combustion (see Equation (9.30).

$$mc_m \frac{\partial T(0,t)}{\partial t} = \dot{q}_{rad,in} + h_{in} A_0 (T_c - T(0,t)) + \kappa A_1 \frac{\partial T(r,t)}{\partial r} \tag{9.30}$$

At the final boundary (r=M, see Figure 9.8), the heat transfer from the thrust chamber wall to the outside flow is governed by the radiation out and convection due to the high speed external flow. (see Equation (9.31)).

$$mc_m \frac{\partial T(L,t)}{\partial t} = \dot{q}_{rad,out} + h_{out} A_M (T(L,t) - T_{amb}) + \kappa A_{M-1} \frac{\partial T(r,t)}{\partial r} \tag{9.31}$$

The temperature distribution over the thickness of the thrust wall can be computationally modeled through discretisation of Equation (9.29), Equation (9.30) and Equation (9.31) by the method of finite difference.

DISCRETIZATION OF THE 1D HEAT EQUATION

The numerical solution of the transient conduction heat equation (Equation (9.29)) requires discretisation in both time and space. At the initial boundary (r=0, see Figure 9.8), the change in temperature of the first element can be approximated by the computing the discretisation of Equation (9.30), yielding Equation (9.32). Note that for Equation (9.32), Equation (9.34), and Equation (9.36) the superscript index i refers to the time while the subscript index m (which ranges from 0 to M as shown in Figure 9.8) refers to the index of the spatial mesh.

$$\rho \Delta V_{element} c_m \frac{T_0^{i+1} - T_0^i}{\Delta t} = q_{rad,in} A_0 + h_{in} A_0 (T_\infty - T_0^i) + \kappa A_1 \frac{T_1^i - T_o^i}{\Delta r} \tag{9.32}$$

$$=> T_o^{i+1} = T_o^i + \frac{\Delta t}{\rho V_{element} c_m} (q_{rad,in} A_0 + h_{in} A_0 (T_\infty - T_o^i) + \kappa A_1 \frac{T_1^i - T_o^i}{\Delta r}) \tag{9.33}$$

The mode of the heat transfer inside the wall of the thrust chamber is conduction. The discretized form of the heat equation (Equation (9.29)) is shown in Equation (9.34).

$$\rho V_{element} c_m \frac{T_m^{i+1} - T_m^i}{\Delta t} = \kappa A_{m-1} \frac{T_{m-1}^i - T_m^i}{\Delta r} + \kappa A_m \frac{T_{m+1}^i - T_m^i}{\Delta r} \tag{9.34}$$

$$=> T_m^{i+1} = \frac{\Delta t}{\rho V_{element} c_m} (\kappa A_{m-1} \frac{T_{m-1}^i - T_m^i}{\Delta r} + \kappa A_m \frac{T_{m+1}^i - T_m^i}{\Delta r}) + T_m^i \tag{9.35}$$

The modes of heat transfer from the thrust chamber wall to the ambient condition of the wind tunnel are radiation and convection. Convection is the most dominant due to the fast moving flow outside the chamber wall. At the last boundary (r=L, see Figure 9.8), the change in temperature of the last element M can be computed by discretising the Equation (9.36).

$$\rho V_{element} c_m \frac{T_M^{i+1} - T_M^i}{\Delta t} = -q_{rad,out} A_M - h_{out} A_M (T_M^i - T_{amb}) + \kappa A_{M-1} \frac{T_{M-1}^i - T_M^i}{\Delta r} \tag{9.36}$$

$$=> T_M^{i+1} = T_M^i + \frac{\Delta t}{\rho V_{element} c_m} (-q_{rad,out} A_M - h_{out} (T_M^i - T_{amb}) + \kappa A_{M-1} \frac{T_{M-1}^i - T_M^i}{\Delta r}) \tag{9.37}$$

An explicit method was used to obtain the numerical solutions. As the explicit method does not guarantee unconditional stability, the largest value of Δt is limited.

9.7.8. STABILITY

The stability of the explicit numerical method is not guaranteed. Thus, to ensure stability of the finite difference method the stability criteria in Equation (9.38) was used. Its derivation can be found in [86].

$$\Delta t = \frac{\Delta x^2}{2\alpha \left(1 + h \frac{\Delta x}{\kappa}\right)} \tag{9.38}$$

Here α is given by the material properties as $\frac{\kappa}{\rho c_m}$. This allows to calculate a time step for a given step size in space, ensuring a converging solution.

The stability criterion has been derived assuming a flat plate [86]. However, upon refinement of spatial meshes, the curvature of areas in contact between the meshes become small enough to be assumed a flat plate. Therefore, the stability criteria in Equation (9.38) has been used to obtain a converging solution.

9.7.9. SENSITIVITY ANALYSIS

Due to uncertainties of combustion stability (fluctuations in pressure) and changes in the specific heat constant at constant pressure over temperature, a sensitivity study for pressure and specific heat c_p has been performed.

According to [85], an increase in c_m by 14 percent was observed when the temperature is increased by 700 K for steel. However, it is unknown if all the analyzed materials show this behavior. Therefore a sensitivity study is done, since a smaller value of c_m would result in a higher inner wall temperature. A decrease in c_m by 20 percent has been compared with the c_m at room temperature to investigate the sensitivity of c_m.

Table 9.4: Sensitivity study of c_m on maximum temperature of combustion chamber with carbon deposits included

	At room temperature c_m	20 % decrease in c_m
Inner wall T_{max}	517.27 K	518.9 K
Outer wall T_{max}	420.31 K	466.3 K

The 20 percent change in c_m resulted in a 3 percent change in maximum temperature of both inner and outer wall as shown in the Table 9.4. Hence, it can be concluded that the results are not sensitive to c_m of the thrust chamber wall material.

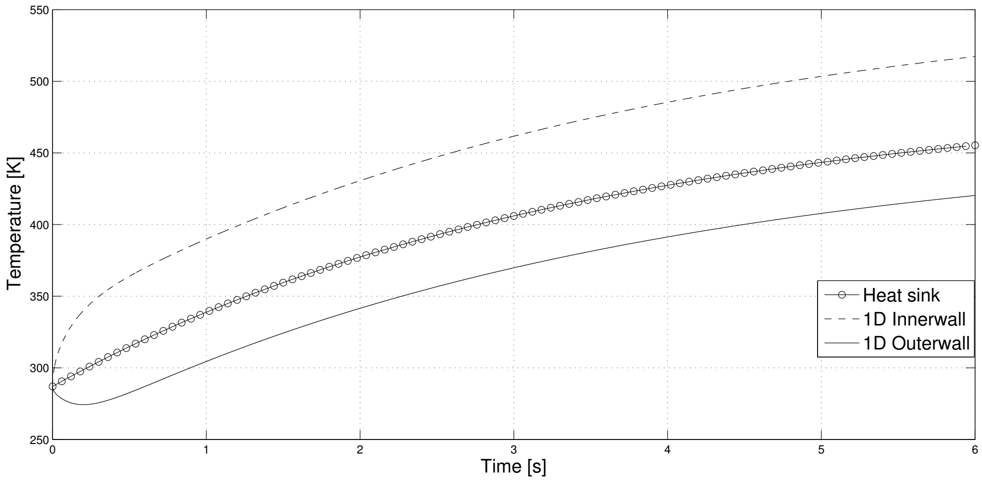

Figure 9.9: Inner and outer wall temperature of finite difference model and heat sink temperature

[30] asserts that the combustion instability of a liquid engine could result in fluctuations of combustion chamber pressure from at least 5 percent to often more than 30 percent. For the sensitivity study, the pressure of the combustion chamber was increased by 33 percent (from 30 to 40 bar) based on the assumption that the pressure fluctuation of more than 33 percent would be deemed as failure of the system.

Table 9.5: Sensitivity study of combustion chamber pressure on maximum temperature and von Mises stress with carbon deposits included

Combustion chamber pressure P_c	30 bar	40 bar
Inner wall T_{max}	517.27 K	518.9 K
Outer wall T_{max}	420.00 K	421.48 K
Von Mises Y	54.67 MPa	72.9 MPa

With a combustion chamber wall thickness of 2.5 mm, the sensitivity study on P_c has shown that the maximum temperature is relatively not sensitive to pressure (see Table 9.5). However, an increase in pressure by 30 percent resulted in approximately 33 percent increase in von Mises yield stress. Therefore, the pressure fluctuations due to combustion instability must be investigated further.

9.7.10. VERIFICATION

To ensure confidence in the finite difference model a verification was conducted. Several steps were taken in the verification. First the code was verified by checking the intermediate outputs. If the numbers were in typical ranges and were agreed by with hand calculations, the results were accepted. Secondly, the inner and outer wall temperature over time were plotted, see Figure 9.9. This graph was made to check whether the results show the expected behavior. It can be seen in the graph that the inner wall gets hotter than the outer wall. This was expected, because due to the finite conduction coefficient the material is not able to distribute all the energy it receives equally. Furthermore, a delay effect of the heating of the outer wall can be seen.

The solution of the heat sink model is also plotted in Figure 9.9. The result of the heat sink model is in between the results of the inner and outer wall calculated with the finite difference model. This is as one would expect since the same amount of energy is distributed unevenly over the thickness, with relatively more energy at the inner wall and less at the outer wall.

An additional check was performed on the convection coefficient calculated with the Bartz method to ensure that the equation was implemented correctly. This additional check was done to perform a proper system test on the software by comparing with an example case from RPA. RPA provides several example engines, of which the SSME 40K engine was chosen. To be able to compare the coefficients, the cooling of this engine

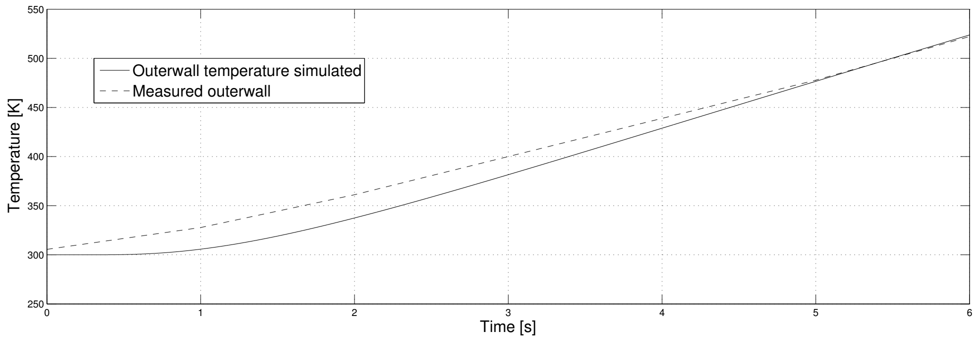

Figure 9.10: Validation measurement data and simulated results

was disabled, since the self developed software is not able to incorporate active cooling. A value of 18000 W/(m^2-K) was found from RPA, the calculated value with the self developed model was 17500 W/(m^2-K). The difference between the two models is small and can be explained by the factor at the beginning of the Bartz equation. For the model a value of 0.026 was used, typically numbers between 0.023-0.028 are used. Therefore, it is expected that RPA uses a different value and it is concluded that the convection coefficient is calculated correctly.

The finite difference model is considered to be verified since the intermediate outputs were found to be correct, ensuring correct coding of the different blocks. The behavior of the results is as one would expect from the physical phenomena and the result from the heat sink model also confirms the results of the finite difference model.

9.7.11. VALIDATION

To guarantee that the model is applicable to simulate HotFire a validation was conducted. The validation must ensure that the right equations were used to resemble the physical phenomena. For validation, the results of measurements conducted during a test are compared by those obtained by the finite difference model.

Robert Watzlavick built an uncooled kerosene-liquid oxygen rocket motor with similar dimensions as HotFire. A six second static test was conducted, in which the outer wall temperature were measured. For the simulation $h_{out} = 0$, since there is no forced convection in a static test. The measured results and the simulated results with the finite difference model are compared in Figure 9.10. It is not possible to validate the convection coefficient for energy going out at the outer wall.

Figure 9.10 shows that the simulation initially underestimates the temperature and then obtains a larger slope giving almost the same temperature at 6 seconds. It is known that in the test there was a slight hick-up in the beginning with the oxygen valve not creating the combustion from t=0. Therefore, the measurement results were started after some time where the walls were already heated up. This explains the underestimating of the temperature at the beginning. The slope of the simulation is higher. This causes the model to overestimate the temperature over time. However, the difference in slope is small, if the temperature of the simulation is forced to match the measurement data at t=1, then the difference at t=6 is approximately 20K. The results of the finite difference model are considered to be a close match with the measurement data. The model is conservative due to the larger slope. It is not possible from this single test to determine which part of the model causes the difference in results.

The discrepancies between the experimental data and the computational model can be explained by the use of assumptions to simplify the numerical model. To be specific, the assumptions of a constant conductivity, constant specific heats, steady state combustion and neglecting the instability of the combustion could result in small discrepancies.

For the validation case the carbon deposit layer was simulated as it was present from t=0. In real life this layer will need some time to build up. The current model is such a close match that it is expected that the layer builds up within the first second. However, from this single comparison it cannot be concluded that it is indeed reasonable to assume that this actually happens, since it could also be caused by a overestimated convection and radiation energy flux or one of the model assumptions.

The finite difference model can be considered validated for convection from the combustion gasses to the combustion chamber wall, for the radiation going in at the combustion chamber inner wall, and for the radiation going out at the combustion chamber outer wall. Since the slope was larger it will overestimate the temperature and therefore it is safe to use the results for the design of HotFire. It can not be concluded how fast the carbon deposit layer is built up over time. Therefore, HotFire will be designed without modelling this layer.

The model cannot be considered validated at the nozzle. There was no data set available to compare the model results with experimental results. From [84] it was concluded that the Bartz method deviates and overestimates the convection coefficient at the nozzle. The model is therefore considered safe to use for the design since convection energy flux is most dominant.

9.7.12. THERMAL EXPANSION

The material which is heated will try to expand. This expansion will influence the area ratio of the divergent part of the nozzle. To keep the exit conditions as close as possible to the desired conditions, the expansions should be as limited as possible.

The expansion of the material is dependent of the thermal expansion coefficient α of the material, the original length of the material L and the temperature difference. It can be calculated with Equation (9.39).

$$dL = \alpha L(T_2 - T_1) \tag{9.39}$$

To calculate the thermal expansion of HotFire the worst case scenario is used. This assumes that the entire structure is heated to the maximum experienced temperature and that all expansion is in one direction to the middle of the cross section. The whole nozzle will be made out of graphite (see Section 9.10). In Chapter 4 an area ratio of 2.77 was determined. For graphite the new area ratio was calculated to be 2.79. In Chapter 4 the influence of this change is determined.

9.8. STRUCTURAL ANALYSIS

For the preliminary design of the combustion chamber and nozzle, an estimation on the stresses is needed to ensure that the structure will not fail under the pressure loads. For the stress calculations, a thick walled pressurized cylinder is assumed with closed end caps. This is a conservative calculation since in real life the combustion chamber and nozzle do not have end caps on both sides, which will give lower longitudinal stresses.

In Equation (9.40), Equation (9.41) and Equation (9.42) [87] the equations are given to calculate the radial, tangential and longitudinal stresses. These depend on the geometry of the cylinder, location in the wall and the pressure in and outside the pressure vessel. For the calculations the outer pressure is assumed to be zero. This will make the calculations conservative since in real life there is an ambient pressure. From the equations it can be seen that the maximum stress is experienced at the inner wall.

$$\sigma_r = \frac{r_{inn}^2 P_{inn} - r_{out}^2 P_{out}}{r_{out}^2 - r_{inn}^2} - \frac{(P_{inn} - P_{out}) r_{inn}^2 r_{out}^2}{(r_{out}^2 - r_{inn}^2) r_{\text{local}}^2} \tag{9.40}$$

$$\sigma_{\text{circ}} = \frac{r_{inn}^2 P_{inn} - r_{out}^2 P_{out}}{r_{out}^2 - r_{inn}^2} + \frac{(P_{inn} - P_{out}) r_{inn}^2 r_{out}^2}{(r_{out}^2 - r_{inn}^2) r_{\text{local}}^2} \tag{9.41}$$

$$\sigma_l = \frac{r_{inn}^2 P_{inn} - r_{out}^2 P_{out}}{r_{out}^2 - r_{inn}^2} \tag{9.42}$$

To relate the stresses to the yield stress of a material, the von Mises yield criterion is used. Using Equation (9.43) the von Mises stress Y can be calculated which should be lower than the yield stress of the material to ensure that the structure does not fail. For the calculations of the von Mises stresses a safety factor of 2 will be used as instructed by the wind tunnel technician [25].

$$Y = \sqrt{\frac{1}{2} \cdot ((\sigma_{\text{circ}} - \sigma_r)^2 + (\sigma_{\text{circ}} - \sigma_l)^2 + +(\sigma_r - \sigma_l)^2)} \tag{9.43}$$

9.9. DESIGN TOOL

The material, thermal, and structural analyses of the combustion chamber and nozzle are combined to determine the design of the combustion chamber and nozzle.

The block "Select material" of the flow chart (Figure 9.11) initializes properties of a specific material. These properties include the material yield stress, conductivity, specific heat constant c_m, and density. All these properties of a material are an input to the thermal and structural analysis parts of the program. For the list of materials considered, refer to Section 9.6.

The purpose of the block "Set thickness" is to find and optimize the thickness of the thrust chamber wall. When a particular thickness fails either thermally or structurally, the thickness is increased by this block.

The block "Thermal analysis to determine maximum temperature" uses the thermal analysis method from Section 9.7 to determine the local maximum temperature the wall will experience in its operational time. The inputs are thickness and material properties, whereas the outputs are the temperature distribution over the thrust chamber.

The "Adjust temperature dependent material properties" function computes the yield stress of the material at the maximum temperature. The yield stress has been found at several temperatures and the theory of polynomial regression was used to interpolate or extrapolate over the ranges of temperature.

The structural analysis of the thrust chamber wall (see Section 9.8) is incorporated in the block "Compute the maximum von Mises stress". Note that the a safety factor of 2 has been applied to the von Mises stress according to the safety criterion [25]. The inputs of the block includes chamber geometry and gas conditions such as the pressure differences between inside and outside of the thrust chamber. The 'Minimum thickness' block stores the minimum thickness.

There exists three iteration loops in the sizing tool. The "Tmax >Tset" decision block ensures that the maximum temperature the thrust chamber wall would reach in its operation would be smaller than the maximum allowed temperature (Tset) of the material. The "von Mises Y > σ yield" decision block ensures that the thickness chosen will not fail structurally. Finally, the "Optimized with respect to materials" block iterates over different materials.

9.10. RESULTS DESIGN TOOL

The results of the full iteration are shown in Table 9.6. The iteration used a thickness vector from 1 mm to 2.5 mm, with steps of 0.5 mm.

It can be concluded that for the combustion chamber steel is the most suitable option. It allows to take a thickness under 2.5mm and is cheaper than titanium. Aluminium is not a suitable option because of its limited capability to withstand a static test, see Section 9.10.1. A final thickness of 2.5mm steel is selected instead of the 1mm needed (see Table 9.6). The 2.5mm is selected since it is the maximum thickness which can be used while still meeting the blockage and length requirement. The 2.5mm thickness is more conservative and allows for a longer test time. In Figure 9.12 the inner and outer wall temperature are plotted over 20 seconds. It shows that the structure will reach steady state after approximately 16 seconds. In steady state the inner wall temperature is about 560K, which will allow for continuous testing.

For the nozzle graphite is the most suitable material. The main reasons are the large uncertainty in temperature at the divergence part of the nozzle, that it is the only material able to withstand the temperatures in the

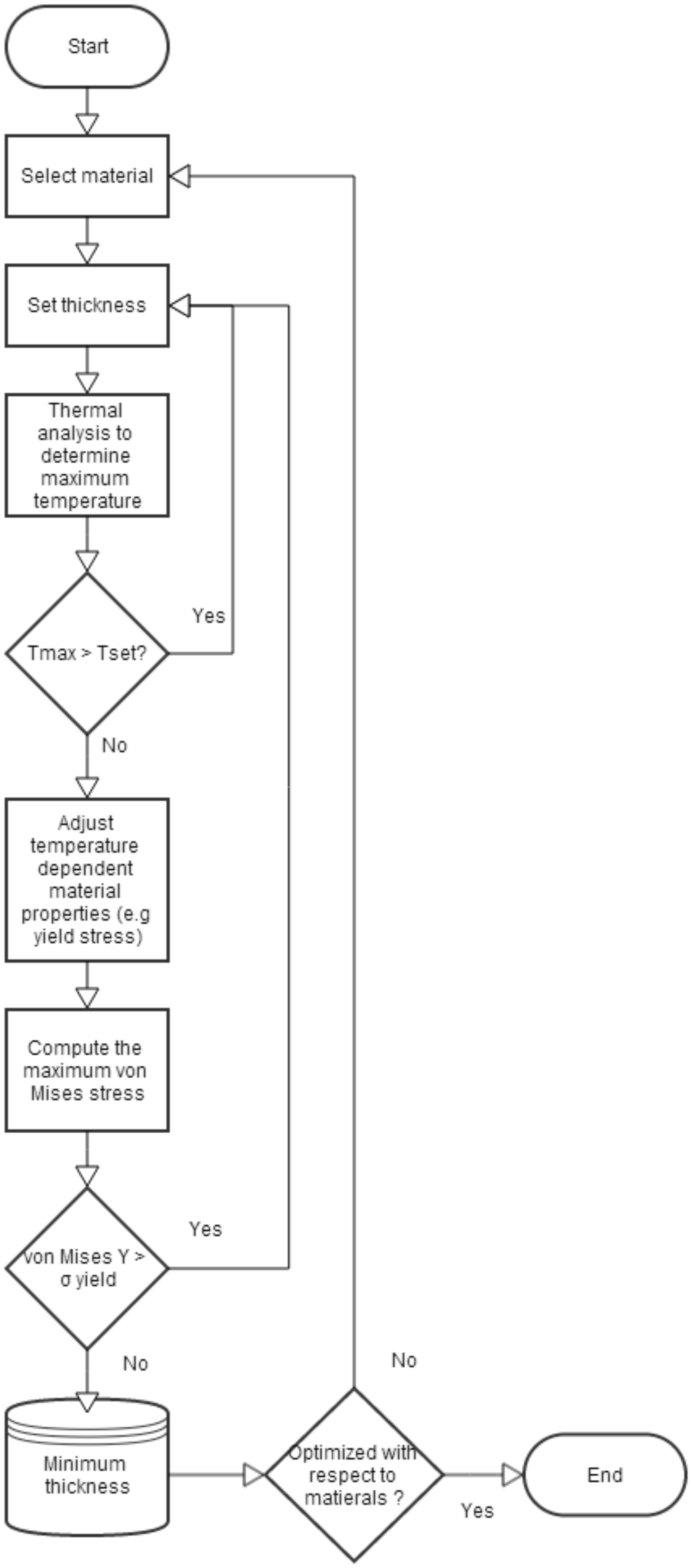

Figure 9.11: Flow chart of the thrust chamber sizing tool

throat, and the low stresses at the nozzle due to the large local thickness. It is unknown what the temperature and velocity are experienced in the base region. This makes it impossible to predict the convection energy

Table 9.6: Results of full iteration

	Steel	Titanium	Aluminium	Graphite
Combustion chamber				
Minimum thickness [mm]	1.0	1.0	1.0	2.5
Inner wall temperature [K]	529.3	554.8	503.4	494.0
Outer wall temperature [K]	486.4	481.3	499.2	481.3
Von Mises [MPa]	124.7	124.7	124.7	54.6
Limiting	Not Limited	Not Limited	Not Limited	Struc-impos
Throat				
Minimum thickness [mm]	2.5	2.5	2.5	1.0
Inner wall temperature [K]	1109.2	1221.1	687.5	812.0
Outer wall temperature [K]	229.1	212.3	412.1	522.9
Von Mises [MPa]	5.84	5.84	5.84	5.87
limiting	Therm-impos	Therm-impos	Therm-impos	Not Limited
Exit				
Minimum thickness [mm]	1.0	1.0	2.5	1.0
Inner wall temperature [K]	872.3	879.7	812.5	881.5
Outer wall temperature [K]	869.2	875.4	810.6	881.3
Von Mises [MPa]	2.91	2.91	1.42	2.91
Limiting	Not Limited	Not Limited	Therm-impos	Not Limited

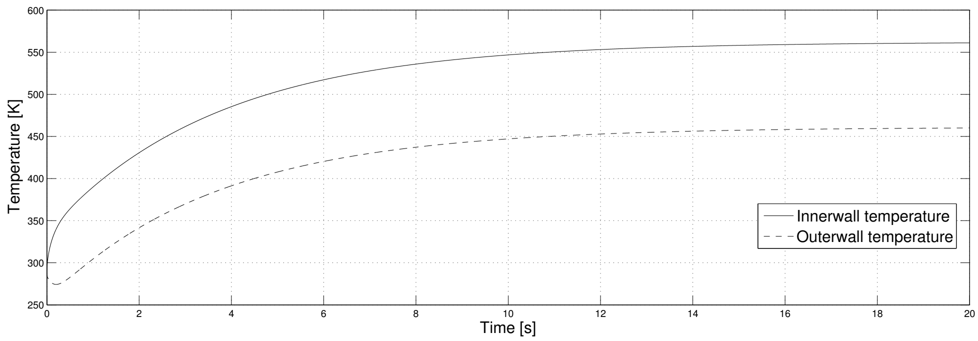

Figure 9.12: Inner wall temperature over 20 seconds

flux in this region. Furthermore graphite allows to take a larger convergence angle. A larger convergence angle will increase the energy flux, but the total temperature is lower than the operating temperature of graphite (see Section 9.6). The low thermal expansion coefficient of graphite will make it possible to keep the area ratio almost constant, from 2.77 to 2.79.

The total material cost of the combustion chamber and nozzle will be 367 euros. This is build up out of one minimum dimension steel (97 euros) and graphite (270 euros) bar.

9.10.1. DISCUSSION OF THERMAL RESULTS

Figure 9.13 shows the temperature over time without modelling the carbon deposit. Figure 9.14 shows the temperature over time with the carbon deposit modelled as it was created instantaneously at t=0. It is expected that the results where the carbon deposit is modelled better represent the physical phenomena due to the close match with the validation data. This mainly affects the expected temperature for the throat section.

Figure 9.15 shows the different energy fluxes of the final HotFire design in the combustion chamber. It is clear that the convection by the combustion gasses is most dominant for the heating. Radiation going in the inner wall is approximately 8.9% of the total ingoing energy flux, which is higher than expected. This can be explained by the fact that HotFire operates at a low pressure which decreases the influence of convection compared to the radiation. The outgoing radiation is almost negligible due to the low outer wall temperatures.

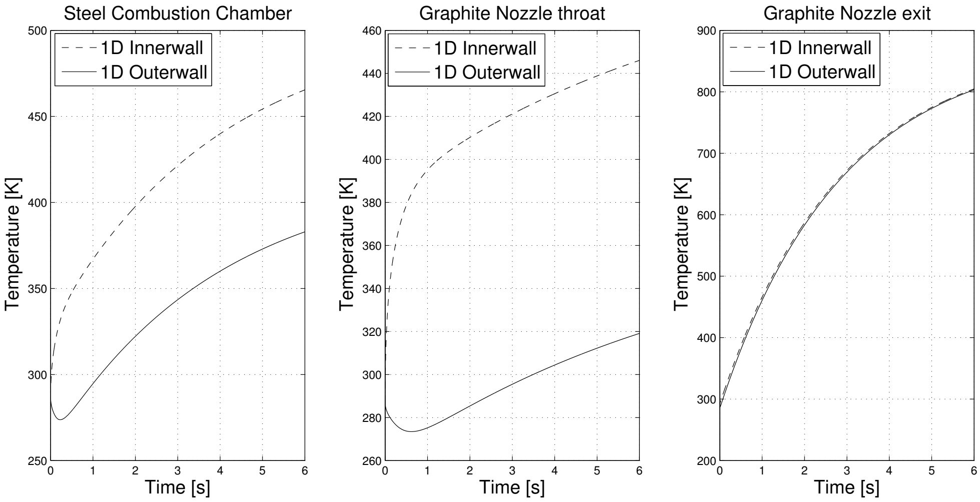

Figure 9.13: Inner and outer wall temperature with carbon deposit

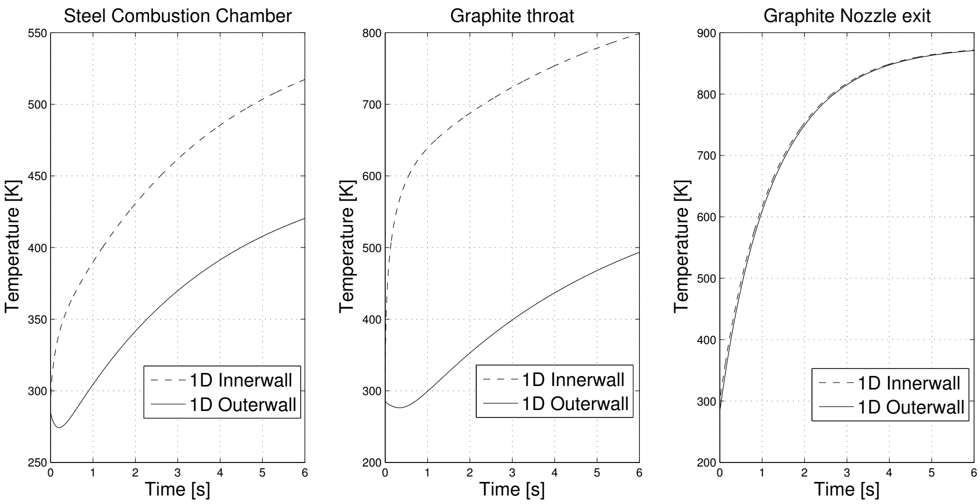

Figure 9.14: Inner and outer wall temperature without carbon deposit

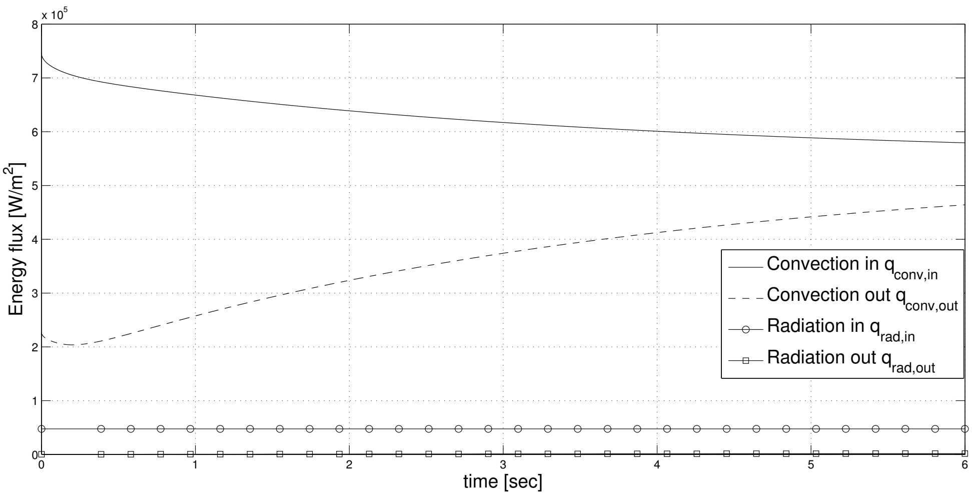

Figure 9.15: Energy fluxes over time without carbon deposit

The convection going out is significant due to the high mass flow of the ambient flow.

Before testing in the actual TST-27 wind tunnel it is necessary to perform a static test outside the wind tunnel to prove the safety of the system [25]. A finite difference simulation was performed, where the convection going out was forced to zero to simulate a static test. This is a conservative assumptions, since in real life there will be free convection. Figure 9.16 shows that the combustion chamber will heat up to 1050 K over 10 seconds, allowing for a 8.6 seconds static test with HotFire outside the wind tunnel. At 8.6 seconds the maximum temperature reaches 1000K, which is the maximum recommended operating temperature of steel S355. The combustion chamber is thermally limited for the static test, since the experienced stress is 54 MPa which is lower than the 60 MPa yield stress at a 1000K. The temperatures of the nozzle were not simulated for a static test since the graphite nozzle will be able to withstand the total temperature. From Figure 9.16 it can also be concluded that aluminium is not a suitable material for the combustion chamber. It heats up above its recommended operational temperature of 573K in 2 seconds due to its limited heat sink capacity.

9.10.2. FINAL COMBUSTION CHAMBER AND NOZZLE DESIGN

Appendix A shows the final design of HotFire with the combustion chamber and nozzle with its dimensions. Table 9.7 summarizes the final dimensions and thicknesses of the combustion chamber and nozzle. During integration with the other subsystem some changes were made to the dimensions. An additional 1cm was added to the length of the nozzle convergent region to provide space for bolts and make a detachable ring. The thickness of combustion chamber was increased to 3mm to provide space for the countersunk head of the bolts. During detailed design these dimensions can be optimized so that the combustion chamber thickness is only locally applied to conserve the combustion chamber volume. Due to the brittleness of graphite a thickness of 2.5mm was given to the nozzle exit. However, this thickness is not yet incorporated in the technical drawings in Appendix A. No material was yet selected for the cold plume nozzle. The cold plume nozzle is not exposed to heating, therefore the left over steel from the combustion chamber could be used.

The base plate is made out of steel S355, although the heating of this base plate cannot be calculated exactly. The exhaust gases coming from the nozzle exit are below 900K. The maximum operating temperature for steel S355 is set to 1000K, therefore no failure regarding the thermal loads is expected.

9.11. RECOMMENDATIONS

It is possible to improve the analysis and thereby improve the design of HotFire. There are several recommendations concerning the different analyses.

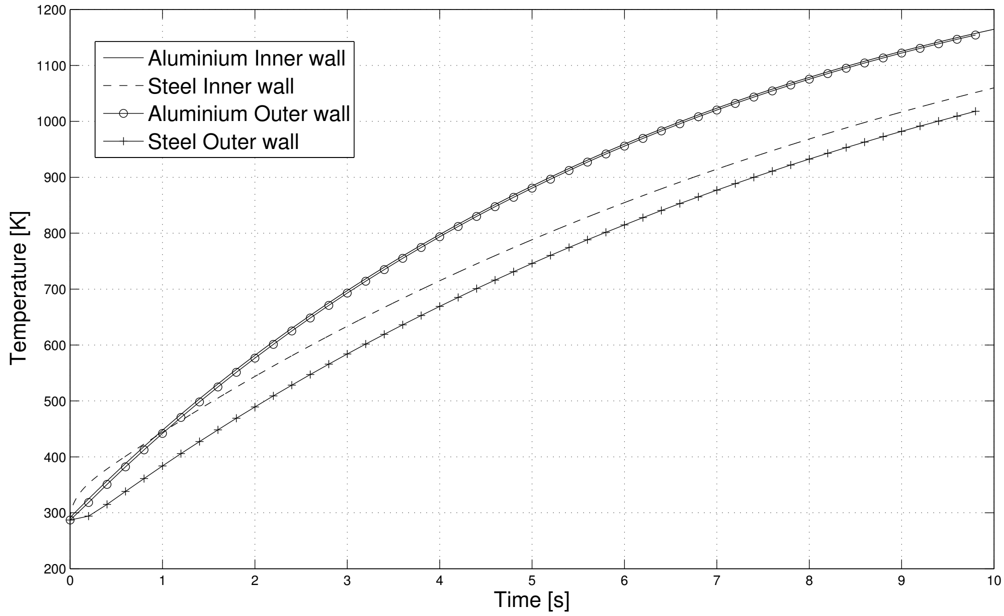

Figure 9.16: Simulated temperature results of the combustion chamber for a static test

Table 9.7: Final dimensions of the combustion chamber and nozzle

	Hot plume	Cold plume
Chamber wall material	Steel S355	Steel S355
Chamber inner length [mm]	50.1	50.1
Chamber inner diameter [mm]	45	45
Chamber outer diameter [mm]	50	50
Chamber thickness [mm]	2.5	2.5
Nozzle material	graphite	t.b.d.
Nozzle exit thickness [mm]	2.5	2.5
Half convergence angle [deg]	60	60
Length of convergent part [mm]	10.4	10.4
Length of divergent part [mm]	8.9	5.2
Length of throat part [mm]	3.6	3.6
Throat diameter [mm]	9.0	12.0
Radius of curvature of throat [mm]	4.5	4.5
Plume exit diameter [mm]	15	15
Initial divergence angle [deg]	45	45
Lip angle [deg]	7.0	10

First of all it is recommended to validate the characteristic length of kerosene and gaseous oxygen. The value of characteristic length is mainly sensitive to pressure, O/F ratio and mixing properties. It is unknown how and to what extend these factors influence the characteristic length. For this reason, the upper value of characteristic length was chosen. The characteristic length can be validated by taking a large volume combustion chamber with the pressure, O/F ratio and mixing properties of HotFire and decreasing its volume until a drop in characteristic velocity is measured, which indicates a drop in performance.

Due to the limited time, only four materials were found with enough data to analyze their possible use in HotFire. It is recommended to gather more data from literature and experiments on different materials for a better decision.

HotFire operates under a relatively low temperature and pressure. The validation experiment showed that the model holds for lower combustion pressures, but the influence of the lower combustion temperature is unknown. It is recommended to perform experiments under the HotFire conditions with a highly overdesigned combustion chamber measuring the temperatures at different outer wall locations to validate the Bartz and Shack method for the lower temperature. Furthermore, it is recommended to implement a temperature dependent conductivity coefficient and specific heat of the material. This should ensure better representation of the physical phenomena in the model.

Currently, a conservative method for calculating the stresses in the combustion chamber and nozzle is used by assuming a closed pressurized thick walled cylinder. It is recommended to perform more analysis on the stresses and stress concentrations. This can be done with commercially available software.

The preliminary design did not take into account the exact method for attachment and full integration with all HotFire subsystems. Therefore, it is recommended to do a detailed analysis on the manufacturing and integration within HotFire, for example the amount of bolts needed and locally increased thickness needed for these bolts.

The model assumes that a steady state combustion is achieved in less than one second. It is unknown how fast the steady state is achieved and to what extent fluctuations will occur. Experiments are needed to determine the time it takes to reach a steady state combustion and the development of the combustion conditions in this phase for proper modelling. Furthermore, the fluctuating properties influencing the energy flux need to be determined to model a worst case of the heat transfer.

It is recommended to use the method of characteristics to define a more efficient nozzle geometry for the divergent part [17].

10

INSTRUMENTATION

The instrumentation of an experiment is at least as important as the experiment itself. The general purpose of HotFire is to produce a plume and also measure the conditions of the base region of that plume. In order to do those measurements, certain systems and measurement devices are necessary. A proper design of the measurement and instrumentation system is of essential importance, as the quality of the outcome of the experiment is defined by the quality of the measurement data.

In this chapter the different possible instrumentation systems are presented and discussed, and the integration into the HotFire system is presented. After discussing the different sensor types, the selection of the sensors is presented followed by the integration in the system. In the last part some recommendations for the instrumentation system are given.

10.1. REQUIREMENTS ON THE INSTRUMENTATION

Different requirements for the overall system have been developed during the HotFire project. Those relevant for instrumentation `HF-TEC-MEA-01` until `HF-TEC-MEA-07`, `HF-CON-COS-03` and `HF-CON-COS-04`. Only a few of them directly related to the measurement system, as for example `HF-TEC-MEA-01` "The plume diameter shall be at least 2 cm" puts a requirement on the plume itself and not on the measurement system. Requirements that are obeyed by the measurement system itself are shown here:

`HF-TEC-MEA-04` The system shall allow for non-visual temperature measurements.

`HF-TEC-MEA-05` The system shall allow for non-visual pressure measurements.

`HF-TEC-MEA-07` The system shall allow for measurements of plume conditions.

`HF-CON-COS-03` The costs of additional modifications to the wind tunnel shall be low.

`HF-CON-COS-04` The overall integrity of the wind tunnel shall not be compromised by modifications.

These five requirements have to be fulfilled by the selection of different sensors. The presentation of possible sensor types is discussed in the next section. In order to fulfill requirements `HF-TEC-MEA-03` and `HF-TEC-MEA-04` only non-visual measurement equipment is considered.

10.2. MEASUREMENT EQUIPMENT

In order to measure pressure, temperature and plume characteristics, HotFire requires four different sensor types, namely pressure sensors, temperature sensors, flow visualization instrumentation, and mass flow sensors. The four different measurement fields are discussed in detail in the subsections hereafter. In order to determine and measure the plume dimensions, visual measurement as well as chamber condition measurements are considered. When the chamber conditions are known, the plume conditions can be calculated.

10.2.1. PRESSURE SENSOR TYPES

Pressure data from the base region of the model has proven to be important for the design of future launchers. In order to get this data, a sensor or another kind of measurement device needs to be installed at the base plate. In a pressure sensor, the pressure of a medium can be measured using a membrane between this medium and a reference medium where the pressure is known. Using a strain gauge, attached to the membrane, one can measure the deflection and can relate this deflection to a certain pressure. There are also other methods measuring the pressure involving capacitive or optical methods.

Generally, pressure measurements can be taken with respect to different zero references; absolute pressure is zero-referenced against perfect vacuum, gauge pressure is referenced against ambient air pressure, differential pressure is the difference in pressure between two points [88]. From the material of the membrane one can determine the pressure range of the sensor. An important point for the pressure measurement is furthermore the measurement of unsteady pressures. These are expected to occur in the base region, as the base region has an unsteady flow field. Due to the size of the model and the temperature at the base plate, it is not possible to locate the sensor directly here; tubes need to connect the base region with the sensor.

A connection between sensor and the base region will make measurements possible. [89] confirms that measurements through a connection tube are possible at low frequencies. However, fluctuations of around $f = 10$ kHz are expected to occur. Therefore, an accurate fluctuation measurement will not be possible without a sensor directly on the base plate.

10.2.2. TEMPERATURE SENSORS

A temperature sensor measures the temperature of a specific point. In many cases thermocouples are used to serve this purpose, as they are easy to install and they provide a high accuracy. A thermocouple consists of two different wires whose ends are connected to the piece where the temperature should be measured. The other ends of the wires are connected to a cold reference piece. Due to the fact that there is a temperature gradient between the measurement piece and the reference piece a voltage is created in the two wires. As the two wires consist of different materials, the voltage differs between them, which can be used to determine the temperature of the measurement piece.

Different types of thermocouples are available; the most commonly used ones are type J ranging from 0 to 750 °C , K ranging from -200 to 1250 °C , E ranging from -200 to 900 °C , and T ranging from -250 to 350 °C [90]. Thermocouples that go up to higher temperatures (2000 °C) experience rapid deterioration under oxidizing conditions, so should not be used in air. For safety, thermal cameras can be used to determine the chamber wall temperature. The thermal cameras will not be used for the base temperature measurement, as non-visual methods are set as requirement, only for indication when the chamber is getting too hot and the engine has to be turned off.

10.2.3. FLOW VISUALIZATION MEASUREMENTS

To perform flow measurements and to visualize the flow, many techniques have been developed. These can mainly be split up into qualitative and quantitative measurements. A popular qualitative measurement technique in Aerospace Engineering is that of shadowgraphy. It is used to visualize shock waves, which cannot be observed with the naked eye. The most-used method is Schlieren photography (SP), which takes advantage of the change in refractive index across shock waves, caused by the gradient flow density across the shock wave. A number of quantitative flow measurement techniques exist that have been developed over the past decades. Commonly used quantitative flow field measurements systems is given below are: Hot-Wire Anemometry (HWA), Laser-Induced Fluorescence (LIF), Laser Doppler Velocimetry (LDV) and Particle Image Velocimetry (PIV) as described in [59, 91].

10.2.4. MASS FLOW MEASUREMENTS

In order to measure the achieved O/F ratio, the mass flow of both oxidizer and fuel has to be measured. The two different options to do this are to include a load cell to measure the weight of the tanks throughout the measurement, or to include mass flow meters to the feed system. From the weight the mass can be calculated using $F = ma$ [92]. In this case the apple is the tank.

10.3. EQUIPMENT SELECTION

For the HotFire system, limited space is available for the installation of different sensors. Therefore, a differential pressure sensor, which measures the pressure different between two points, is disregarded for space reasons. All other measurement sensors are considered feasible for the size requirement. The pressure in the base region is expected to be 0.2–2.3 bar as the free flow has a static pressure of 0.2 bar and the exit pressure of the plume is 2.3 bar which leads to a range from 0.1–5 bar including a safety margin of 2.

The temperature range is guided by the wind tunnel temperature (160 K static temperature) and the local temperature when the engine is running. As described in Section 10.5, the temperature sensor is located in the mount, where a temperature of maximum 504 K is expected. Therefore the temperature range of the sensor should be between 160–504 K static temperature. The sampling rate of the sensor needs to be at least 10 kHz [93]. A sensor which fulfills all these requirements is the HI2200 high temperature pressure transducer from ESI technology [94], but any other pressure sensor fulfilling these requirements can be used as well.

Furthermore, the pressure in the combustion chamber needs to be measured. The sampling rate for the combustion chamber pressure has minor importance, as only the average chamber pressure need to be measured during operation. The pressure range the sensor needs to be capable to measure ranges between 0–60 bar as the pressure in the combustion chamber is expected to be 30 bar and a safety margin of 2 is considered. As the sensor is mounted in the nose cone, its temperature range should allow for operating temperatures between 160–300 K, guided by the wind tunnel temperature and the temperature at a hot summer day for the static testing campaign (30 °C). A sensor which fulfills all the criteria for the combustion chamber pressure sensor a Parker ASIC from 0–60 bar can be used [95], which is also used in rocket tests [96].

The size of a thermocouple is so small, that this sensor can easily be placed on the base plate of the model. For the HotFire system, where temperature between 500–600 K are reached at the outer wall of the combustion chamber, see Chapter 9, type K thermocouples with a range from 73–1500 K are the most applicable, as afterburning and conduction between the graphite nozzle and the chamber wall could increase the local temperature of the base plate. The wire of the thermocouple generally is out of the same material as the measurement unit and withstands therefore the same temperatures. At the faculty of Aerospace engineering, a thermal camera which can be used for monitoring the chamber wall temperature is already available.

Given the availability of PIV equipment and the high reputation for PIV of the Aerodynamics Laboratory at Delft University of Technology and the fact that PIV is capable of measuring the flow field without any adapting anything inside the region of interest, PIV will most probably be used to visualize the flow field in the base region. PIV works by shining laser light into the region of interest. Particles seeded in the flow will reflect the light, which is captured by cameras. This gives the position of the particles in space, and with a second frame recorded a few nanoseconds later the velocity can be derived (because the flow behavior is known, it can be identified which particle went where). Using more cameras, the accelerations can be captured as well, allowing experimentalists to solve the Navier-Stokes equations and get flow properties from the measurements.

The PIV system consists of three components; the camera, the laser and a particle seeding system. At the University in Delft a Nd:YAG-Laser is used. Multiple Photron APX-RS CMOS cameras can be used to take images of the base region of the model. The seeding particles are oil particles or titanium oxide particles.

The two options for the mass flow determination were identified as a load cell or a mass flow meter. As a mass flow meter interrupts the flow and can cause a pressure drop, therefore, a load cell is a better option for determining the mass flow. Throughout the burn the mass of each tank can be measured using the load cell and afterwards the change in mass over time can be calculated analysis the mass data. A load cell which can be used for the weight measurement is the LBC 250, but any other load cell which is able to measure weight up to 1000 N is applicable as well.

10.4. BUDGET

The budget of the HotFire system includes any cost for the sensors. Table 10.1 summarizes the cost budget of the measurement system. Note the cost of the flow field measurement are assumed to be zero, as the cameras, the laser and the mirrors are available equipment at Delft University of Technology. Summing up the cost of the different components shows that the measurement system lies within the cost budget.

Table 10.1: Price budget for the measurement system excluding shipping cost

Sensor	Description	Price per piece	#	Price overall	Source
Pressure	HI2200 and Parker ASIC	€920 and €285	1, 1	€1205	[97, 98]
Temperature	Type K Thermocouple	€45	1	€45	[99]
Flow field	PIV system of AeroLab	€0	-	€0	[-]
Mass flow	Load cell LBC- 250	€260	2	€520	[100]
Chamber Temperature	Infrared camera	€0	1	€0	[-]

10.5. INTEGRATION

The integration of the sensors (so the placement and selection of the measurement region) is of utmost importance when talking about a measurement system. An overview of were the measurements are taken and were the sensors are located is given in Figure 10.1a.

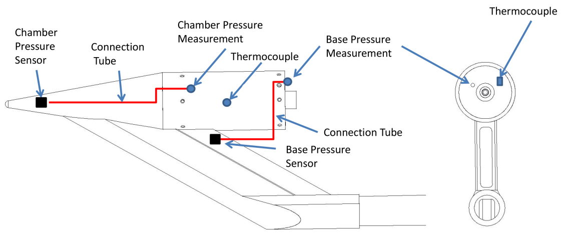

(a) A initial consideration of the sensor locations

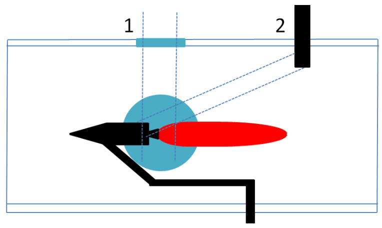

(b) Possible positions of the PIV laser system

Figure 10.1: Integration of the instrumentation system into HotFire

As shown in this figure both pressure and temperature sensors take measurements of the base region of the HotFire. In order for pressure sensors to fit, tubes are connecting the sensor to the measurement location. Therefore the nozzle ring has a slot where plastic tubes for the pressure measurement are running. The pressure sensor itself is mounted inside a slot at the back of the mount. For the combustion chamber pressure, a hole can be drilled into the injector. The sensor itself can than be placed in the nose cone or can be fitted into the mount as well, as no fluctuations need to be measured. The thermocouples are glued to the base region and the cables are running along the mount and chamber tube.

For the PIV system, a periscope-like laser transmission device has to be placed into the wind tunnel to allow for a measurement. The laser equipment has to be placed in such a way, that the laser sheet is located perpendicular to the cameras and that the equipment itself is not inside the plume to avoid heating. Figure 10.1b indicates two different options for achieving this. One option is to use a periscope which can be adjusted such, that a laser sheet can be shone into the base region from the top wall. A second option is to have a second window directly on top of the base region to shine the laser through. Both options involve minor changes to the wind tunnel, which will neither influence the overall integrity of the wind tunnel, nor will it increase the costs.

The load cell for the mass flow measurement are scale like load cells and measures the weight in compression. Therefore, the tanks can simply be placed on these sensors.

10.6. RECOMMENDATIONS

It is recommended to test the whole measurement system when conducting the static test series before deploying the HotFire in the wind tunnel, as errors in the measurement system will have a large impact on the outcome and can easily be avoided by testing. Further research into the correct positioning of the pressure and temperature sensor is recommended, as at the moment, no pressure fluctuations can be measured. The outcome of the pressure measurement is dependent on the positioning of the pressure measurement location. Different pressure sensors located at different positions will provide more accurate data about the pressure field at the base plate. In order to decrease the cost of the measurement system, the instrumentation can be rented from the measurement shop in Delft. Different types of sensor as for example thermocouples and data logging devices can be rented for a test.

11

Safety and Operations

While HotFire is not yet a finalized design, the procedures required to operate the system safely can already be outlined. In addition to that, a number of risks were identified, based on which the safety of the design can be evaluated.

11.1. Safety Plan

Safety is a point of concern for the HotFire test facility due to the inherent dangers associated with operating a rocket engine not only inside a building but even inside another piece of vulnerable machinery. Therefore, the various subsystems (Chapter 5 to Chapter 10) were designed with respect to various applicable safety regulations. They were obtained after consulting the wind tunnel technicians and tutors. In the detailed design phase, close contact will have to be maintained to ensure that the test facility can indeed be operated in the TST-27 wind tunnel at the aerodynamics laboratory.

11.1.1. Reliability, Availability, Maintainability and Safety

Throughout the design, these regulations and advice have been implemented as much as possible. Given the many redundancies present in the design and the mitigation of the remaining risks by extensive testing, it can be concluded that the system is safe to store, install and operate, fulfilling the safety criterion.

In the case of HotFire, reliability and safety are very similar to one another. Usually, reliability concerns the performance of the system over extended periods of time. However, the intent of HotFire is to perform a rather limited number of tests, spread out over a long period of time. After each test the system will be disassembled, cleaned, and checked for any faults. Therefore, reliability the way it is usually defined, is not a point of concern for the HotFire test facility.

Provided the required propellants are obtained in time for the test, there is no part of HotFire that would require extensive preparation with the exception of the installation of the model in the wind tunnel. Since wind tunnel test schedules are planned sufficiently in advance, the test facility will be available when needed.

Maintainability – while not being a design objective – is an inherent quality of HotFire due to the fact that the entire system can be disassembled and parts can be replaced as necessary. In case of failure of a component, it can be replaced while reusing all other parts of the system due to the modular design.

11.1.2. Risk Assessment

During the operation of HotFire, several scenarios could occur that would pose a safety risk to the wind tunnel, personnel or both. An attempt has been made to anticipate all of these scenarios and to employ appropriate mitigation measures, both during design and during operation. Table 11.1 presents the resulting list of risk events. Various mitigation measures are outlined in the respective column. A major countermeasure throughout the design process has been to ensure redundancies in all critical parts, such as to avoid any single points of failure. This is especially the case for the feed system (see Chapter 5), where including redundancies is more easily possible than for other subsystems because of less strict limitations on available space. Risks that are not mitigated by a design feature will mainly addressed by extensive testing outside of the wind tunnel.

Table 11.1: Safety risks of the HotFire test facility and their mitigation measures

ID	Cause	Event	Consequence	Mitigation measures
1	Excessive wind tunnel start-up loads	Structural failure of model	Loose parts damaging wind tunnel	Static load test; vibrational test bench; initial wind tunnel testing without engine operation to limit impact of failure (no fire hazard)
2	Excessive combustion chamber pressure loads	Structural failure of model	Loose parts damaging wind tunnel; Fire outbreak due to escaping combustion gases	Test series outside at a safe distance from buildings and people
3	Excessive combustion chamber heat loads	Melting or structural failure of model	Damage to wind tunnel, buildings and injury of people	Validation tests with temperature sensors (conservative test because of lack of cooling by outside flow)
4	Off-design injection pressure	Varying plume conditions; varying oxidizer-fuel ratios	Varying combustion chamber temperature, possibly exceeding design loads	Adjust pressure regulator and control valve settings according to test results; possibly redesign/modify injector
5	Ignitor not powerful enough	No ignition	Fire hazard due to flow of large amounts of unburned propellants into wind tunnel	Short term: close propellant control valves; long term: redesign igniter
6	Failure of control valves	Loss of control over HotFire	Fire hazard due to uncontrolled propellant flow	Duplicate all valves in the system to incorporate redundancies
7	Failure of pressure regulators	Pressurization of the entire feed system at the reservoir pressure	Bursting of feed lines or connections	Incorporating relief valves in the feed system
8	Operation of relief valves due to pressure regulator failure	Venting of combustible pressurized propellants into the wind tunnel building	Fire hazard or explosion	Control valves in oxidizer branch of the feed system located before pressure regulators to stop propellant flow
9	Power failure	Loss of control over HotFire	Fire hazard due to uncontrolled propellant flow	Use of spring-loaded valves that automatically close in case of power failure
10	Bursting of feed lines or connections	Spillage of propellants	Fire hazard or explosion	Validation tests at safe distances to populated areas; emergency stop button; possibly automatic system using pressure sensors (to stop propellant flow in case of sudden pressure drop)
11	Plume size not predictable	Plume growing too large	Plume touching surroundings	Compare extensive CFD analysis with test results from an outside test to predict plume size; monitor plume size and shut off plume generator in case of unexpected plume size
12	Plume touching the wind tunnel wall	Overheating of wind tunnel wall	Damage to wind tunnel and fire hazard	Test hot plume generator in similar surroundings (e.g. wind tunnel mock-up) with appropriate adjustments to incorporate for different pressure ratio between plume and ambient; install temperature sensors on wind tunnel wall and shut off system in case of exceeding the limit value

— Continued on next page —

Table11.1 – continued from previous page

ID	Cause	Event	Consequence	Mitigation measures
13	Plume touching sting	Failure of mount due to overheating of sting	Loose parts damaging wind tunnel; fire hazard due to uncontrolled plume direction	Test hot plume generator outside (under the same conditions as suggested for risk event 13)
14	Plume touching PIV mirror	Overheating of PIV mirror	Damage to PIV system and fire hazard	Test hot plume generator in similar surroundings (see risk event 13)
15a	Unexpected heat loads in base region	Overheating of base plate of model	Structural or thermal failure of model, with the resulting risks of damage to wind tunnel and fire hazards	Outside testing; installation of temperature sensors and shutting off of system in case of exceeding limit temperature
15b	Unexpected heat loads in base region	Overheating of temperature and pressure sensors in base region	No measurements possible; potential damage to wind tunnel from loose/molten parts of sensors	Validation tests outside of wind tunnel

The biggest risks of the HotFire system in its current state of design are the heat loads and the prediction of the plume size. The heat loads itself are not the problem, but the control of the system is. The combustion chamber can withstand the heat loads for a limited time, so in the detailed design of the feed system controls that limited time should be thoroughly implemented. For plume size prediction, CFD analysis was done and the preliminary conclusion is that the plume will not physically touch the walls or sting. It should be further investigated if the outside combustion of the kerosene influences the heating of walls and sting.

11.2. OPERATIONAL MANUAL

Improper operation of a liquid rocket engine can cause serious damage to the operators or surrounding structure. This section specifies how HotFire should be operated. It does not state the exact actions required but is meant as a basis for all considerations concerning storage, installation, operation and shut down/deinstallation of the system.

11.2.1. STORAGE

Storing the HotFire system is mostly influenced by the applicable regulations set forth by the Facility Management of the AeroLab. No consultation was done on this part but the advice anticipated is to store oxidizer and fuel separately and to use certified, commercially available gas cylinders. The latter is commonly checked and maintained by the gas suppliers. The remaining parts of HotFire (feed lines, valves, mount, model, nose cone, injector assembly, nozzle and the aft bulk head) should be thoroughly cleaned and dried before they brittle sealings.

11.2.2. INSTALLATION

When installing the Hotfire system, the following steps should be considered in the corresponding order listed below. The philosophy of this order is to avoid risky situations: Cleaning to avoid combustion inside of the oxygen lines, leak testing without ignitor and wind tunnel closing while having the system depressurized.

- **Cleaning** the system thoroughly. Contaminated oxygen lines can spontaneously ignite when high velocity oxygen flow is fed trough them.
- **Assembly of the model** from sting, mount, combustion chamber, injector, nozzle and nose cone
- **Attachment** to wind tunnel mounting point
- **Sensor** connection to data storage and calibration (if required)
- **Ignitor** connection and testing, afterwards disconnect

- **Feed system** assembly excluding injector connection
- **Feed system** leak testing with pressurized air or nitrogen by blocking the injector end of the lines
- **Kerosene** bladder filling and connecting within the kerosene tank
- **Fuel line** connection to the injector and tanks
- **Pressurize** the system with gas-tanks connected and test for leaks
- **Depressurize** the system
- **Ignitor** connection
- **Wind tunnel** closing
- **Pressurize** the system

11.2.3. OPERATION

Note that fine-tuning the combustion chamber pressure to find proper settings for the pressure regulator as well as determining the time to stabilize the plume is done while testing the HotFire system outside of the wind tunnel. Figure 11.1 shows the steps required in operating HotFire in the TST-27 wind tunnel at the system's current state of design. Important in this is the handling and monitoring of the data. Data for scientific purposes consists of the base pressure, temperature and other desired measurements (PIV, Schlieren flow visualization), whereas data for safety purposes consists of the combustion chamber pressure as well as model and wind tunnel wall temperatures. The latter might need to be recorded with infrared equipment because of the undesired but expected thermal inertia of thermocouples.

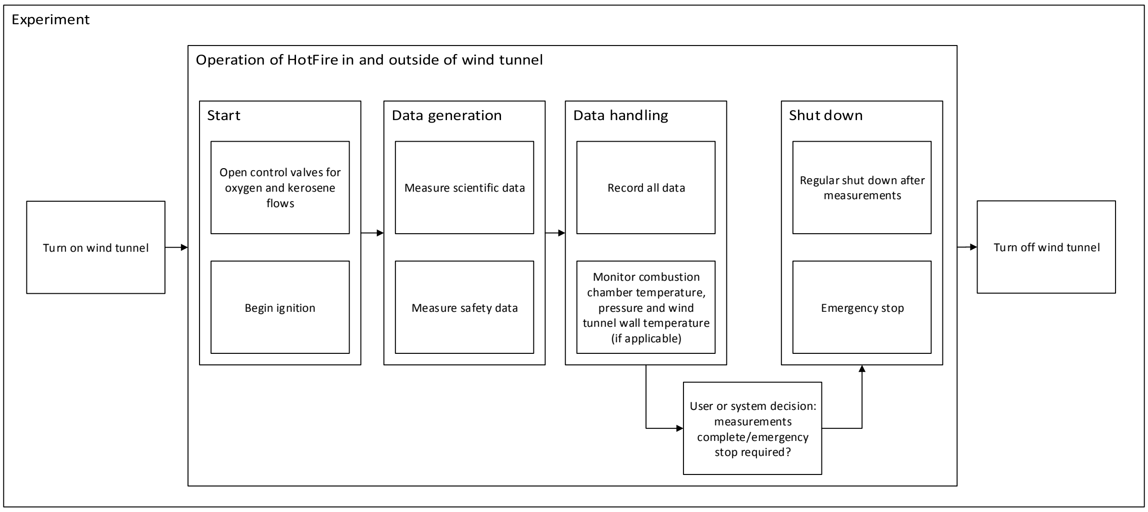

Figure 11.1: Overview of procedures required to operate HotFire

11.2.4. DEINSTALLATION

The deinstallation of the system is straightforward. Following an appropriate cooling period, the wind tunnel can be opened and the feed system disconnected. It is important to be aware of the fact that the feed lines might still be partly filled with oxidizer and fuel. After draining these propellants, the feed system can be uncoupled and the model disassembled. Following proper cleaning, the system can be stored according to Section 11.2.1.

12

FUTURE DEVELOPMENT AFTER THE DSE

This DSE work created valuable results, which can be used for the realization of HotFire. Due to the limited time of the project, no hands-on product could be developed, and therefore a proposal for the post-DSE phase is made. This will improve the likeliness of HotFire becoming operational in the future.

First, a project development and design logic (PDDL) diagram is presented to show what activities are required to arrive at a finalized HotFire system. Further, a manufacturing plan and a cost breakdown structure is given. The chapter concludes with a proposal for a static engine test to investigate the combustion stability addressed earlier.

12.1. PROJECT DEVELOPMENT AND DESIGN LOGIC

To identify the steps required to further develop HotFire after the ending of this DSE, the PDDL diagram in Figure 12.1 is used. It shows the activities necessary and gives an indication on time needed in a PD&D diagram. The time line of these is given in Figure 12.3 (Gantt chart for the post-DSE time).

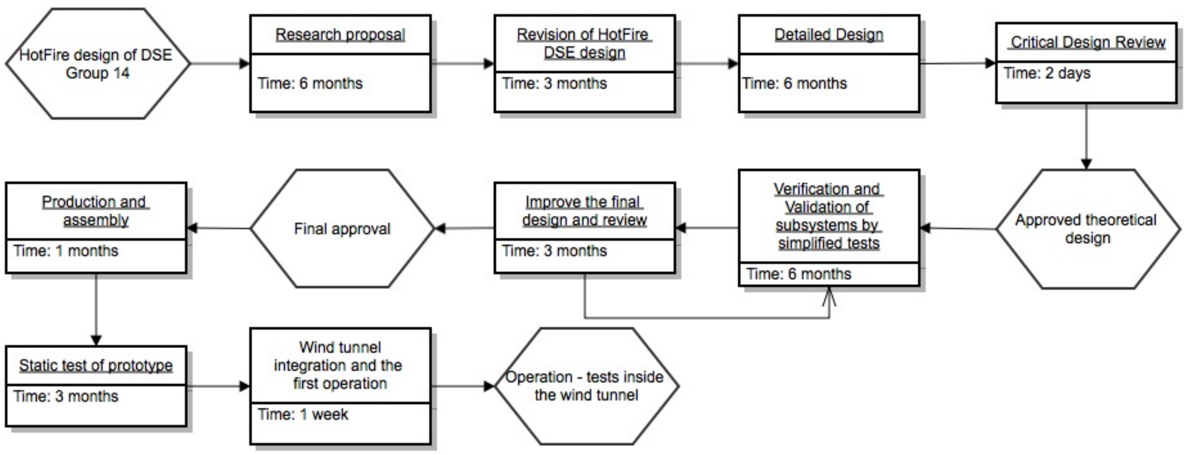

Figure 12.1: Project development and design logic diagram

This DSE served as a basis, by achieving a preliminary design through literature study and feasibility study of the system. To realize HotFire, funds need to be obtained first. This can be achieved by submitting a research proposal to, for example, ESA, Astrium, or DNW (Duits-Nederlandse Windtunnels). Funds will allow for an academic staff member to work on a revision of the current HotFire design and arrive at a detailed design. This design can then be reviewed by an experienced staff member to judge the concept.

A test series with a simplified model can be used to verify and validate the detailed design. These test aim to prove the analysis methods used and ultimately prove the functionality of the HotFire design. The test results can also be used to improve the HotFire design. Another test series is proposed if any significant changes to the design are made as a result of the initial test. The final validated design must pass a final review before entering production.

In the final phase, HotFire will be manufactured and assembled. Before HotFire can be operated in the wind tunnel, a static test outside the wind tunnel must be performed. This static test aims to prove the functioning and safety of the system. A final test will be performed in the wind tunnel, proving the full functionality and safety under operational conditions. HotFire will be ready for operations in the TST-27 wind tunnel when it has successfully completed all these steps.

12.2. MANUFACTURING PLAN

Table 12.1 shows the different HotFire parts, their method for manufacturing, and the estimated time needed for manufacturing (if applicable). Appendix A shows that all parts except the mount can be joined together with bolts and O-rings. The mount will be connected to the combustion chamber as was shown in Chapter 7. These can either be joined together by gluing, welding, or bolting.

Welding is not preferred due to warping of material. Gluing could provide a precise method for joining, but the bond needs to be able to sustain its strength at the high temperatures that are expected. Bolts would need a locally increased thickness of the combustion chamber wall. Further analysis is needed to find the most suitable method for joining.

Table 12.1: Production method and expected time per part

Subsystem	Production method	Expected time
Oxidizer tank	Off-the-shelf	n/a
Fuel tank	Off-the-shelf	n/a
Feed system	Off-the-shelf	n/a
Injector	Lathe & Milling	1 day
Ignitor	Off-the-shelf	n/a
Nose cone	Lathe	1 day
Combustion	Lathe	1 day
Nozzle	Lathe, use of sandpaper to smoothen graphite	1 day

12.3. OVERALL COST BREAKDOWN STRUCTURE

Figure 12.2 shows the cost breakdown structure for HotFire. It is an AND tree of the cost of the post-DSE activities described previously in Section 12.1. The costs that are included in the budget management in this report (Section 3.3) is highlighted and will not result in additional costs in the future.

The majority of the cost are expected to occur in the development, production, and operations of HotFire. This is mainly due to the high cost for the academic staff member working on the development as well as the high cost for operating the wind tunnel and the labor needed during operation. The production and material cost are expected to be relatively small in the overall cost.

12.4. PROPOSAL FOR A STATIC TEST OF COMBUSTION STABILITY

The requirement `HF-TEC-MEA-08` “The plume conditions shall not vary by more than 1% over time" is directly related to the stability of the combustion. A stable combustion would guarantee the variation of the plume conditions to be less than 1% over time.

Unfortunately, the requirement cannot be analyzed within the scope of the DSE for two reasons: For one thing, a prediction of the combustion (in)stability requires complex simulation tools and advanced knowledge of chemistry. For another thing, testing is required, which is time consuming in its planning and execu-

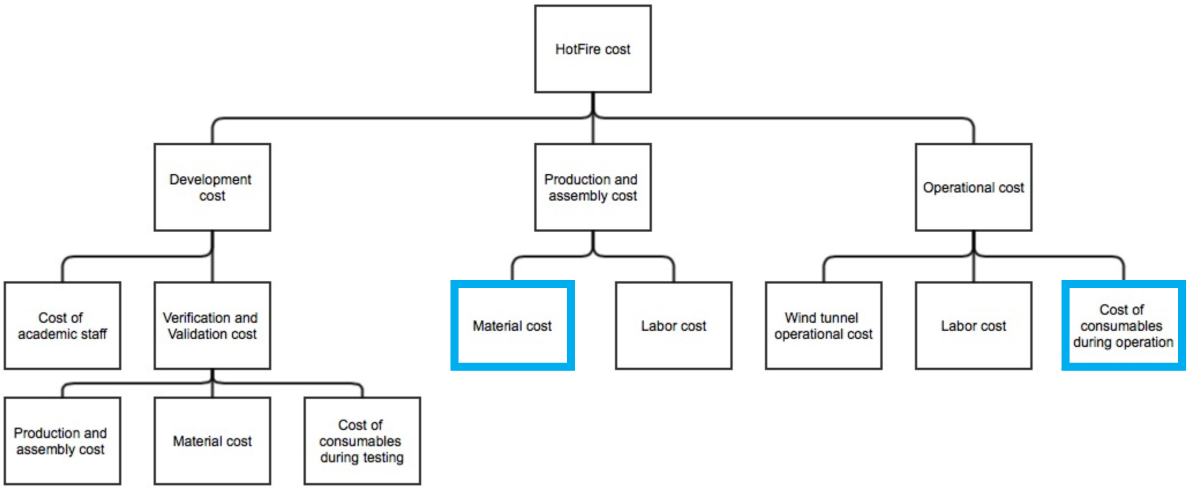

Figure 12.2: Cost Breakdown Structure

tion, and thus violates HF-CON-DEV-01, saying that the design has to be finished within 11 weeks. Therefore, a proposal for the test plan is included here, to allow for verification the requirement in the near future.

According to [30], instability of the combustion or variation of the plume conditions can be characterized by fluctuations of the pressure. These oscillations of the pressure also results in oscillations of the thrust. Hence, the pressure and the thrust can be measured at static conditions by integrating the model into for example, the test benches of DARE in order to investigate the issue of combustion stability. This provides a cheap and fast, yet good solution.

When fluctuations of pressure have been found to be more than 1%, [30] proposed several standard measures. Firstly, the pressure drop over the injector can be increased for damping the low frequency chamber pressure fluctuations under 100 Hz (Chugging). Secondly, the chugging and acoustical instabilities sometimes relate to the natural frequency of feed system components which are free to move. Their movement induces a pumping effect causing pressure fluctuations. This can be avoided by altering the points of attachment of the feed system. Lastly, the injector face baffles can be used for high frequencies below 4000 Hz. The baffles minimize the influential coupling and amplification of gas dynamic forces within the chamber. Also, cavities along the chamber wall near the injector end can be used to remove energy from the vibratory system.

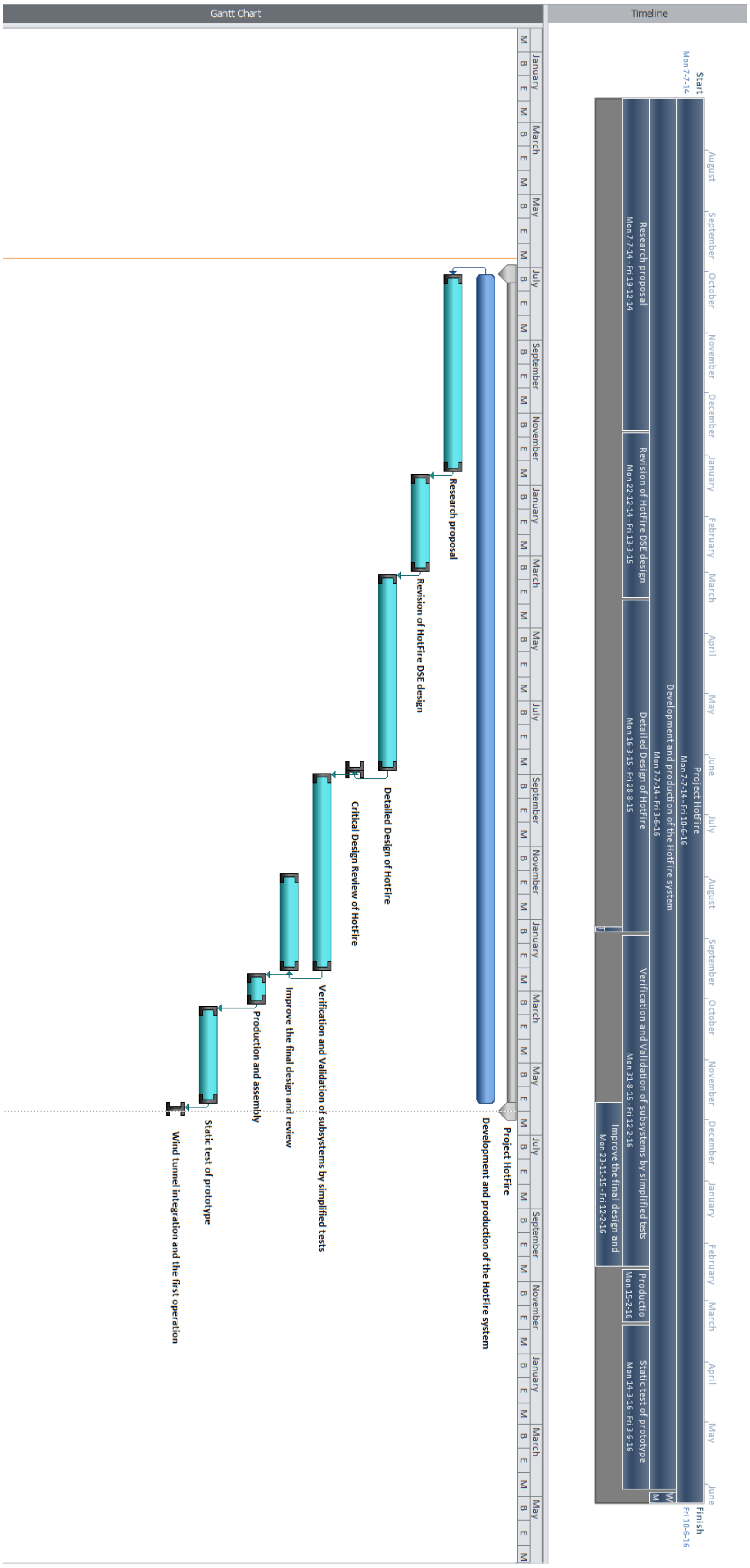

Figure 12.3: Project Gantt chart for the post-DSE phase

13

Conclusions and Recommendations

A preliminary design of the hot plume test facility "HotFire" has been presented and its technical feasibility was demonstrated. The preliminary design of HotFire consists of a rocket engine using liquid propellants, whose nozzle exit conditions produce a flow field similar to that of a real rocket exhaust plume. This is achieved by the components of the HotFire test facility: propellants, feed system, aerodynamic shape, mount, ignition system, combustion chamber, nozzle, and instrumentation.

Propellant Selection

The completed HotFire system comprises of a hot plume model and a cold plume model which are designed to match each other as close as possible in terms of similarity, while still being similar to an actual launcher. This similarity is quantified through several flow similarity parameters, namely the initial inclination angle of the plume and the pressure, momentum flux, mass flux, and kinetic energy ratios of plume to freestream. These are discussed in detail in Chapter 4.

Various oxidizer and fuel combinations were studied in order to select an optimum propellant for the hot plume test facility. Based on commercial availability, lack of toxicity and characteristic length, a propellant combination with gaseous oxygen as oxidizer and kerosene as fuel has been selected. For the cold plume, helium was selected as it best matched the hot plume in terms of the similarity parameters. When comparing the hot and cold plumes to the launchers, J-2 (Saturn V) and Vulcain 2 (Ariane 5) motors could be simulated with sufficient accuracy in a wind tunnel test set-up. Since the Vulcain 2 engine is more modern, it was chosen as the reference launcher. The deviations of the similarity parameters from the reference launcher is shown in the Table 13.1. The cold plume can better match the mass flux ratio. However, due to the absence of the base heating and large deviations in kinetic energy, the hot plume still performs better than the cold plume.

Table 13.1: Comparison of the hot and the cold plume to Vulcain 2 engine of Ariane 5 launcher

Similarity parameters	Hot vs Launcher	Cold vs Launcher	Hot vs Cold
Pressure ratio	6.64%	6.64%	0%
Initial inclination angle	15.40%	15.21%	0.22%
Momentum flux ratio	55.45%	55.51%	0.04%
Mass flux ratio	115.59%	5.78%	56.3%
Kinetic energy ratio	12.09%	156.67%	129%

Feed System

The feed system has to guide the propellants from the tanks to the combustion chamber. A blow-down system was selected over a turbopump system because of its low complexity and the short run time for HotFire. The feed system consists of propellant tanks, feed lines, control valves, pressure regulators, relief valves, pressure gauges and the injector. Due to the safety aspects associated with the feed system, an interview with the wind tunnel technician took place, resulting in the following requirements:

- The entire set-up should be remotely controlled.
- There shall be no single points of failure.
- The amount of stored propellants should be as small as possible.
- In case of power failure, the system should turn to a safe state.
- A safety factor of 2 should be implemented.

Commercially available feed lines were selected to withstand the pressure and handle the reactive behavior of the propellant. Electronically operated valves were chosen to enable remote control. Pressure regulators are placed as close to the pressurized tanks as possible to minimize the size of the highly pressurized system. Relief valves were added to the system to avoid single points of failure. The propellant tanks are located outside of the rocket model and wind tunnel to avoid any volume constraints. Commercially available, pressurized tanks were selected to ensure safe operation, while storing a minimum amount of propellant. To ensure the desired combustion conditions, the pressure drops over each component were calculated.

A combination of coaxial and splash plate injector was designed to create an impingement point between the fuel and oxidizer flows to promote mixing. The pressure drop over the kerosene injector is calculated to ensure a stable combustion pressure. The pressure drop over the gaseous oxygen injection was not analyzed due to the complexity of compressible flow and time constraints.

To enable a cold plume generation, a redesign of the injector is needed. Furthermore, the cold gases need to be fed through two lines to achieve the required mass flow. This requires some limited redesign of mount and model.

The feed system amounts to a material cost of €3 460, due to all components being of heavy duty industrial quality.

AERODYNAMIC SHAPE

The HotFire test facility must ensure flow conditions that are similar to the launchers. Therefore, the function of the aerodynamic shape is to avoid flow instability and shock wave interaction with the base region. An analysis on the velocity field inside the test section has been performed both analytically and numerically to optimize the aerodynamic shape of the mount and the nose cone.

The geometry of the nose cone has been optimized to place the reflected shock waves farthest away from the base region. The outcome of the optimization was a nose cone angle of 10.5 degrees, resulting in a distance of 3.06 times the model diameter between the base of the model and the reflected shock waves. The length of the nose cone was directly influenced by the diameter of the thrust chamber. Furthermore, a diameter of 6 mm was selected for the tip of the nose cone. This is manufacturable and aerodynamically desired; a too sharp nose cone will create flow separation, while a too blunt nose cone will create a bow shock. Lastly, zig-zag tape will be placed directly after the nose cone in order to make the flow entering the base region turbulent.

The geometry of the mount has been mainly optimized structurally. However, the aerodynamic optimization of the front section of the mount is important to reduce the drag and the pressure drop across the shock waves, which will consequently result in the reduction of the amount of loads acting on the mount. A sharp angle of 16.7 degrees for the front section will ensure a low deflection angle of the oblique shock. This will result in a reduction of the Mach number across the shock, which yields less static pressure acting on the front of the mount, reducing the drag. The width of the inclined beam was designed to be 18 mm due to the size of the fuel lines. The length of the sharp frontal section of the mount was designed to have a length of 30 mm.

MOUNT

The mount is the connecting element between the rocket model and the wind tunnel. The mount has to be designed to sustain all loads during start up and operation and to provide enough space inside to house the propellant lines. A sting mount was selected over a window mount to enable Schlieren visualization and because it produces less blockage. A static and dynamic structural analysis was carried out on the mount. The mount is designed for start up loads due to their high magnitude in the static load case. Pressure fluctuations at the base region and combustion instability could trigger the natural frequency. This could result in failure of the system and needs to be investigated more closely. ANSYS was used to analyze the static load case and find the natural frequencies. An analytical model was used to verify ANSYS and was found to be a close match with the exception of the deflections, which can be explained by the discretization of the beam in the analytical model.

An angle of 30 degrees of the mount beam was found to be optimum for blockage. Space was allocated to allow the placement of instrumentation in the mount. The instrumentation is located in the mount due to the high temperatures at the actual base plate. Thermal heating by radiation was found not to be critical for the mount. For the mount material, Uddeholm Impax Supreme, which is a pre-hardened Cr-Ni-Mo-alloyed mould steel, has been selected on the recommendation of the wind tunnel technician, because it has been used before for wind tunnel models.

IGNITION SYSTEM

A flammability analysis has been performed in Chapter 8 to determine what the requirements are for an ignitor to successfully start the combustion of the kerosene-oxygen propellant mixture. This was done by analyzing the upper and lower flammability limits of the volume fraction. Next, an autoignition temperature of 1200 K has been determined from experimental data on ignition delay experiments. Heating the propellant mixture to the autoignition temperature leads to certain combustion. From this temperature, the mass flow rate, and the heat capacity, the total required energy to heat the propellant mixture is calculated to be 151.6 J. Also, a maximum ignition duration of 5 s has been established.

To select the best ignitor design, several ignitor types have been researched and evaluated based on ignition energy, ignition duration and ignitor size. The spark plug, the resistive heating ignitor, and the pyrotechnic ignitor scored the best on these criteria and are all considered possible options for the HotFire system. The spark plug has the preference over the other two due to its commercial availability and ease of use. Regarding the positioning of the ignitor in the combustion chamber, it is generally desired to have it placed near the mixing point of the propellants.

Despite the extensive analysis, tests are required to confirm that the selected ignitor design works.

COMBUSTION CHAMBER AND NOZZLE

The propellant is ignited inside the combustion chamber and expanded through the nozzle to create the desired plume conditions. Both the combustion chamber and nozzle must have a certain geometry to perform their functions efficiently. Moreover, the combustion chamber and nozzle must not fail thermally and structurally. To optimize the structural and thermal aspects of the subsystems, several materials have been analyzed to select the most suitable one.

The concept of a cylindrical chamber was selected as it provided the minimum cross section area and length. For the nozzle, the concepts of bell shaped and conical nozzles for the hot plume were studied. From the estimation of their lengths, the conical nozzle was found to be too long. Moreover, the lip angle of 7 degrees resulted in an unconventional divergence angle which was not desired for the efficiency of the nozzle. Therefore, a bell shaped nozzle was selected. For the cold plume nozzle, an interchangeable nozzle with the hot plume combustion chamber was decided to be the best option as it does not require a new model that would eventually result in extra costs.

The wall thickness of the combustion chamber was determined by structural and thermal analysis. An iteration was done over different materials in order to compute the optimum thickness for the corresponding materials. The results of the analysis showed that steel and titanium with a thickness of 2.5 mm can be used for the combustion chamber with sufficient design margins. Steel S355 was selected as the combustion chamber material since it is cheaper and weight optimization was not required for the project. For the nozzle, graphite was selected due to high temperatures at the throat and uncertainty of the base heating for the divergent region of the nozzle. Lastly, a CFD based estimation on the plume size showed that the current design of the combustion chamber and nozzle can produce the required plume size.

INSTRUMENTATION

An important part of a test set-up is the instrumentation. Only creating the desired phenomena with a test model will not result in test data. Within the limited space available for the HotFire system, several sensors have to be placed to perform the desired measurements.

For the measurement of base region pressure, a Series TG pressure transmitter from REOTEMP has been selected, which is able to operate within the expected surrounding conditions of 0.1-5 bar (including a safety margin of 2) and 160 K static temperature. It also exceeds the minimum sampling rate of 10 kHz. For the pressure measurement in the combustion chamber, a Parker ASIC pressure sensor has been selected that is able to operate in the pressure range of 0-60 bar (including a safety margin of 2). This sensor has been used previously in rocket tests.

Thermocouples, which are used for temperature measurements, are small in size and can be placed on the base plate of the rocket model. The temperature of the exhaust gases entering the base region is under 1000 K during operation, leading to the choice of a type K thermocouple. This type of thermocouple can be used within a temperature range of 73 to 1500 K.

Given the availability of PIV equipment at the Aerodynamics Laboratory at Delft University of Technology, this can be used to visualize the flow field in the base region. The available PIV system consists of a Nd:YAG-Laser and multiple Photron APX-RS CMOS cameras. For seeding, oil or titanium oxide particles can be used.

FUTURE DEVELOPMENT AFTER THE DSE

A project development and design logic diagram, cost breakdown, and a test proposal for the phase after the DSE were made to improve the likelihood of HotFire to become operational. It showed that approximately 28 months are needed before HotFire can become operational and that the main cost will be in the development and operational phase. A test plan was made which allows to eliminate the remaining uncertainties which cannot be analyzed with sufficient accuracy.

OVERALL SYSTEM RECOMMENDATIONS

The current design of HotFire is based upon the previously selected design point for similarity. The selection was done based on a preliminary analysis of what was considered to be feasible. During the preliminary design phase, analysis tools were developed to judge the feasibility of the HotFire design in more detail. The developed analysis tools would allow to iterate over this design point and optimize the design to find a better match in similarity. For example, achieving a higher pressure in the combustion chamber would result in a better match of similarity parameters.

To match the similarity with the real flight as closely as possible, various wind tunnel options other than the TST-27 wind tunnel must be investigated. Bigger wind tunnels would allow for better wind tunnel simulation. In other words, the space constrains from blockage and the shock wave interaction with the base region can be relieved by integrating the model into a bigger wind tunnel. Consequently, bigger engines can be used where the achievable combustion chamber pressure, temperature, plume size, and burn time of the engine can be enormously improved to match the similarity parameters to an even larger extent.

REFERENCES

[1] B. Roberts, R. Wallace, M. Craig, and D. Kanipe, *Rocket Exhaust Plume Induced Flowfield Interaction Experiences with the Space Shuttle,* AIAA **18**, 1 (1983).

[2] Figure 1.1a, `http://media.creativebloq.futurecdn.net/sites/creativebloq.com/files/images/2012/10/step4.jpg`.

[3] Figure 1.1b, `http://www.arianespace.com/images/missionup-dates/2010/739_lg.jpg`.

[4] Figure 1.1c, `http://chamorrobible.org/images/photos/gpw-20051129-NASA-S68-27366-Apollo-6-Saturn-V-rocket-Spacecraft-020-Florida-19680404.jpg`.

[5] Figure 1.1d, `http://agaudi.files.wordpress.com/2009/07/a14_s6939958.jpg`.

[6] A. Gulhan, *RESPACE - Key Technologies for Reusable Space Systems, Results of a Virtual Institute Programme of the German Helmholtz-Association,* Notes on Numerical Fluid Mechanics and Multidisciplinary Design, Vol. 98 (Springer, 2003-2007).

[7] S. Stephan, R. Radespiel, and R. Muller-Eigner, *Jet Simulation Facility using the Ludwieg Tube Principle,* in *5th European Conference for Aeronautics and Space Sciences (EUCASS)* (2013).

[8] M. Pindzola, *Jet Simulation in Ground Test Facilities,* AGARDograph **79**, 1 (1963).

[9] G. Brauckmann, J. Greathouse, and M. White, *Rocket Plume Scaling for Orion Wind Tunnel Testing,* in *29th AIAA Applied Aerodynamics Conference proceedings* (2011).

[10] W. Peters, *An evaluation of jet simulation parameters for nozzle afterbody testing at transonic mach numbers,* in *Arnold Engineering Development Center* (1976).

[11] W. Bannink, E. Houtman, and P. Bakker, *Base flow / underexpanded exhaust plume interaction in a supersonic external flow,* in *American Institute of Aeronautics and Astronautics Inc.* (1998).

[12] N. T. Musial and J. J. Ward., *Base flow characteristics for several four-clustered rocket configurations at mach numbers from 2.0 to 3.5,* in *NASA Washington* (1961).

[13] N. N. S. Research, *Global Satellite Manufacturing and Launch MGlobal*, Tech. Rep. (NSR, 2012).

[14] T. Saaty, *The Analytic Hierarchy Process*, 1st ed. (McGraw-Hill, 1980).

[15] Pulstar, *They are not spark plug but pulse plugs.* `http://www.pulstar.com/home2/part-finder/` (2014), Accessed: 27-06-2014.

[16] B. T. C. Zandbergen, *Thermal Rocket Propulsion, lecture notes* (TU Delft, 2010).

[17] B. Zandbergen, *Thermal Rocket Propulsion*, 2nd ed. (Faculty of Aerospace Engineering, 2010).

[18] S. Farokhi, *Aircraft Interaction*, 1st ed. (John Wiley & Sons, 2009).

[19] H. Korst, *Approximate Determination of Jet Contours Near the Exit of Axially Symmetrical Nozzles as a Basis for Plume Modelling*, Tech. Rep. AD-756 380 (Army Missile Command, Redstone Arsenal, Alabama, 1972).

[20] J. Suttles and R.L. James, Jr., *Effect of Nose-Mounted Control-System Jets in Roll-Control Positions on the Aerodynamics of a Space Vehicle,* NASA Technical Note **1** (1966).

[21] W. I. Scallion, *Effects of Nozzle Exit Geometry and Pressure Ratio on Plume Shape for Nozzles Exhausting Into Quiescent Air,* NASA Technical Memorandum **1** (1996).

[22] T. Hartley, R. Brandis, and F. Mossayebi, *Exact and Approximate Solutions to the Oblique Shock Equations for Real-Time Applications*, NASA Contractor Report 187173 (NASA, 1991).

[23] J.D. Anderson, Jr., *Fundamentals of Aerodynamics*, 5th ed. (McGraw-Hill, 2011).

[24] A. Ponomarenko, *Rocket Propulsion Analysis,* `http://propulsion-analysis.com/`, Accessed: 02-06-2014.

[25] H. J. Siemer, *Interview on safety regulations,* (May 2014).

[26] NASA, *Saturn V F-1 Engine Fact-Sheet,* http://history.msfc.nasa.gov/saturn_apollo/documents/F-1_Engine.pdf (), Accessed: 04-05-2014.

[27] NASA, *Saturn v j2 engine properties,* http://www.nasa.gov/centers/marshall/pdf/499245main_J2_Engine_fs.pdf (2014).

[28] NASA, *RS-25 Space Shuttle Main Engine Properties,* http://www.ingaero.uniroma1.it/attachments/617_PSP%20Lez.%2007%20SUMMARY%20OF%20ROCKET%20NOZZLE%20RELATIONSHIPS.pdf (2014), Accessed: 15-06-2014.

[29] European Space Agency, *Boosters EAP,* http://www.esa.int/Our_Activities/Launchers/Launch_vehicles/Boosters_EAP, Accessed: 15-04-2014.

[30] G. Sutton and O. Biblarz, *Rocker Propulsion Elements,* 7th ed. (John Wiley & Sons, 2001).

[31] SunFlex, *Oxygen charging PTFE hose 744-04,* http://www.sunflex.com.sg/products/, Accessed: 20-06-2014.

[32] Parker, *Parflex Thermoplastic Hose, Tubing, Fittings and Accessories,* http://www.parker.com/literature/Parflex/B-Parflex%20PDF%20and%20Images/CAT%204660.pdf, Catalog 4660-WEB, August 2007.

[33] IJzershop, *Staalplaat,* http://www.ijzershop.nl/301-staalplaat, Accessed: 20-06-2014.

[34] IJzershop, *Buizen,* http://www.ijzershop.nl/293-buis, Accessed: 20-06-2014.

[35] *Linde - Industrial gases,* http://www.linde-gas.nl/nl/products_and_supply/industrial_gases/index.html (), Accessed: 23-06-2014.

[36] Anderson-Bolds webshop, *Parker 2-Way Solenoid Valves,* Accessed: 20-06-2014.

[37] Valin webshop, *Relief Valves,* http://www.valinonline.com/products/4M4F-RH4A-VT-SS-K3 (), Accessed: 20-06-2014.

[38] Valin webshop, *High Pressure Instrument Regulator (cylinder/supply),* http://www.valinonline.com/products/HPR801S5P20404PM (), Accessed: 20-06-2014.

[39] F. M. White, *Fluid Mechanics,* 4th ed. (McGrawHill, 1998).

[40] D. W. G. Robert H. Perry, *Perry's Chemical Engineers' Handbook,* edited by D. W. G. Robert H. Perry (McGraw-Hill, 1997).

[41] R. P. Benedict, *Fundamentals of Pipe Flow* (John Wiley & Sons, 1980).

[42] *G.D. Jones SPECIFICATION FOR KEROSENE,* https://www.gdjones.co.uk/Content/UserFiles/files/TDS_Kerosene.pdf (), Accessed: 23-06-2014.

[43] California Environmental Protection Agency - Air Resources Board, *Kerosene,* http://www.arb.ca.gov/db/solvents/solvent_pages/Hydrocarbon-HTML/kerosene.htm, Accessed: 23-06-2014.

[44] Kaye & Laby - Tables of Physical & Chemical Constants - National Physical Laboratory, *Viscosities of Gases and Vapours,* http://www.kayelaby.npl.co.uk/general_physics/2_2/2_2_3.html, Accessed: 23-06-2014.

[45] Valin webshop, *Pipe fittings,* http://www.valinonline.com/items/Fluid-Management/Fittings/Metal/Pipe-Fittings.aspx (), Accessed: 20-06-2014.

[46] Valin webshop, *Parker Series NR nylon tubing,* http://www.valinonline.com/products/NBR-4-050 (), Accessed: 20-06-2014.

[47] Adams Gas, *Nitrogen for Air Conditioning,* http://www.adamsgas.co.uk/nitrogen-gas/nitrogen-for-air-conditioning/trade-gas-ofn-nitrogen-20l-200bar-new-bottle-85-155-detail (), Accessed: 20-06-2014.

[48] Adams Gas, *Industrial Gas Suppliers,* http://www.adamsgas.co.uk/welding/industrial-gas/industrial-gas-oxygen-gas-50l-200bar-refill-only-91-detail (), Accessed: 20-06-2014.

[49] Liquid Containment, *Fuel Bladders,* http://liquidcontainment.com.au/cartpage/viewproduct/17/3-5-litre-back-pack, Accessed: 20-06-2014.

[50] RS components, *Pressure Gauges,* http://uk.rs-online.com/web/p/analogue-positive-pressure-gauges/4146425/, Accessed: 20-06-2014.

[51] Nir Kalush, *MatLab Central; Oblique Shock Wave Relations,* http://www.mathworks.nl/matlabcen

tral/fileexchange/9234-oblique-shock-wave-relations/content/theta_beta_mach_relation.m.

[52] National Aeronautics and Space Administration, *Supersonic Flow Past a 3D Cone,* http://www.grc.nasa.gov/WWW/k-12/airplane/coneflow.html.

[53] Frits Donker Duyvis, *Interview on Wind Tunnel Start-up Loads,* date: June 2014.

[54] NASA, *General thrust equations,* http://www.grc.nasa.gov/WWW/k-12/airplane/thrsteq.html (), Accessed: 06-06-2014.

[55] F. Dionisio and A. Stockenstrom, *Aerodynamic Wind-tunnel Test of a Ramjet Projectile,* 19th International Symposium of Ballistics, Interlaken, Switzerland **19**, 529 (2001).

[56] F. D. Duyvis, *Interview on Mount Material Selection,* date: June 2014.

[57] Uddeholms AB, *Uddeholm Impax Supreme,* http://www.uddeholm.com/files/PB_impax_supreme_english.pdf (2011), Accessed: 22-06-2014.

[58] Uddeholms AB, *Material data, Uddeholm Impax Supreme,* http://www.uddeholm.com/files/PS_Materialdata_Impax_Supreme.pdf, Accessed: 22-06-2014.

[59] F. Scarano, *Overview of PIV in Supersonic Flows* (Aerospace Engineering Department, Delft University of Technology, The Netherlands, 2008).

[60] F. Bos, O. de Bruijn, N. van Hinsberg, T. Lombaerts, P. Lucas, D. Luchtenburg, J. Witteveen, and K. van der Zee, *DSE Final Report*, Tech. Rep. (Delft University of Technology, 2001).

[61] B. van Oudheusden and F. Scarano, *PIV Investigation of Supersonic Base-Flow-Plume Interaction*, Particle Image Velocimetry (Springer, 2007).

[62] R. Stephens, *Strength of Materials: Theory and Examples* (Arnold, 1970).

[63] T. Megson, *Structural and Stress Analysis* (Butterworth-Heinemann, 2005).

[64] R. C. Hibbeler, *Mechanics of Materials* (Pearson, 2011).

[65] T. Irvine, *Bending Frequencies of Beams, Rods and Pipes,* http://www.vibrationdata.com/tutorials2/beam.pdf (2012), Accessed: 16-05-2014.

[66] D. J. Inman, *Engineering Vibration*, 3rd ed. (Pearson International, 2007).

[67] F. Orban, *Damping of Materials and Members in Structures,* in *5th International Workshop on Multi-Rate Processes and Hysteresis*, Journal of Physics: Conference Series No. 268 (University of Pecs, Hungary, 2011).

[68] J. Outinen, *Mechanical Properties of Structural Steel at Elevated Temperatures and After Cooling Down,* Fire and Materials Conference **2**, 273 (2006).

[69] U. AB, *Stål Formar en Bättre Framtid,* http://www.jernkontoret.se/ladda_hem_och_bestall/publikationer/stal_och_stalindustri/rapport_stalformarenbattreframtid2013.pdf (2013), Accessed: 20-06-2014.

[70] V. P. Zhukov, V. A. Sechenov, and S. A. Yu., *Autoignition of kerosene (Jet-A)/air mixtures behind rejected shock waves,* Elsevier **126** (2014).

[71] H. F. Coward and G. W.Jones, *Limits of Flammability of Gases and Wapors* (United States Government Printing Office, 1952).

[72] P. J. Wen, C. M. Shu, Z. C. Chang, S. C. Chen, and M. L. Shyu, *Effects of Initial Pressure on the Flammability Limit of OX-Air Mixture with 20-L-Appartus,* in *17th annual conference of Asia Pacific Occupational Safety & Health Organization* (2001).

[73] B. T. C. Zandbergen, *Interview about ignition delay times and igniter design,* Date: 10-06-2014.

[74] C. T. Johansen, *Shock Tube Image,* http://www.ucalgary.ca/johansen/files/johansen/images/shocktube.png, Accessed: 11-06-2014.

[75] H. J. Davis and H. D. Curchack, *Shock Tube Techniques and Instrumentation,* Us Army Mteriel Command. - Harry Diamond Laboratories **1** (1969).

[76] P. Brimblecombe, *Air Composition and Chemistry,* edited by P. P. Campbell (Cambridge Enviromental Chemistry Series, 1995).

[77] D. Huzel and D. Huang, *Design of Liquid Propellant Rocket Engines*, edited by National Aeronautics and Space Admission (1967).

[78] B. Buyens, *Combustion Characteristics of a Nitrousoxide-Ethane Rocket Engine*, Master's thesis, Delft University of Technology (2013).

[79] S. Powell, *DARE - Interview on the Igniter design,* date: 12-05-2014.

[80] H. E. N. Donald R. Boldman and J. F. Schmidt, *Heat Transfer in* 30° *and* 60° *Nozzles with various Diameter Uncooled Pipe Inlets Half-Angle of Convergence*, Tech. Rep. (NASA Lewis research center, Washington D.C, 1967).

[81] D. K. Huzel and D. H. Huang, *Modern-Engineering for Design of Liquid-Propellant Rocket Engines*, edited by A. R. Seebass (AIAA, 1992).

[82] Advanced Materials Technolgoies, *Materials,* `http://www.amt-advanced-materials-technology.com/materials/`, 20-06-2014.

[83] Entegris, *Properties and Characteristics of Graphite* (2013).

[84] C. Kirchberger, A. Hupfer, and H.-P. Kau, *Improved Prediction of Heat Transfer in a Rocket Combustor for GOX/Kerosene,* in *47th AIAA Aerospace Sciences Meeting* (2009).

[85] M. Spittel and T. Spittel, *4.4 specific heat capacity of steel,* in *Metal Forming Data of Ferrous Alloys - deformation behaviour*, Landolt-Brnstein - Group VIII Advanced Materials and Technologies, Vol. 2C1, edited by H. Warlimont (Springer Berlin Heidelberg, 2009) pp. 98–103.

[86] Y. A. Cengel and A. J.Ghajar, *Heat and Mass Transfer: Fundamentals & Applications* (MCGraw-Hill, 2011).

[87] Y. Zhu, *Thick-Walled Cylinders,* `http://www.mae.ncsu.edu/zhu/courses/mae316/lecture/3-ThickWalledCylinder_and_PressShrinkFit_Shig.pdf`, Accessed: 23-06-2014.

[88] *Middle East Technical University slides,* `http://ocw.metu.edu.tr/pluginfile.php/1865/mod_resource/content/0/AE547/AE547_3_Pressuremeasurements.pdf`, Accessed: 02-06-2014.

[89] M. Lee, *Dynamic Response of Pressure Measuring Systems*, Tech. Rep. (Department of Defence, Aeronautical Research Laboratory, 1993).

[90] OMEGA engineering, *Introduction to Thermocouples,* `http://www.omega.com/prodinfo/thermocouples.html`, Accessed: 25-06-2014.

[91] R. Adrian, *Twenty years of particle image velocimetry,* AIAA **7**, 159 (2000).

[92] I. Newton, *Philosphiæ Naturalis Principia Mathematica* (London, 1687).

[93] F. Schrijer, *Interview on Pressure Sensor Sampling Rate,* date: 24-06-2014, DSE Status meeting 9.

[94] ESI, *HI2200,* `http://www.dinobuy.com/p/hi2200-hi2300-downhole-temperature-pressure-sensor-imported-special-high-temperature-pressure-sensor-p21504227.html`, Accessed: 28-06-2014.

[95] Parker, *PTDSB0601B1C2 Pressure Transducer,* `http://www.parker.com` (2014).

[96] J. Wink, T. Knop, R. Hiujsman, S. Powell, K. Samarawickrama, A. Fraters, R. Werner, C. Becker, F. Lindemann, J. Ehlen, A. Cervone, and B. T. C. Zandbergen, *Test Campaign on a 10kN Class Sorbitol-Based Hybrid Rocket Motor for the Stratos II Sounding Rocket,* Space Propulsion Conference, Cologne, Germany **2014**, 1 (2014).

[97] I. Process and S. IPScustom, *Trans-P Series TG General Purpose Transmitters,* `http://www.ipscustom.com/Trans-P-Series-TG-General-Purpose-Transmitters-P247C35.aspx`, Accessed: 25-06-2014.

[98] RS - Online, *Parker Hydraulic Pressure Sensor PTDVB0601B1C2, M12, 0 to 5V dc, 60bar, 0bar,* `http://uk.rs-online.com/web/p/hydraulic-pressure-sensors/0561031/`, Accessed: 25-06-2014.

[99] M. D. Store, *Cement On Polyimide Thin Film Thermocouples Type K,* `http://www.microdaq.com/thermocouples/thin-film.php`, Accessed: 18-06-2014.

[100] Transducer Techniques, *Lbc- 250,* `http://www.transducertechniques.com/lbc-load-cell.aspx`, Accessed: 18-06-2014.

A

TECHNICAL DRAWINGS

The following technical drawings are included in this appendix:

Figure A.1: Exploded view of the rocket model, indicating all parts

Figure A.2: Assembly drawing of the rocket model, indicating placement of parts

Figure A.3: Rocket model part: Chamber tube

Figure A.4: Rocket model part: Injector

Figure A.5: Rocket model part: Nose cone

Figure A.6: Rocket model part: Nozzle

Figure A.7: Mount to which the rocket model is attached

There are a few inconsistencies when comparing the technical drawings in the main body of the report and those presented in this appendix. This is mostly caused by some minor changes in the design for the successful integration of all the subsystems, which were done at a later stage.

The most noteworthy change is the addition of a 90 deg elbow connection piece to the fuel injector (absent in Section 5.3.1). The reason for this addition is to make it easier to connect the fuel line to the injector by preventing the need to make a sharp bend with the fuel line. Also, the fuel line does not have enter the nose cone this way, which prevents contact between the nose cone wall that could damage the line.

Other discrepancies are between Figure 6.7 and the design outcome of Chapter 7, where in this appendix there are filleted corners in the feed line and sensor pockets to reduce stress concentrations. Finally, Figure 6.7 also has a too short nozzle protrusion.

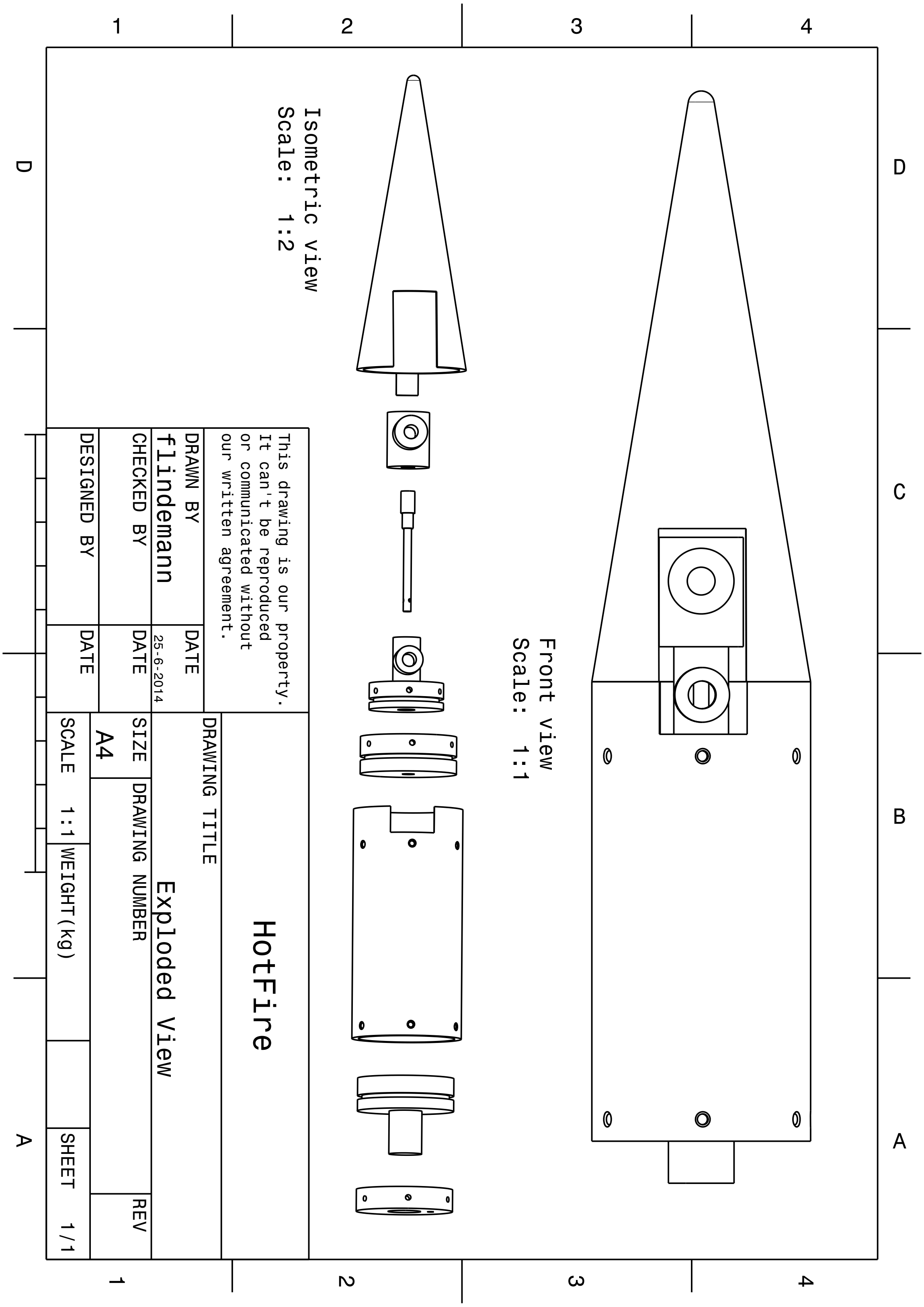

Figure A.1: Exploded view indicating all parts of the model

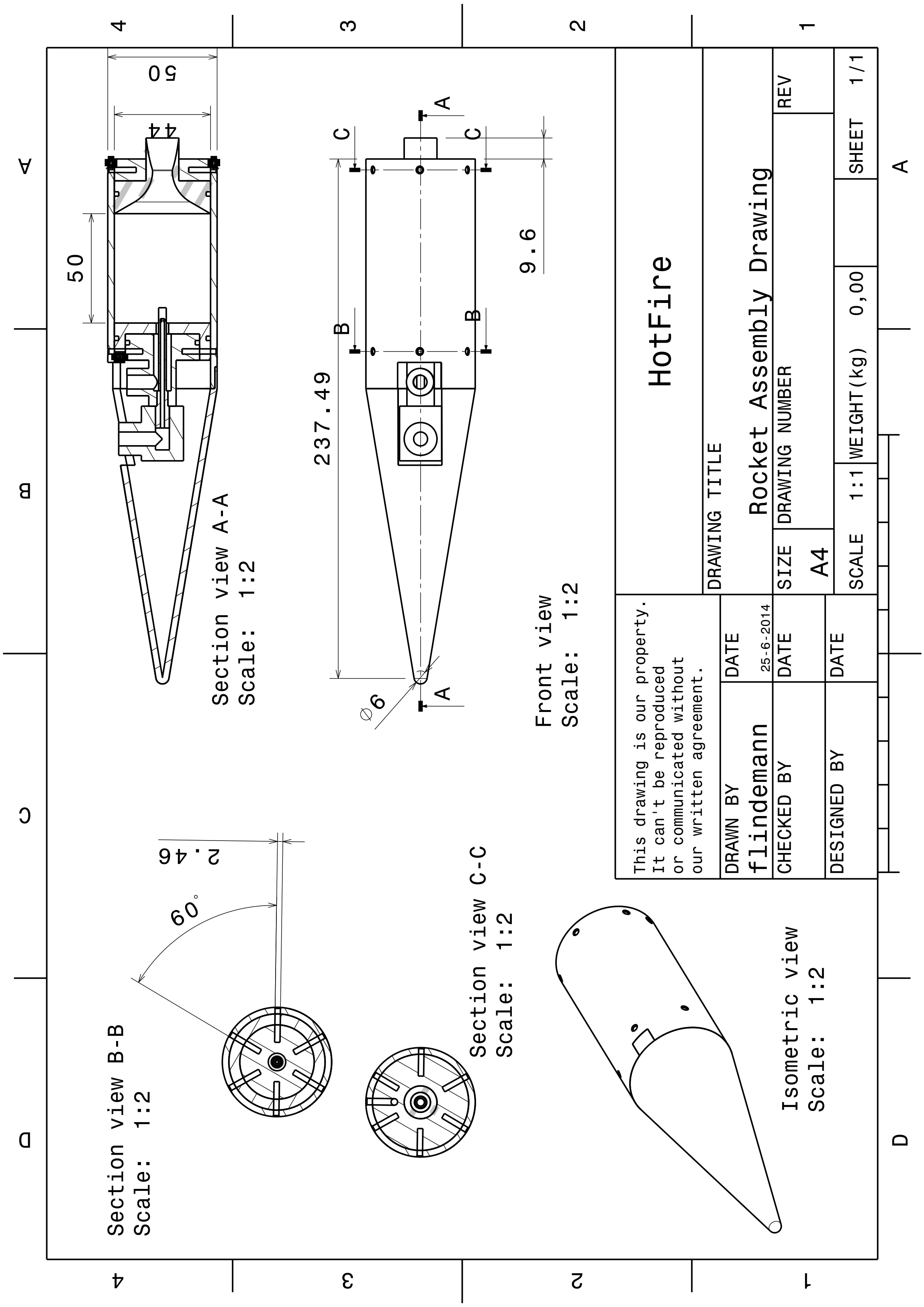

Figure A.2: Assembly drawing of the rocket model

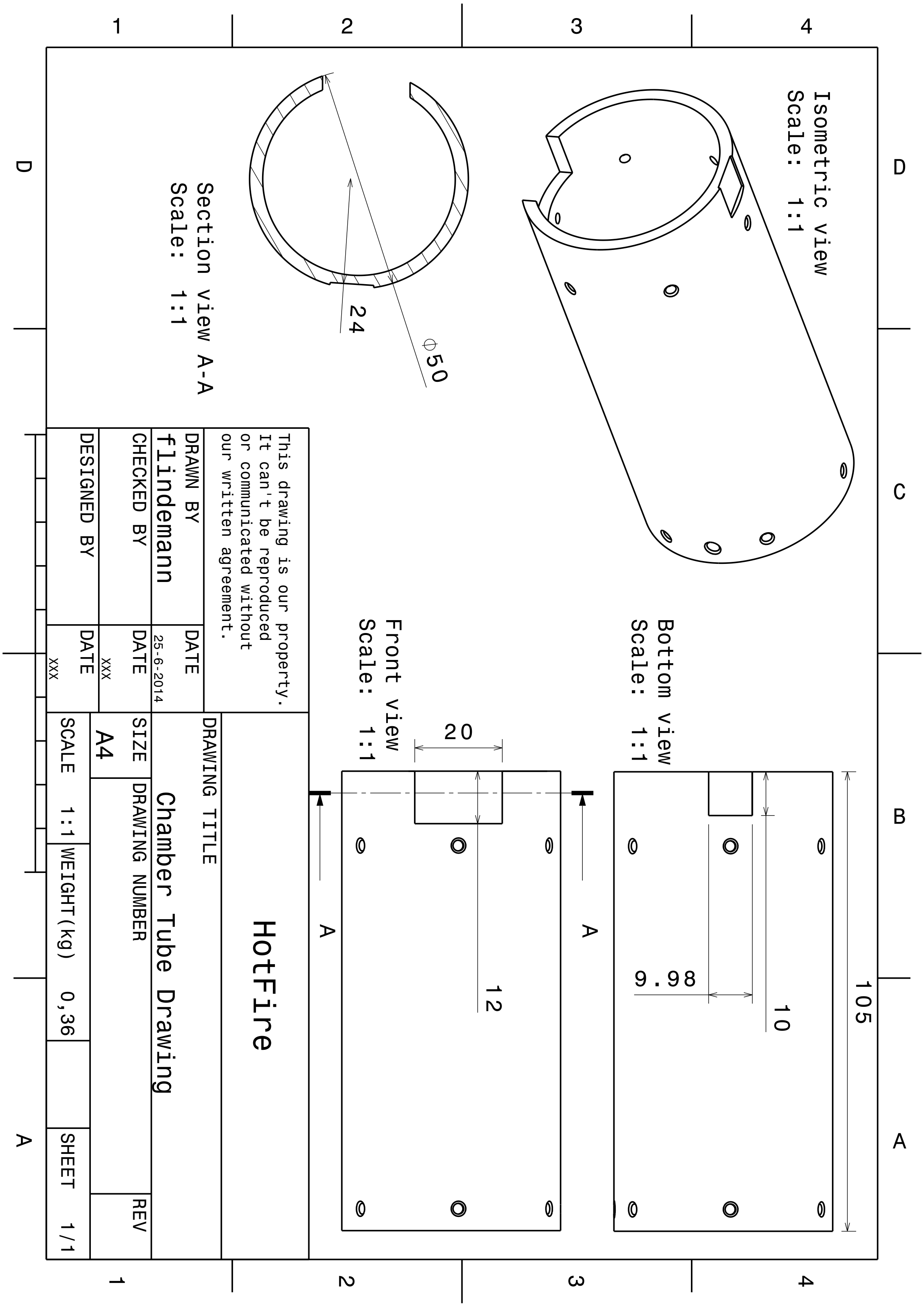

Figure A.3: Rocket model part: Chamber tube

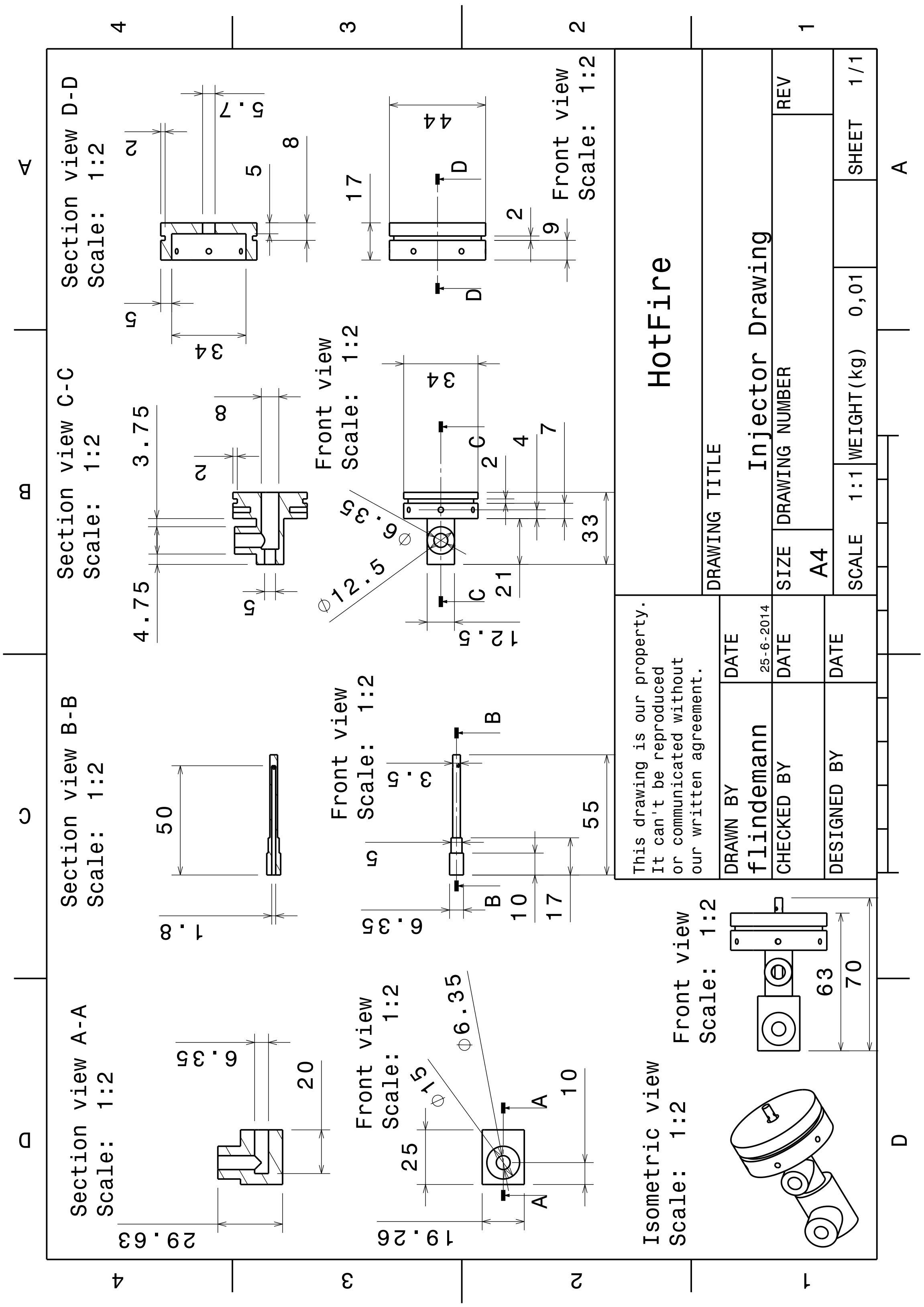

Figure A.4: Rocket model part: Injector

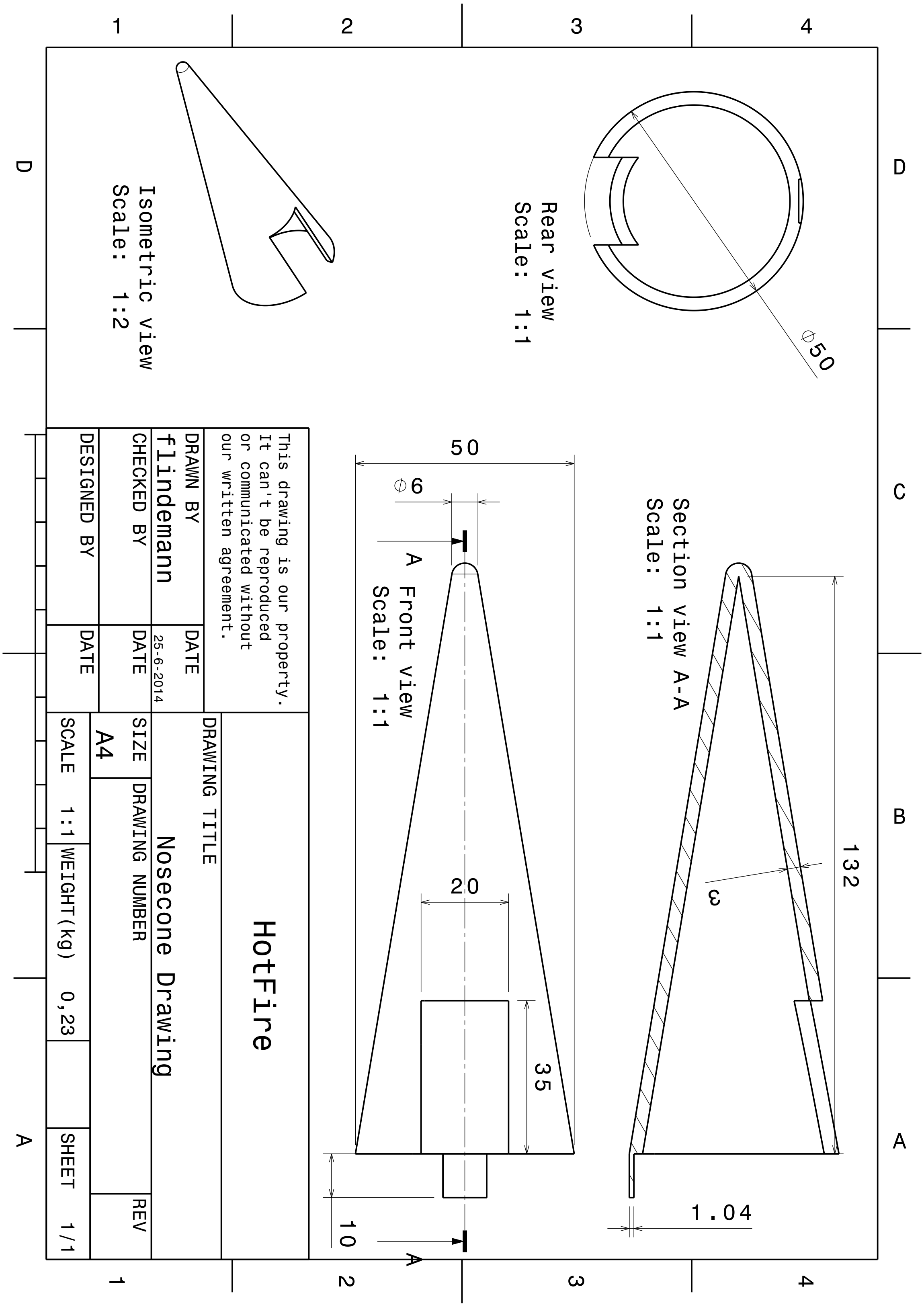

Figure A.5: Rocket model part: Nose cone

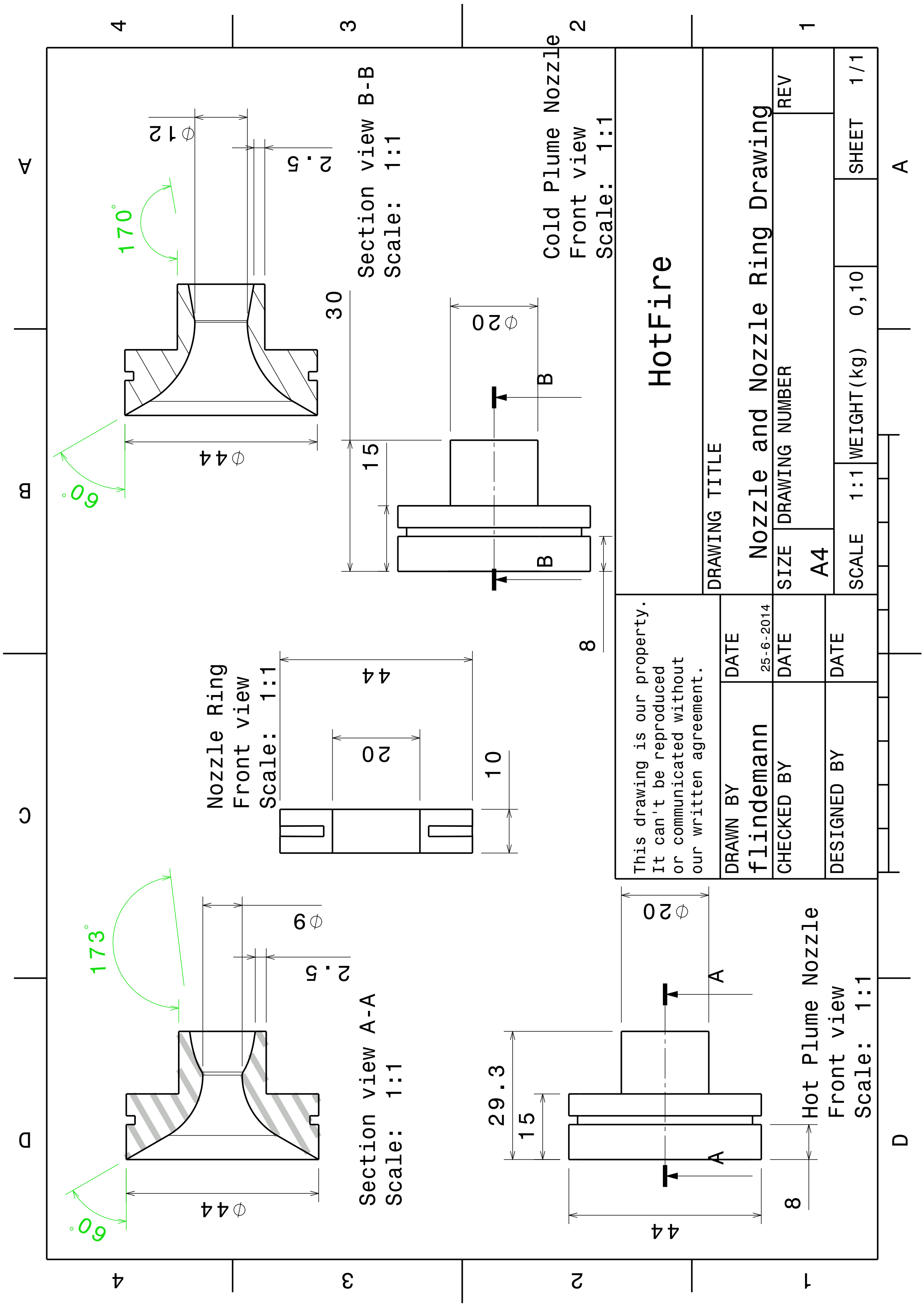

Figure A.6: Rocket model part: Nozzle

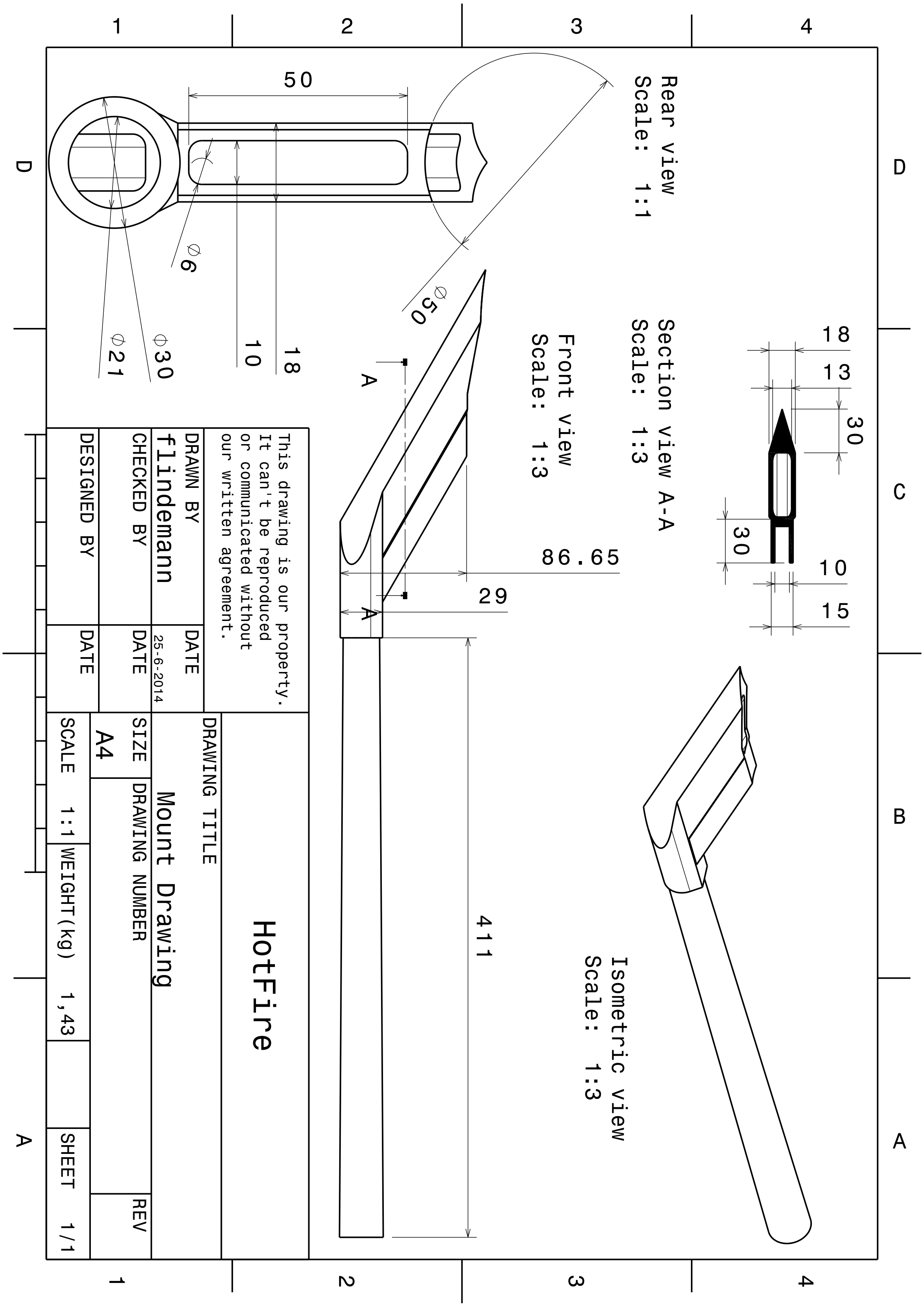

Figure A.7: Mount to which the rocket model is attached

B

Design Tool Outputs

The following figures are included in this appendix:

Figure B.1: Outputs of the Feed System design tool

Figure B.1a: Command line output

Figure B.1b: Tank pressure and temperature drop during operation

Figure B.2: Outputs of the Rocket Propulsion Analysis software tool for the selected design conditions

```
Fuel feed system pressures [bar]:
    in combustion chamber: 30.00
    before injector (inner tube): 36.58
    before bend: 36.86
    before feed line: 39.19
    before valve: 39.22
    before valve 2: 39.25
    before kerosene tank: 39.25
    ----------------------------------
    after pressure regulator: 39.25
    before pressure regulator
        (pressure in pressurant tank):
        max. 200.00, min. 189.76

Oxidizer feed system pressures [bar]:
    in combustion chamber: 30.00
    before injector (outer tube): 41.40
    before bend: 42.02
    before feed line: 45.60
    before valve: 45.68
    ----------------------------------
    after pressure regulator: 45.68
    before pressure regulator
        (pressure in pressurant tank):
        max. 200.00, min. 161.08
```

(a) Command line output

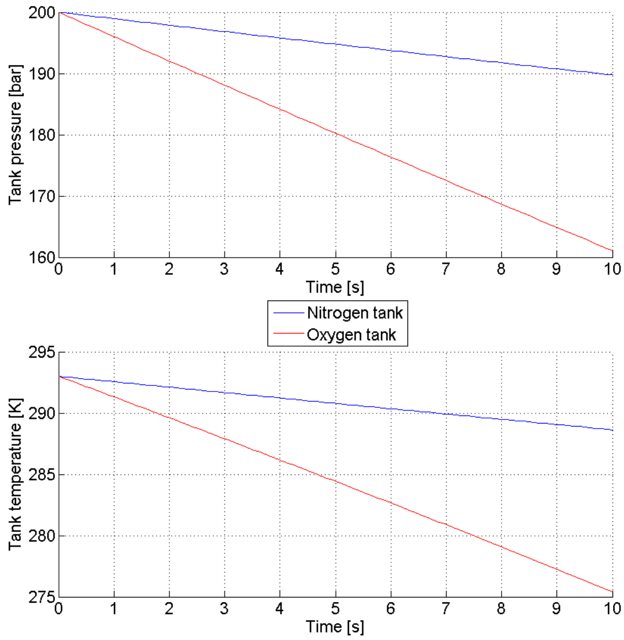

(b) Tank pressure and temperature drop during operation

Figure B.1: Outputs of the Feed System design tool

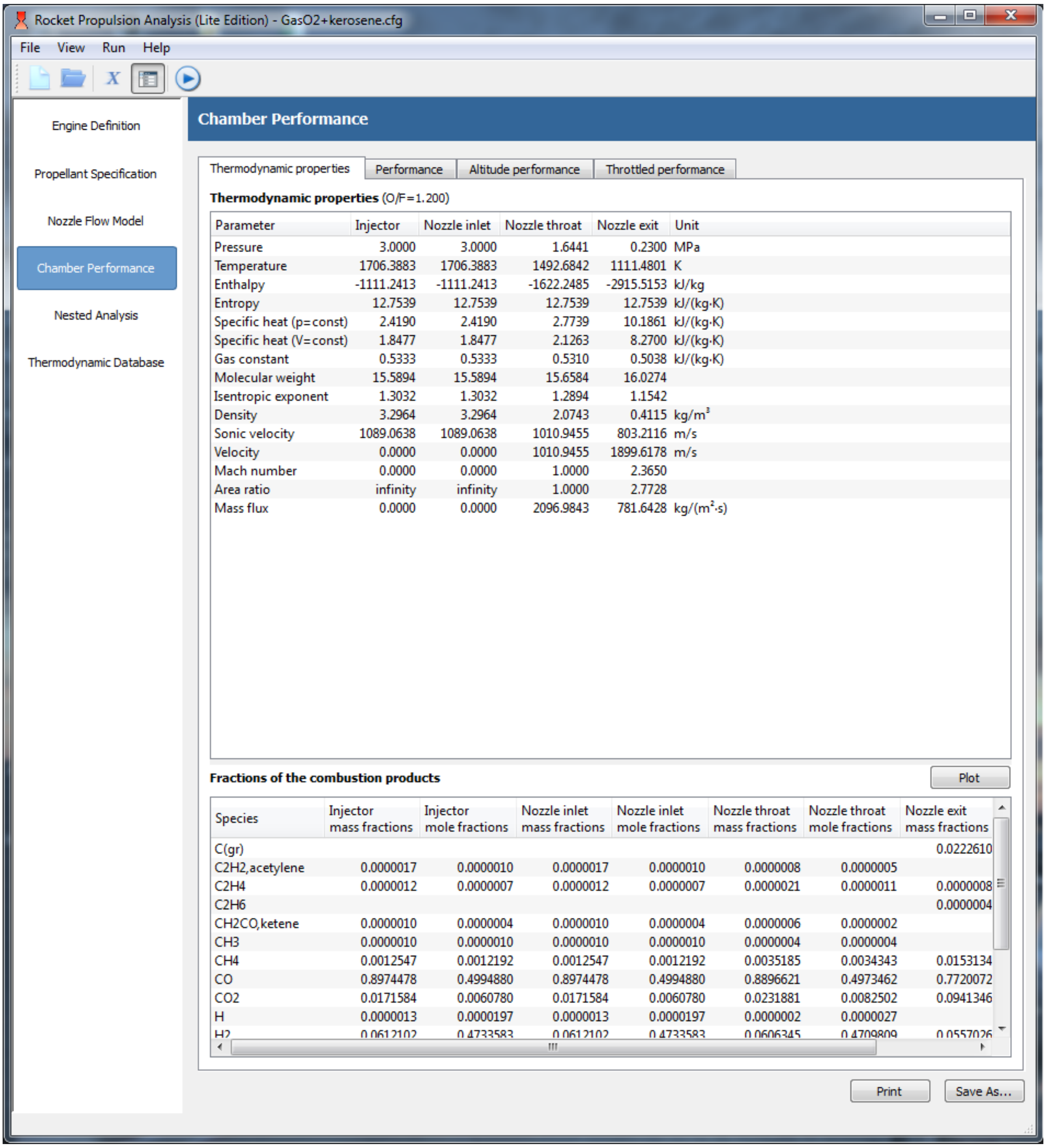

Figure B.2: Outputs of the Rocket Propulsion Analysis software tool for the selected design conditions